

UNIVERSITY OF BIRMINGHAM

ARTIFICIAL METALLOPEPTIDES AS MRI CONTRAST AGENTS

by

GIULIA MOLINARO

A thesis submitted to the University of Birmingham for the degree of

DOCTOR OF PHILOSOPHY

School of Chemistry

College of Engineering and Physical Sciences

University of Birmingham

August 2023

UNIVERSITY OF
BIRMINGHAM

University of Birmingham Research Archive

e-theses repository

This unpublished thesis/dissertation is copyright of the author and/or third parties. The intellectual property rights of the author or third parties in respect of this work are as defined by The Copyright Designs and Patents Act 1988 or as modified by any successor legislation.

Any use made of information contained in this thesis/dissertation must be in accordance with that legislation and must be properly acknowledged. Further distribution or reproduction in any format is prohibited without the permission of the copyright holder.

ABSTRACT

Concerns of potential Gd(III) toxicity, in particular related to the use of Gd(III)-based MRI contrast agents in patients with compromised renal function, has driven the development of MRI contrast agents with high efficiencies (defined as MRI relaxivities). The use of alternative paramagnetic metals than Gd(III), such as Mn(II), or different MRI techniques (chemical exchange saturation transfer, CEST) are currently being investigated. In this context, Cu(II) has been generally disregarded for use in MRI contrast agents because of its intrinsic low paramagnetism. This is despite it having other favourable physical properties, being less toxic than Gd(III), less expensive and its natural resources more easily exploited.

The work in this thesis is the first report of a Cu(II) coiled-coil with relaxivities comparable or even higher than its Gd(III) analogue and clinical Gd(III) agents, at a low, clinically relevant magnetic field (1.4 T). This is due to the inclusion of the metal ion within a macromolecule scaffold, which reduces molecular tumbling, and to the presence of two water molecules bound to Cu(II), compared to zero in the Gd(III) analogue.

The translation of the binding site along the coiled-coil and second-sphere mutations are explored to determine the impact of water accessibility to the binding site on Cu(II) affinity and MRI relaxivities. Again, Cu(II) complexes show different behaviour compared to the Gd(III) analogues. First-sphere mutations (such as introduction of His residues) are shown to lead to higher Cu(II) affinity constants. Moreover, this strategy provides a powerful tool to modulate relaxivities of the mutated complexes.

Mn(II) binding to the same class of coiled-coils is also explored, in terms of thermodynamic (Mn(II) affinity constants) and kinetic (Zn(II) transmetallation) stability. Such compounds show very high relaxivities, which can be attributed mainly to the presence of a large number of water molecules bound to Mn(II).

Coiled-coils with multiple binding sites are designed, aiming to introduce more than one metal (Gd or Cu) ion within the same scaffold. Here, a coiled-coil able to bind to three Ln(III) ions is reported. Similar conclusions as for the mono-binding metallopeptides are drawn: when a Gd(III) binding site is located at an extremity of the coil, the associated relaxivity is higher than for a complex with a buried binding site. In contrast, Cu(II) analogues present higher relaxivities in the presence of buried and hydrated binding sites. However, it is shown that two binding sites

should be separated by at least on heptad to enable water entering in the hydrophobic core of the coiled-coil.

Finally, this work reports for the first time a Nd(III)-based coiled-coil able to generate CEST effect. This opens up further opportunities for the use of coiled-coils binding to a number of lanthanides, others than Gd(III), as paraCEST contrast agents.

ACKNOWLEDGEMENTS

Firstly, I would like to thank my two supervisors, Dr. Anna Peacock and Dr. Melanie Britton. I am so grateful to them for their guidance in developing my PhD project and for the important life lessons I learnt from them.

I would also like to thank the Peacock and Britton groups, past members and present members, for their help and support. In particular, Dr. Claire Doswell, for the time spent with me on my NMR experiments, and also for her guidance at the beginning of my PhD; Joseph Phillips and Dr. Ivy Ghosh, who always had an open door for giving advice; Kate Hadley, for her friendly help and collaboration. A special mention must go to Dr. Valentina Borghesani for her guidance at the beginning of my PhD, and for the long conversations we had during these years. I also would like to thank Dr. Cécile LeDuff for her help with NMR and for her support.

In addition, I wish to thank Professor Mauro Botta and Professor Claudio Luchinat for useful discussions about my work and for their advice for understanding aspects of the chemistry of MRI contrast agents.

PUBLICATIONS

- Design of the elusive proteinaceous oxygen donor copper site suggests a promising future for copper for MRI contrast agents

  A. Shah (*), M. J. Taylor (*), G. Molinaro (*), S. Anbu, M. Verdu, L. Jennings, I. Mikulska, S. Diaz-Moreno, H. El Mkami and G. M. Smith, *PNAS*, 2023, 120, e2219036120.
  (*) A.S., M.J.T., and G.M. contributed equally to this work.

- A new class of MRI contrast agents based on copper(II) coiled-coils

  G. Molinaro, L. N. Slope, M. M. Britton, A. F.A. Peacock, Manuscript in preparation.

- Understanding the mechanism by which Gd(III) coiled coils achieve magnetic resonance relaxivity – a study into the water coordination chemistry

  S. L. Newton, A. Franke, G. Molinaro, A. Kenwright, D. J. Smith, I. Ivanovic-Burmazovic, M. M. Britton, A. F. A. Peacock, Accepted for publication by *Dalton Trans.*

ACRONYMS AND CODES

CA	Contrast agent
CC	Coiled-coil
CD	Circular Dichroism
CEST	Chemical Exchange Saturation Transfer
CPMG	Carr-Purcell-Meiboom-Gill experiment
CS	Curie spin
DC	Dipolar coupling
DCM	Dichloromethane
DF	Due ferri
DIPEA	N,N-diisopropylethylamine
DMF	Dimethylformamide
DOTA	Tetraxetan, $(CH_2CH_2NCH_2CO_2H)_4$
DPDP	Dipyridoxyl diphosphate
DTPA	Diethylenetriamine pentaacetate
EDTA	Ethylenediaminetetraacetic acid
EPR	Electron paramagnetic resonance
ESI-MS	Electrospray Mass Spectrometry
FID	Free Induction Decay
Fmoc	Fluorenylmethoxycarbonyl
GBCA	Gadolinium -based contrast agent
HBTU	(2-(1*H*-benzotriazol-1-yl)-1,1,3,3-tetramethyluronium hexafluorophosphate
HEPES	2-(4-(2-hydroxyethyl)piperazin-1-yl)ethanesulfonic acid
HOBt	Hydroxybenzotriazole
HPLC	High pressure liquid chromatography
HSA	Human serum albumin
IR	Inversion recovery experiment
IZ	Isoleucine-zipper
mdeg	Millidegrees
MRI	Magnetic Resonance Imaging
NHE	Normal hydrogen electrode

NMP	N-methyl-2-pyrrolidone
NMR	Nuclear Magnetic Resonance
NSF	Nephrogenic Systemic Fibrosis
PARACEST	Paramagnetic Chemical Exchange Saturation Transfer
PCS	Pseudo Contact Shift
PDB	Protein data bank
RP-HPLC	Reverse phase-high pressure liquid chromatography
SC	Scalar coupling
SPPS	Solid-phase peptide synthesis
TFA	Trifluoroacetic acid
UV	Ultraviolet
UV-Vis	Ultraviolet-Visible

PEPTIDE SEQUENCES

Table showing the peptide sequences presented in this thesis. Residues designed for metal binding are underlined and coloured red (Asp), blue (Asn) and green (His).

MB1-2	Ac-G IAAIEQK IAANEWK DAAIEQK IAAIEQK IAAIEQK G-NH_2
MB1C	Ac-G IAAIEQK IAAIEWK IAAIEQK IAAIEQK IAAIEQK G-NH_2
MB1-1	Ac-G IAANEWK DAAIEQK IAAIEQK IAAIEQK IAAIEQK G-NH_2
MB1-4	Ac-G IAAIEQK IAAIEQK IAAIEQK IAANEWK DAAIEQK G-NH_2
MB1-1 2F	Ac-G FAANEWK DAAIEQK IAAIEQK IAAIEQK IAAIEQK G-NH_2
MB1-1 2W	Ac-G WAANEQK DAAIEQK IAAIEQK IAAIEQK IAAIEQK G-NH_2
LS4-2	Ac-G IAAIEQK IAAHEWK DAAIEQK IAAIEQK IAAIEQK G-NH_2
CS1-2	Ac-G IAAIEQK IAAIEWK DAAIEQK IAAIEQK IAAIEQK G-NH_2
GM3	Ac-G IAAIEQK IAAIEWK HAAIEQK IAAIEQK IAAIEQK G-NH_2
GM4	Ac-G IAAIEQK IAADEWK HAAIEQK IAAIEQK IAAIEQK G-NH_2
CS1-1	Ac-G IAAIEWK DAAIEQK IAAIEQK IAAIEQK IAAIEQK G-NH_2
LS2-1,2	Ac-G IAAIEWK DAANEWK DAAIEQK IAAIEQK IAAIEQK IAAIEQK G-NH_2
LS2-1,3 21W	Ac-G IAAIEWK DAAIEQK IAANEWK DAAIEQK IAAIEQK IAAIEQK G-NH_2
LS2-1,3 21Q	Ac-G IAAIEWK DAAIEQK IAANEQK DAAIEQK IAAIEQK IAAIEQK G-NH_2
LS2-2,3	Ac-G IAAIEQK IAANEWK DAANEWK DAAIEQK IAAIEQK IAAIEQK G-NH_2
GM2	Ac-G IAAIEWK DAANEWK DAANEWK DAAIEQK IAAIEQK IAAIEQK IAAIEQK G-NH_2

AMINO ACIDS

A	Ala	Alanine
C	Cys	Cysteine
D	Asp	Aspartic acid
E	Glu	Glutamic acid
F	Phe	Phenylalanine
G	Gly	Glycine
H	His	Histidine
I	Ile	Isoleucine
L	Leu	Leucine
M	Met	Methionine
N	Asn	Asparagine
P	Pro	Proline
Q	Gln	Glutamine
R	Arg	Arginine
S	Ser	Serine
T	Thr	Threonine
U	Sec	Selenocysteine
V	Val	Valine
W	Trp	Tryptophan
Y	Tyr	Tyrosine

TABLE OF CONTENTS

Abstract **II**

Acknowledgements **IV**

Publications **V**

Acronyms and codes **VI**

Peptide sequences **VIII**

Amino acids **IX**

Chapter 1 – Introduction **1**

1.1 Overview 1

1.2 Introduction to NMR and MRI 1

1.3 MRI contrast agents 3

1.3.1 Gadolinium based contrast agents 4

1.3.2 Manganese based contrast agents 6

1.4 Theory of relaxation 7

1.4.1 Water coordination 9

1.4.2 Water residence time 11

1.4.3 Rotational correlation time 13

1.4.4 r_2 dependence to magnetic field, τ_m and τ_R 15

1.5 The use of copper(II) as relaxation agent 17

1.6 Macromolecular contrast agents 18

1.6.1 Nanoparticles, dendrimers, liposomes and micelles 18

1.6.2 Proteins and peptides 19

1.7 *De novo* designed metallopeptides 21

1.7.1 Coiled-coils formation and assembly – the hydrophobic core 21

1.7.2 Salt bridges, external positions and length of the coil 22
1.7.3 Introducing a metal binding site 23
1.7.4 Copper coiled-coils 24
1.7.5 Manganese metallopeptides and metal clusters 29
1.7.6 Lanthanide coiled-coils 30
1.8 Chemical Exchange Saturation Transfer (CEST) 33
1.8.1 CEST Contrast Agents 33
1.8.2 Lanthanides in paramagnetic CEST (paraCEST) contrast agents 35
1.9 The aim of this work 37
References 38
Chapter 2 – Experimental techniques **46**
2.1 Solid-phase peptide synthesis 46
2.2 Reverse-Phase High Performance Liquid Chromatography (RP-HPLC) 49
2.3 Mass spectrometry 50
2.4 UV-Visible spectroscopy 51
2.5 Emission spectroscopy 53
2.6 Circular Dichroism spectroscopy 54
2.7 Nuclear Magnetic Resonance (NMR) spectroscopy 55
2.7.1 Introduction to NMR 55
2.7.2 T_1 and T_2 relaxation 58
2.7.3 Experimental determination of T_1 and T_2 relaxation 59
2.7.4 Chemical Exchange Saturation Transfer (CEST) 62
2.8 Electron Paramagnetic Resonance (EPR) spectroscopy 63
References 65
Chapter 3 – A new copper(II)-based MRI contrast agent **67**
3.1 Introduction 67
3.2 Experimental 68

3.2.1 Materials ... 68
3.2.2 Peptide synthesis ... 69
3.2.3 Peptide purification and characterisation ... 69
3.2.4 UV-Vis spectroscopy ... 70
3.2.5 Circular Dichroism (CD) spectroscopy ... 70
3.2.6 Emission spectroscopy ... 71
3.2.7 Nuclear magnetic resonance ... 71
3.2.8 Relaxivity simulations ... 73
3.3 Results ... 73
3.3.1 Peptide design ... 73
3.3.2 Determining copper binding and complex stoichiometry ... 75
3.3.3 UV-Visible spectroscopy of *d-d* transitions ... 78
3.3.4 Folding kinetics and thermal stability ... 78
3.3.5 Evaluation of the required amount of peptide to ensure Cu(II) complexation ... 80
3.3.6 Relaxivity measurement ... 82
3.3.7 Prediction of parameters influencing relaxivity ... 85
3.3.8 Influence of HEPES buffer on relaxation times and relaxivities ... 88
3.3.9 Influence of pH on relaxation times and relaxivity ... 89
3.3.10 Cu(II) displacement in the presence of Zn(II) ... 91
3.3.11 Stability in Phosphate Buffer Saline (PBS) and in human serum ... 92
3.4 Discussion ... 99
3.5 Conclusions ... 100
References ... 101
Chapter 4 – Translation of the copper(II) binding site **104**
4.1 Introduction ... 104
4.2 Experimental ... 105
4.2.1 UV-Visible spectroscopy ... 105

4.2.2 Circular Dichroism (CD) spectroscopy 106
4.2.3 Emission spectroscopy 106
4.2.4 Nuclear magnetic resonance 107
4.2.5 Relaxivity simulations 108
4.3 Results 108
4.3.1 Peptide design 108
4.3.2 Copper binding: peptide folding, quenching of Trp fluorescence and log K_a determination 110
4.3.3 Copper binding: UV-visible spectroscopy of *d-d* transitions 113
4.3.4 NMR relaxation times at increasing peptide trimer equivalents and in the absence of Cu(II) 114
4.3.5 MRI relaxivities 115
4.3.6 Prediction of parameters influencing relaxivity 117
4.4 Discussion 119
4.5 Conclusions 121
References 122
Chapter 5 – Mutation of the residues in copper(II) first coordination sphere 123
5.1 Introduction 123
5.2 Experimental 124
5.2.1 UV-Visible spectroscopy 124
5.2.2 Circular Dichroism (CD) spectroscopy 124
5.2.3 Emission spectroscopy 124
5.2.4 Nuclear magnetic resonance 124
5.3 Results 126
5.3.1 Peptide design 126
5.3.2 Copper binding: peptide folding, quenching of Trp fluorescence and log K_a determination 127
5.3.3 Copper binding: peptide folding at higher concentration of peptide monomer . 132

5.3.4 Copper binding: UV-Visible spectroscopy of *d-d* transitions 133

5.3.5 Copper binding: folding kinetics and thermal stability 135

5.3.6 NMR relaxation times at increasing peptide trimer equivalents and in the absence of Cu(II) 137

5.3.7 MRI relaxivities 138

5.3.8 Influence of pH on metal binding and relaxivity 142

5.3.9 Cu(II) displacement in the presence of Zn(II) 145

5.4 Discussion 146

5.5 Conclusions 148

References 149

Chapter 6 – Manganese(II) coiled-coils **151**

6.1 Introduction 151

6.2 Experimental 152

6.2.1 UV-Vis spectroscopy 152

6.2.2 Circular Dichroism (CD) spectroscopy 152

6.2.3 Nuclear magnetic resonance 153

6.3 Results 155

6.3.1 Peptide design 155

6.3.2 Establishing peptide folding and log K_a determination for Mn(II) binding 157

6.3.3 Influence of peptide concentration on metal binding and peptide folding 158

6.3.4 Folding kinetics and thermal stability 159

6.3.5 MRI relaxivity at 1.4 T 160

6.3.6 NMR relaxation times as a function of magnetic field 162

6.3.7 Mn(II) displacement in the presence of Zn(II) 163

6.4 Discussion 164

6.5 Conclusions 166

References 168

Chapter 7 – Multi metallo coiled-coils **170**

7.1 Introduction ... 170

7.2 Experimental ... 171

7.2.1 UV-Vis spectroscopy ... 171

7.2.2 CD spectroscopy ... 171

7.2.3 Emission spectroscopy ... 172

7.2.4 Nuclear magnetic resonance ... 172

7.2.5 Relaxivity simulations ... 173

7.3 Results ... 174

7.3.1 Peptide design ... 174

7.3.2 Lanthanide binding ... 175

7.3.3 Copper binding ... 179

7.3.4 Precipitation ... 184

7.3.5 Relaxivity ... 184

7.3.6 Impact of rotational correlation times ... 186

7.4 Discussion ... 188

7.5 Conclusions ... 190

References ... 191

Chapter 8 – Exploring the use of lanthanide coiled-coils as paraCEST contrast agents **193**

8.1 Introduction ... 193

8.2 Experimental ... 195

8.2.1 Materials ... 195

8.2.2 Sample preparation ... 196

8.2.3 NMR spectra ... 196

8.3 Results ... 196

8.3.1 Identification of exchangeable protons ... 196

8.3.2 Z-spectrum ... 199

8.4 Discussion 199

8.5 Conclusions and future work 200

References 201

Chapter 9 – Conclusions, future work and applications **202**

9.1 Conclusions 202

9.2 Future work and applications 205

References 207

Appendix A – Analytical HPLC and mass spectra of pure peptides **208**

Appendix B – MATLAB scripts **224**

B.1 Script 1: r_1 as a function of r_{MH} and τ_m (Chapters 3 & 4) 224

B.2 Script 2: r_1 as a function of τ_R and τ_m (Chapter 7) 227

CHAPTER 1

INTRODUCTION

1.1 Overview

Magnetic Resonance Imaging (MRI) provides a powerful tool for medical diagnosis.[1, 2] It allows the visualisation of soft tissues in the body such as brain, muscles and heart without using ionising radiation, such as X-rays. Moreover, images with high spatial resolution (submillimetre) can be generated.[3] MRI contrast agents are used to improve the visibility of internal body structures. The most used compounds are Gd(III)-based contrast agents, which can shorten the NMR relaxation times of nuclei within body tissues following oral or intravenous administration.[4] Because of safety concerns for their use, the research is currently investigating alternative metal ions (such as Mn(II), able to provide a contrast enhancement comparable to Gd(III), but reduced toxicity.[5] Moreover, the use of more sensitive MR techniques such as chemical exchange saturation transfer (CEST) is studied.[6, 7]

The use of proteins and peptides-based contrast agents provides an opportunity to generate MRI contrast agents which combine biocompatibility, target selectivity and superior efficiency at clinically relevant magnetic fields.[8] This work investigates the use of Cu(II) and Mn(II) as alternative metals to Gd(III) in MRI contrast agents, by including the metals into peptides able to self-assemble into coiled-coils in the presence of metal ions. Moreover, their first and second sphere coordination spheres is modified to establish structure-performance/activity relationships. In addition, coiled-coils with multiple Gd(III) and Cu(II) binding sites are studied. Finally, the potential use of Ln(III)-based coiled-coils as CEST contrast agents is explored.

1.2 Introduction to NMR and MRI

MRI is based on Nuclear Magnetic Resonance (NMR), which employs non-ionising radio waves. NMR is a technique used to investigate the interactions between nuclear spins and an external magnetic field. The most studied system in clinical MRI is the interaction of water hydrogen nuclear spin (^{1}H, $S = 1/2$) with a strong external magnetic field.

In NMR, the relaxation process occurs after radio frequency (RF) pulses are applied and can be described using NMR relaxation times:

- **T_1, longitudinal (spin-lattice) relaxation:** the time constant of the exponential rise and recovery of the longitudinal magnetisation along the *z*-axis (Figure 1.1a,b), which corresponds to the orientation of the external magnetic field. It arises from the transfer of energy of the excited nucleus to its environment.
- **T_2, transversal (spin-spin) relaxation:** the time constant of the exponential decay of the magnetisation on the transversal *xy*-plane (Figure 1.1a,c). It is an exchange of energy that corresponds to spin dephasing on the transversal plane due to inhomogeneities of the environment.
- **T_2^*:** related to T_2, takes into account the inhomogeneity of the local magnetic field (B_0) (Equation 1)

$$\frac{1}{T_2^*} = \frac{1}{T_2} + \gamma \Delta B_0 \qquad (1)$$

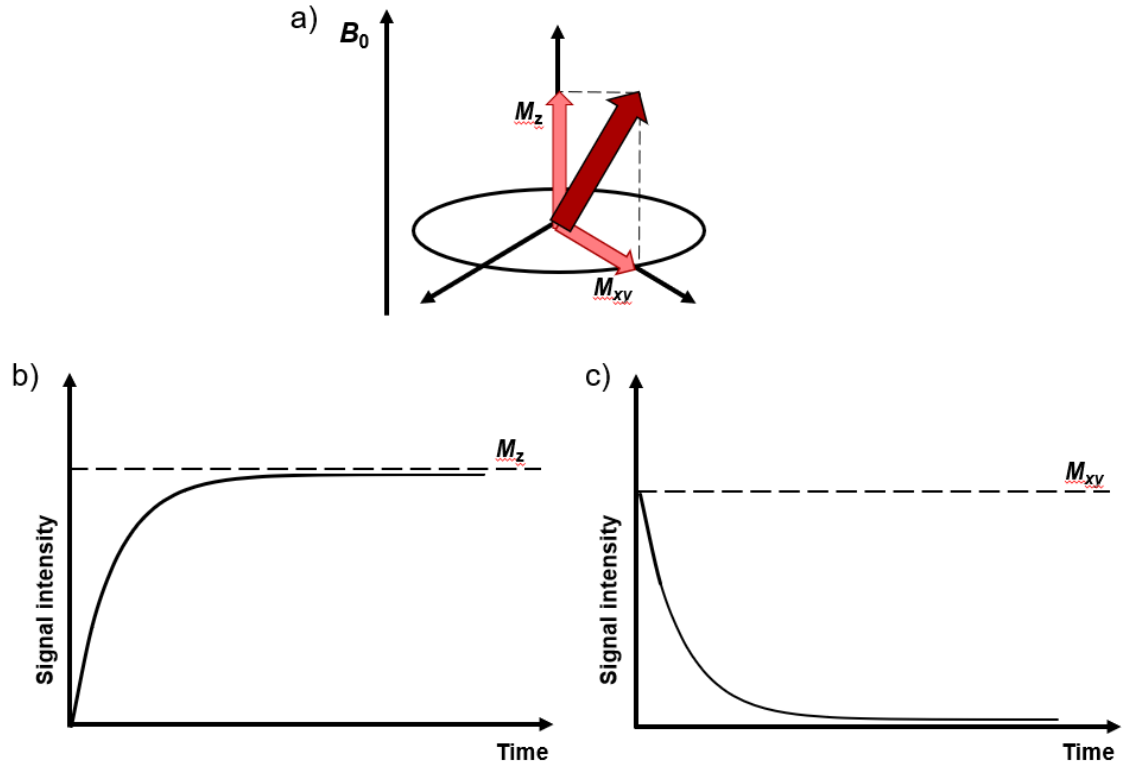


Figure 1.1: Diagram showing (a) M_z and M_{xy} components of the magnetisation; (b) Recovery of the magnetization along the *z*-axis; (c) Decay of the magnetisation on the *xy*-plane.

NMR signal intensity depends on different parameters such as proton density, T_1, T_2. T_2^* relaxation times and the pulse sequence applied.[1, 2, 4, 9] To generate MR images, the NMR signal

needs to be spatially detected by applying additional gradient coils in the three orthogonal directions $\boldsymbol{G}_x$, $\boldsymbol{G}_y$, and $\boldsymbol{G}_z$. The differences in frequency measurements can be used to distinguish MR signals at different positions in space and allow an image reconstruction in three dimensions.[10]

1.3 MRI contrast agents

The contrast within an MR image is generated by differences in the NMR relaxation times of water protons, which are mainly due to variable dipolar interactions, different chemical environment, diffusion and chemical exchange.[11-13] By setting specific RF pulse sequences, changes in T_1 (T_1-weighted) and T_2 (T_2-weighted) can be underlined so that the characteristics of a particular tissue can be emphasised.[14]

Since image contrast resolution is sometimes not optimal for underlying pathological features such as tumors,[1, 4, 9] the use and development of chemical entities known as contrast agents can help to highlight anatomic and pathologic features which would be otherwise invisible.[2, 3, 15] MRI contrast agents are not directly imaged, but they are indirectly detected by how they affect the signal of surrounding water molecules.

Contrast agents that shorten NMR T_1 and T_2 proton relaxation times are the most common. They are generally named positive contrast agents if they affect mainly T_1 and negative contrast agents if they shorten preferentially T_2. Positive contrast agents generate an increase in signal and brighter image in T_1-weighted images in the area where they distribute, while negative contrast agents provide darker images in T_2-weighted images as they are correlated to a fast signal loss.

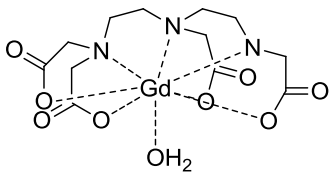
The most common positive T_1-contrast agents are paramagnetic metal complexes. The presence of unpaired electrons determines high magnetic susceptibilities which leads to more efficient relaxation processes.[3] Their efficiency in increasing relaxation rates ($1/T_1$ and $1/T_2$) is measured as MRI relaxivity (r_1 and r_2, respectively). Relaxivity depends on a series of molecular parameters relative to the contrast agent, such as the number of water molecules in the metal hydration sphere, the relative molecular exchange with bulk water and the molecular tumbling of the overall complex. External parameters that influence relaxivity are the static magnetic field strength and temperature. The factors affecting relaxivity are explored in Section 1.4.

1.3.1 Gadolinium based contrast agents

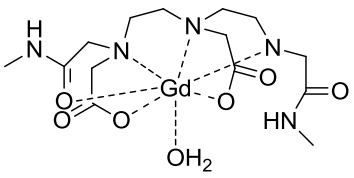
The most common paramagnetic ion in use as MRI contrast agent is gadolinium, Gd(III), with 7 unpaired 4*f* electrons that produce a strong magnetic moment capable of inducing magnetic relaxation in nearby nuclei.[16] Moreover, its *f*-orbitals are isotropic, meaning that there is a symmetric distribution of electrons within the orbitals. This leads to long electron-spin relaxation times, in the order of ns, which finally allow an efficient proton relaxation in proximity of Gd(III).[4] Electron relaxation is discussed in Section 1.4. Since it is also highly toxic in its free form due to similar coordination chemistry to calcium(II) ions,[17] a series of acyclic and macrocyclic ligands have been developed to decrease the toxicity of the metal substantially and by obtaining thermodynamically and kinetically stable complexes *in vivo* (Figure 1.2a). Generally, acyclic ligand complexes suffer from low kinetic stability.[4, 7, 18] The use of cyclic ligands solves this problem because they form gadolinium complexes with high thermodynamic and kinetic stability,[4, 7, 18] with very similar relaxivities (Figure 1.2b).[3, 4] The Gd-based contrast agents (GBCAs), which have been approved for use in diagnostics, are generally all stable with respect to dissociation *in vivo*.[4]

GBCAs can display negative side effects. If their elimination from the body through glomerular filtration is not efficient, GBCAs can concentrate in the kidneys and the complex can undergo dechelation and release free Gd(III).[19] In 2006, it became apparent that the use of GBCAs increased the risk to develop nephrogenic systemic fibrosis in patients with severe kidney dysfunction.[20] Therefore, the use of other paramagnetic metals is actively being investigated in an effort to obtain MRI contrast agents with a safer profile.

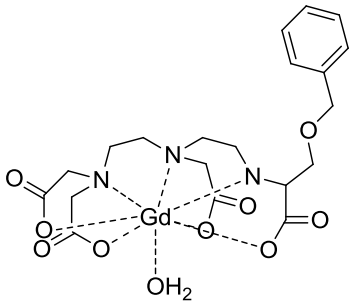
a)



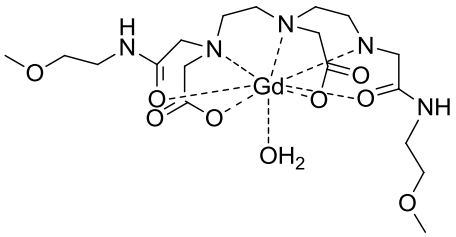
[Gd(DTPA)(H$_2$O)]$^{2-}$ Magnevist



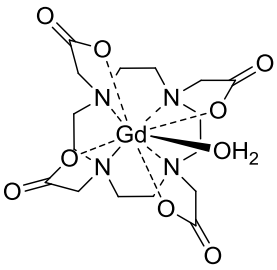
[Gd(DTPA-BMA)(H$_2$O)] Omiscan



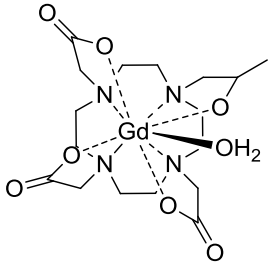
[Gd(BOPTA)(H$_2$O)]$^{2-}$ MultiHance



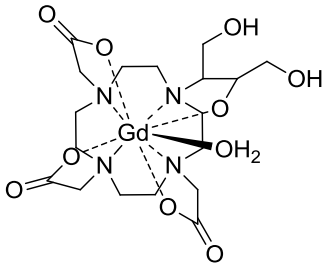
[Gd(DTPA-BMEA)(H$_2$O)] OptiMARK



[Gd(DOTA)(H$_2$O)]$^{-}$ Dotarem



[Gd(HP-DO3A)(H$_2$O)] ProHance



[Gd(DO3A-butrol)(H$_2$O)] Gadovist

b)

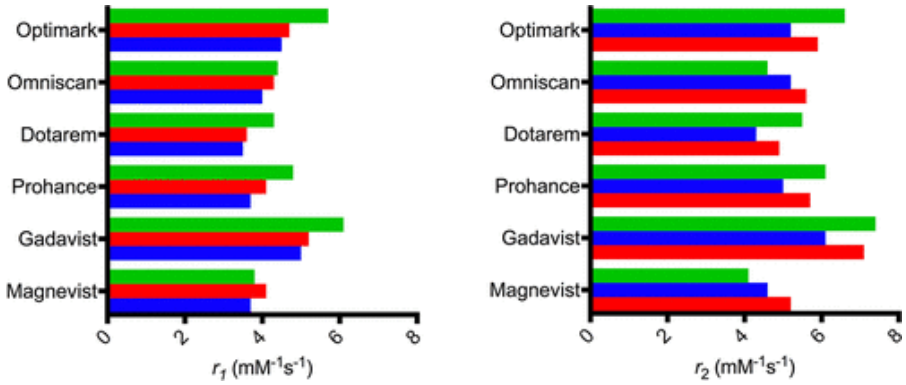


Figure 1.2: a) Chemical structures of clinically used GBCAs with relative chemical and product name; b) Comparison of GBCAs r_1 relaxivities at 0.47 T (green), 1.5T (red) and 3 T (blue), (Reprinted with permission from J. Wahsner, E. M. Gale, A. Rodríguez-Rodríguez and P. Caravan, *Chem. Rev.*, 2018, 119, 957-1057. Copyright 2018 American Chemical Society)

1.3.2 Manganese based contrast agents

Manganese, in the form of Mn(II) ion, has fewer unpaired electrons than Gd(III), resulting in lower magnetic moments.[21] However, it is an attractive alternative, as it is an essential metal ion which contribute to numerous biological functions. Mn(II) is an essential cofactor for different enzymes, such as arginase, pyruvate carboxylase and manganese superoxide dismutase.[22] Its five unpaired electrons, long electron-spin relaxation times similar to Gd(III) and fast water exchange, result in good relaxivity of the related compounds.[23, 24] Therefore, its use in MRI contrast agents offers a valuable alternative to Gd(III). Moreover, an efficient system of regulation via biliary excretion is adopted by the body (in mice, LD50 of $GdCl_3$[25] 100-200 mg/kg compared to $MnCl_2$[26] 1330 mg/kg), making these compounds a valuable alternative to GBCAs in case of renal insufficiency.[5]

Despite the important biological roles of Mn(II), large doses of this metal ion are toxic.[27, 28] Overexposure to Mn(II) can develop neurological diseases, such as manganism, a form of Parkinsonism.[29] Therefore, acyclic and cyclic complexes have been designed to prevent dissociation and the associated acute toxicity.

Usually, Mn(II) has coordination numbers of 6 or 7. In order to show sufficient efficiency as contrast agent, at least one water molecule must be bound to Mn(II) (see Section 1.4.1). However, this often leads to low thermodynamic and kinetic stability. Finding a balance between high relaxivity and stability is the main challenge associated with the development of Mn(II) contrast agents.

Research focused on increasing Mn(II) complex stability, has led to PyC3A,[5] a hexadentate ligand that forms a 7-coordinate ternary complex with Mn(II) (Figure 1.3). It was shown to have a r_1 comparable to Gd(DTPA) and Gd-DOTA and excreted via hepatobiliary and renal pathways.

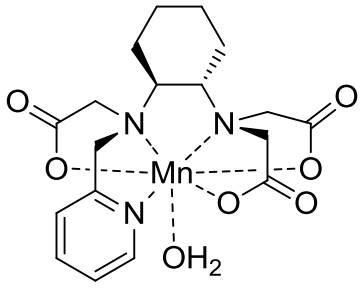


Figure 1.3: Chemical structure of [Mn(PyC3A)(H_2O)].

1.4 Theory of relaxation

In this section, the molecular parameters that modulate MRI relaxivity are explored, with a focus on the parameters that can be tuned to optimise relaxivity. The first theories of relaxation were firstly introduced by Bloembergen, Purcell and Pound, which were further developed by Solomon and Morgan.[11, 30-32] In a metallo-complex, different hydration spheres can be identified, inner-sphere, second-sphere and outer-sphere (Figure 1.4). Relaxivity arising from these three solvation spheres contribute to overall relaxivity (Equation 2). Water directly coordinated to the metal center is defined as inner-sphere water and its contribution to relaxivity is given by the number of molecules in the sphere q, their relaxation T_{1M} and residence time τ_M in the solvation sphere (Equation 3). Second-sphere is constituted by water hydrogen-bonded to inner sphere water or to the ligand. Second-sphere relaxivity is governed by the same parameters as inner-sphere (Equation 4) appropriately modified (generally a higher number of water molecules are involved with shorter residence times).

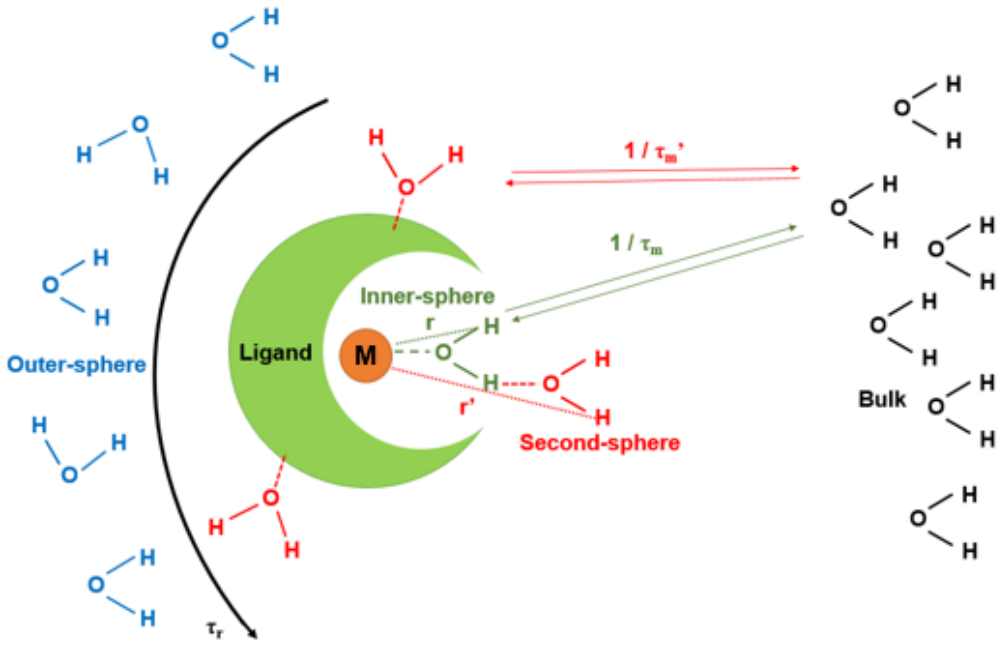


Figure 1.4: Representation of metal complex hydration spheres, with rotational correlation time τ_R. Inner-sphere water is directly bound to the metal, with distance r between the metal ion and the water protons, and water residence time τ_m. Second-sphere is hydrogen-bonded either to inner-sphere water or to the complex and with distances r' and residence times τ_m'. Outer-sphere is not directly bound to the complex.

$$r_i = r_i^{IS} + r_i^{SS} + r_i^{OS}; i = 1,2 \tag{2}$$

$$r_i^{IS} = \frac{q/[H_2O]}{T_{iM} + \tau_M}; i = 1,2 \tag{3}$$

$$r_i^{SS} = \frac{q'/[H_2O]}{T_{iM}{}' + \tau_M{}'}; i = 1,2 \tag{4}$$

The mechanisms that lead to paramagnetic relaxation (T_{iM}) are dipolar coupling (DC), scalar coupling (SC) and Curie spin relaxation (CS).[7] Dipolar coupling refers to the coupling between the unpaired electrons on the paramagnetic ion and the nuclear spin of water hydrogen (Equation 5 and Equation 8), whereas scalar coupling results from contact between the spins (Equation 6 and Equation 9). In 1962, Gueron described a third mechanism defined as Curie spin relaxation.[33] This arises from dipolar interaction of the nuclear spin with the thermal average of electron spins (defined as Curie spin) and contributes significantly at high fields (Equation 7 and Equation 10).

$$\frac{1}{T_{1M,\mathrm{DC}}} = \frac{2}{15}\left(\frac{\mu_0}{4\pi}\right)^2 \frac{\hbar^2\gamma_S^2\gamma_H^2}{r_{MH}^6} S(S+1)\left(\frac{3\tau_{c1}}{1+\omega_H^2\tau_{c1}^2} + \frac{7\tau_{c2}}{1+\omega_S^2\tau_{c2}^2}\right) \tag{5}$$

$$\frac{1}{T_{1M,\mathrm{SC}}} = \frac{S(S+1)}{3}\left(\frac{A}{\hbar}\right)^2 \left(\frac{\tau_{sc2}}{1+\omega_S^2\tau_{sc2}^2}\right) \tag{6}$$

$$\frac{1}{T_{1M,\mathrm{CS}}} = \frac{2}{5}\left(\frac{\mu_0}{4\pi}\right)^2 \frac{\omega_I^2\mu_B^4\mu_{eff}^4}{(3k_bT)^2 r_{MH}^6}\left(\frac{3\tau_{Cu}}{1+\omega_I^2\tau_{cs}^2}\right) \tag{7}$$

$$\frac{1}{T_{2M,\mathrm{DC}}} = \frac{1}{15}\left(\frac{\mu_0}{4\pi}\right)^2 \frac{\hbar^2\gamma_S^2\gamma_H^2}{r_{MH}^6} S(S+1)\left(4\tau_{c1} + \frac{3\tau_{c1}}{1+\omega_H^2\tau_{c1}^2} + \frac{13\tau_{c2}}{1+\omega_S^2\tau_{c2}^2}\right) \tag{8}$$

$$\frac{1}{T_{2M,\mathrm{SC}}} = \frac{S(S+1)}{3}\left(\frac{A}{\hbar}\right)^2 \left(\frac{\tau_{sc2}}{1+\omega_S^2\tau_{sc2}^2} + \tau_{sc1}\right) \tag{9}$$

$$\frac{1}{T_{1M,\mathrm{CS}}} = \frac{1}{5}\left(\frac{\mu_0}{4\pi}\right)^2 \frac{\omega_I^2\mu_B^4\mu_{eff}^4}{(3k_bT)^2 r_{MH}^6}\left(4\tau_{Cu} + \frac{3\tau_{Cu}}{1+\omega_I^2\tau_{cs}^2}\right) \tag{10}$$

Here, S is the spin quantum number, r_{MH} is the ion-proton distance, ω_H is the Larmor frequency of the proton (rad/s), ω_s is the Larmor frequency of the electron, γ_H and γ_S are the proton and electron gyromagnetic ratio, respectively, g_e is the electronic g-factor ($g_e = 2$), μ_B is the Bohr magneton, μ_{eff} is the magnetic moment of the molecule, μ_0 is the permittivity of vacuum, $A/\hbar$ is the hyperfine coupling constant between the ion and the hydrogen nucleus, k_B is the Boltzmann constant, and T is the absolute temperature. Because the electron Larmor frequency ω_s is much higher than the proton frequency ω_I, the product $\omega_s\tau_{c2}$ becomes very large at magnetic fields above 0.1 T. Therefore, many of the terms in Equations 5-10 can be neglected.[3] In Gd(III) and Mn(II)

compounds, dipolar relaxation is the only contribution to T_1 relaxation at magnetic fields higher than 1.5 T.[7] On the other side, in T_2 relaxation all three mechanisms are involved.

The relaxation mechanisms described above, are modulated by correlation times, one for each mechanism (for dipolar coupling τ_C, for scalar coupling τ_{SC} and for Curie spin relaxation τ_{CS}). Rotational correlation time τ_R, water residence time τ_m and electron relaxation time τ_s affect correlation times as in Equations 11, 12, 13 which are valid at magnetic fields above 1.5 T.

$$\frac{1}{\tau_{c,i}} = \frac{1}{\tau_m} + \frac{1}{\tau_R} + \frac{1}{\tau_s} \; ; \; i = 1,2 \tag{11}$$

$$\frac{1}{\tau_{sc,i}} = \frac{1}{\tau_m} + \frac{1}{T_{i,e}} \; ; \; i = 1,2 \tag{12}$$

$$\frac{1}{\tau_{cs}} = \frac{1}{\tau_m} + \frac{1}{\tau_R} \tag{13}$$

Electron relaxation τ_s in Gd(III) and Mn(II) complexes is the result of zero-field-splitting interactions (ZFS).[34] For example, in a symmetric octahedral complex such as $[Mn(H_2O)_6]^{2+}$, only transient ZFS contribute to relaxation and these arise from temporal distortions of symmetry. Bloembergen and Morgan described the contribution of longitudinal (T_{1e}) and transverse (T_{2e}) electron relaxation in the presence of ZFS using Equations 14 and 15, where electron relaxation times are modulated by the correlation time τ_v in the order of picoseconds and by the mean squared amplitude of the ZFS $\Delta^2 = (2/3)D^2 + 2E^2$ where D and E are crystal field parameters. Electron relaxation is generally in ns range at very low fields (<0.5 T). This value becomes very long and negligible at higher fields according to correlation time τ_v.

$$\left(\frac{1}{T_{1e}}\right)^{ZFS} = \frac{2}{50}(4S(S+1)-3)\Delta^2\left(\frac{\tau_v}{1+\omega_S^2\tau_v^2} + \frac{4\tau_v}{1+4\omega_S^2\tau_v^2}\right) \tag{14}$$

$$\left(\frac{1}{T_{2e}}\right)^{ZFS} = \frac{1}{50}(4S(S+1)-3)\Delta^2\left(3\tau_v + \frac{5\tau_v}{1+\omega_S^2\tau_v^2} + \frac{2\tau_v}{1+4\omega_S^2\tau_v^2}\right) \tag{15}$$

1.4.1 Water coordination

As for Equation 3, relaxivity directly depends on the number q of water molecules coordinated to the metal (inner-sphere water) or hydrogen bonded to either inner-sphere water or the metal complex (second-sphere water). Moreover, there is a 6th power dependence to the distance between the metal ion and the proton on the water molecule. Distances are normally 2.7-3.3 Å for Gd(III) complexes or even lower for Mn(II) compounds. This determines a stronger

influence of inner-sphere water molecules than second-sphere, to the overall relaxivity. Equation 4 shows that a very simple method to improve relaxivity is to increase the number of inner-sphere (and second-sphere) water molecules. This could be achieved by reducing the number of donor atoms from 9 to 8 or 7 in the case of Gd(III) and lower than 7 or 6 in the case of Mn(II).[3, 15, 35] However, the major drawback of this strategy, is that thermodynamic and kinetic stabilities are consequently reduced, especially in the case of manganese compounds.[5, 36] In addition to this, endogenous anion ligands, such as phosphates or bicarbonates, can potentially coordinate the metal instead of water and reduce the relaxivity.[36]

Second- and outer-sphere water

Water in the second-sphere also contributes to the overall relaxivity, generally 40% in mono-hydrated Gd(III) complexes at clinically relevant magnetic fields.[37] The discrimination with inner-sphere water is that this is directly coordinated to the metal while second-sphere interacts by hydrogen bonding with inner-sphere water or to the complex. As shown in Equation 5, the same parameters that affects inner-sphere relaxivity also modulates second-sphere relaxivity, with faster water exchange values, higher number of water molecules in the solvation shell at longer distances. On the other side, the second-sphere water molecules can be differentiated from outer-sphere water molecules (as described by Freed[38, 39]) because the existence of interactions between the second-sphere water and the complex implies water residence times longer than simple diffusion (which governs outer-sphere relaxation).[37] Moreover, as with inner-sphere water relaxation, second-sphere relaxation is also field-dependent. Consequently, long rotational correlation times are associated with high second-sphere contribution to relaxivity at low magnetic fields. This can be used to discriminate between the presence of second-sphere or outer-sphere relaxation. An example of this is given by $[Gd(C_{11}\text{-DOTP})]^{5-}$, where $q = 0$. [40] The NMRD profile (Figure 1.5)[36] of $[Gd(C_{11}\text{-DOTP})]^{5-}$ shows that its relaxivity is slightly higher than for $[Gd(L0)]^{4-}$, a Gd(III) triethylenetetraamine hexaacetate complex with similar molecular weight.[36] However, when rotation is slowed by binding of the complexes to serum albumin, the relaxivity of the $[Gd(C_{11}\text{-DOTP})]^{5-}$ adduct is markedly increased, more than in the case of $[Gd(L0)]^{4-}$ bound to serum albumin. An explanation of that is that in $[Gd(C_{11}\text{-DOTP})]^{5-}$ a second sphere contribution to relaxivity arises from the exchangeable protons of its negatively charged phosphonate groups.[36] In 2022, Botta and co-workers developed a nanogel with $[Gd(DOTP)]^{5-}$ ($q = 0$) as cross-linkers.[41] At 20 MHz, they measured a relaxivity value of 78.0 $mM^{-1}\ s^{-1}$ about 20 times greater than that of the free complex. They concluded that second sphere water molecules generate a sufficiently strong and slow-exchanging hydrogen bonding network with the complex.

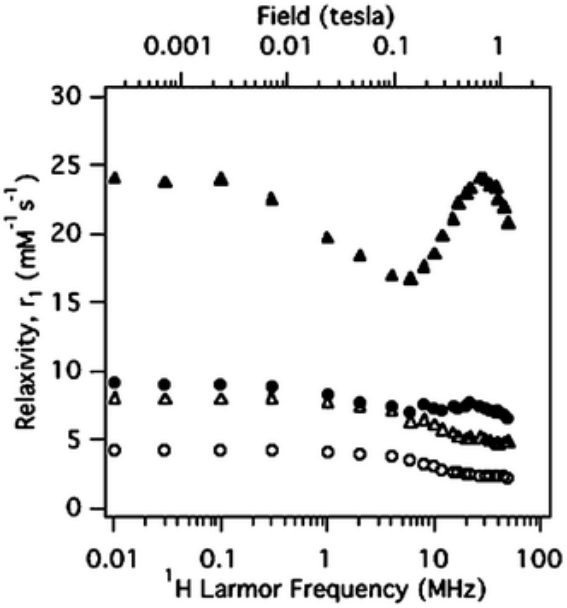


Figure 1.5: NMRD profile showing relaxivity of $[Gd(L0)]^{4-}$ (circles) and $[Gd(C_{11}\text{-DOTP})]^{5-}$ (triangles) in the presence (solid symbols) or absence (open symbols) of HSA at 25°C, pH 7.4. (Reprinted with permission from P. Caravan, *Chem. Soc. Rev.*, 2006, 35, 512-523)

1.4.2 Water residence time

Water residence time refers to the time when a water molecule is bound to the metal in a complex. To provide an efficient relaxation, water molecules need to be in exchange with bulk water at a rate denominated k_{ex}, where $k_{ex} = 1/\tau_m$. This chemical exchange should be fast, to allow a large number of water molecules to get in proximity to the metal center. However, it should be long enough to efficiently lead to relaxation of the bound water. In the fast exchange limit, τ_m becomes the limiting factor to correlation time (Figure 1.6). Moreover, the plot shows that there is an optimal range of water exchange rates that provide high relaxivity but this happens only if τ_R is optimized.[4] In $[Gd(H_2O)_8]^{3+}$, water exchange is fast ($k_{ex}^{298} = 8.04\times10^8$ s^{-1}) and it is reduced when Gd(III) is complexed,[42] with the slowest exchange measured for DOTA-tetraamide derivates ($k_{ex}^{298} = 5.0\text{-}12.5\times10^4$ s^{-1}).[21] Water exchange in $[Mn(H_2O)_6]^{2+}$ is slower ($k_{ex}^{298} = 2.1\text{-}2.8\times10^7$ s^{-1})[43, 44] and Mn^{2+} complexation generally leads to exchanges, ranging from 10^6 to 10^9 s^{-1}.[45, 46]

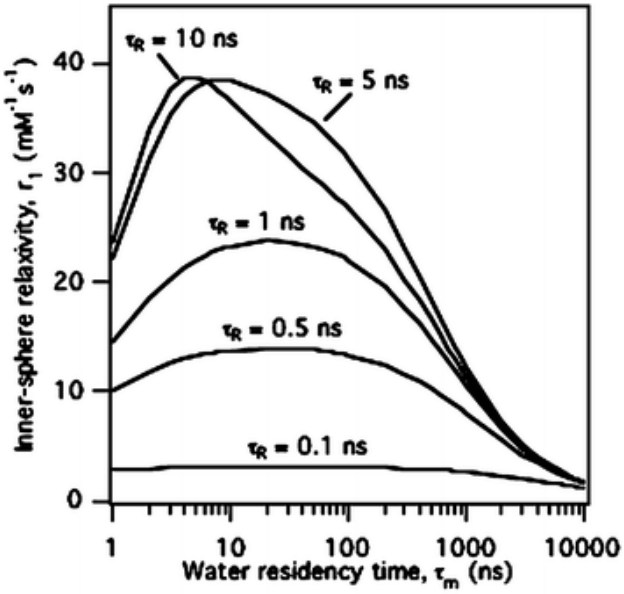


Figure 1.6: Simulation of inner sphere relaxivity of a Gd(III) complex as a function of water residency time for different rotational correlation times at 1.5 T for a q = 1 compound with long electronic relaxation time (τ_s >10 ns). (Reprinted with permission from P. Caravan, J. J. Ellison, T. J. McMurry and R. B. Lauffer, *Chem. Rev.*, 1999, 99, 2293-2352. Copyright 1999 American Chemical Society)

Beside the nature of the metal ion in the complex, some of the main factors that influence the water residence time are:[47, 48]

- Modification of the charge density of the metal and of the overall complex charge

  Water exchange can be profoundly modulated by the donor atoms to the metal, as water residence time is proportional to the Lewis acidity of the metal. Thus, negatively charged electron donor ligands (*e.g.,* carboxylate donors) leads to faster exchange kinetics[42] than analogues with electron withdrawing ligands[47] (*e.g.,* amide donors). Moreover, negatively charged complexes usually present faster exchange than neutral or positively charged complexes.[49, 50]

- Modification of ligand side chains

  The polarity of the ligand side chain also influences water exchange due to hydrogen bonding of water to the complex which reduces exchange. Hermann and co-workers,[51] showed that when a carboxylic acid group was substituted with a phenyl side chain containing a phosphate group in the DTPA chelate, τ_m was reduced from 303 to 90 ns.

- Modification of steric hindrance at the water-binding site

  Steric hindrance at the water coordination site influences water exchange rates. High steric hindrance leads to faster water exchange in complexes when water molecules exchange through a dissociative mechanism as steric hindrance helps dissociation of the coordinated

water molecule (rate-limiting step).[48] Oppositely, sterically preventing water access using bulky side chains is effective on slowing water exchange for complexes undergoing associative exchange, due to reduction of local water concentration around the metal.[52, 53]

1.4.3 Rotational correlation time

Rotational correlation time is related to molecular tumbling which generates a continuous reorientation of the metal ion and solvent vectors.[4] The reorientation of a molecule is influenced by its shape and size. If the size of a chelate can be approximate to a sphere, the Stokes-Einstein equation can be used where a is the radius of the sphere, η is the viscosity of the medium, B is the Boltzmann constant and T is the absolute temperature (Equation 16).

$$\tau_R = \frac{4\pi a^3}{3KT} \tag{16}$$

For paramagnetic ions with long τ_s, rotational correlation time is the factor that most contributes to correlation time at low magnetic fields, but this enhancement is limited by τ_m (and τ_s at very low magnetic fields).[23] Since reciprocal correlations times are involved in Equations 11, 12, 13, the shortest correlation time is the factor that contributes to the overall correlation time more strongly.

The strategies for reducing molecular tumbling of metal complexes are different. The complex can be covalently attached to a macromolecule such as a protein (which generally has $\tau_R \geq 10$ ns) or can be designed to non-covalently bind to larger molecules in tissues or to distribute in tissues with high microviscosity.[23]

MS-325 is a remarkable example of an approved blood pool contrast agent which is able to modulate its relaxivity upon binding to human serum albumin (HSA).[54-56] After complexation to serum through non-covalent interactions between the diphenylcyclohexylphosphodiester group on the agent and site II in HSA, the relaxivity was enhanced 3- to 6-fold (Figure 1.7). This was attributed to a 60- to 100-fold increase in rotational correlation time (τ_R = 0.1 ns free to 10.1 ± 2.6 ns bound), due to the complex being part of a macromolecular scaffold. NMRD profiles suggested that binding to HSA leads to longer inner-sphere water residence time (τ_m = 69 ±20 ns free to 170 ± 40 ns bound, reasons were unclear), to an increased second-sphere water residence times (above 1 ns) and a reduction in the electron relaxation rate (1.1×10^9 s^{-1} free to 2.0×10^8 s^{-1} bound).

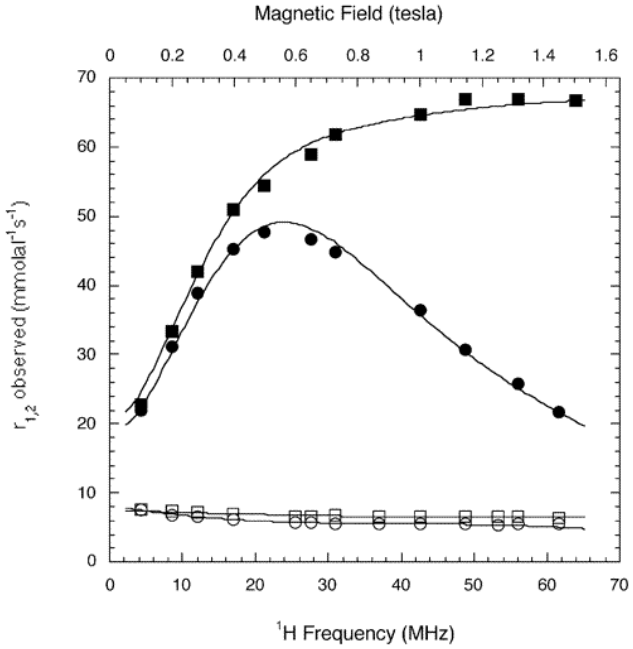


Figure 1.7: Plot of measured longitudinal (r_1, circles) and transverse (r_2, squares) ^{1}H-MRI relaxivity for MS-325 in the presence (filled symbols) and in the absence (open symbols) of 22.5% (w/v) HSA at 37°C, PBS buffer, pH 7.4. (Reprinted with permission from P. Caravan, N. J. Cloutier, M. T. Greenfield, S. A. McDermid, S. U. Dunham, J. W. Bulte, J. C. Amedio, R. J. Looby, R. M. Supkowski and W. D. Horrocks, *J. Am. Chem. Soc.*, 2002, 124, 3152-3162. Copyright 2002 American Chemical Society)

Since the contribution of rotational correlation time is field-dependent, it should be noted that the previous strategies are effective to enhance inner and second-sphere relaxation only at low magnetic fields. At high fields this strategy is no longer able to provide high relaxivities, and at very low fields τ_s becomes the limiting factor to correlation time (Figure 1.8).[4, 23, 36]

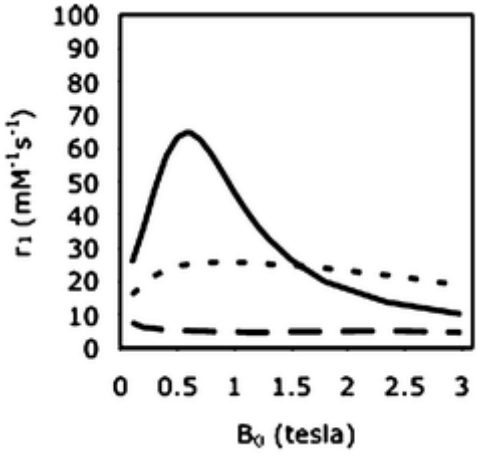


Figure 1.8: Simulation of inner sphere ^{1}H-MRI relaxivity of a Gd(III) complex as a function of magnetic field strength B_0 for different rotational correlation times (full line: τ_R = 10 ns as albumin adducts; dotted line τ_R = 1 ns typical of molecules with intermediate correlation time; dashed line τ_R = 0.1 ns as small, fast tumbling small contrast agent). (Reprinted with permission from P. Caravan, J. J. Ellison, T. J. McMurry and R. B. Lauffer, *Chem. Rev.*, 1999, 99, 2293-2352. Copyright 1999 American Chemical Society)

1.4.4 r_2 dependence to magnetic field, τ_m and τ_R

Previously, Caravan and co-workers have simulated r_1 and r_2 dependence with magnetic field, τ_m and τ_R, in Gd(III) and Mn(II) compounds (Figure 1.9 and Figure 1.10).[57] They show that longer τ_R leads to higher relaxivities at low magnetic fields (< 3 T). However, at higher fields this strategy is no longer effective. On the other hand, r_2 profiles are quite different comparing the two metal ions.[57] In Gd(III) compounds, there is a relative field-independent r_2 relaxivity proportional to τ_R. In contrast, because the hyperfine interactions $A/\hbar$ between Mn(II) and water protons are generally about an order of magnitude higher than normal values for Gd(III) compounds, r_2 relaxation is strongly modulated by scalar relaxation in Mn(II) complexes. Scalar coupling (Equation 9) is modulated by scalar correlation time, which is affected by electron relaxation (which becomes longer as the magnetic field increases, so its contribution becomes insignificant at high fields) and water residence time (Equation 12). Consequently, in Mn(II) compounds, r_2 decreases with increasing the magnetic field and rises with long τ_m.

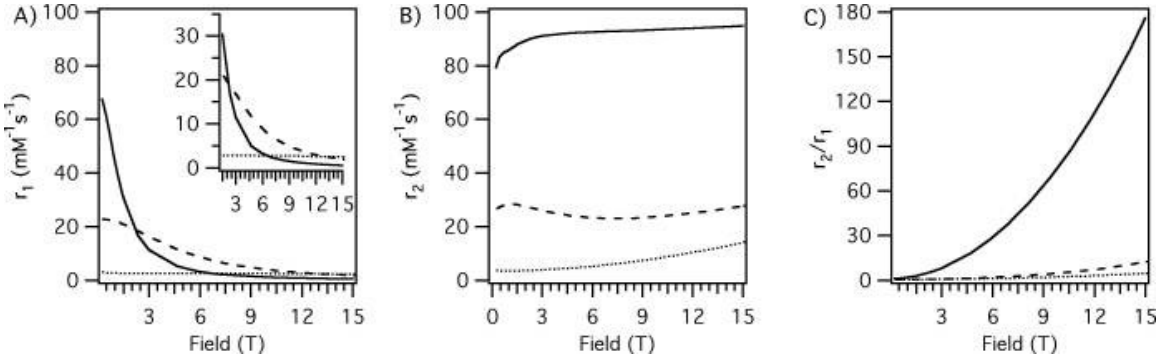


Figure 1.9: Simulated NMRD profiles showing relaxivity (A: r_1, B: r_2 and C: ratio r_2/r_1) of one inner-sphere water with 100 ns residence time as function of the applied magnetic field for Gd^{3+}-complexes with different rotational correlation times (dotted line: $\tau_R = 0.1$ ns, dashed line: $\tau_R = 1.0$ ns or full line: $\tau_R = 10$ ns). Insert in A is a magnified view. (Reprinted with permission from P. Caravan, C. T. Farrar, L. Frullano and R. Uppal, *Contrast Media Mol. imaging*, 2009, 4, 89-100. Copyright 2009 John Wiley & Sons, Ltd.)

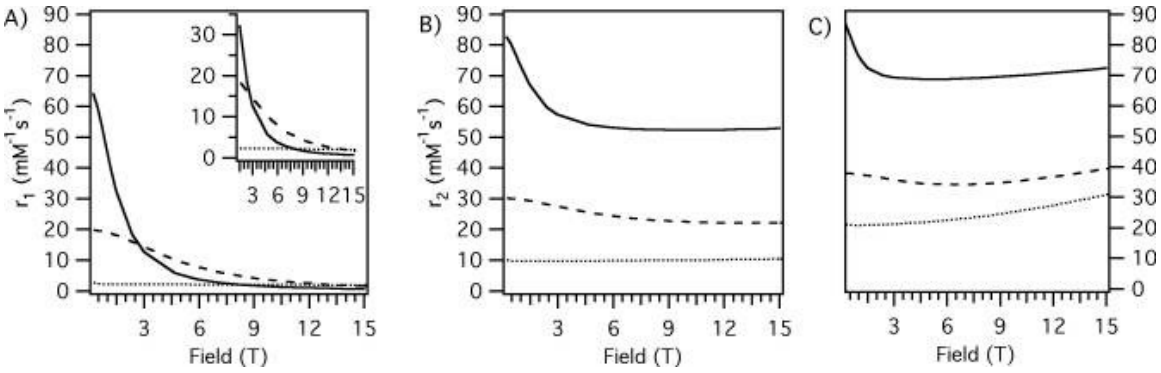


Figure 1.10: Simulated NMRD profiles showing relaxivity (A: r_1, B,C: r_2) of one inner-sphere water with B) 5 and C) 100 ns water residence time as function of the applied magnetic field for Mn^{2+}-complexes with different rotational correlation times (dotted line: $\tau_R = 0.1$ ns, dashed line: $\tau_R = 1.0$ ns or full line: $\tau_R = 10$ ns). Insert in A is a magnified view. (Reprinted with permission from P. Caravan, C. T. Farrar, L. Frullano and R. Uppal, *Contrast media & molecular imaging*, 2009, 4, 89-100. Copyright 2009 John Wiley & Sons, Ltd.)

1.5 The use of copper(II) as relaxation agent

With only one unpaired electron, Cu(II) has been largely considered unsuitable for use in MRI imaging.[21] In the literature, some examples are reported with low relaxivities when compared with analogous Gd(III) compounds (Table 1.1).[58-62]

Table 1.1: Comparison of r_1 ^{1}H-MRI relaxivity of Cu(II) and Gd(III) analogous small complexes.

Complex	r_1 / mM^{-1} s^{-1}	Freq / MHz	Temp / °C	Ref.
$Gd[H_2O]_6$	9.1	20	35	58
$Cu[H_2O]_6$	0.7	60	20	59
GdEDTA	5.4	20	37	60
CuEDTA	0.2	60	20	59
GdDTPA	4.8	20	25	58
CuDTPA	0.1	60	20	61

However, the use of Cu(II) within contrast agents would have advantages over Gd(III) in terms of toxicity (in mice, LD50 of $GdCl_3$[25] 100-200 mg/kg compared to $CuSO_4$[26] 481 mg/kg). The lower toxicity of copper arise from the fact that it is an essential nutrient, serves as a cofactor for many biological processes such as catalytic and structural processes and signalling events in the brain[63], and its concentration can be controlled by biliary excretion.[64] Part of its importance is due to its redox chemistry (between Cu(I)/Cu(II) states) in biological environment.

In terms of contrast agent efficiency, the relaxivities of Cu(II) compounds would suffer from the presence of only one unpaired electron compared to the seven found in Gd(III), as shown earlier (Table 1.1). However, Cu(II) complexes generally show fast water exchange rates (for copper aqua complex $k_{ex}^{298} = 4.4 \pm 0.1 \times 10^9$ s^{-1}) and long electron relaxation times, comparable to Gd(III).[65-67] However, in Cu(II) complexes, electron relaxation is not governed by modulation of ZFS as in Gd(III) and Mn(II) complexes. In Cu(II) complexes, other electron relaxation processes occur at room temperature that are generally field-independent.[68-70]

There are only few reports of copper-based contrast agents. An example is given by Luxol fast-blue (LFB), a Cu(II) phthalocyanine complex with $r_1 = 0.09 \pm 0.04$ at 600 MHz (14 T).[62] Another report describes the use of D-penicillamine bound to Cu(II) as a potential MRI contrast agent for plants.[71] Additionally, Dunbar and co-workers demonstrate the potential use of Cu(II)

complexes as redox active MRI contrast agents, by exploiting the redox couple converting paramagnetic Cu(II), into diamagnetic Cu(I),[72] with r_1 varying from 0.11 to 0.46 mM^{-1} s^{-1}.

1.6 Macromolecular contrast agents

As shown in Sections 1.3.1 and 1.4.3, MRI contrast agents based on small molecule complexes display fast rotational correlation times, generally in the order of ps, and, therefore, their longitudinal and transverse relaxivities, r_1 and r_2, are low (less than 10 $mM^{-1}s^{-1}$ compared to a theoretical maximal value of greater than 100 mM^{-1} s^{-1}).[36, 73] Strategies to make τ_R longer are through covalent or non-covalent conjunction of the metal complex to a macromolecule[74,75] or through direct coordination of the metal to a binding site within the macromolecular scaffold.[76] Moreover, macromolecules often allow the inclusion of a greater number of metal ions within their structure, leading to a substantial relaxivity enhancement per molecule. There are several examples of macromolecules adopted for this purpose: modified polymers, dendrimers, liposomes, nanoparticles (see Section 1.6.1), nanotubes,[77-79] as well as natural biological macromolecules[4, 73, 80, 81] such as carbohydrates[82] and proteins (see Section 1.6.2). These offer a wide range of possibilities for the development of complexes that have good biodistribution and selective targeting.[4]

Moreover, small complexes, because of their low molecular weight, are mostly nonspecific extracellular contrast agents and undergo rapid extravasation. Therefore, after injection, these agents rapidly move from the blood into the interstitial space. In this context, the use of macromolecules enable for better imaging of the blood pool for their longer retention into the blood stream.[4, 83]

1.6.1 Nanoparticles, dendrimers, liposomes and micelles

The use of nanoparticles has several advantages, such as the possibility to load a high number of paramagnetic moieties within a single nanoparticle and to tune the surface to target a specific region of the body.[84] Nanoparticles of copper[85] and copper(II) oxide[86] have shown r_1 relaxivity ranging from 0.38 (CuO, at 9.4 T)[86] to 4.26 $mM^{-1}s^{-1}$ per Cu^{2+} ion (NanoQ, copper oleate nanocolloids, at 3 T)[85].

Dendrimers are nanometre-scale macromolecules which are highly branched and star-shaped. Amino functional groups on their surface have been used to conjugate with DTPA and DOTA chelates.[87] Their three-dimensional branched structure provides rigidity compared with linear analogues, resulting in low rotational freedom compared with linear polymers, leading to

increased r_1: the relaxivities for polymers are about 12-20 $mM^{-1}s^{-1}$, while the r_1 of the dendrimer-based contrast agents have been reported to be 20-35 $mM^{-1}s^{-1}$ at clinically relevant magnetic fields.[88-90]

Liposomes and micelles are macromolecular aggregates which are generated from the spontaneous assembly of amphiphilic molecules in aqueous solution.[91] They are promising candidates as carriers of complexes to improve their contrast efficacy, because of the relative ease in tuning their structures[91] and consequently their pharmacokinetics. A possible approach consists of grafting Gd(III) complexes onto the surface, leading to an increase in r_1 because of the reduction in rotational tumbling.[92, 93] Alternatively, lipophilic contrast agents such as Gd-DTPA, Gd-DTPA-BMA have been incorporated within the lipid bilayer of a liposome, leading to shorter T_1 and T_2 relaxation times (Figure 1.11).[94-96]

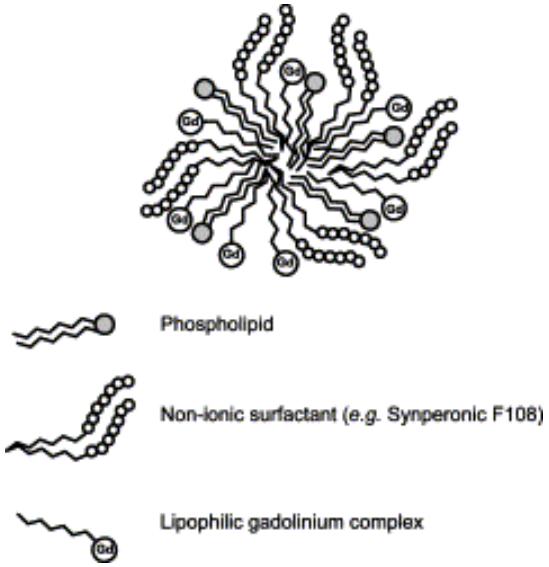


Figure 1.11: Scheme of a mixed three-component micelle, aggregate of a non-ionic, biocompatible surfactant (e.g. Synperonic® F108), a phospholipid and a lipophilic gadolinium complex. (Reprinted with permission from L. Lattuada and G. Lux, *Tetrahedron Lett.*, 2003, 44, 3893-3895. Copyright 2003 Elsevier Science Ltd.)

1.6.2 Proteins and peptides

The use of proteins and peptides within contrast agents, provide an opportunity to generate contrast agents, which combine biocompatibility and target selectivity with high efficiency. There are different strategies for the design of such agents. One approach has been to covalently bind a Gd(III) or Mn(II) complex to larger proteins such as human serum albumin.[97] Another strategy consists in the substitution of a native metal site with Gd(III) or Mn(II) to an existing

metalloprotein. A heme-protein able to bind to both nitric oxide and oxygen (H-NOX) was studied as a MRI contrast agent by substituting natural Fe(II) for metals such as Gd(III) and Mn(II).[98] Alternatively, Gd(III) complexes have been coupled with short peptides. These peptides can selectively bind to a target protein substrate or self-assemble into a macromolecular structure. An example of the former was developed by León-Rodriguez and co-workers,[99] who reported the synthesis of a DOTA complex conjugated to a 12-mer peptide, with high affinity for its protein-binding target (Gal-80). Upon complexation, detection of Gal-80 at μM levels was possible as the peptide-protein complex showed relaxivity $r_1 = 44.8 \pm 1.7\ mM^{-1}s^{-1}$ at 20 MHz and 25°C. An example of peptide self-assembly is given by Meade and co-workers, who designed an amphiphilic peptide-DOTA conjugate, able to self-assemble into nanofibers[100], leading to a three-fold increase in the longitudinal relaxivity over Gd-DOTA under the same conditions.[101]

Finally, metalloproteins, where the metal binding site is generated by amino acids residues within the sequence, represent a new approach in developing novel MRI contrast agents.[73, 76, 102] Gadolinium binding chemistry is dominated by the similarity of the coordination chemistry of lanthanide ions and Ca(II). The substitution of Ln(III) in native Ca(II) binding proteins, such as that of calmodulin, allows to obtain complexes such as CA1.CD2 (Figure 1.12), showing high affinities and relaxivities when binding Gd(III). [73, 76, 102]



Figure 1.12: Modelled structure of Gd(III)−CA1.CD2 based on the NMR structure 1T6W. Ligand residues E15, E56, D58, D62, and D64 at the B, E, and D β-strands of the protein CD2 are shown in red. (Adapted with permission from J. J. Yang, J. Yang, L. Wei, O. Zurkiya, W. Yang, S. Li, J. Zou, Y. Zhou, A. L. W. Maniccia and H. Mao, *J. Am. Chem. Soc.*, 2008, 130, 9260-9267. Copyright 2008 American Chemical Society)

An entire class of protein-based MRI contrast agents was developed.[103] One of them, named ProCA32, was obtained by engineering high-affinity Gd(III)-binding pockets in rat and human α-parvalbumin.[104] The measured dissociation constants comparable to GdDTPA and high selectivity was found over physiological ions such as Zn(II), Ca(II) and Mg(II).

1.7 *De novo* designed metallopeptides

De novo design is a strategy to generate miniature artificial peptide scaffolds from first principles. A primary amino acid sequence can be designed to form predictable secondary, tertiary or even quaternary structures.[105, 106] The advantage of this approach is that, because the portions of the proteins non-needed for activity are removed, the resulting systems can be synthetised rather than expressed in cellular cultures and they are generally easier to be characterised than large proteins.[107, 108]

Therefore, the synthetic advantages of small molecules can be exploited within macromolecular designs which retain the original active region (Figure 1.13).[107] Moreover, the use of relatively small macromolecular structures increase the possibilities of predicting interactions between the residues and structure-function relationships which can be finally optimised.[109]

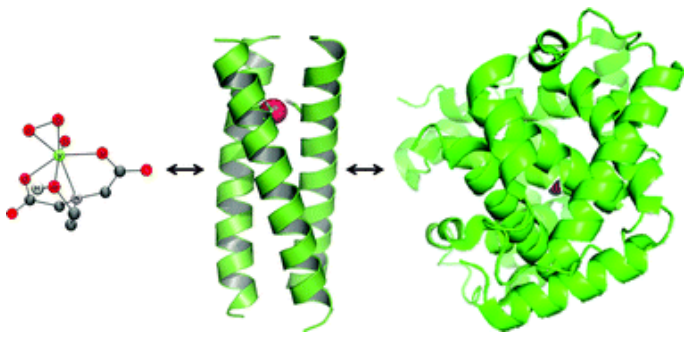


Figure 1.13: Representation of d*e novo* designed metallopeptides with intermediary complexity between small molecule metal complexes and larger natural biological metal complexes. (Reproduced with permission from A. F. Peacock, O. Iranzo and V. L. Pecoraro, *Dalton Trans.*, 2009, 2271-2280. Copyright 2009 Royal Society of Chemistry)

1.7.1 Coiled-coils formation and assembly – the hydrophobic core

Coiled-coils consist of a supercoil structure of multiple strands of α-helices. The coiled-coil motif occur in 10% of eukaryotic proteome[110] and can be found in fibrous proteins such as α-

keratin.[111] Normally, they are formed by seven-residue repeats of hydrophobic (*H*) and polar (*P*) amino acid residues $(HPPHPPP)_n$ represented as ***a, b, c, d, e, f*** and ***g*** position respectively.[112] As slightly more than 3.5 residues form a complete turn of a helix, residues in ***a*** and ***d*** position will point inside a supercoiled structure forming a hydrophobic core. The generation of a hydrophobic core is the primary driving force for protein folding, which is entropically favoured for the release of water molecules from the non-polar groups. It was proposed by Crick that the hydrophobic core assembles into a 'knobs-into-holes' structure, with the residues in ***a*** and ***d*** positions as knobs inside the holes left from another layer.[113] In their work, Harbury and co-workers developed GCN4 leucine zipper mutants and showed how mutations in the hydrophobic ***a*** and ***d*** positions allow to modulate oligomerisation of the structures. When Ile was placed in ***a*** position and Leu in ***d***, a dimer structure was formed, whereas either two Ile or two Leu in ***a*** and ***d*** position led to trimers. Leu in ***a*** and Ile in ***d*** position generated a tetramer structure (Figure 1.14).[112, 114] These ideas where further developed by Woolfson and co-workers to define key features in sequence design for generating predictable structures.[115]

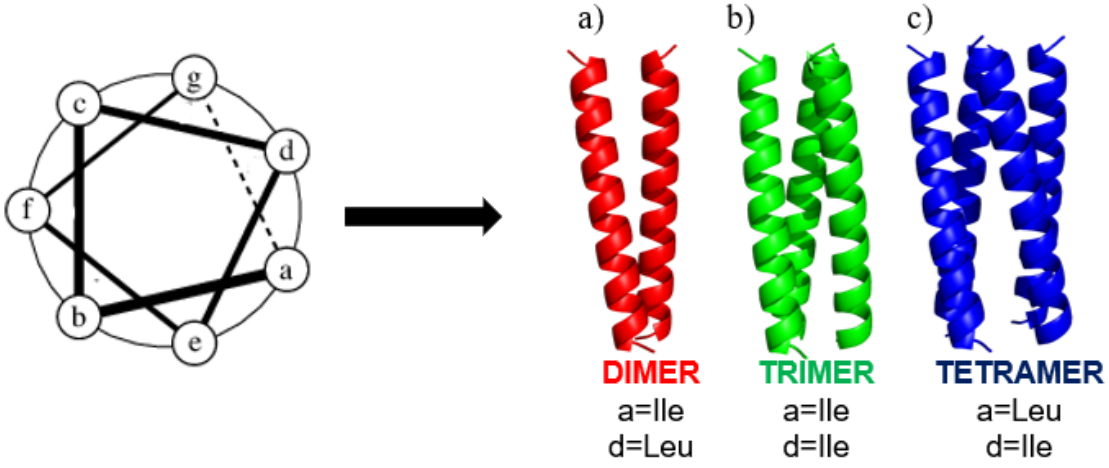


Figure 1.14: Schematic representation showing *de novo* designed amino acid sets leading to dimer, trimer and tetramer structures.

1.7.2 Salt bridges, external positions and length of the coil

Amino acids in ***e*** and ***g*** positions are generally polar and are involved in the formation of interhelical salt-bridges (Figure 1.15).[116-119] Woolfson and co-workers reported a prevalence of glutamic acid (Glu, E), glutamine (Gln, Q) and lysine (Lys, K) and some cases of arginine (Arg, R) in these positions.[115] Salt bridges are constituted by oppositely charged residues where the

residue in ***e*** and ***g*** positions interact with residue in ***g*** and ***e*** positions on adjacent strand(s) (***e→g'*** and ***g→e'*** in homomeric, parallel coiled-coils). The formation of salt bridges is highly dependent on pH, which determines protonation or deprotonation of charged residues.[109, 116-120]

Residues in ***b***, ***c*** and ***f*** positions do not tend to influence the stability or the oligomerisation of the coiled-coil significantly. Alanine (Ala, A) can be introduced to promote helicity,[115] glutamine (Gln, Q) or lysine (Lys, K) to help solubility and tryptophan (Trp, W) provides a useful UV chromophore.

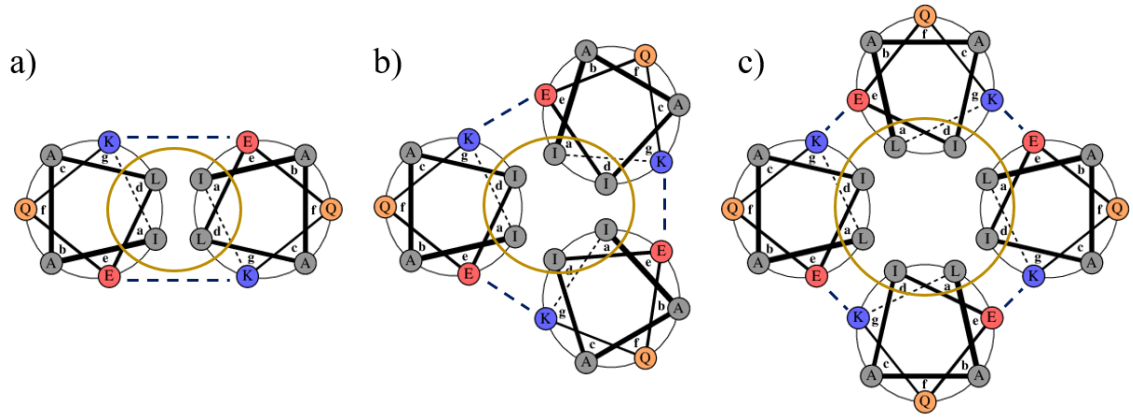


Figure 1.15: Helical wheel diagrams (made using DrawCoil) of a a) dimeric, b) trimeric and c) tetrameric coiled-coil, highlighting hydrophobic interactions between *a* and *d* residues (gold circles) and salt-bridge interactions between *e* and *g* residues (dashed lines).

Finally, sequence length is another important factor that influences the stability of a coiled-coil structure. Longer sequences form more hydrophobic and salt bridge interactions, with sequences of three heptads being the shortest sequence capable of forming coiled-coils.[120, 121]

1.7.3 Introducing a metal binding site

A metal-binding site can be introduced by substituting hydrophobic residues at the ***a*** and ***d*** positions in the core of the structure with amino acids capable of coordinating metal ions.[109] The hard oxygen atoms of the carboxylate side chains of aspartic acid (Asp) and glutamic acid (Glu) prefer to bind to hard metals such as Ca(II), Ln(III) and Mg(II).[122] In contrast, the soft thiolate group of cysteine binds preferentially to softer metals such as Cd(II) and Hg(II), while the nitrogen of the imidazole of histidine can bind to either hard, borderline (*e.g.* Cu(II)) or soft metals.[122]

There are many examples of structures with more than one metal ion.[123-127] Metals can be incorporated into more than one distinct binding site or as metal clusters. Metal ions within the same scaffold can be of one type[124] or different,[125, 126, 128] which can be more challenging.

1.7.4 Copper coiled-coils

Cu(II) is a d^9 system that is often found coordinated by 4, 5, or 6 ligands, in square planar, square pyramidal, or axially distorted octahedral geometries, the latter being the result of Jahn–Teller distortion. While Cu(I) is a soft acid, Cu(II) is borderline, thus, copper binding sites in natural proteins generally consist of amino acids containing side chains with soft (cysteine, Cys, methionine, Met) or borderline (histidine, His) ligands.[129] Many redox-active copper proteins that cycle between Cu(I) and Cu(II) states can be found predominately in distorted tetrahedral geometry and include His in the donor set to ensure a high affinity for both Cu(I) and Cu(II).[130]

Copper proteins are generally divided into categories on the basis of their spectroscopic features.[129, 131] Table 1.2 and Figure 1.16 show the main copper sites: Type 1, Type II, Type III, A and B centers (Cu_A, Cu_B) and Z centers (Cu_Z). These types of binding sites offer the basis for copper-binding peptide design. One of the first reports of Cu(II) promoting the stabilization of monomeric α-helices was by Ghadiri and Choi.[132] In their design, two His residues on the same side of the helix generate the binding site. The addition of Cu(II) led to a stabilisation of the α-helical secondary structure determined, as α-helical content, which increased from 50% to around 90%.

Table 1.2: Types of natural Cu centers, number of coordinated ions, geometry and residues involved.

Type	*Number Cu*	*Geometry*	*Coordination*
Type I Class I	1	Tetrahedral	$Cu(N^{\delta}His)_2S^{\gamma}CysS^{\delta}Met$
Type I Class II	1	Tetrahedral	$Cu(N^{\delta}His)_2S^{\gamma}CysO^{\epsilon}Glu$
Type I Class III	1	Trigonal bipyramidal	$Cu(N^{\delta}His)_2S^{\gamma}CysS^{\delta}MetOGly$
Type 2	1	Square pyramidal	$Cu(N\delta His)_3H_2O$
Type 3	2	Trigonal bipyramidal	$\mu O_2[Cu(N^{\delta}His)_3]_2$
Type A	2	Tetrahedral	$\mu(S^{\gamma}Cys)2[CuN^{\delta}HisS^{\delta}Met][CuN^{\delta}HisOGlu]$
Type B	1	Trigonal pyramidal	$Cu(N^{\delta}His)_3$
Type Z	4	Tetrahedral	$4Cu(N_{\delta}His)_7$

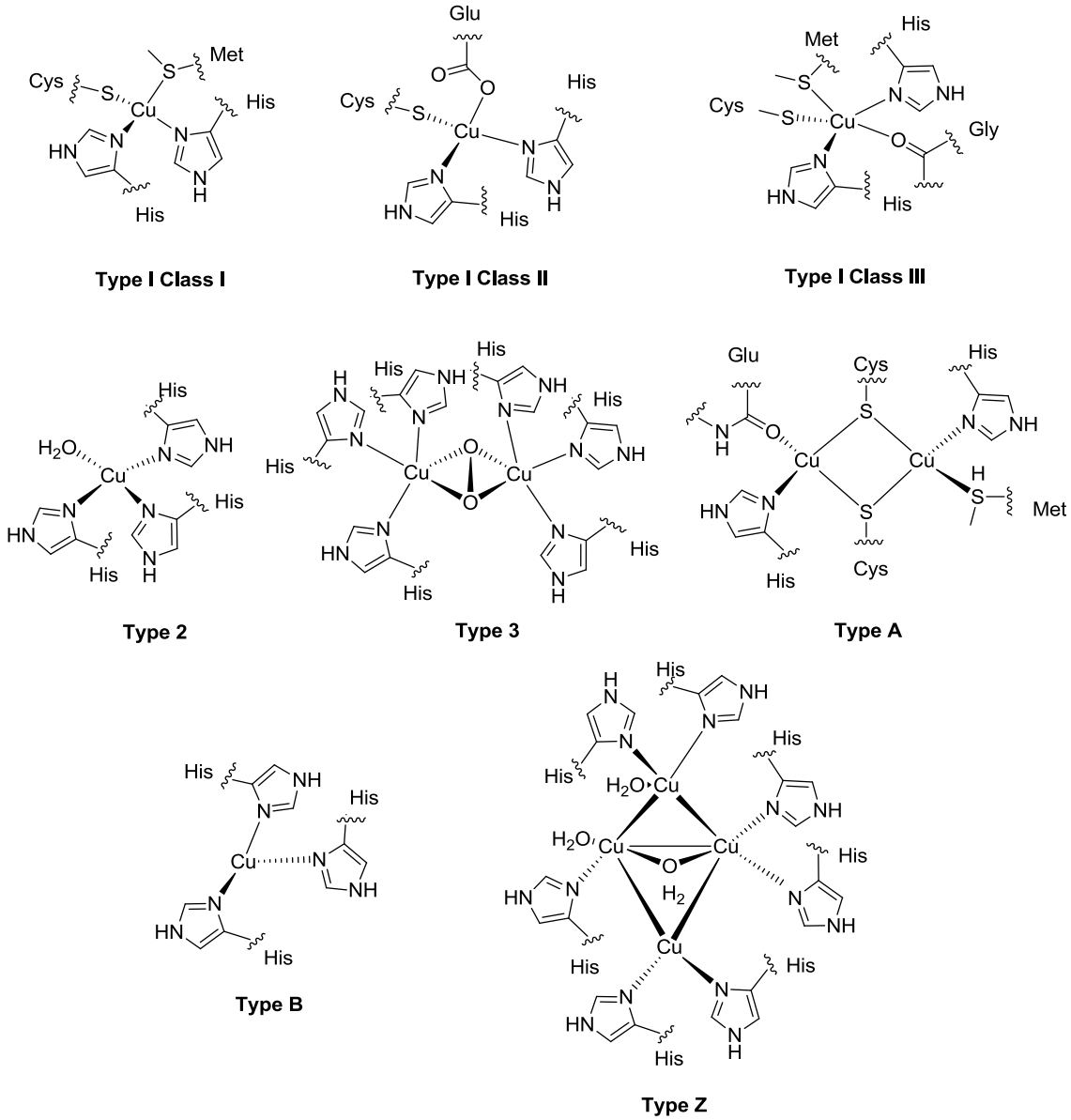


Figure 1.16: Scheme of copper binding sites Type 1 class I,II,III, Type 2, Type 3, CuA, CuB and CuZ with relevant residues.

Mixed Nitrogen/Oxygen binding sites

Ghadiri and co-workers designed a peptide able to assemble in a three-stranded coiled-coil upon Ru(II) complexation with a 2,2'-bipyridine moiety at N-terminus.[133] At the C-terminus a His_3 binding site was designed for Cu(II) binding, resulting in a Type 2 Cu(II) coordination of His_3 and one or more oxygen donors from water and/or buffer.[128]

The isoleucine zipper (IZ) is a family of peptides whose sequence is based on the heptad repeat IEAIEKK. These peptides fold spontaneously into three-stranded coiled-coils.[134] By

mutation of select Ile residues to His, Tanaka and co-workers designed the IZ-3adH peptide,[135] which features two adjacent His residues in ***a*** and ***d*** sites, for binding Ni(II), Zn(II), or Cu(II) in an octahedral His_6 site. IZ-3aH, containing only one His residue in an ***a*** layer, was able to bind Zn(II) and Cu(II), but not Ni(II).[136] Based on these results, Tanaka and co-workers designed the peptide IZ(5)-2a3adH[137] formed of 5 heptads with 3 His residues, and demonstrated that it binds Ni(II) and Cu(II). In their model, Ni(II) binds to 4 His residues in a square planar geometry, while Cu(II) binds to the remaining 3 His residues in a tetrahedral geometry, with the fourth ligand an exogenous water (Figure 1.17).

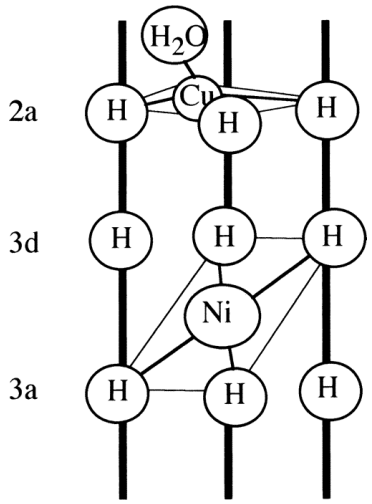


Figure 1.17: Model of possible coordination Ni(II)-Cu(II) peptide complex. Ni(II) ions prefer a square-planar coordination geometry, while Cu(II) is bound to the planar three His residues and water. The three vertical bold bars represent the α-helix strands. (Reprinted with permission from T. Tanaka, T. Mizuno, S. Fukui, H. Hiroaki, J.-i. Oku, K. Kanaori, K. Tajima and M. Shirakawa, *J. Am. Chem. Soc.*, 2004, 126, 14023-14028. Copyright 2004 American Chemical Society.)

They also designed IZ-HH, a metal-ion-binding three α-helical coiled-coil designed with 12 His residues in the hydrophobic core of the coiled-coil structure. The structure was observed to fold in the presence of two equivalents of divalent metal ions, such as Cu(II).[138] Moreover, they were able to design a stable four-stranded α-helical coiled-coil structure (Figure 1.18a) with two equatorial His residues and one Asp (peptide AM2D, square-planar structure) or Glu (peptide AM2E, distorted square-planar structure) residues and a molecule of water for coordinating the metal ions (Figure 1.18b,c).[139]

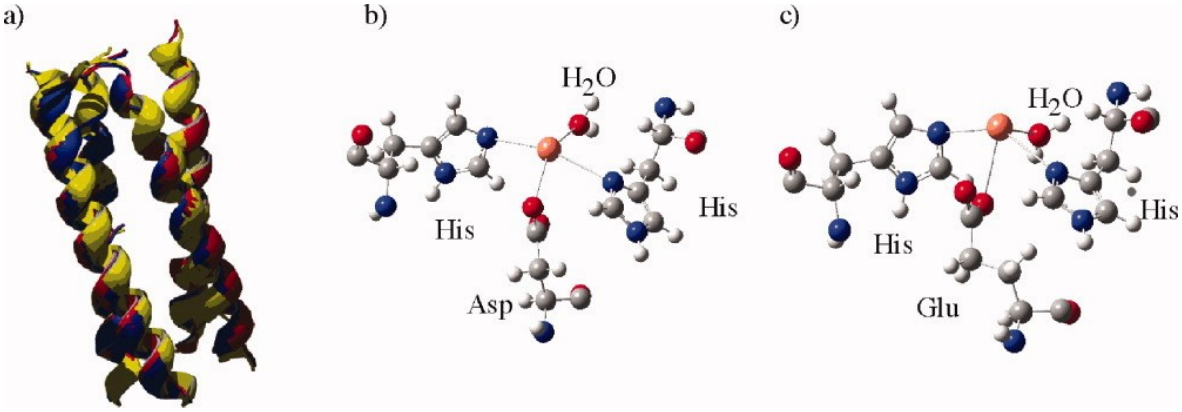


Figure 1.18: (a) Superposition of the minimized structures of AM2D (red) and AM2E (blue) on the starting structure (yellow). Representation of (b) AM2D and (c) AM2E minimized structures of models. Coordination bonds were drawn between Cu(II) ion and one water molecule, one two His residues and one Asp (AM2D) and one Glu (AM2E). (Reprinted with permission from D. Shiga, D. Nakane, T. Inomata, H. Masuda, M. Oda, M. Noda, S. Uchiyama, K. Fukui, Y. Takano and H. Nakamura, *Biopolymers*, 2009, 91, 907-916. Copyright 2009 Wiley Periodicals, Inc.)

Pecoraro and co-workers designed a catalytic copper Type 2 site within a designed three-stranded coiled-coil.[130] They engineered a Type 2 Cu(II)His_3 center within a three-stranded coiled-coil (named TRIL23H) for generating a high-affinity binding site for both Cu(I) and Cu(II), thus allowing cycling between the two redox states, mimicking the action of a nitrite reductase. They also investigated the effect of the presence of specific secondary interactions[140] by designing TRIL23H mutant peptides with different charge in the binding site, which were obtained by mutation of a Glu and a Lys in close proximity of the His binding site. The hypothesis was that Glu was able to form a hydrogen bond with the His, leading to changes in the electron-donating abilities of the His imidazole, determining pH-dependent reduction potentials and variable Cu(II)/Cu(I) affinities. They observed that, at a specific pH, peptide mutations were directly related to variation in Cu(I) peptide affinity, through modification of the overall charge in the binding site. Oppositely, for a specific peptide, variable pH lead to variance in Cu(II) affinity. In both cases, the result was modulation of reduction potentials.

In 2020, Pecoraro and co-workers reported on copper-binding *de novo* designed scaffolds, named GRα_3D (Figure 1.19).[141, 142] These peptides were based on α_3D family, originally designed by DeGrado and co-workers.[142] The authors included copper binding sites generating the His_3, His_4, His_2AspHis and His_3Asp mutants. These sequences assembled into antiparallel helical bundles with Cu(II) binding sites and were capable of superoxide dismutase activity (SOD). They concluded that CuHis_3X was present in all cases, with the fourth ligand (X) nitrogen from His or oxygen from Asp or from water. Variation of ligands around Cu(II) ion led to different Cu(II)

affinities, with His_4 as the weakest, and to different catalytic activity, though all of them were determined to be three order of magnitude less efficient than the native SOD.

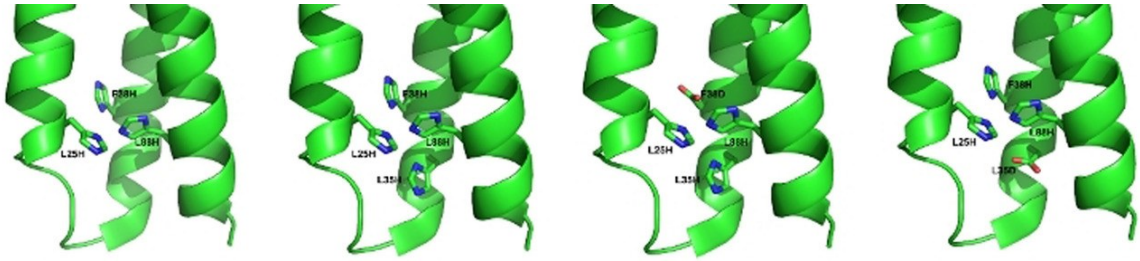


Figure 1.19: PyMol representations of the designed His_3, His_4, $His_2AspHis$, and His_3Asp active sites inside $GR\alpha_3D$ scaffold, based on the crystal structure of $GR\alpha_3D$ (PDB: 6DS9). (Reprinted with permission from E. Mathieu, A. E. Tolbert, K. J. Koebke, C. Tard, O. Iranzo, J. E. Penner-Hahn, C. Policar and V. Pecoraro, *Chem. Eur. J.,* 2020, 26, 249-258. Copyright 2020 Wiley-VCH Verlag GmbH & Co. KGaA, Weinheim)

Mixed Nitrogen/Sulphur binding sites – Type1 and Type A centres

Copper Type 1 and Type A sites feature sulphur donor atoms.[129, 131, 143] Therefore, coordination under aerobic conditions is extremely difficult as the oxidation of thiolate to disulfide occurs rapidly with relative electron transfer and Cu(I) formation.[144] Tanaka and co-workers designed a copper Type 1 site within a four-helix bundle AM2C. Copper was coordinated with a trigonal planar geometry formed by two His and a Cys residue.[145] This site was only stable under anaerobic conditions, due to oxidation of the Cys thiolate to a sulfonyl group. It was proposed that the copper site was not sufficiently buried within the folded scaffold to prevent site access of oxygen.[108]

Haehnel and co-workers designed copper centres within template-assembled synthetic proteins (TASP), consisting of four-stranded coiled-coils.[146, 147] Three out of the 96 mutants presented significant stability and bound copper to similar tetragonal $Cu(His)_2Cys$ sites, with the fourth position occupied by an exogenous ligand such as water. Three different copper centres were designed: Type 1, Type 2 and Type A copper centers.[147] Interestingly, one Type A site, a $Met(His)_2Cys$, contains a bridging cysteine between the two copper ions.

Other examples of a multinuclear copper site engineered within coiled-coils has been reported by Tanaka and co-workers who designed bi-AM2C.[127] Bi-AM2C is a four-helix bundle capable of binding to two copper ions through two His residues, a Cys and oxygen from a Glu carbonyl group on the main chain, generating an unusual copper Type A site that lacks a Met. An example of a coiled-coil, with a copper metal cluster bound in the hydrophobic core, is found in

the work of Ogawa and co-workers, who developed a peptide incorporating a Cys-XX-Cys motif which was able to coordinate a tetranuclear copper(I) cluster.[148]

1.7.5 Manganese metallopeptides and metal clusters

Manganese(II) is a hard cation, therefore, in proteins mononuclear Mn sites are typically coordinated by two to four aspartate, glutamate, histidine residues or solvent molecules in an octahedral geometry, square pyramidal or trigonal bipyramidal geometry, and occasionally in a tetrahedral geometry.[149] In biology, manganese proteins are involved in many biological processes such as the Oxygen Evolving Complex of Photosystem, Superoxide Dismutase, due to rich $Mn^{2+}/Mn^{3+}/Mn^{4+}$ redox chemistry.[149]

Biological metalloproteins can also feature Mn-clusters.[150] Examples of Mn-clusters are the Mn_4Ca-cluster of Photosystem II[151, 152] and the Mn_2-cluster of Mn-catalase.[153, 154] A four-helix bundle protein which contains a dinuclear Mn centre formed by two bridging Glu, two chelating Glu side chains, and two His ligands was designed into the Due Ferri (DF) structure by DeGrado and co-workers.[123, 124] Allen and co-workers designed a family of four-helix bundles based on the same DF family able to bind one, two and three di-Mn(II) sites.[155, 156] The first peptide was designed to have Glu11, Glu41 and His44 in the middle as coordinating residues to a dinuclear Mn-center (Figure 1.20a,b). Four other proteins were designed, and they displayed the metal-binding sites near the connecting loops. They demonstrated that the Mn-proteins with three metal centres were more efficient at electron transfer for the conversion of hydrogen peroxide into molecular oxygen, than the Mn-proteins with one or two metal centers.[127]

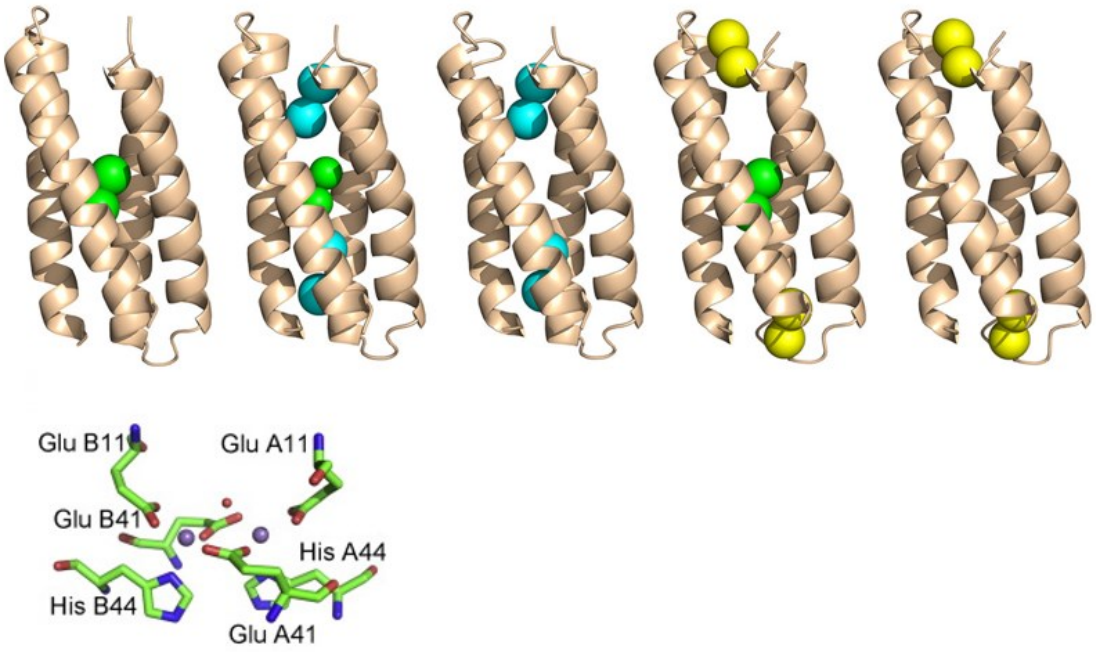


Figure 1.20: Model of four-helix bundles with one, two, or three dinuclear Mn(II).centers (Mn(II) ion shown as sphere), with insight to the coordination donor atoms constituted by carboxylates (Glu) and imidazole (His), colored by atom type. A water molecule is present within the coordination sphere (red sphere). (Adapted with permission from T. L. Olson, E. Espiritu, S. Edwardraja, C. R. Simmons, J. C. Williams, G. Ghirlanda and J. P. Allen, *Biochim. Biophys. Acta (BBA)-Bioenergetics*, 2016, 1857, 539-547. Copyright 2015 Elsevier B.V.)

1.7.6 Lanthanide coiled-coils

Lanthanide binding is generally 9- or 8-coordinate, depending on the size of the lanthanide ion, which gradually decreases through the series due to the lanthanide contraction. Ln(III) ions are hard metals which bind preferentially to hard donor atoms, such as oxygen of Asp or Glu.

Their incorporation into enzymes was only demonstrated in 2011, with the isolation of a bacterial lanthanide- and pyrroloquinoline-dependent methanol dehydrogenase.[157] In 2018, a novel EF hand-containing protein was discovered and named lanmodulin, with a 10^8-fold selectivity for Ln(III) over Ca(II).[158] EF-hand motifs consists a metal binding loop, connecting two α-helices. They are typical motifs in Ca(II) binding proteins, such as calmodulin, where Asp, Asn, and Glu residues are typically involved in Ca(II) binding. The selectivity of lanmodulin for Ln(III) ions over Ca(II) was thought to be due to and additional Asp residue at the ninth position, leading to higher coordination numbers, preferred by Ln(III) ions (Figure 1.21).

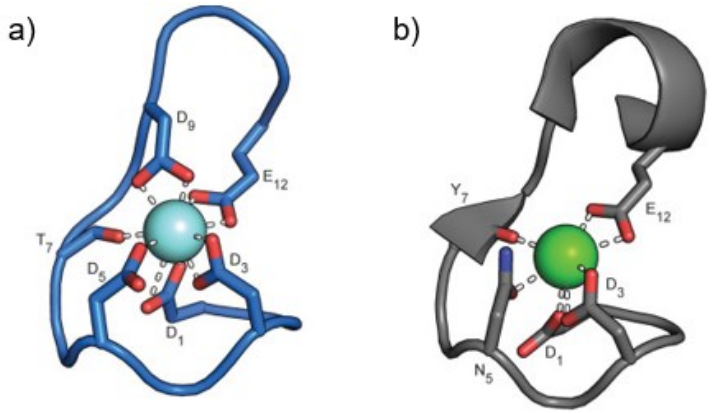


Figure 1.21: Comparison between the metal binding sites of a) lanmodulin and b) calmodulin. Y(III) shown as light blue sphere and Ca(II) as green sphere. Oxygen donors (Asp) shown in red and nitrogen atoms in blue (Asn). (Adapted with permission from E. R. Featherston and J. A. Cotruvo Jr, *Biochim. Biophys. Acta (BBA)-Molecular Cell Research*, 2021, 1868, 118864).[159]

Hodges and co-workers[160, 161] reported the design of a two-stranded coiled-coil that assembles in the presence of Ca(II) and Ln(III), with metal binding to charged Glu or non-natural amino acid γ-carboxyglutamic acid residues at the α-helical interface. Kashiwada and co-workers[162] developed a Ln(III) binding site within the hydrophobic core of a three-stranded coiled-coil, formed by γ-carboxyglutamic acid residues. They showed that, Ln(III) binding induced folding.

Berwick and co-workers[76] designed the first Gd(III)-binding coiled-coil, named MB1-2 (sequence in Table 1.3). They investigated the relative Tb(III) complex for its luminescence properties, whereas the Gd(III) complex was investigated as a MRI contrast agent. The binding site was formed by one asparagine (Asn, N) and one aspartic acid (Asp, D) layer as shown in Figure 1.22.[163] The structure is poorly folded in the absence of Ln(III) ions as the negative charges on the Asp residues repel each other. MB1 folding was induced on addition of Gd(III), forming a trimeric $Gd(MB1)_3$ structure with a log K_a of 5.11 ± 0.04. The Gd(III) coiled-coil is capable of remarkable reduction of transverse relaxivity (r_2 = 18.9 ± 1.5 $mM^{-1}s^{-1}$ at 7 T) compared with reference Dotarem GdDOTA (r_2 = 5.7 ± 1.8 mM^{-1} s^{-1} at 7 T) and similar longitudinal relaxivity (for $Gd(MB1)_3$ r_1 = 6.3 ± 2.1 $mM^{-1}s^{-1}$ and for GdDOTA r_1 = 4.3. ± 1.0 $mM^{-1}s^{-1}$ at 7 T).

Table 1.3: Amino acid sequences of the four MB1 peptides with Ln(III) sites at different linear locations.

MB1-1	Ac-G IAANEWK DAAIEQK IAAIEQK IAAIEQK IAAIEQK G-NH_2
MB1-2	Ac-G IAAIEQK IAANEWK DAAIEQK IAAIEQK IAAIEQK G-NH_2
MB1-3	Ac-G IAAIEQK IAAIEQK IAANEWK DAAIEQK IAAIEQK G-NH_2
MB1-4	Ac-G IAAIEQK IAAIEQK IAAIEQK IAANEWK DAAIEQK G-NH_2

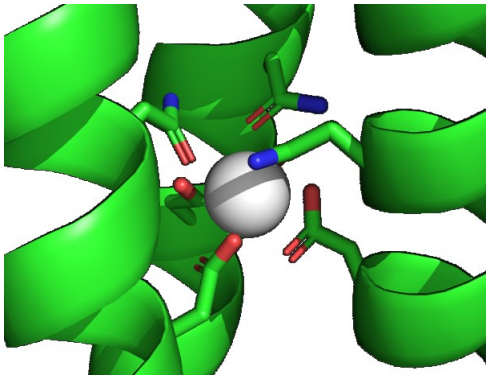


Figure 1.22: Cartoon representing the Ln(III) binding site in HC02 (PDB 7P3H),[163] featuring the same Asn_3-Asp_3 binding site as MB1-2 and amino acid sequence appropriately modify to promote crystallisation. Peptide backbone shown as a helical ribbon and side chains shown as sticks, with oxygen in red and nitrogen in blue. Tb(III) ion shown as white sphere. The Asp layer provides 6 potential oxygen donor atoms for Ln(III) coordination, and an Asn layer introduced directly above in *d* sites provide a potential 3 additional oxygen donors to generate an potential 9-coordinate site.

Based on these promising results, Berwick and co-workers designed a series of coiled-coils (Table 1.3 and Figure 1.23) containing the same Ln(III) binding site as the MB1-2 peptide but located at different positions along the coiled-coil (Table 1.3).[164]

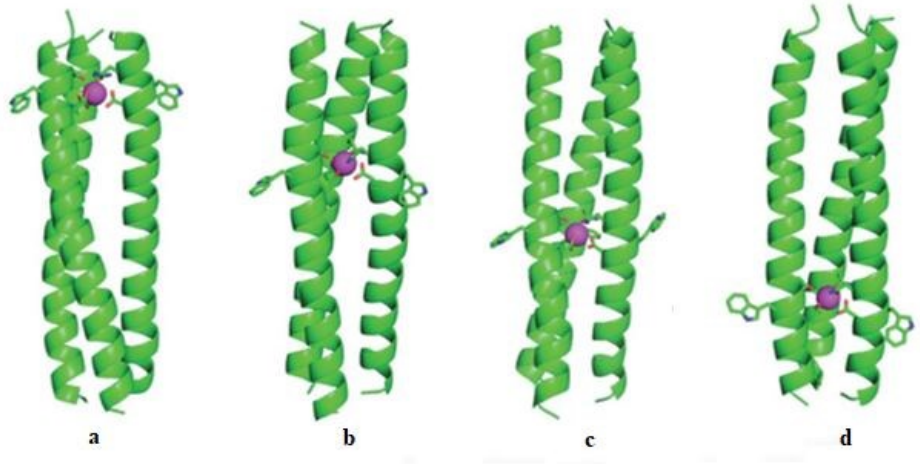


Figure 1.23: Representation of a) $Gd(MB1\text{-}1)_3$, b) $Gd(MB1\text{-}2)_3$, c) $Gd(MB1\text{-}3)_3$ and d) $Gd(MB1\text{-}4)_3$.

When the Ln(III) binding site is buried in the centre of the coiled-coil (MB1-2 and MB1-3), the apo peptide is poorly folded. In contrast, when the binding site is located at either terminus of the coiled-coil (MB1-1 and MB1-4) the apo peptide was found to be well structured as a consequence of many adjacent hydrophobic layers and the addition of Ln(III) did not substantially enhance folding. Tb(III) luminescence titration were used to assess metal binding and to determine the affinity constants log K_a, which were found to be similar (Table 1.4).

Luminescence lifetime decay studies of the $Tb(MB1)_3$ peptides were undertaken to obtain the hydration number q (Table 1.4), and r_1 and r_2 relaxivities of the analogue Gd(III) complexes were determined. The translation of Ln(III) binding site was found to modulate both hydration and relaxivity of the metallopeptides (Table 1.4). The presence of the Ln(III) binding site at the C-terminus (MB1-1) and the N-terminus (MB1-4) of the coiled-coil enabled a higher number of water molecule to coordinate to Ln(III) in the inner-sphere (q = 3 and 2, respectively), leading to enhanced r_1 and r_2 relaxivities compared to GdDOTA. In contrast, MB1-2 and MB1-3 peptides, with q = 0, showed only modest relaxivity.[76, 163, 164, 165] However, molecular modelling was used to identify the presence of a water channel which enables the water molecules to get in proximity to the Ln(III) ion bound to a MB1-2 trimer.[166]

Table 1.4: Affinity constants log K_a, hydration numbers q and relaxivities for the MB1 series compared with GdDOTA (7 T).

	log K_a	q	r_1 / $mM^{-1}s^{-1}$	r_2 / $mM^{-1}s^{-1}$
MB1-1	5.30 ± 0.15	3.1 ± 0.2	10.0 ± 1.5	89.3 ± 16.8
MB1-2	5.48 ± 0.20	0.0 ± 0.1	4.2 ± 1.2	21.3 ± 2.6
MB1-3	5.16 ± 0.26	0.0 ± 0.1	4.0 ± 1.0	20.9 ± 1.0
MB1-4	5.26 ± 0.36	1.8 ± 0.4	7.5 ± 4.1	37.9 ± 4.0
GdDOTA	–	1.0 ± 0.0	4.3 ± 1.0	5.7 ± 1.8

1.8 Chemical Exchange Saturation Transfer (CEST)

1.8.1 CEST Contrast Agents

Chemical exchange saturation transfer (CEST) contrast agents are an emerging class of MRI contrast agent that offer an alternative to traditional gadolinium-based agents. In 2000, the use of exchangeable protons for generating MRI contrast was proposed by Ward and Balaban,[6] extending the range of possible MRI agents to include diamagnetic compounds. They showed that, by exploiting a saturation transfer mechanism (see Section 2.7.4), it is possible to turn

contrast on and off, by applying selective radiofrequency saturation of the protons in chemical exchange with water. This technique provides a negative contrast in the MR image.[167, 168]

CEST contrast agents are either diamagnetic[169] or paramagnetic[47] molecules that possess exchangeable protons (NH or OH) or bound water molecules that resonate at chemical shifts different from the bulk water.[3] The CEST effect is influenced by several parameters including: instrumental parameters such as the frequency of saturation pulse $\boldsymbol{B}_1$ and the duration of the pulse; the separation $\Delta\omega$ between the chemical shifts of the exchanging protons and water; the exchange rate of the mobile protons/bound water k_{ex} and the number of exchangeable protons n and NMR T_1 and T_2 of the bulk water.[168, 170, 171] k_{ex} should be long enough to have efficient saturation transfer during the RF pulse, but also not too fast to prevent coalescence. To be able to detect exchange, k_{ex} must be much lower than the separation between the frequencies $\Delta\omega$.[7]

Since the chemical shift of the exchanging protons of diamagnetic molecules differs from the chemical shift of bulk water within 6 ppm (Figure 1.24), their CEST effect is reduced and a smaller range of chemical exchange rates satisfies the proportion $k_{ex} << \Delta\omega$. Moreover, for chemical shifts near to that of bulk water (~ 4.8 ppm), a strong background signal from water is present, leading to magnetisation transfer from bulk water.[168, 172] In contrast, paramagnetic species such as lanthanide complexes or paramagnetic liposomes, show chemical shifts in the order of few hundreds of ppm, allowing a wider range of chemical exchange rates to be used and reducing magnetisation transfer (Figure 1.24).[7, 173]

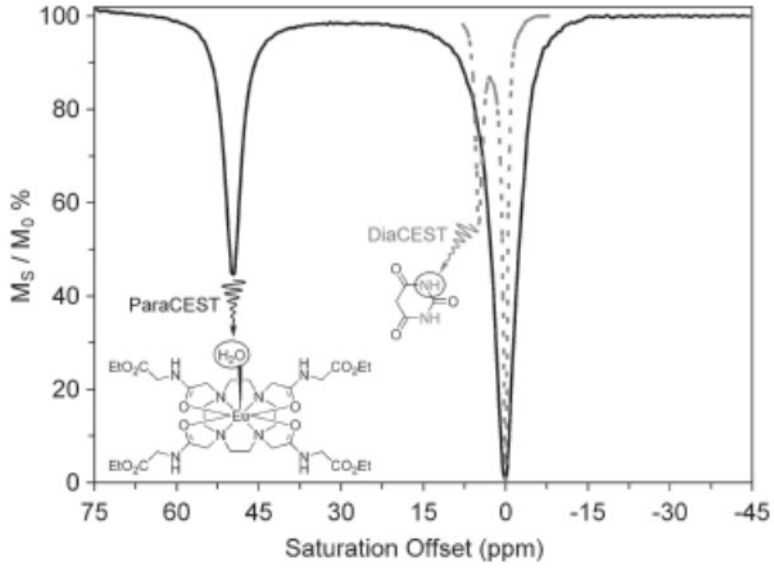


Figure 1.24: Z-spectrum showing $\Delta\omega$ for paramagnetic and for diamagnetic species measured as difference in chemical shift from bulk water (0 ppm). (Reprinted with permission from I. Hancu, W. T. Dixon, M. Woods, E. Vinogradov, A. D. Sherry and R. E. Lenkinski, *Acta Radiol.*, 2010, 51, 910-923. Copyright 2010, SAGE Publications)

1.8.2 Lanthanides in paramagnetic CEST (paraCEST) contrast agents

Paramagnetic Resonance Enhancement (PRE) effects dominate for metal ions such as Gd(III) and Mn(II), with isotropic distributions of *f*- or *d*-orbitals, respectively, leading to slow electron relaxation times. In complexes of these metals, Curie relaxation is generally negligible at low fields, but becomes significant at high fields for large molecules.[174, 175] Moreover, Curie relaxation dominates for metal ions with short electronic relaxation times (such as Ln(III) ions except from Gd(III) due to anisotropic arrangement of electrons in the *f*-orbitals). This finally leads to short T_2 relaxation times and large Pseudo-Contact Shift (PCS).[176] In 1958, McConnell and Robertson reported PCS dependence on the distance (r^{-3}), the metal magnetic susceptibility anisotropy tensor ($\Delta\chi$) its angle (θ, ϕ) relative to the principal axis.[177] (Equation 17).

$$\Delta\delta^{\mathrm{PCS}} = \frac{1}{12\pi r^3}[\Delta\chi_{ax}(3\cos^2\theta - 1) + 1.5\Delta\chi_{rh}\sin^2\theta\cos 2\phi] \qquad (17)$$

PCS give rise to a hyperfine shift in the resonances ($\Delta\omega$) of exchangeable protons (such as metal-bound water) and bulk water. Hyperfine shifts induced by lanthanide ions can be up to several hundred ppm, especially for protons that are part of the lanthanide complex (which can be a protein) or for metal-bound water.[176]

Practically, CEST efficiency can be evaluated by recording the Z-spectrum (or CEST-spectrum) by selectively presaturating the sample in incremental steps over a range of frequencies and plotting the residual bulk water signal, M_S/M_0, versus saturation frequency (as shown in Figure 1.25a,b).[7] In paramagnetic complexes, the CEST effect can arise from water molecule(s) bound to the metal or from -NH or -OH protons on the complex.[7] Of particular relevance are the LnDOTA-tetra(amide) complexes for slow exchange of the water molecule bound to the lanthanide, with water exchange rates from 2 to 1300 μs for the Eu(III) complexes.[178-184] Sherry and co-workers have demonstrated that water exchange rates are sensitive to the ionic radii of the lanthanide[183] in a given complex and recorded Z-spectra, showing the peaks relative to Ln-bound water in the Nd(III) and Eu(III) compounds (Figure 1.25a,b).[185] Water exchange has also been modulated by changes in the electronic properties of ligand atoms, through the presence of electron donating or electron withdrawing groups on the pendant arms.[186] The shifted amide NH protons in paramagnetic LnDOTA-tetra(amide) complexes, have also been used as exchangeable protons alternatively to bound water and found to efficiently transfer saturation to bulk water.[181, 187]

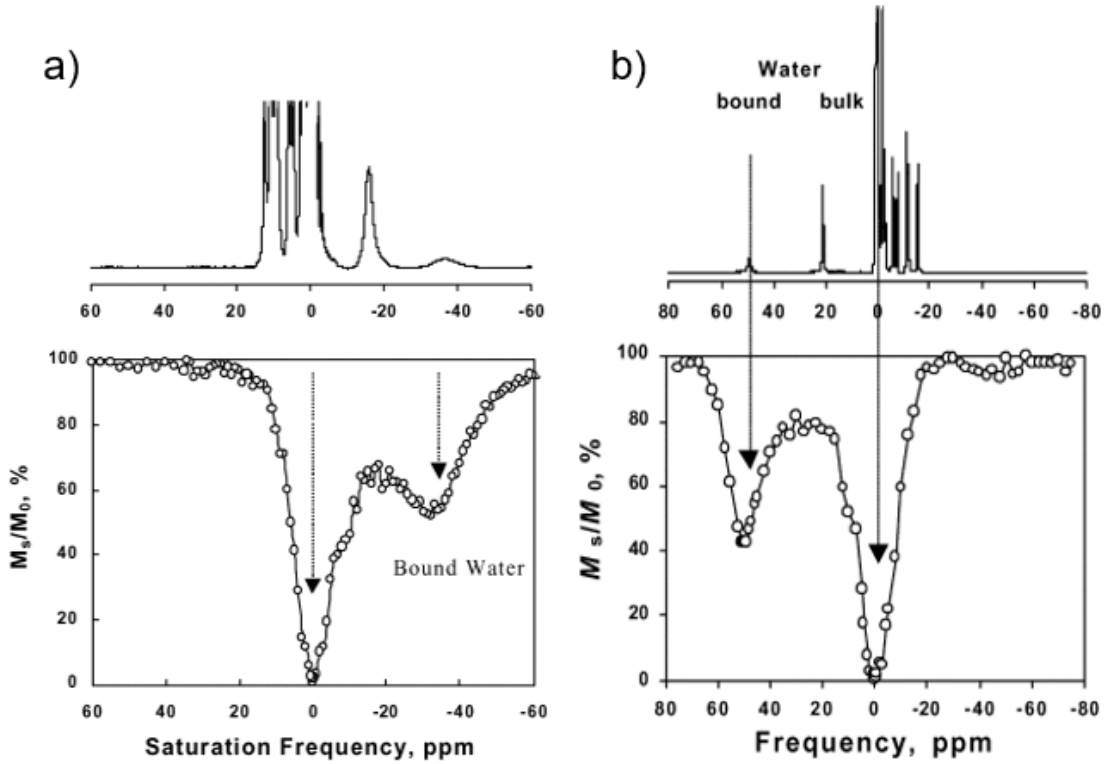


Figure 1.25: a) 500 MHz ^{1}H-NMR spectrum of [Nd(complex)(H_2O)](triflate)$_3$ acetonitrile with 2–4% H_2O and 25°C (top); and an Z-spectrum of [Nd(complex)(H_2O)]Cl_3 at pH 7.0 and room temperature (bottom). b) ^{1}H-NMR spectrum of [Eu(complex)(H_2O)]Cl_3 in aqueous solution at pH 7.0 and 25°C (top); and an Z-spectrum [Eu(complex)(H_2O)]Cl_3 at pH 7.0 and room temperature (bottom). (Adapted with permission from S. Zhang and A. D. Sherry, *J. Solid State Chem.*, 2003, 171, 38-43. Copyright 2002 Elsevier Science (USA)).

An important application for paraCEST agents are as responsive contrast agents which are sensitive to important biological parameters, such as pH,[170, 188] the presence of cations, such as Ca(II),[189] or DNA.[190] Moreover, redox properties of tissues can be detected because of the presence of some reductants such as NADH or NADPH, which can accumulate in oxygen deficient areas.[191] In addition, enzymatic activities can be monitored.[192] Within the development of novel paraCEST contrast agents with enhanced efficiency, macromolecules such as proteins,[193, 194] polymers[195] and liposomes[196] with paramagnetic sites can be used, as they feature a large number of exchangeable protons.

1.9 The aim of this work

On the basis of the promising relaxivities displayed by the Gd(III) coiled-coils,[76, 164, 197] this work looks to explore the alternatives to Gd(III) by incorporating essential metals such as Cu(II) and Mn(II), to improve MRI contrast agents efficiency by incorporating multiple metal ions within a coiled-coil and to evaluate the potential use of the analogous Ln(III) coiled-coils as paraCEST contrast agents.

The first aim of this work is to investigate the intrinsic low efficiency of Cu(II) compounds as MRI contrast agents, which arises from the presence of a single unpaired electron in the metal centre. The strategy adopted consists of including Cu(II) into a coiled-coil, aiming to slow down the molecular tumbling of the metallopeptide to finally enhance relaxivity. Moreover, the first and second sphere Cu(II) coordination spheres are modified to establish structure/activity relationships in such Cu(II) complexes. Mn(II) binding to designed coiled-coil is explored and the relative MRI relaxivities are determined and compared with other Mn(II)-based contrast agents. The impact of the introduction of more Gd(III) and Cu(II) binding sites within a coil is determined and compared. Finally, the potential use of Ln(III)-based coiled-coils as paraCEST contrast agents is investigated.

References

1. A. S. Merbach, L. Helm and É. Tóth, *The chemistry of contrast agents in medical magnetic resonance imaging*, John Wiley & Sons, 2013.
2. D. Gaynor and D. M. Griffith, *Dalton Trans.*, 2012, **41**, 13239-13257.
3. J. Wahsner, E. M. Gale, A. Rodríguez-Rodríguez and P. Caravan, *Chem. Rev.*, 2018, **119**, 957-1057.
4. P. Caravan, J. J. Ellison, T. J. McMurry and R. B. Lauffer, *Chem. Rev.*, 1999, **99**, 2293-2352.
5. E. M. Gale, I. P. Atanasova, F. Blasi, I. Ay and P. Caravan, *J. Am. Chem. Soc.*, 2015, **137**, 15548-15557.
6. K. Ward, A. Aletras and R. S. Balaban, *J. Magn. Reson.*, 2000, **143**, 79-87.
7. V. C. Pierre and M. J. Allen, Eds., *Contrast agents for MRI: experimental methods*, Royal Society of Chemistry, 2017.
8. B. L. Oliveira and P. Caravan, *Dalton Trans.*, 2017, **46**, 14488-14508.
9. S. Aime, M. Botta and E. Terreno, *Adv. Inorg. Chem.*, 2005, **57**, 173-237.
10. M. A. Brown and R. C. Semelka, *Radiology*, 1999, **213**, 647-662.
11. N. Bloembergen, E. M. Purcell and R. V. Pound, *Phys. Rev.*, 1948, **73**, 679.
12. H. Y. Carr and E. M. Purcell, *Phys. Rev.*, 1954, **94**, 630.
13. J. Simpson and H. Carr, *Phys. Rev.*, 1958, **111**, 1201.
14. R. Bitar, G. Leung, R. Perng, S. Tadros, A. R. Moody, J. Sarrazin, C. McGregor, M. Christakis, S. Symons and A. Nelson, *RadioGraphics*, 2006, **26**, 513-537.
15. S. Aime, S. G. Crich, E. Gianolio, G. Giovenzana, L. Tei and E. Terreno, *Coord. Chem. Rev.*, 2006, **250**, 1562-1579.
16. S. Aime, M. Botta, M. Fasano and E. Terreno, *Chem. Soc. Rev.*, 1998, **27**, 19-29.
17. M. Rogosnitzky and S. Branch, *BioMetals*, 2016, **29**, 365-376.
18. T. J. Clough, L. Jiang, K.-L. Wong and N. J. Long, *Nat. Commun.*, 2019, **10**, 1420.
19. L. D. Besheli, S. Aran, K. Shaqdan, J. Kay and H. Abujudeh, *Clin. Radiol.*, 2014, **69**, 661-668.
20. C. L. Bennett, Z. P. Qureshi, A. O. Sartor, L. B. Norris, A. Murday, S. Xirasagar and H. S. Thomsen, *Clin. Kidney J.*, 2012, **5**, 82-88.
21. D. D. Schwert, J. A. Davies and N. Richardson, in *Contrast Agents I*, Springer, 2002, pp. 165-199.
22. A. Santamaria, *Indian J. Med. Res.*, 2008, **128**, 484.
23. R. B. Lauffer, *Chem. Rev.*, 1987, **87**, 901-927.
24. E. Boros, E. M. Gale and P. Caravan, *Dalton Trans.*, 2015, **44**, 4804-4818.
25. J. M. Caille, B. Lemanceau and B. Bonnemain, *Am. J. Neuroradiol.*, 1983, **4**, 1041-1042.
26. R. E. Lenga, *The Sigma-Aldrich library of chemical safety data*, Sigma-Aldrich Corp., 1988.
27. A. C. Silva, J. H. Lee, I. Aoki and A. P. Koretsky, *NMR Biomed.*, 2004, **17**, 532-543.

28. M. Aschner, K. M. Erikson and D. C. Dorman, *Crit. Rev. Toxicol.*, 2005, **35**, 1-32.
29. R. M. de Bie, R. M. Gladstone, A. P. Strafella, J.-H. Ko and A. E. Lang, *Arch. Neurol.*, 2007, **64**, 886-889.
30. N. Bloembergen, *J. Chem. Phys.*, 1957, **27**, 572-573.
31. I. Solomon, *Phys. Rev.*, 1955, **99**, 559.
32. N. Bloembergen and L. Morgan, *J. Chem. Phys.*, 1961, **34**, 842-850.
33. M. Guéron, *J. Magn. Reson. (1969)*, 1975, **19**, 58-66.
34. M. Rubinstein, A. Baram and Z. Luz, *Mol. Phys.*, 1971, **20**, 67-80.
35. G. A. Rolla, C. Platas-Iglesias, M. Botta, L. Tei and L. Helm, *Inorg. Chem.*, 2013, **52**, 3268-3279.
36. P. Caravan, *Chem. Soc. Rev.*, 2006, **35**, 512-523.
37. M. Botta, *Eur. J. Inorg. Chem.*, 2000, **2000**, 399-407.
38. L. P. Hwang and J. H. Freed, *J. Chem. Phys.*, 1975, **63**, 4017-4025.
39. J. H. Freed, *J. Chem. Phys.*, 1978, **68**, 4034-4037.
40. P. Caravan, M. T. Greenfield, X. Li and A. D. Sherry, *Inorg. Chem.*, 2001, **40**, 6580-6587.
41. F. Carniato, M. Ricci, L. Tei, F. Garello, E. Terreno, E. Ravera, G. Parigi, C. Luchinat and M. Botta, *Inorg. Chem.*, 2022, **61**, 5380-5387.
42. D. H. Powell, O. M. N. Dhubhghaill, D. Pubanz, L. Helm, Y. S. Lebedev, W. Schlaepfer and A. E. Merbach, *J. Am. Chem. Soc.*, 1996, **118**, 9333-9346.
43. D. Esteban-Gómez, C. Cassino, M. Botta and C. Platas-Iglesias, *RSC Adv.*, 2014, **4**, 7094-7103.
44. Y. Ducommun, K. E. Newman and A. E. Merbach, *Inorg. Chem.*, 1980, **19**, 3696-3703.
45. B. Drahoš, J. Kotek, I. Císařová, P. Hermann, L. Helm, I. Lukeš and É. Tóth, *Inorg. Chem.*, 2011, **50**, 12785-12801.
46. E. Molnar, N. Camus, V. Patinec, G. A. Rolla, M. Botta, G. Tircso, F. K. Kalman, T. Fodor, R. Tripier and C. Platas-Iglesias, *Inorg. Chem.*, 2014, **53**, 5136-5149.
47. S. Zhang, M. Merritt, D. E. Woessner, R. E. Lenkinski and A. D. Sherry, *Acc. Chem. Res.*, 2003, **36**, 783-790.
48. B. N. Siriwardena-Mahanama and M. J. Allen, *Molecules*, 2013, **18**, 9352-9381.
49. F. Botteman, G. M. Nicolle, L. Vander Elst, S. Laurent, A. E. Merbach and R. N. Muller, *Eur. J. Inorg. Chem.*, 2002, **2002**, 2686-2693.
50. É. Tóth, L. Burai, E. Brücher and A. E. Merbach, *J. Chem. Soc., Dalton Trans.*, 1997, 1587-1594.
51. P. Hermann, J. Kotek, V. Kubíček and I. Lukeš, *Dalton Trans.*, 2008, 3027-3047.
52. J. Xu, S. J. Franklin, D. W. Whisenhunt Jr and K. N. Raymond, *J. Am. Chem. Soc.*, 1995, **117**, 7245-7246.
53. K. Nwe, L. H. Bryant Jr and M. W. Brechbiel, *Bioconjugate Chem.*, 2010, **21**, 1014-1017.

54. P. Caravan, N. J. Cloutier, M. T. Greenfield, S. A. McDermid, S. U. Dunham, J. W. Bulte, J. C. Amedio, R. J. Looby, R. M. Supkowski and W. D. Horrocks, *J. Am. Chem. Soc.*, 2002, **124**, 3152-3162.

55. R. B. Lauffer, D. J. Parmelee, S. U. Dunham, H. S. Ouellet, R. P. Dolan, S. Witte, T. J. McMurry and R. C. Walovitch, *Radiology*, 1998, **207**, 529-538.

56. K. Shamsi, E. K. Yucel and P. Chamberlin, *Invest. Radiol.*, 2006, **41**, 822-830.

57. P. Caravan, C. T. Farrar, L. Frullano and R. Uppal, *Contrast Media Mol. Imaging*, 2009, **4**, 89-100.

58. S. Koenig and R. Brown 3rd, *Magn. Reson. Annu.*, 1987, 263-286.

59. J. Oakes and E. G. Smith, *J. Chem. Soc., Faraday Transactions 1*, 1983, **79**, 543-552.

60. M. Tweedle, H. Brittain, W. Eckelman, G. Gaughan, J. Hagan, P. Wedeking and V. Runge, *Partain, C. L., Price, R. R., Patton, J. A., Kulkarni, V., James, A. E. Jr., Eds.*, 1987, 793-809.

61. J. Oakes and C. G. van Kralingen, *J. Chem. Soc., Dalton Trans.*, 1984, 1133-1137.

62. M. L. Blackwell, C. T. Farrar, B. Fischl and B. R. Rosen, *NeuroImage*, 2009, **46**, 382-393.

63. P. Chen, M. R. Miah and M. Aschner, *F1000Res.*, 2016, **5**.

64. L. M. Gaetke and C. K. Chow, *Toxicology*, 2003, **189**, 147-163.

65. D. H. Powell, L. Helm and A. E. Merbach, *J. Chem. Phys.*, 1991, **95**, 9258-9265.

66. D. H. Powell, P. Furrer, P.-A. Pittet and A. E. Merbach, *J. Phys. Chem.*, 1995, **99**, 16622-16629.

67. A. Pasquarello, I. Petri, P. S. Salmon, O. Parisel, R. Car, É. Tóth, D. H. Powell, H. E. Fischer, L. Helm and A. E. Merbach, *Science*, 2001, **291**, 856-859.

68. S. Hoffmann and J. Goslar, *Appl. Magn. Reson.*, 1998, **14**, 293-303.

69. I. Bertini, C. Luchinat, R. D. Brown III and S. H. Koenig, *J. Am. Chem. Soc.*, 1989, **111**, 3532-3536.

70. C. Luchinat and Z. Xia, *Coord. Chem. Rev.*, 1992, **120**, 281-307.

71. T. Kupka, J. O. Dzięgielewski, G. Pasterna and J. G. Małecki, *Magn. Reson. Imaging*, 1992, **10**, 855-858.

72. L. Dunbar, R. J. Sowden, K. D. Trotter, M. K. Taylor, D. Smith, A. R. Kennedy, J. Reglinski and C. M. Spickett, *BioMetals*, 2015, **28**, 903-912.

73. J. J. Yang, J. Yang, L. Wei, O. Zurkiya, W. Yang, S. Li, J. Zou, Y. Zhou, A. L. W. Maniccia and H. Mao, *J. Am. Chem. Soc.*, 2008, **130**, 9260-9267.

74. R. C. Brasch, *Magn. Reson. Med.*, 1991, **22**, 282-287.

75. M. D. Ogan, U. Schmiedl, M. E. Moseley, W. Grodd, H. Paajanen and R. C. Brasch, *Invest. Radiol.*, 1987, **22**, 665-671.

76. M. R. Berwick, D. J. Lewis, A. W. Jones, R. A. Parslow, T. R. Dafforn, H. J. Cooper, J. Wilkie, Z. Pikramenou, M. M. Britton and A. F. Peacock, *J. Am. Chem. Soc.*, 2014, **136**, 1166-1169.

77. B. S. Harrison and A. Atala, *Biomaterials*, 2007, **28**, 344-353.

78. K. B. Hartman, S. Laus, R. D. Bolskar, R. Muthupillai, L. Helm, E. Toth, A. E. Merbach and L. J. Wilson, *Nano Lett.*, 2008, **8**, 415-419.

79. B. Sitharaman, M. Van Der Zande, J. S. Ananta, X. Shi, A. Veltien, X. F. Walboomers, L. J. Wilson, A. G. Mikos, A. Heerschap and J. A. Jansen, *J. Biomed. Mater. Res. Part A*, 2010, **93**, 1454-1462.

80. Q. Xu, L. Zhu, M. Yu, F. Feng, L. An, C. Xing and S. Wang, *Polymer*, 2010, **51**, 1336-1340.

81. B. Sitharaman, K. R. Kissell, K. B. Hartman, L. A. Tran, A. Baikalov, I. Rusakova, Y. Sun, H. A. Khant, S. J. Ludtke and W. Chiu, *Chem. Comm.*, 2005, 3915-3917.

82. E. Battistini, E. Gianolio, R. Gref, P. Couvreur, S. Fuzerova, M. Othman, S. Aime, B. Badet and P. Durand, *Chem. Eur. J.*, 2008, **14**, 4551-4561.

83. J. Estelrich, M. J. Sánchez-Martín and M. A. Busquets, *Int. J. Nanomedicine*, 2015, **10**, 1727.

84. A. Louie, *J. Magn. Reson. Imaging*, 2013, **38**, 530-539.

85. D. Pan, S. D. Caruthers, A. Senpan, C. Yalaz, A. J. Stacy, G. Hu, J. N. Marsh, P. J. Gaffney, S. A. Wickline and G. M. Lanza, *J. Am. Chem. Soc.*, 2011, **133**, 9168-9171.

86. O. Perlman, I. S. Weitz and H. Azhari, *Phys. Med. Biol.*, 2015, **60**, 5767.

87. T. Barrett, G. Ravizzini, P. L. Choyke and H. Kobayashi, *IEEE Eng. Med. Biol. Mag.*, 2009, **28**, 12.

88. A. Gossmann, Y. Okuhata, D. M. Shames, T. H. Helbich, T. P. Roberts, M. F. Wendland, S. Huber and R. C. Brasch, *Radiology*, 1999, **213**, 265-272.

89. J. Bremerich, M. F. Wendland, H. Arheden, R. Wyttenbach, D. W. Gao, J. P. Huberty, M. W. Dae, C. B. Higgins and M. Saeed, *J. Am. Coll. Cardiol.*, 1998, **32**, 787-793.

90. H. Kobayashi, S. Kawamoto, T. Saga, N. Sato, T. Ishimori, J. Konishi, K. Ono, K. Togashi and M. W. Brechbiel, *Bioconjugate Chem.*, 2001, **12**, 587-593.

91. A. Accardo, D. Tesauro, L. Aloj, C. Pedone and G. Morelli, *Coord. Chem. Rev.*, 2009, **253**, 2193-2213.

92. M. Grogna, R. Cloots, A. Luxen, C. Jérôme, C. Passirani, N. Lautram, J.-F. Desreux and C. Detrembleur, *Polym. Chem.*, 2010, **1**, 1485-1490.

93. L. Lattuada and G. Lux, *Tetrahedron Lett.*, 2003, **44**, 3893-3895.

94. G. Kabalka, E. Buonocore, K. Hubner, T. Moss, N. Norley and L. Huang, *Radiology*, 1987, **163**, 255-258.

95. C. W. Grant, S. Karlik and E. Florio, *Magn. Reson. Med.*, 1989, **11**, 236-243.

96. T. Fritz, G. Wu, D. Shen, B. Kulik, T. New, M. Crowell, N. Wilke and E. Unger, *J. Liposome Res.*, 1994, **4**, 811-834.

97. V. Henrotte, S. Laurent, V. Gabelica, L. V. Elst, E. Depauw and R. N. Muller, *Rapid Commun. Mass Spectrom.*, 2004, **18**, 1919-1924.

98. M. B. Winter, P. J. Klemm, C. M. Phillips-Piro, K. N. Raymond and M. A. Marletta, *Inorg. Chem.*, 2013, **52**, 2277-2279.

99. L. M. De León-Rodríguez, A. Ortiz, A. L. Weiner, S. Zhang, Z. Kovacs, T. Kodadek and A. D. Sherry, *J. Am. Chem. Soc.*, 2002, **124**, 3514-3515.

100. S. R. Bull, M. O. Guler, R. E. Bras, T. J. Meade and S. I. Stupp, *Nano Lett.*, 2005, **5**, 1-4.

101. S. R. Bull, M. O. Guler, R. E. Bras, P. N. Venkatasubramanian, S. I. Stupp and T. J. Meade, *Bioconjugate Chem.*, 2005, **16**, 1343-1348.

102. P. Caravan, J. M. Greenwood, J. T. Welch and S. J. Franklin, *Chem. Comm.*, 2003, 2574-2575.

103. S. Xue, J. Qiao, J. Jiang, K. Hubbard, N. White, L. Wei, S. Li, Z. R. Liu and J. J. Yang, *Med. Res. Rev.*, 2014, **34**, 1070-1099.

104. S. Xue, H. Yang, J. Qiao, F. Pu, J. Jiang, K. Hubbard, K. Hekmatyar, J. Langley, M. Salarian and R. C. Long, *PNAS*, 2015, **112**, 6607-6612.

105. L. Regan and W. F. DeGrado, *Science*, 1988, **241**, 976-978.

106. W. F. DeGrado, Z. R. Wasserman and J. D. Lear, *Science*, 1989, **243**, 622-628.

107. K. J. Grayson and J. R. Anderson, *J. R. Soc. Interface*, 2018, **15**, 20180472.

108. M. Tegoni, *Eur. J. Inorg. Chem.*, 2014, **2014**, 2177-2193.

109. A. F. Peacock, O. Iranzo and V. L. Pecoraro, *Dalton Trans.*, 2009, 2271-2280.

110. J. Liu and B. Rost, *Protein Sci.*, 2001, **10**, 1970-1979.

111. F. H. Crick, *Nature*, 1952, **170**, 882-883.

112. P. B. Harbury, T. Zhang, P. S. Kim and T. Alber, *Science*, 1993, **262**, 1401-1407.

113. F. Crick, *Acta Cryst.*, 1953, **6**, 689-697.

114. P. B. Harbury, P. S. Kim and T. Alber, *Nature*, 1994, **371**, 80-83.

115. J. M. Fletcher, A. L. Boyle, M. Bruning, G. J. Bartlett, T. L. Vincent, N. R. Zaccai, C. T. Armstrong, E. H. Bromley, P. J. Booth and R. L. Brady, *ACS Synth. Biol.*, 2012, **1**, 240-250.

116. N. E. Zhou, C. M. Kay and R. S. Hodges, *J. Mol. Biol.*, 1994, **237**, 500-512.

117. W. D. Kohn, C. M. Kay and R. S. Hodges, *J. Mol. Biol.*, 1998, **283**, 993-1012.

118. H. R. Bosshard, D. N. Marti and I. Jelesarov, *J. Mol. Recognit.*, 2004, **17**, 1-16.

119. M. Meier, J. Stetefeld and P. Burkhard, *J. Struct. Biol.*, 2010, **170**, 192-201.

120. A. J. Gamble and A. F. Peacock, *Protein Design: Methods and Applications*, 2014, 211-231.

121. J. Y. Su, R. S. Hodges and C. M. Kay, *Biochemistry*, 1994, **33**, 15501-15510.

122. R. G. Pearson, *Chemical hardness*, Wiley Online Library, 1997.

123. S. Geremia, L. Di Costanzo, L. Randaccio, D. E. Engel, A. Lombardi, F. Nastri and W. F. DeGrado, *J. Am. Chem. Soc.*, 2005, **127**, 17266-17276.

124. A. Lombardi, C. M. Summa, S. Geremia, L. Randaccio, V. Pavone and W. F. DeGrado, *PNAS*, 2000, **97**, 6298-6305.

125. P. Teare, C. F. Smith, S. J. Adams, S. Anbu, B. Ciani, L. J. Jeuken and A. F. Peacock, *Dalton Trans.*, 2018, **47**, 10784-10790.

126. B. A. Krantz and T. R. Sosnick, *Nat. Struct. Biol.*, 2001, **8**, 1042-1047.

127. D. Shiga, Y. Funahashi, H. Masuda, A. Kikuchi, M. Noda, S. Uchiyama, K. Fukui, K. Kanaori, K. Tajima and Y. Takano, *Biochemistry*, 2012, **51**, 7901-7907.

128. M. R. Ghadiri and M. A. Case, *Angew. Chem. - Int. Ed. Eng.*, 1993, **32**, 1594-1597.

129. J. T. Rubino and K. J. Franz, *J. Inorg. Biochem.*, 2012, **107**, 129-143.

130. M. Tegoni, F. Yu, M. Bersellini, J. E. Penner-Hahn and V. L. Pecoraro, *PNAS*, 2012, **109**, 21234-21239.

131. A. Messerschmidt, *Handbook of metalloproteins*, Wiley, 2001.

132. M. R. Ghadiri and C. Choi, *J. Am. Chem. Soc.*, 1990, **112**, 1630-1632.

133. M. R. Ghadiri, C. Soares and C. Choi, *J. Am. Chem. Soc.*, 1992, **114**, 825-831.

134. K. Suzuki, H. Hiroaki, D. Kohda and T. Tanaka, *Protein Engineering, Design and Selection*, 1998, **11**, 1051-1055.

135. K. Suzuki, H. Hiroaki, D. Kohda, H. Nakamura and T. Tanaka, *J. Am. Chem. Soc.*, 1998, **120**, 13008-13015.

136. T. Kiyokawa, K. Kanaori, K. Tajima, M. Koike, T. Mizuno, J. I. Oku and T. Tanaka, *J. Pept. Res.*, 2004, **63**, 347-353.

137. T. Tanaka, T. Mizuno, S. Fukui, H. Hiroaki, J.-i. Oku, K. Kanaori, K. Tajima and M. Shirakawa, *J. Am. Chem. Soc.*, 2004, **126**, 14023-14028.

138. T. Mizuno, K. Murao, Y. Tanabe, M. Oda and T. Tanaka, *J. Am. Chem. Soc.*, 2007, **129**, 11378-11383.

139. D. Shiga, D. Nakane, T. Inomata, H. Masuda, M. Oda, M. Noda, S. Uchiyama, K. Fukui, Y. Takano and H. Nakamura, *Biopolymers*, 2009, **91**, 907-916.

140. F. Yu, J. E. Penner-Hahn and V. L. Pecoraro, *J. Am. Chem. Soc.*, 2013, **135**, 18096-18107.

141. E. Mathieu, A. E. Tolbert, K. J. Koebke, C. Tard, O. Iranzo, J. E. Penner-Hahn, C. Policar and V. Pecoraro, *Chem. Eur. J.*, 2020, **26**, 249-258.

142. J. W. Bryson, J. R. Desjarlais, T. M. Handel and W. F. Degrado, *Protein Sci.*, 1998, **7**, 1404-1414.

143. R. H. Holm, P. Kennepohl and E. I. Solomon, *Chem. Rev.*, 1996, **96**, 2239-2314.

144. A. M. Thomas, B.-L. Lin, E. C. Wasinger and T. D. P. Stack, *J. Am. Chem. Soc.*, 2013, **135**, 18912-18919.

145. D. Shiga, D. Nakane, T. Inomata, Y. Funahashi, H. Masuda, A. Kikuchi, M. Oda, M. Noda, S. Uchiyama and K. Fukui, *J. Am. Chem. Soc.*, 2010, **132**, 18191-18198.

146. R. Schnepf, P. Hörth, E. Bill, K. Wieghardt, P. Hildebrandt and W. Haehnel, *J. Am. Chem. Soc.*, 2001, **123**, 2186-2195.

147. R. Schnepf, W. Haehnel, K. Wieghardt and P. Hildebrandt, *J. Am. Chem. Soc.*, 2004, **126**, 14389-14399.

148. O. A. Kharenko and M. Y. Ogawa, *J. Inorg. Biochem.*, 2004, **98**, 1971-1974.

149. D. W. Christianson, *Prog. Biophys. Mol. Biol.*, 1997, **67**, 217-252.

150. F. A. Armstrong, *Phil. Trans. R. Soc. B*, 2008, **363**, 1263-1270.

151. Y. Umena, K. Kawakami, J.-R. Shen and N. Kamiya, *Nature*, 2011, **473**, 55-60.

152. M. Suga, F. Akita, K. Hirata, G. Ueno, H. Murakami, Y. Nakajima, T. Shimizu, K. Yamashita, M. Yamamoto and H. Ago, *Nature*, 2015, **517**, 99-103.

153. D. W. Yoder, J. Hwang and J. E. Penner-Hahn, in *Metal ions in biological systems*, CRC Press, 2000, pp. 575-606.

154. V. V. Barynin and J. W. Whittaker, *Handbook of Metalloproteins*, 2006.

155. T. L. Olson, E. Espiritu, S. Edwardraja, E. Canarie, M. Flores, J. C. Williams, G. Ghirlanda and J. P. Allen, *Biochim. Biophys. Acta (BBA)-Bioenergetics*, 2017, **1858**, 945-954.

156. T. L. Olson, E. Espiritu, S. Edwardraja, C. R. Simmons, J. C. Williams, G. Ghirlanda and J. P. Allen, *Biochim. Biophys. Acta (BBA)-Bioenergetics*, 2016, **1857**, 539-547.

157. T. Nakagawa, R. Mitsui, A. Tani, K. Sasa, S. Tashiro, T. Iwama, T. Hayakawa and K. Kawai, *PLoS ONE*, 2012, **7**, e50480.

158. J. A. Cotruvo Jr, E. R. Featherston, J. A. Mattocks, J. V. Ho and T. N. Laremore, *J. Am. Chem. Soc.*, 2018, **140**, 15056-15061.

159. E. R. Featherston and J. A. Cotruvo Jr, *Biochim. Biophys. Acta (BBA)-Molecular Cell Research*, 2021, **1868**, 118864.

160. W. D. Kohn, C. M. Kay and R. S. Hodges, *J. Pept. Res.*, 1998, **51**, 9-18.

161. W. D. Kohn, C. M. Kay, B. D. Sykes and R. S. Hodges, *J. Am. Chem. Soc.*, 1998, **120**, 1124-1132.

162. A. Kashiwada, K. Ishida and K. Matsuda, *BCSJ*, 2007, **80**, 2203-2207.

163. L. N. Slope, O. J. Daubney, H. Campbell, S. A. White and A. F. Peacock, *Angew. Chem.*, 2021, **133**, 24678-24682.

164. M. R. Berwick, L. N. Slope, C. F. Smith, S. M. King, S. L. Newton, R. B. Gillis, G. G. Adams, A. J. Rowe, S. E. Harding and M. M. Britton, *Chem. Sci.*, 2016, **7**, 2207-2216.

165. L. N. Slope, PhD, University of Birmingham, 2017.

166. S. L. Newton, PhD, University of Birmingham, 2018.

167. E. Terreno, D. D. Castelli, A. Viale and S. Aime, *Chem. Rev.*, 2010, **110**, 3019-3042.

168. I. Hancu, W. T. Dixon, M. Woods, E. Vinogradov, A. D. Sherry and R. E. Lenkinski, *Acta Radiol.*, 2010, **51**, 910-923.

169. J. Zhou and P. C. Van Zijl, *Prog. Nucl. Magn. Reson. Spectrosc.*., 2006, **48**, 109-136.

170. S. Aime, D. Delli Castelli and E. Terreno, *Angew. Chem. Int. Ed.*, 2002, **41**, 4334-4336.

171. E. Vinogradov, S. Zhang, A. Lubag, J. A. Balschi, A. D. Sherry and R. E. Lenkinski, *J. Magn. Reson.*, 2005, **176**, 54-63.

172. L. J. Martin, M. J. Hähnke, M. Nitz, J. Wöhnert, N. R. Silvaggi, K. N. Allen, H. Schwalbe and B. Imperiali, *J. Am. Chem. Soc.*, 2007, **129**, 7106-7113.

173. S. Aime, D. Delli Castelli and E. Terreno, *Angew. Chem. Int. Ed.*, 2003, **42**, 4527-4529.

174. T. C. Soesbe, M. E. Merritt, K. N. Green, F. A. Rojas-Quijano and A. D. Sherry, *Magn. Reson. Med.*, 2011, **66**, 1697-1703.

175. M. Norek and J. A. Peters, *Prog. Nucl. Magn. Reson. Spectrosc.*., 2011, **59**, 64-82.

176. G. Pintacuda, M. John, X.-C. Su and G. Otting, *Acc. Chem. Res.*, 2007, **40**, 206-212.

177. H. M. McConnell and R. E. Robertson, *J. Chem. Phys.*, 1958, **29**, 1361-1365.

178. S. Aime, A. Barge, M. Botta, A. S. De Sousa and D. Parker, *Angew. Chem. Int. Ed.,* 1998, **37**, 2673-2675.

179. S. Aime, A. Barge, J. I. Bruce, M. Botta, J. A. Howard, J. M. Moloney, D. Parker, A. S. De Sousa and M. Woods, *J. Am. Chem. Soc.*, 1999, **121**, 5762-5771.

180. F. A. Dunand, S. Aime and A. E. Merbach, *J. Am. Chem. Soc.*, 2000, **122**, 1506-1512.

181. S. Aime, A. Barge, D. Delli Castelli, F. Fedeli, A. Mortillaro, F. U. Nielsen and E. Terreno, *Magn. Reson. Med.*, 2002, **47**, 639-648.

182. S. Zhang and A. D. Sherry, 2002.

183. S. Zhang, K. Wu and A. D. Sherry, *J. Am. Chem. Soc.*, 2002, **124**, 4226-4227.

184. S. Zhang, K. Wu and A. D. Sherry, *Invest. Radiol.*, 2001, **36**, 82-86.

185. S. Zhang and A. D. Sherry, *J. Solid State Chem.*, 2003, **171**, 38-43.

186. S. J. Ratnakar, M. Woods, A. J. Lubag, Z. Kovács and A. D. Sherry, *J. Am. Chem. Soc.*, 2008, **130**, 6-7.

187. S. Zhang, L. Michaudet, S. Burgess and A. D. Sherry, *Angew. Chem. Int. Ed.*, 2002, **41**, 1919-1921.

188. V. R. Sheth, G. Liu, Y. Li and M. D. Pagel, *Contrast Media Mol. Imaging*, 2012, **7**, 26-34.

189. G. Angelovski, P. Fouskova, I. Mamedov, S. Canals, E. Toth and N. K. Logothetis, *ChemBioChem*, 2008, **9**, 1729-1734.

190. K. Nwe, C. M. Andolina, C.-H. Huang and J. R. Morrow, *Bioconjugate Chem.*, 2009, **20**, 1375-1382.

191. P. B. Tsitovich, P. J. Burns, A. M. McKay and J. R. Morrow, *J. Inorg. Biochem.*, 2014, **133**, 143-154.

192. B. Yoo and M. D. Pagel, *J. Am. Chem. Soc.*, 2006, **128**, 14032-14033.

193. O. Vasalatiy, R. D. Gerard, P. Zhao, X. Sun and A. D. Sherry, *Bioconjugate Chem.*, 2008, **19**, 598-606.

194. O. Vasalatiy, P. Zhao, M. Woods, A. Marconescu, A. Castillo-Muzquiz, P. Thorpe, G. E. Kiefer and A. D. Sherry, *Bioorg. Med. Chem.*, 2011, **19**, 1106-1114.

195. N. Goffeney, J. W. Bulte, J. Duyn, L. H. Bryant and P. C. Van Zijl, *J. Am. Chem. Soc.*, 2001, **123**, 8628-8629.

196. E. Terreno, D. Delli Castelli, C. Cabella, W. Dastrù, A. Sanino, J. Stancanello, L. Tei and S. Aime, *Chem. Biodivers.*, 2008, **5**, 1901-1912.

197. L. N. Slope, M. G. Hill, C. F. Smith, P. Teare, F. J. de Cogan, M. M. Britton and A. F. Peacock, *Chem. Comm.*, 2020, **56**, 3729-3732.

CHAPTER 2

EXPERIMENTAL TECHNIQUES

2.1 Solid-phase peptide synthesis

The solid-phase peptide synthesis (SPPS) concept was introduced by Merrifield in 1963.[1] In SPPS, a peptide sequence is synthetised on a solid support, often referred to as resin, where the C-terminus of the first amino acid is coupled through the carboxyl group. To prevent polymerisation side reactions, the N-terminus is temporarily protected. To allow a further coupling reaction (the addition of amino acids), the protection on the N-terminus is selectively removed. The coupling reaction takes place between the deprotected amine on the N-terminus and an excess of the second amino acid, through its carbonyl group, which is made more reactive by an activator added to the mixture.

Any unreacted reagent is removed by washing, followed by another deprotection and coupling reactions until the desired sequence is produced. With peptide getting longer on the resin, deprotection and coupling reactions become more difficult thus generating more deletions. For these reasons, only peptides with sequences shorter than about 50 amino acids are routinely made with this technique.[2, 3] Figure 2.1 shows the reactions occurring during the peptide synthesis.

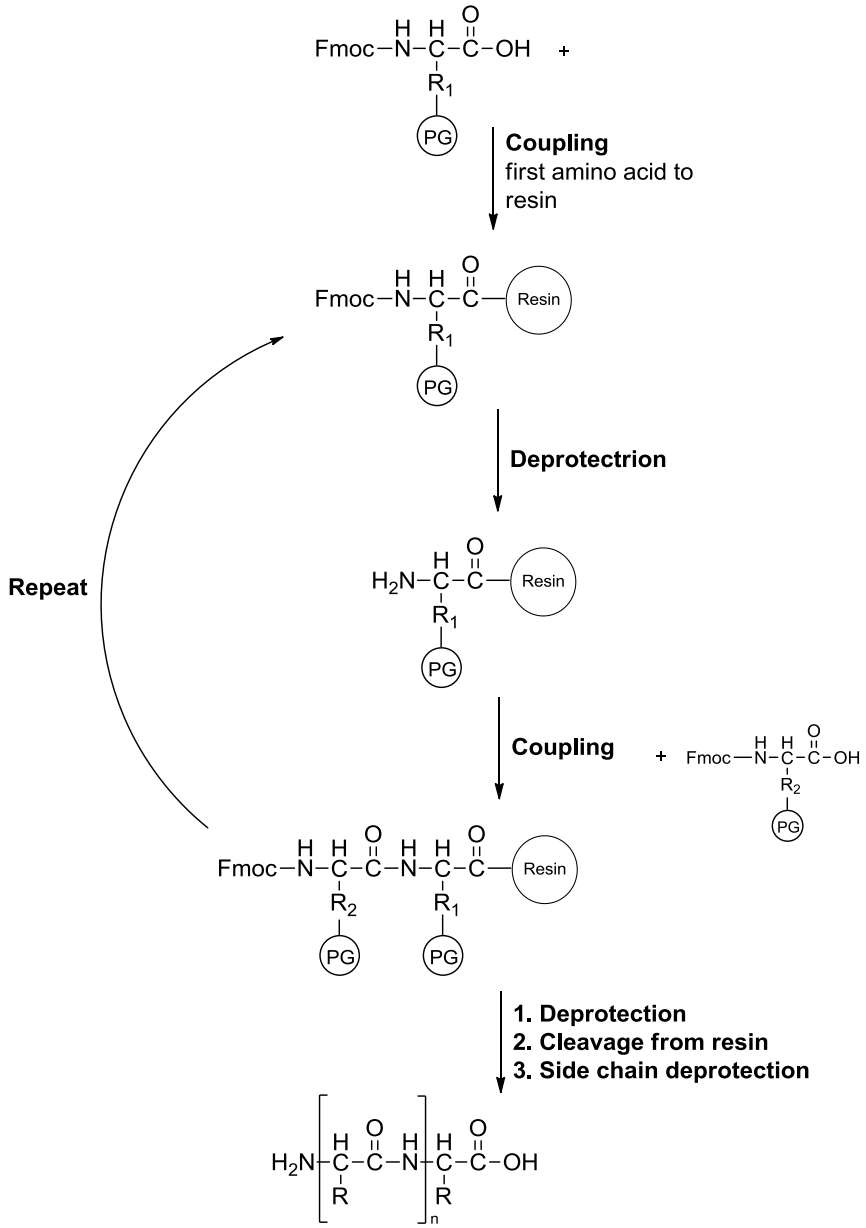


Figure 2.1: Scheme of the solid-phase peptide synthesis (SPPS) cycle. The coupling of the first amino acid, featuring protecting group (PG), to the resin is followed by the deprotection of the Fmoc (Fluorenylmethoxycarbonyl) group allowing for the coupling with the next amino acid. The procedure is repeated until the whole peptide is synthetised. Finally, the peptide is cleaved from the resin and side chains are deprotected.

Deprotection and coupling reactions can be microwave-assisted, allowing more complex sequences to be constructed and preventing aggregation and secondary structure formation.[4-6] The peptides can be synthetised using Fmoc-SPPS, where Fmoc (Fluorenylmethoxycarbonyl) is a protecting group commonly used to protect amines. This can be removed under basic conditions, such as with piperidine, to generate the free amine for subsequent coupling (Figure 2.2).

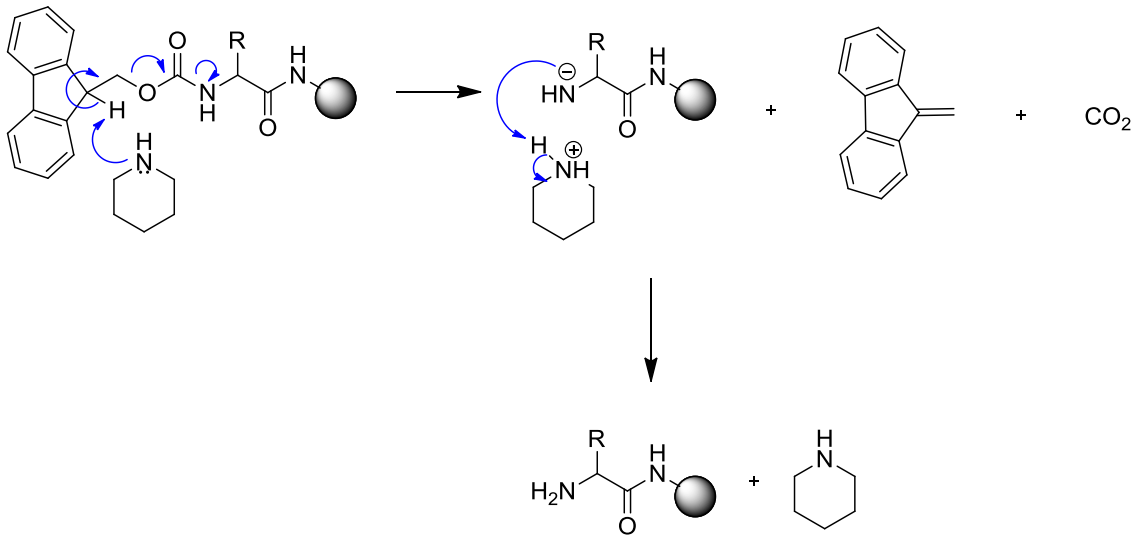


Figure 2.2: Scheme showing deprotection at the N-terminus from Fmoc using peperidine. Resin shown as black sphere.

A rink amide 4-methylbenzhydrylamine (MBHA) resin can be used as a solid support, while (O-(benzotriazol-1-yl)-N,N,N',N'- tetramethyluronium) hexafluorophosphate (HBTU) and diisopropylethylamine (DIPEA) are used to activate the carboxyl and amine groups, respectively, to allow the peptide amide bond formation (Figure 2.3). Protecting groups are used to prevent side reactions through amino acid side chains. These protecting groups, generally acid-liable, can be removed orthogonally from the N-terminal protecting group, thus they are not removed during the deprotection steps in the synthesis process. At the end of the synthesis, the final amino acid can be acetylated at the N-terminus, using acetic acid and DIPEA, to prevent any further coupling reaction.[7] Finally, the peptide is simultaneously cleaved from the resin and the amino acid side chain protecting groups removed, by treatment with trifluoroacetic acid (TFA).[2, 3]

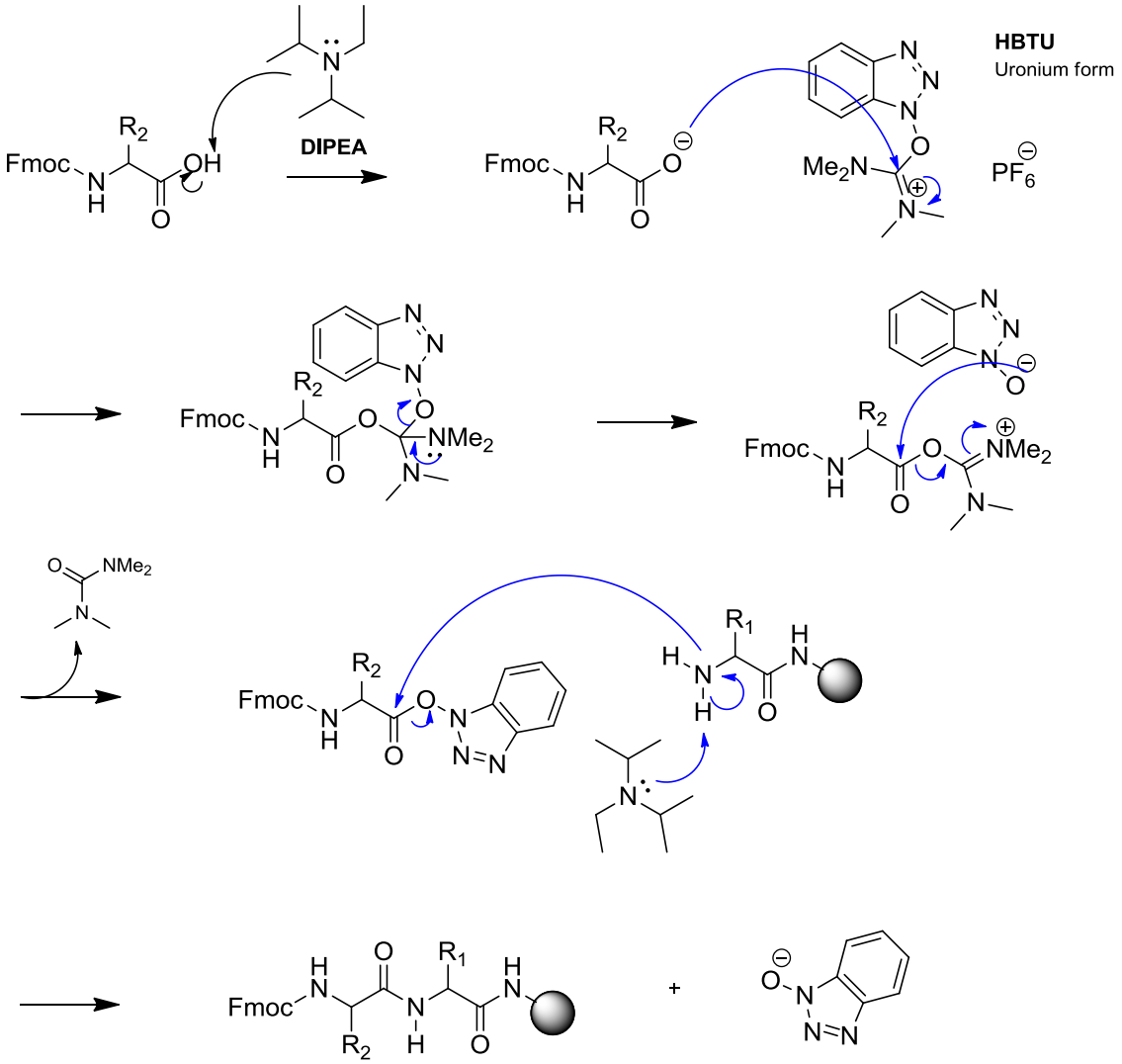


Figure 2.3: Scheme showing the mechanism associated with amide bond formation through activation by (O-(benzotriazol-1-yl)-NN,N',N'-tetramethyluronium) hexafluorophosphate (HBTU) and diisopropyl-ethylamine (DIPEA). Resin shown as black sphere.

2.2 Reverse-Phase High Performance Liquid Chromatography (RP-HPLC)

Liquid chromatography is used to separate compounds according to their charge, molecular size, hydrophobicity and absorption properties.[8-11] The sample is loaded onto a stationary phase and a mobile phase (solvent) is passed through the sample at high pressure, allowing the components to move along the stationary phase at different rates. Sample retention on the column is dependent on the increased interaction and affinity of the sample to the stationary rather than the mobile phase.[8-11] In normal high performance liquid chromatography (HPLC) the stationary phase is polar. Reverse-Phase High Performance Liquid Chromatography (RP-HPLC) is a

common technique used to analyse and purify peptides and proteins.[9] Here, the stationary phase is non-polar, and is normally composed of aliphatic carbon chains (such as C_{18} used in this work) on a silica support.

Based on their hydrophobicity and size, different molecules can be separated by varying the polarity of the mobile phase (eluent). The weaker the interaction with the non-polar stationary phase, or stronger with the polar mobile phase, the faster the sample will be eluted. This means that low molecular weight and polar peptides display short retention times. The polarity of the eluent can be controlled using a mixture of different solvents, such as acetonitrile and water. Polarity can be kept constant (isocratic) or can be varied during the separation (gradient). TFA can be used in small amount to interact with positive charged ionic groups (ion pairing) and, therefore, increase the retention time of the proteins/peptides on the column. Moreover, TFA helps to suppress adverse ionic interactions between peptides and silanol groups on the silica, leading to increased sharpness and symmetry of peaks. Moreover, TFA helps to increase peptide solubility of proteins/peptides containing a large number of hydrophobic residues.[8-11] UV-Visible absorption can be used to monitor the eluent. In proteins, the peptide bond absorption is below 240 nm and aromatic amino acid side chain absorption is in the range 260 to 320 nm.[12] Wavelengths of 210 nm and 280 nm can used to monitor the absorption of organic molecules, including peptides, and of the tryptophan (Trp, W), respectively.

2.3 Mass spectrometry

Mass spectrometry is an analytical technique where a sample is ionised and then separated according to its mass (m) to charge (z) ratio (m/z). Ionisation can be produced using different techniques.[11] Electron Impact (EI) uses high energy focused beam of electrons, generating ionisation and fragmentation of the sample. It is generally considered too harsh for use with peptides, therefore, electron spray ionisation (ESI) and matrix assisted laser desorption ionisation (MALDI) are preferred as softer ionisation techniques.[11]

In ESI, a volatile liquid containing the sample passes through a small, charged capillary at high pressure into vacuum. This results in a fine spray of charged droplets, which then evaporate to give the ionised molecules. This is a soft ionisation technique which does not normally lead to fragmentation. Normally, a variety of charged adducts are produced, with peptides generally yielding a characteristic charged envelope of peaks in the mass spectrum.[11,13,14]

MALDI is a soft ionisation technique which uses a UV absorbing matrix to form a co-crystal with the analyte. Upon irradiation with a high energy laser beam, the matrix first

absorbs this energy which is then transferred to the analyte, allowing for its gentle and simultaneous vaporisation and ionisation, normally generating charged ions. Time-of-flight (TOF) detectors are used to measure the time taken for the ions to travel down the drift tube, determining their m/z value.[11, 13, 14]

2.4 UV-Visible spectroscopy

When molecules and atoms are irradiated with electromagnetic radiation in the UV-Visible spectrum range, they can absorb energy. This energy can promote electronic transitions between the ground state to an excited state, which have a lower or higher energy level, respectively. If the energy associated with the radiation is exactly the same as the energy difference between the electronic states on the molecule, then absorption can occur. The energy difference between these levels, ΔE, is related to the frequency (ν) and wavelength (λ) of electronic radiation by Equation 1:

$$\Delta E = h\nu = \frac{hc}{\lambda} \quad (1)$$

where h is Planck's constant and c is the speed of light in vacuo.

Transitions are allowed only if the selection rules are obeyed. These rules state that a variation in the orbital (l) and magnetic (m_l) quantum number must take place and no variation in the spin quantum number (S) associated to the orbitals (Equation 2, 3, 4). The first rule, known as Laporte selection rule (Equation 2), states that in the presence of a centre of symmetry on the molecule, transitions within a given type of *p*- or *d*-orbitals are forbidden.

$$\Delta l = \pm 1 \quad (2)$$

$$\Delta m_l = \pm 1 \quad (3)$$

$$\Delta S = 0 \quad (4)$$

In transition metal complexes, transitions may occur between *d*-orbitals under certain circumstances, such as for asymmetrical vibrations, but they generally display low intensities. However, *d-d* transitions can be very useful to examine the nature of ligands within a metal complex.[15, 16] According to the crystal field theory, the presence of ligands breaks the *d*-orbital degeneracy, leading to orbital splitting, known as crystal field splitting (ΔE or Δ), which is dependent on the geometry of the complex and on the type of ligands.

In an octahedral system, the electrons in the d_{z2} and d_{x2-y2} orbitals (which lie along ligand axes) experience greater repulsion and their absoption is shifted at higher energies. d_{xy}, d_{xz}, and d_{yz} orbitals decrease in energy and become more stable. In octahedral complexes, crystal field

splitting is denoted as Δ_o. When radiation is absorbed, an electron is promoted from the t_{2g} to e_g orbitals (Figure 2.4a).

In tetrahedral complexes, the *d*-orbitals also split into two different energy levels. Because the orbitals are directed on the axes, while the ligands are not, the d_{xy}, d_{xz}, and d_{yz} orbitals (t_2) are not split to higher energies, while the $d_{x2-y2}$and d_{z2} (e) orbitals are stabilized (Figure 2.4b). The splitting in tetrahedral complexes, Δ_t is generally lower than Δ_o. However, *d-d* transitions in tetrahedral complexes are allowed, leading to more intense electronic transitions than in octahedral complexes.

Crystal field splitting is strongly dependent on the nature of the ligand and the electrostatic interactions generated within the complex. Ligands can be classified as strong or weak based on the spectrochemical series:

$I^- < Br^- < Cl^- < \underline{S}CN^- < F^- < OH^- < ox^{2-} < \underline{O}NO^- < H_2O < SC\underline{N}^- < EDTA^{4-} < NH_3 < en < \underline{N}O_2^- < CN^-$

The stronger the ligand, the larger is the splitting of the *d*-orbitals. Therefore, complexes will absorb energy at different wavelengths according to the nature of the ligand.

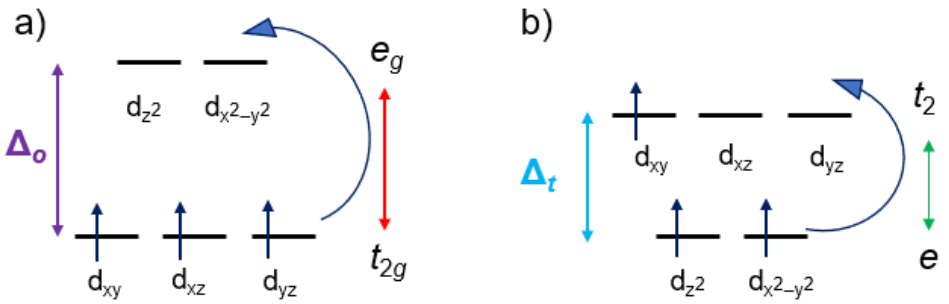


Figure 2.4: Scheme showing *d*-orbitals splitting in a d^3 compound with either a) octahedral and b) tetrahedral geometry. Δ_O and Δ_t denotes crystal field splitting, t_{2g}, e_g, e and t_2 the symmetry of d-orbitals in octahedral and tetrahedral ligand distribution. The blue arrow represents electron excitation following radiation absorption.

Transmittance (T) of light is the intensity of light of the sample (I) compared with the blank (I_0). Absorbance is related to transmittance by Equation 5. Beer-Lambert law (Equation 6) show the dependence of absorbance to the concentration of the sample (c), its extinction coefficient (ε) and the pathlength (l).

$$A = \log(I_0/I) = -\log(T) \quad (5)$$

$$A = \varepsilon c l \quad (6)$$

In peptides and proteins, the amide backbone strongly absorbs light around 200 nm, due to $\pi \rightarrow \pi^*$ transition. Moreover, in sequences containing aromatic residues such as tryptophan, the peptide concentration can be calculated using the Beer-Lambert law (for tryptophan, $\varepsilon = 5690\ M^{-1}cm^{-1}$).

2.5 Emission spectroscopy

Emission spectroscopy studies how the electromagnetic radiation can be emitted by a molecule or an atom as consequence of transition from an excited state (S_1) to a lower energy level (S_0). After radiation is absorbed and electrons are promoted to higher energy level (Figure 2.5), the system returns to equilibrium thorough radiative pathways (emission of radiation) or non-radiative pathways. This implies that emitted wavelength is longer than the excitation wavelength (fluorescence). As the electrons in the excited and ground states are spin-paired (opposite spin), the transition is spin-allowed and consequently has a short lifetime.[11, 17, 18] On the other hand, phosphorescence occurs from an excited triplet state (T_1) where electrons have the same spin orientation as the electron in the ground state. For this reason, the transition is spin-forbidden and the emission rate is slow.[18]

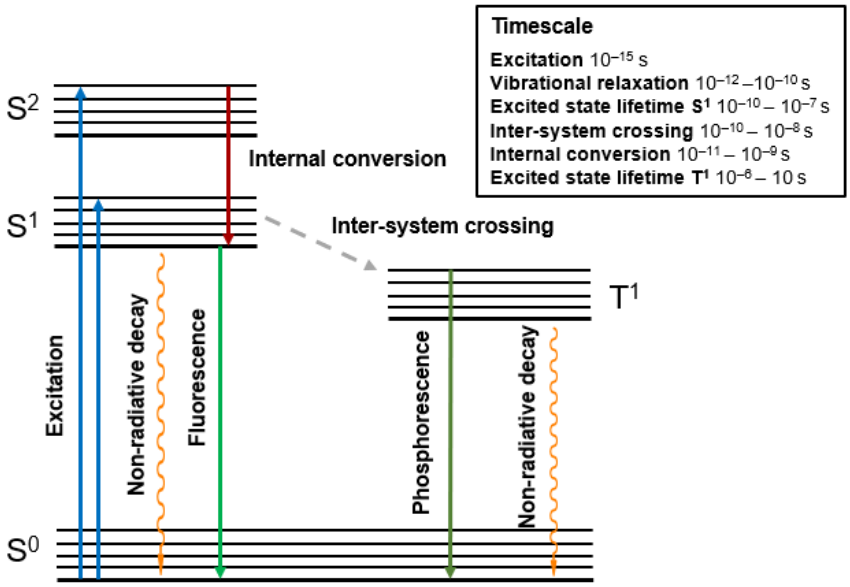


Figure 2.5: Jablonski diagram showing excitation from S^0 ground state to S^1 and S^2 excited states. Internal conversion and inter-system crossing leads to electron transfer between different excited states (internal conversion) and spin states (inter-system crossing). Energy can be then transferred thorough radiative (fluorescence and phosphorescence) and non-radiative pathways. The insert reports the timescale of processes following excitation.

Non-radiative pathways can lead to fluorescence quenching as a result of different mechanisms involving collisions or interactions with other molecules.[19] The presence of cations with partially filled *d*-orbitals, such as d^9 Cu(II), promotes electron and energy transfer processes from an adjacent excited chromophore, resulting in its partial or total fluorescence quenching.[20]

2.6 Circular Dichroism spectroscopy

Circular Dichroism (CD) spectroscopy is the measure of the optical activity of asymmetric molecules or symmetric molecules in an asymmetric environment. CD uses right and left-handed circularly polarised light. The activity is measured as the difference in absorbance between the right and left-handed polarisations (A_R and A_L, respectively), reported as value Θ_{obs} in mdeg (Equation 7) which, for asymmetric molecules $\Theta_{obs} \neq 0$.[17]

The relative molar ellipticity per residue $[\Theta]$ (deg $dmol^{-1}$ cm^2) is related to the number of amino acid residues (n), the concentration (c) and the pathlength (l) by Equation 8.[17, 21]

$$\Theta_{\text{obs}} = A_L - A_R \tag{7}$$

$$[\Theta] = \frac{\Theta_{\text{obs}}}{10\ lcn} \tag{8}$$

Proteins and peptides are examples of asymmetric macromolecules, as they are made up by chiral amino acids and fold in chiral secondary structures, such as α-helices. Therefore, they are suitable for being analysed by CD, aiming to elucidate their secondary, tertiary and quaternary structures.[17]

The spectra obtained for common peptide secondary structures are shown in Figure 2.6. α-helices show absorbance minima at 208 nm and 222 nm. If the ratio is 1.00, their structure is a simple α-helix. If the ratio between the absorbance at these wavelengths ratio is below 0.83, then the structure is mostly a random coil or a poorly folded coiled-coil.[22-24] A decrease in the absorbance at 208 nm is indicative of coiled-coil formation.[22, 25]

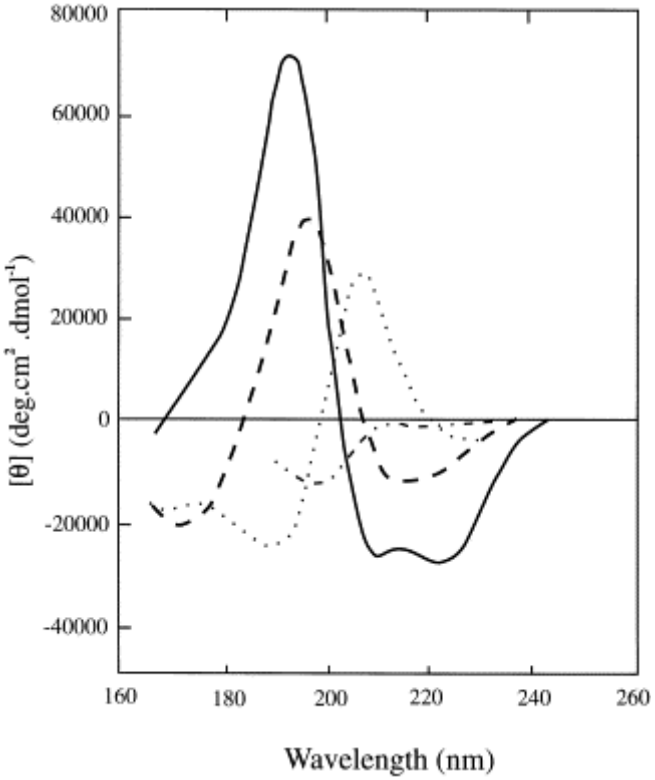


Figure 2.6: Far-UV CD spectra of different secondary structures: ***α***-helix (solid curve); anti-parallel ***β***-sheet (long dashes); type I ***β***-turn (dots); random structure (dots and short dashes). (Reprinted with permission from S. M. Kelly and N. C. Price, *Biochim. Biophys. Acta (BBA)-Protein Structure and Molecular Enzymology*, 1997, 1338, 161-185. Copyright 1997 Elsevier Science B.V.)

The helical content can be calculated as the percentage folded using Equation 9, where the denominator represents the molar ellipticity at 222 nm for a fully-folded coiled-coil composed of *n* amino acids.[26]

$$\% \text{ Folded} = \frac{([\Theta]_{222} - 640)}{\left((-42500(1 - 3/n)) - 640\right)} \tag{9}$$

2.7 Nuclear Magnetic Resonance (NMR) spectroscopy

2.7.1 Introduction to NMR

Nuclear Magnetic Resonance (NMR) investigates magnetic properties of a nucleus, which are sensitive to its chemical environment. Only nuclei with spin quantum number $I \neq 0$ can be detected by NMR, as they possess intrinsic angular momenta, which give rise to a nuclear magnetic moment (μ) through Equation 10 (Figure 2.7a). The gyromagnetic ratio (γ) is a constant value that is relative to the type of nuclei.[27, 28]

$$\mu = \gamma I \tag{10}$$

In a static magnetic field $\boldsymbol{B}_0$, the magnetic moment will align with $m = 2I+1$ possible orientation (where m is the magnetic quantum number). For a $I = 1/2$ nucleus, such as ^{1}H, there are 2 possible orientations, as shown in Figure 2.7b. Under this condition, the spins state will move from a degenerate state to a split state. Some of them will orientate in the same direction as the field, occupying the lowest energy level ($m = +1/2$), and others will populate the highest energy level ($m = -1/2$) as their direction is in opposite to the field.[28] The two spin states are also referred to as spin up and spin down. The difference in energy (ΔE, Equation 11) between the states is related to the magnetic field ($\boldsymbol{B}_0$), the gyromagnetic ratio, the frequency of electromagnetic radiation (ν) and the Planck's constant (h).[27, 28]

$$\Delta E = h\nu = \frac{h\gamma B_0}{2\pi} \tag{11}$$

When an external magnetic field is applied, the spins will precess relative to $\boldsymbol{B}_0$ magnetic field at Larmor frequency (ω), which is related to the magnetic field through the gyromagnetic ratio (γ), as in Equation 12.[27, 28] Under these conditions, there is a Boltzmann distribution between the spins state, meaning that the lowest energy state will be preferred, giving rise to a net magnetization parallel to the external field M_0 (Figure 2.7c).

$$\omega = \gamma B_0 \tag{12}$$

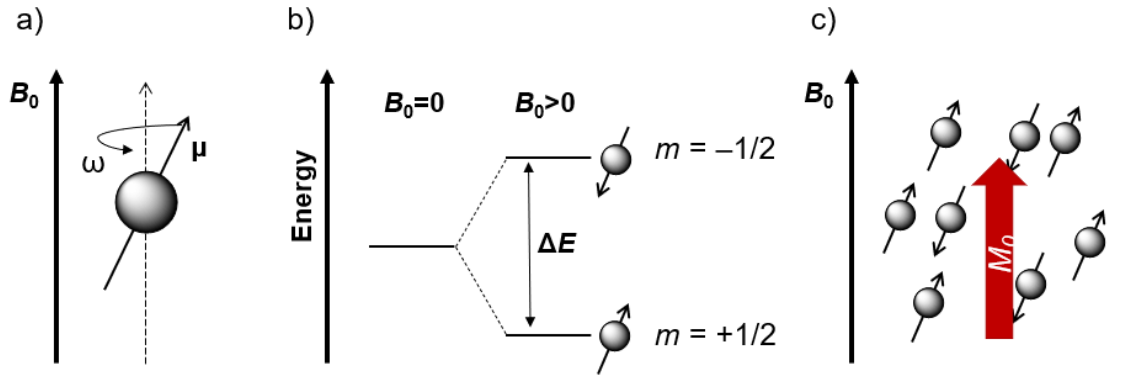


Figure 2.7: Scheme showing a) a nucleus with magnetic moment (μ) precessing at Larmor frequency (ω) in a magnetic field (B_0). b) energy levels splitting for a I = ½ nucleus into m = +1/2 and m = -1/2 spin states. c) Boltzmann distribution of nuclear spins leading to net macroscopic magnetisation (M_0, red arrow) parallel to the external magnetic field (B_0) direction.

When a radiofrequency (RF) pulse is applied with equal energy difference between the spin states (ΔE), transitions between the spin states will be induced. The RF pulse is generated by

perpendicular RF coils ($\boldsymbol{B}_1$) for a short period of time. The net magnetisation will be rotated by an angle θ (Equation 13), which is dependent on the amplitude ($\boldsymbol{B}_1$) and the duration t of the pulse.[27]

$$\theta = 2\pi B_1 t \tag{13}$$

The application of $\theta = 90°$ pulse along the y-axis will move $\boldsymbol{M}_0$ on the *xy*-plane where will precess at Larmor frequency with phase coherence (Figure 2.8a). A receiver located on the third axis will detect an oscillating signal. As the system is left to equilibrate due to relaxation, the signal will decay to zero. The receiver will detect the decay over time, known as Free Induction Decay (FID) (Figure 2.8b). Finally, Fourier Transform (FT) is used to provide signal as function of frequency and the relative NMR spectrum. If the same nucleus is put in different chemical environments, this will result in different energy states and, consequently, different precession rates. After Fourier transformation, different precession rates will lead to multiple frequencies in signals. The difference between the frequency of one signal relative to a reference frequency is known as chemical shift. Therefore, the analysis of chemical shifts, provide useful information about the structure and the chemical environment of a molecule.[27, 28]

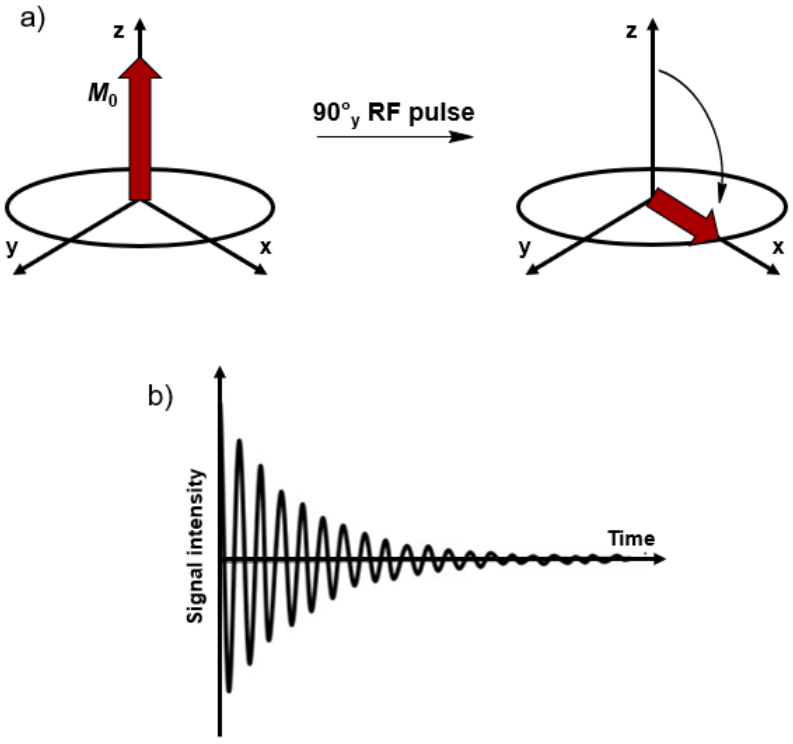


Figure 2.8: a) Representation of net macroscopic magnetisation (M_0) tilt after a 90°$_y$ pulse onto the transverse plane. b) NMR signal generated due to precession of magnetisation on the transverse plane (Free Induction Decay, FID).

The decay in the NMR signal, due to relaxation mechanisms, occurs because of energy loss. Relaxation can occur through two different processes: longitudinal and transverse relaxation processes; T_1 and T_2, respectively (Figure 2.9).[27]

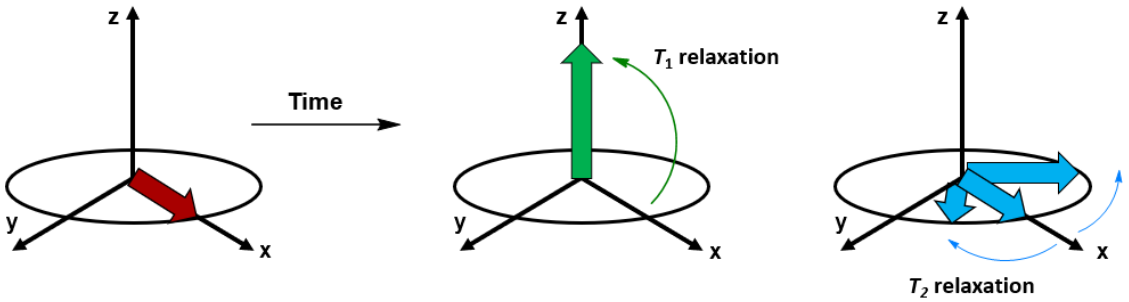


Figure 2.9: Representation of magnetisation loss on the transverse plane due to T_1 and T_2 relaxation.

2.7.2 T_1 and T_2 relaxation

Longitudinal relaxation T_1 is related to the recovery of the magnetisation parallel to the z-axis. Also known as spin-lattice relaxation, it refers to the repopulation of spin states at thermal equilibrium, through energy loss to the lattice. Transverse relaxation T_2 is generated by loss of phase coherence on the transverse plan, due to molecular interactions that cause spins to process at different rates.

As introduced in Chapter 1, the presence of paramagnetic species in solution, which possesses a strong magnetic moment (arising from unpaired electrons) leads to alteration of the relaxation process and shortening of the relaxation times. At clinically relevant magnetic field and higher, only dipolar coupling (between the paramagnetic metal and the proton) influences both T_1 and T_2 relaxation, while other mechanisms affect T_2 relaxation, known as scalar coupling and Curie-spin relaxation.[29-33]

MRI relaxivity is defined as the enhancement of relaxation rates (reciprocal of the relaxation times) as a function of the concentration of the paramagnetic agent (contrast agent) with units $mM^{-1}s^{-1}$. (Equation 14) The higher the relaxivity, the higher the increase in relaxation rates for a given concentration of contrast agent. Since the enhancement in relaxation rates is linear as the concentration of the contrast agent increases, relaxivity can be determined experimentally as slope of the fitting line (Figure 2.10).

$$r_i = \frac{\Delta\left(\frac{1}{T_i}\right)}{[\mathrm{CA}]} \quad i = 1,2 \tag{14}$$

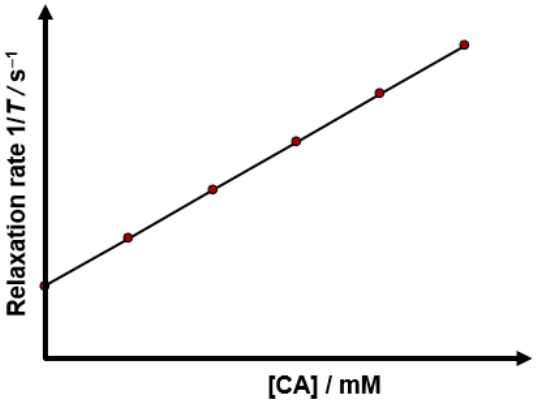


Figure 2.10: Plot showing linear dependence of NMR relaxation rates to the relative concentration of contrast agent (CA). The slope of the fitting curve determines relaxivity.

2.7.3 Experimental determination of T_1 and T_2 relaxation

T_1 relaxation behaviour is exponential and refers to the first order time constant, determined from the magnetisation on the z-axis, $\boldsymbol{M}_z$ at time τ, with $\boldsymbol{M}_0$ as magnetisation at thermal equilibrium (Equation 15).[27] Experimentally, T_1 relaxation can be measured using an inversion recovery (Figure 2.11a,c) or saturation recovery experiment (Figure 2.12a).[27]

In an inversion recovery experiment, a 180° pulse is applied, resulting in the net magnetisation to be rotated onto the negative *z*-axis. After a delay τ, a 90° pulse is applied, moving the magnetisation vector to the negative *x*-axis and the receiver will detect negative signal. If τ is set to increase, before the second pulse is applied, some relaxation will occur. This allows the magnetisation to move back towards equilibrium on the positive *z*-axis, leading to increase of signal. Signal intensities as function of increasing delays can be fitted using Equation 15 to determine T_1 as parameter (Figure 2.11b, Figure 2.12b).

$$M_z = M_0\left(1 - 2e^{-\tau/T_1}\right) \tag{15}$$

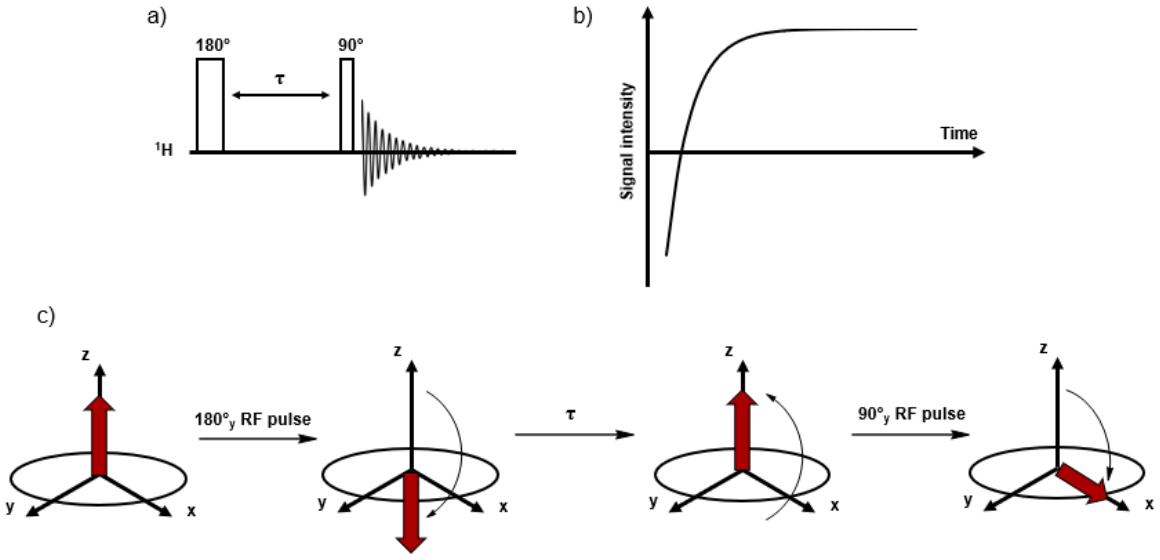


Figure 2.11: Representation of a) inversion recovery pulse sequence, b) recovery of signal intensity with increasing time τ and c) evolution of macroscopic magnetisation after the 180° pulse, delay time τ when magnetisation is allowed to recover and after the final 90° pulse.

Saturation recovery is an alternative, faster method to measure T_1. This method relies on a series of 90° pulses separated by variable delays τ, which are used to "destroy" the magnetisation (Figure 2.12). The delay times are set not to allow the magnetisation to recover at the beginning of the experiment, while, as the experiment proceeds, more time is given to let the magnetisation grow back again on z-axis. The evolution of the magnetisation on z-axis, as function of variable increasing delays values τ, is described by Equation 16.

$$M_z = M_0\left(1 - e^{-\tau/T_1}\right) \tag{16}$$

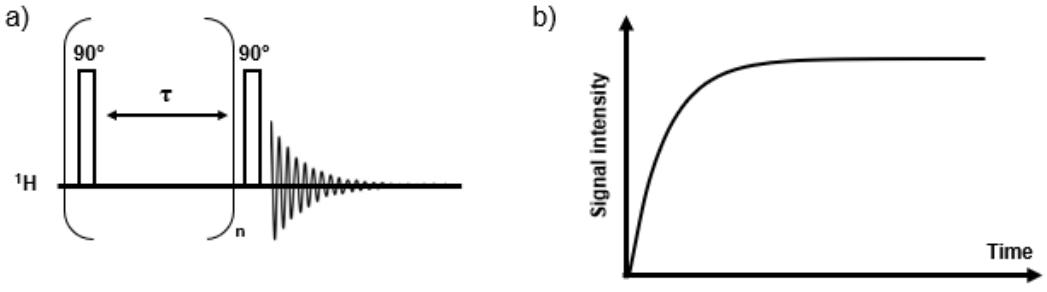


Figure 2.12: Representation of a) saturation recovery pulse sequence, b) recovery of signal intensity with increasing time τ.

On the other hand, the magnetisation on the transverse plane ($\boldsymbol{M}_{xy}$) is related to evolution time (τ), exponentially, with T_2 relaxation as constant as Equation 17.[27]

$$M_{xy} = M_0 e^{-2\tau/T_2} \tag{17}$$

Field inhomogeneities can be eliminated using a Carr-Purcell-Meiboom-Gill (CPMG) pulse sequence (Figure 2.13).[27] After a 90˚ pulse, spins begin to dephase during the delay time τ. A 180˚ pulse is applied leading to refocus of the signals, generating an echo. Multiple 180˚ pulses are used with a constant delay time τ and the process is repeated a defined number of times before data collection. Finally, signal intensity and the decay time can be fitted to obtain T_2. If a short echo time is used, relative to diffusion of the spins, only the intrinsic T_2 is measured.[27]

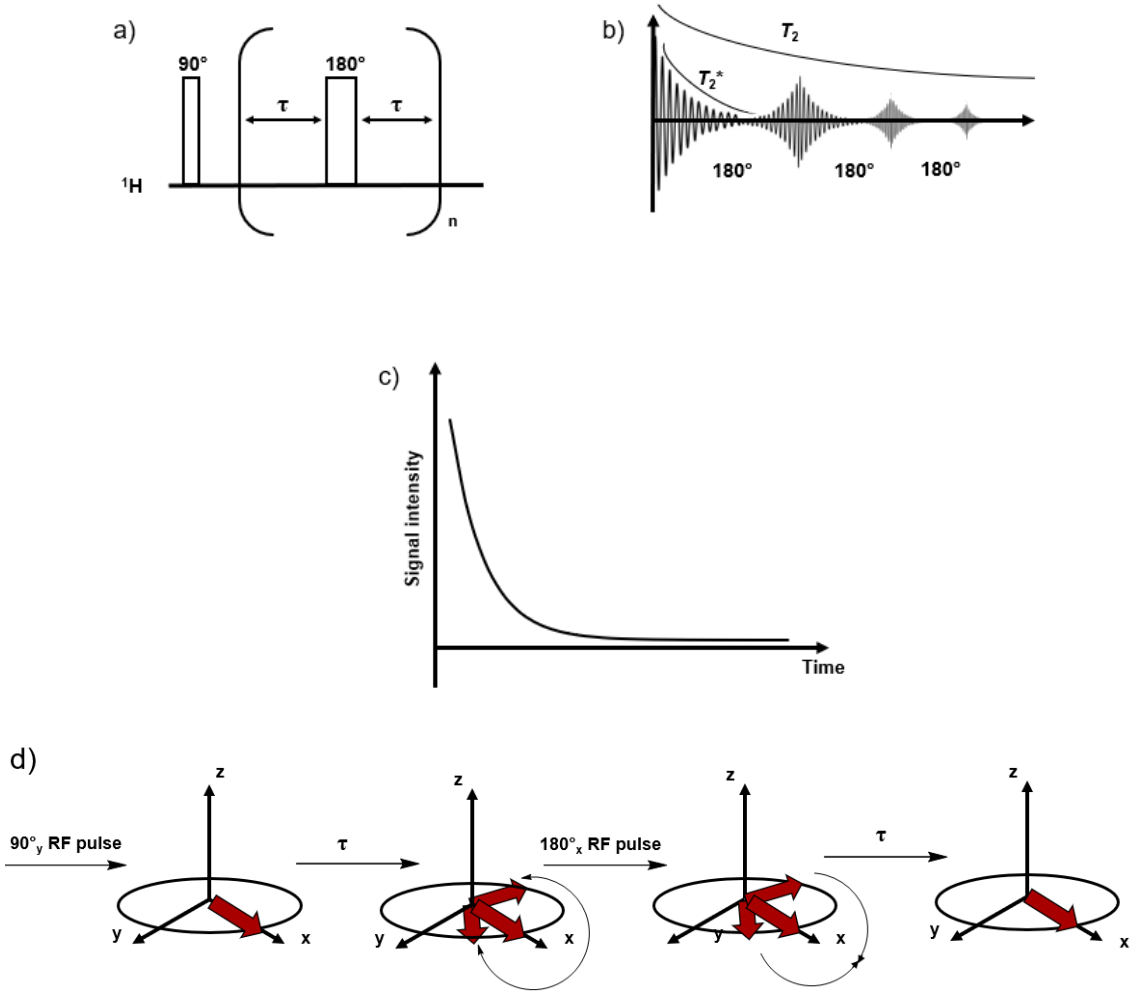


Figure 2.13: Representation of a) CPMG pulse sequence and b) the echoes generated from *n* repeat of 180° pulses, c) decay of signal intensity with increasing time (2τ) and d) evolution of macroscopic magnetisation after 90° pulse, delay time τ when T_2 relaxation occurs, a 180° pulse which inverts dephased magnetisation and final delay time τ which allows magnetisation to refocus.

2.7.4 Chemical Exchange Saturation Transfer (CEST)

CEST contrast is generated when protons in exchange with bulk water are selectively saturated by applying a proper radiofrequency pulse (Figure 2.14). If this pulse is long enough, saturation can be transferred to bulk water by chemical exchange (each exchanging saturated solute proton is replaced by a non-saturated water proton, which is then again saturated). This determines a reduction in signal intensity of bulk, providing negative contrast.[34, 35]

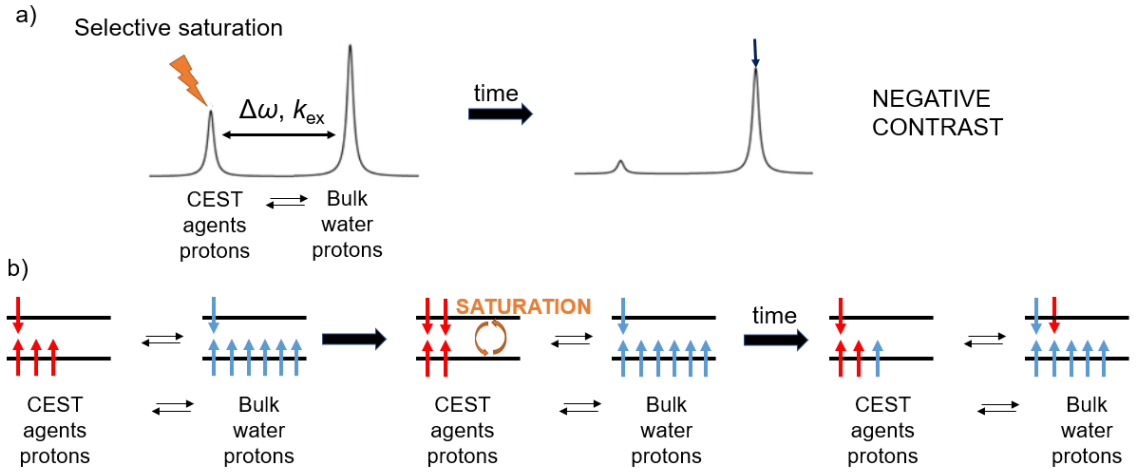


Figure 2.14: Representation of saturation transfer: a) ^{1}H-NMR spectrum before and after selective saturation, leading to reduction in water NMR signal intensity and negative contrast; b) Effect of saturation of the spin level population and relative evolution over time with exchange of saturated spins to bulk water.

To generate CEST effect, the exchange rates k_{ex} between the protons on the CEST agent and those of bulk water, must satisfy the slow-to-intermediate exchange condition $\Delta\omega > k_{ex}$ (were $\Delta\omega$ is the resonance frequency difference between the protons on the molecule and bulk water).[1] Also, NMR T_1 relaxation times have to be long enough to enable proton exchange to occur before relaxation.

CEST efficiency can be evaluated by generating a Z-spectrum, which presents on the *x*-axis the frequency offset ($\Delta\omega$) relative to bulk water (for bulk water, $\Delta\omega$ = 0 ppm) and on the y-axis the ratio between the signal of bulk water in the presence (M) and in the absence (M_0) of the presaturation pulse at a given frequency.

A Z-spectrum can be collected using NMR spectroscopy using a sequence where a long presaturation pulse is applied at low power (duration D1 and power PL9) before a 90° pulse and data collection (Figure 2.15).

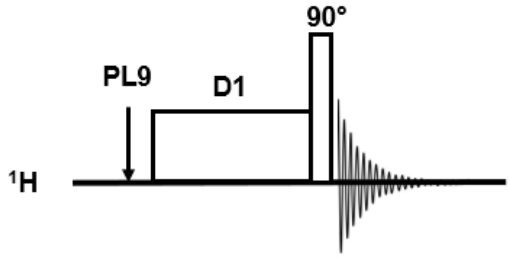


Figure 2.15: Representation of a presaturation pulse sequence (zgpr), where the presaturation pulse is applied with power PL9 and duration D1.

2.8 Electron Paramagnetic Resonance (EPR) spectroscopy

EPR (electron paramagnetic resonance) spectroscopy employs microwave radiation to investigate the structure and dynamics of systems which contain unpaired electrons such as those of paramagnetic ions or radicals.[36] In EPR, microwave radiation is used to detect unpaired electron(s) ($S \neq 0$). In a static magnetic field $\boldsymbol{B}_0$, electrons with $S = 1/2$ populate lower and a higher energy states (Zeeman effect), with energy difference (Equation 18):

$$\Delta E = h\nu = g\beta B_0 \tag{18}$$

where β is the Bohr magneton and g is a value named g-factor, where a free electron in vacuum has $g_e = 2.00232$. The value of g depends on the molecule ($g = g_e + \Delta g$), and provides information about the molecule. The g-factor of many paramagnetic species (such as Cu(II)), is anisotropic, which means that its value is relative to the orientation of the electron spins in the magnetic field, in crystalline systems.

In EPR, hyperfine coupling is generated through the electron magnetic moment to the magnetic moment of its own nucleus or a different atom. The hyperfine splitting constant (a) is measured from the distance between hyperfine lines in an EPR spectrum and then converted to the value of A, in Hz (Equation 19).

$$hA = g\beta a \tag{19}$$

For example, in Cu(II) (nuclear spin, $I = 3/2$), hyperfine splitting results in four lines of intensity 1:1:1:1. When the ion is coordinated to $I \neq 0$ nuclei (such as ^{14}N, $I = 1$), the interaction leads to a characteristic hyperfine pattern.[37] In such complex spin systems, where unpaired electron spins are coupled with several neighbouring nuclei, often overlapping signals are present. This severely limits assignment of hyperfine coupling parameters and identification of nuclei. To solve this, electron-nuclear double resonance (ENDOR) and electron spin-echo envelope modulation (ESEEM) spectroscopy are able to greatly simplify spectra and reduce the number of peaks by using microwave and radio frequency radiation. Pulsed ESEEM experiments can be

used to determine the number of bound water molecules to a metal as reported by Hoogtraten and Britt.[38] This can be done by comparing the spectra of a complex of an EPR active metal in D_2O and in H_2O with an aqueous complex of the metal as reference standard. Peacock and co-workers reported experimental details for Cu(II) inner-sphere water determination.[39]

References

1. R. B. Merrifield, *J. Am. Chem. Soc.*, 1963, **85**, 2149-2154.
2. W. Chan and P. White, *Fmoc solid phase peptide synthesis: a practical approach*, OUP Oxford, 1999.
3. J. Jones, *Amino acid and peptide synthesis*, Oxford University Press, USA, 1992.
4. H. M. Yu, S. T. Chen and K. T. Wang, *J. Org. Chem.*, 1992, **57**, 4781-4784.
5. J. M. Collins and N. E. Leadbeater, *Org. Biomol. Chem.*, 2007, **5**, 1141-1150.
6. F. Rizzolo, C. Testa, D. Lambardi, M. Chorev, M. Chelli, P. Rovero and A. M. Papini, *J. Pept. Sci.*, 2011, **17**, 708-714.
7. A. J. Doig and R. L. Baldwin, *Protein Sci.*, 1995, **4**, 1325-1336.
8. J. Glajch, M. Quarry, J. Vasta and L. Snyder, *Anal. Chem.*, 1986, **58**, 280-285.
9. J. M. Conlon, *Nature Protocols*, 2007, **2**, 191-197.
10. T. Imoto and H. Yamada, *Mol. Cell. Biochem.*, 1983, **51**, 111-121.
11. V. A. Gault and N. H. McClenaghan, *Understanding bioanalytical chemistry: principles and applications*, John Wiley & Sons, 2013.
12. S. M. Kelly, *Biochim. Biophys. Acta (BBA)-Proteins and Proteomics*, 2005, **1751**, 119-139.
13. J. B. Fenn, M. Mann, C. K. Meng, S. F. Wong and C. M. Whitehouse, *Science*, 1989, **246**, 64-71.
14. R. Aebersold and M. Mann, *Nature*, 2003, **422**, 198-207.
15. J. S. Griffith, *The theory of transition-metal ions*, Cambridge University Press, 1961.
16. G. Basu, R. L. Belford and R. Dickerson, *Inorg. Chem.*, 1962, **1**, 438-439.
17. T. E. Creighton, *Protein structure: a practical approach*, Oxford University Press, 1997.
18. J. R. Lakowicz, *Principles of fluorescence spectroscopy*, Springer, 2006.
19. B. Valeur and M. N. Berberan-Santos, *Molecular fluorescence: principles and applications*, John Wiley & Sons, 2012.
20. L. Fabbrizzi, M. Licchelli, P. Pallavicini, D. Sacchi and A. Taglietti, *Analyst*, 1996, **121**, 1763-1768.
21. D. Ghosh, K.-H. Lee, B. Demeler and V. L. Pecoraro, *Biochemistry*, 2005, **44**, 10732-10740.
22. S. M. Kelly and N. C. Price, *Biochim. Biophys. Acta (BBA)-Protein Structure and Molecular Enzymology*, 1997, **1338**, 161-185.
23. N. E. Zhou, C. M. Kay and R. Hodges, *J. Biol. Chem.*, 1992, **267**, 2664-2670.
24. K. Dutta, A. Alexandrov, H. Huang and S. M. Pascal, *Protein Sci.*, 2001, **10**, 2531-2540.
25. T. M. Cooper and R. W. Woody, *Biopolymers*, 1990, **30**, 657-676.
26. J. K. Myers, C. N. Pace and J. M. Scholtz, *PNAS*, 1997, **94**, 2833-2837.
27. T. D. Claridge, *High-resolution NMR techniques in organic chemistry*, Elsevier, 2016.
28. P. J. Hore, *Nuclear magnetic resonance*, Oxford University Press, USA, 2015.

29. N. Bloembergen, E. M. Purcell and R. V. Pound, *Phys. Rev.*, 1948, **73**, 679.

30. N. Bloembergen, *J. Chem. Phys.*, 1957, **27**, 572-573.

31. I. Solomon, *Phys. Rev.*, 1955, **99**, 559.

32. N. Bloembergen and L. Morgan, *J. Chem. Phys.*, 1961, **34**, 842-850.

33. M. Guéron, *J. Magn. Reson. (1969)*, 1975, **19**, 58-66.

34. I. Hancu, W. T. Dixon, M. Woods, E. Vinogradov, A. D. Sherry and R. E. Lenkinski, *Acta Radiol.*, 2010, **51**, 910-923.

35. V. C. Pierre and M. J. Allen, Eds., *Contrast agents for MRI: experimental methods*, Royal Society of Chemistry, 2017.

36. S. Stoll and D. Goldfarb, Eds., *EPR spectroscopy: fundamentals and methods,* John Wiley & Sons, 2018.

37. W. R. Hagen, *Biomolecular EPR spectroscopy*, CRC Press, 2008.

38. C. G: Hoogstraten and R. D. Britt, *RNA*, 2002, **8**, 252-260.

39. A. Shah, M. J. Taylor, G. Molinaro, S. Anbu, M. Verdu, L. Jennings, I. Mikulska, S. Diaz-Moreno, H. El Mkami and G. M. Smith, *PNAS*, 2023, **120**, e2219036120.

CHAPTER 3

A NEW COPPER(II)-BASED MRI CONTRAST AGENT

3.1 Introduction

The use of clinically approved Gd(III)-based contrast agents is a powerful tool to improve the contrast within MR images to allow detection, for instance, of tumours and blood vessel disruptions. They are based on small Gd(III) complexes[1-4] with relaxivity (efficiency) of around 4-6 $mM^{-1}s^{-1}$ at clinically relevant magnetic fields.[4] Their relaxivity depends on the metal spin quantum number and its electron relaxation time and a number of molecular parameters, such as the number of inner- and second-sphere water molecules and their residence times in the hydration sphere. In addition, rotational correlation time, which is associate with molecular tumbling, impact on relaxivity especially at clinically relevant magnetic fields (0.5-1 T).

Following the injection of a contrast agent into a patient, the compound distributes preferentially in the blood or in extracellular space.[4] Their half-life for blood elimination is about 1.5 hours in patients with normal renal function[5, 6] and they have been shown to be excreted rapidly and intact.[5] Gd(III) contrast agents are exclusively eliminated by the kidneys,[7] therefore, in patients with renal diseases or insufficiency, the half-life for elimination can increase up to days.[4, 7, 8] Slow elimination of Gd(III) complexes can lead to metal release with Gd(III) deposition in the brain, skin and internal organs.[7, 9] Gd(III) can dissociate from the ligand and form insoluble inorganic salts with carbonate or phosphate anions. Because of similar coordination chemistry, Gd(III) can replace Ca(II) in native calcium binding proteins,[5, 10] resulting in inhibition of protein function. Moreover, endogenous metals, such as Zn(II), Cu(II) or Fe(III), with high affinity for the ligand can increase the rate of transmetallation (a process which involves transfer of ligands from a metal to another) as well as Gd(III) complexation by anions such as phosphate or carbonate.[4, 5]

In an effort to find alternatives to Gd(III)-based contrast agents, research is focussing on metal ions with lower toxicity profiles, able to provide comparable efficiency to those already in clinical use. Cu(II) represents a valuable alternative in terms of toxicity because it is an essential nutrient, is involved biological processes such as catalytic and structural processes, and can be eliminated through either renal or biliary excretion.[11] However, the presence of one unpaired

electron in Cu(II) ion appears to be the main limiting factor for developing copper based-contrast agents, whereas water exchange rates and Cu(II) electron relaxation times are similar to Gd(III).[12-16]

The aim of this chapter is to improve the intrinsically low efficiency of copper by including the metal into macromolecules with long rotational correlation time. The relaxivities of serum proteins, which possess high affinity for copper,[17, 18] have been reported to be higher compared to the Cu(II)-aquo complex (Table 3.1).[19] Moreover, including the metal into peptides designed to bind metal ions has been shown to be successful in developing Gd(III) contrast agents.[20, 21]

Table 3.1: Relaxivity values of copper albumin, α-globulin, γ-globulin, lysozyme and fibrinogen compared to water measured at 1.5 T.[19]

	Cu^{2+}-albumin	Cu^{2+}-α-globulin	Cu^{2+}-γ-globulin	Cu^{2+}-lysozime	Cu^{2+}-fibrinogen	$[Cu(H_2O)_6]^{2+}$
r_1 / mM^{-1}/s^{-1}	1.68	1.84	2.18	1.76	2.24	0.9
r_2 / mM^{-1}/s^{-1}	2.84	4.68	3.39	1.75	1.45	2.05

This chapter presents, for the first time, a Cu(II) compound showing high MRI relaxivity which is comparable to the analogous Gd(III) compound, challenging the common belief that Cu(II) is unsuitable for use as a MRI contrast agent, due to the presence of a single unpaired electron. Moreover, the impact of the presence of buffer and of pH variation on MRI relaxivities is determined. Finally, the Cu(II) complex is also tested under "physiological-like" conditions, such as in the presence of Zn(II) ions, competitive with copper for peptide binding, and serum proteins, competitive with the peptide for Cu(II) binding.

3.2 Experimental

3.2.1 Materials

Chemicals were used as received and purchased from: Sigma Aldrich (diethyl ether, copper(II) chloride, Pepceuticals (Nα-fluorenylmethoxycarbonyl (Fmoc) protected amino acids, O-benzotriazole-N,N,N',N-tetramethyluronium-hexafluorophosphate (HBTU), AGTC Bioproducts Ltd. (rink amide 4-methylhydrylamine (MBHA) resin, N-methyl-2-pyrrolidone (NMP), hydroxybenzotriazole (HOBt), N,N-diisopropylethylamine (DIPEA) and

dichloromethane (DCM), Acros Organics (acetic anhydride, triisopropylsilane (TIPS) and trifluoroacetic acid (TFA)), Rathburn Chemicals Ltd. (>99.9% DMF), Fisher Scientific Ltd. (high performance liquid chromatography (HPLC) grade water and acetonitrile, 2-[4-(2-hydroxyethyl)piperazin-1-yl]ethanesulfonic acid (HEPES), urea). All water, except that used for HPLC, was ultrapure grade obtained from a Millipore Elix-Gradient A10 system.

3.2.2 Peptide synthesis

Peptides were synthesised using standard SPPS protocol using a CEM Liberty Blue Automated Peptide Synthesiser.[22] The peptide was synthesised on a 0.25 mmol scale using a Rink Amide MBHA resin (0.372 g, 0.65 meq g^{-1}) and Nα-fluorenylmethoxycarbonyl (Fmoc) protected L-amino acids. The Fmoc amino acid solutions were made up using DMF and the deprotection solution was made up of 20% piperidine in DMF (650 mL) and activator was made up of HBTU in DMF (0.5 M) and activator base (2 M) made up of DIEA in NMP. Reagents were then loaded appropriately onto the Liberty Blue Automated Peptide Synthesiser. The first heptad and the final two heptads were double coupled (25 W, 90ºC, 420 s). The other heptads of the sequence were single coupled (25 W, 75ºC, 720 s).

On removal from the synthesiser, the resin was swollen in DMF (12 mL) for 20 mins before a capping mixture of DIEA (4 mL) and acetic anhydride (4 mL) was added and shaken for 25 mins. The mixture was then filtered and washed with DCM (3 × 5 mL) and diethyl ether (3 × 5 mL) before being left to dry for an hour.

A cleavage cocktail of TFA (19 mL), TIPS (0.5 mL) and MQ water (0.5 mL) was added to the resin for 2 hours. The solution was filtered and washed with TFA (1 × 5 mL) to remove the resin before the yellow/brown filtrate was reduced to approximately 12 mL by using nitrogen gas. The peptide solution was then added dropwise to cold diethyl ether (4 × 40 mL non-skirted falcon tubes) and left in the freezer for 30 mins to precipitate out the peptide. The solid was isolated by centrifugation (using an Eppendorf centrifuge 5702 with rotor A-4-38 and rotational speed of 4400 rpm for 10 mins) and diethyl ether was removed; this was repeated before the crude peptide was dissolved up in 50% water 50% acetonitrile (ca. 10 mL) and filtered using a Millex syringe-driven filter unit (33 mm with 0.45 μm pore size) ready for HPLC purification.

3.2.3 Peptide purification and characterisation

The peptides were purified using reversed phase HPLC on a preparative C18 column using a water/acetonitrile + 0.05% TFA gradient that was ramped from 0 to 100% acetonitrile over 60 mins then remained constant for 10 mins before returning to 0% acetonitrile. The pure peptide

was collected between 20-25 mins and was reduced *in vacuo*, to remove acetonitrile, and lyophilised to produce pure peptides as white powders. The purity of pure peptide was characterised by analytical HPLC using a 0 to 100% water:acetonitrile + 0.05% TFA gradient in 60 mins and characterised by ESI+ mass spectrometry.

3.2.4 UV-Vis spectroscopy

UV-Vis experiments, to determine peptide concentration, were recorded on a Cary 50 UV Spectrophotometer, recorded in single beam mode with a medium scan speed, slit width 1.0 nm, data interval of 1.0 nm and scan range 800-200 nm using a 1 cm pathway quartz cuvette.

The concentrations of freshly prepared peptide stock solutions (obtained by dissolving pure peptide in MQ water) were measured using the absorption of tryptophan at 280 nm (ε = 5690 L mol^{-1} cm^{-1}). A blank aqueous solution of 7 M urea was recorded, and solutions prepared by adding 10 µl of freshly prepared peptide stock solution to 690 µl 7 M urea. The peptide stock solution was then diluted to the desired concentration in 10 mM HEPES pH 7.0. The concentration of the peptide solution was calculated again by UV-Vis avoiding the dilution in 7 M urea. All measurements were performed in triplicate.

Cu(II) electronic *d-d* transition were monitored on a Cary 5000 UV Spectrophotometer, recorded in single beam mode with a medium scan speed, slit width 1.0 nm, data interval of 1.0 nm and scan range 850-200 nm using a 1 cm pathway quartz cuvette.

3.2.5 Circular Dichroism (CD) spectroscopy

CD spectra were recorded on a Jasco J-715 Spectropolarimeter. The optical chamber was purged with nitrogen and kept under a nitrogen atmosphere throughout the duration of the experiments. A 1 mm pathlength, 300 µl quartz cuvette was used with three scans recorded from 400-200 nm using a 100-200 nm min^{-1} scan rate with 1 nm bandwidth and a 1 s response.

A pH 7.0 HEPES buffer solution was recorded as a blank before $CuCl_2$ was titrated into a solution of peptide monomer with concentration previously determined by UV-Vis analysis. All solutions were left to equilibrate for 15 mins before scanning. The ellipticity (θ_{obs}) data collected in millidegrees (mdeg). The molar ellipticity was calculated through Equation 1.

$$[\theta] = \frac{\theta_{\text{obs}}}{10\ lcN} \tag{1}$$

where θ_{obs} is the measured ellipticity at 222 nm in mdeg, c is the concentration in M, N is the number if amino acids in the sequence and l is the pathlength in cm, was used to convert ellipticity at 222 nm (mdeg) to molar ellipticity per residue, [θ] (deg dmol^{-1} cm^2).

The helical content was then calculated as the percentage folded using Equation 2, where the denominator represents the molar ellipticity for a fully folded coiled-coil.[23]

$$\% \text{ Folded} = \frac{[\theta_{222}] - 640}{\left(-42500 \times \left(1 - {}^{3}/_{N}\right)\right) - 640} \quad (2)$$

Kinetic folding data were recorded by monitoring the ellipticity at 222 nm (θ_{obs}) of either 30 or 150 μM solution of MB1-2 peptide monomer (10 or 50 μM MB1-2 peptide trimer, respectively) in 10 or 50 mM HEPES buffer pH 7.0 (respectively) in the absence and presence of 1 equivalent $CuCl_2$ per equivalent of peptide trimer (10 or 50 μM $CuCl_2$, respectively), at 20°C. Data were collected ~3 seconds after $CuCl_2$ addition. θ_{obs} was converted to % folding using Equations 1 and 2.

Thermal unfolding data were recorded by monitoring the ellipticity at 222 nm of a 150 μM solution of MB1-2 peptide monomer in 50 mM HEPES buffer pH 7.0 in the absence and presence of 50 μM $CuCl_2$, using a Jasco Peltier Type PTC-4235 temperature controller ramping from 20°C to 40°C.

3.2.6 Emission spectroscopy

Emission spectra were recorded in a 1 cm pathlength quartz cuvette using a Jasco FP-8500 fluorescence spectrometer. Aliquots of a 1 mM stock solution of $CuCl_2$ were titrated into a 30-35 μM solution of peptide monomer in 10 mM HEPES buffer pH 7.0 and the emission profile recorded after 20 minutes of equilibration. Solutions were excited at 280 nm and the emission was scanned from 300-455 nm (Trp emission peak region) using an excitation slit width of 2.5 nm and bandwidth of 2.5 nm.

3.2.7 Nuclear magnetic resonance

^{1}H-NMR measurements, at high magnetic field (7 T), were performed on a Bruker Avance III HD spectrometer, operating at proton resonance frequency of 300.13 MHz. All measurements were performed at 20 ± 0.2°C. Data were acquired using 5 mm ^{1}H coil in a Bruker Diff30 probe. A 90° pulse duration calibrated for each sample was used for the experiments. For T_1 NMR relaxation measurements, a Saturation Recovery sequence (described in Section 2.7.3) was used. A series of 8 spectra were collected with logarithmically spaced recovery delays from 0.01 s to a maximum of 12-15 s, with 8 signal averages, 8k data points and spectral width of 10 kHz. For T_2 NMR relaxation measurements the Carr-Purcell-Meiboom-Gill (CPMG) pulse sequence (described in Section 2.7.3) was used with a repetition time > $5T_1$ (≥ 10 s), 8 signal averages, 16k data points and spectral width of 10 kHz. The variable counter list, for the CPMG experiments,

consisted of 10 values logarithmically spaced from 2 to 1024, with a CPMG echo time value of 2 ms.

^{1}H-NMR measurements at low magnetic fields (1.4 T) were performed on a Spinsolve benchtop NMR (Magritek, Aachen, Germany), operating at proton resonance frequency of 61 MHz. Data were acquired at 21.0 ± 0.5°C (controlled room temperature) using 3 mm NMR tubes and an automated 90° pulse width of 7 µs. For T_1 NMR relaxation measurements, an Inversion Recovery sequence (described in Section 2.7.3) was used with a repetition time > $5T_1$ (≥ 10 s). A series of 11 spectra were collected with delays linearly spaced from 0.001 s to a maximum of 5-10 s, 8 signal averages and 32k points. For T_2 NMR relaxation measurements a CPMG pulse sequence was used with a repetition time > $5T_1$ (≥ 10 s). A series of 10 spectra were recorded with a 2 ms CPMG echo time and final echo time of 5 s, 8 signal averages and 32k data points. All data were analysed using Prospa (Magritek, Aachen, Germany). Signal intensity curves were fitted in KaleidaGraph (Synergy, USA).

Binding of Cu(II) by MB1-2 peptide trimer was monitored by measuring the ^{1}H T_1 and T_2 magnetic resonance relaxation times of solutions of 40 µM $CuCl_2$ in the presence of increasing concentrations of peptide monomer, in 100 mM HEPES buffer pH 7.0. The r_1 and r_2 relaxivities were calculated from the gradients of plots of the average, based on three independent repeats, ^{1}H magnetic resonance relaxation rates ($1/T_1$ and $1/T_2$ respectively), as a function of $CuCl_2$/$GdCl_3$ concentration. A range of solutions were measured, containing 0, 10, 20, 30, 40 µM $CuCl_2$/$GdCl_3$ and 15 equivalents of peptide monomer (5 equivalents peptide trimer per equivalent of $CuCl_2$/$GdCl_3$), to drive Cu(II)/Gd(III) complexation. Analogous control experiments were performed for solutions of peptide in the absence of $CuCl_2$. The r_2 relaxivity of the apo MB1-2 peptide was used to correct r_2 for the $Cu(MB1\text{-}2)_3$ and $Gd(MB1\text{-}2)_3$ complexes, by accounting for the contribution of excess unbound MB1-2 (7 T r_1 = 0.0 ± 0.0 mM^{-1} s^{-1}; r_2 = 0.48 ± 0.01 mM^{-1} s^{-1}; 1.4 T r_1 = 0.02 ± 0.01 mM^{-1} s^{-1}; r_2 = 0.09 ± 0.01 mM^{-1} s^{-1}). Relaxivity experiments for $CuCl_2$ (0, 10, 20, 30 and 40 µM), in the presence of MB1C (15 equivalents of peptide monomer), were also performed. Relaxivity experiments were performed on solutions prepared in 100 mM HEPES buffer pH 7.0 or PBS buffer pH 7.4.

Relaxivity experiments for $CuCl_2$, in the absence and presence of MB1-2 (5 equivalents of peptide trimer, which correspond to 15 equivalents of peptide monomer per equivalent of $CuCl_2$), were also performed in nanopure water in the absence of HEPES buffer. In these samples, pH was manually adjusted to 6.0 or 7.0, by the addition of concentrated stock solutions of NaOH and HCl (0.01, 0.1 and 1 M). The r_1 and r_2 relaxivities were determined from plots of the average,

based on three independent repeats, relaxation rate ($1/T_1$ and $1/T_2$ respectively) as a function of $CuCl_2$ concentration (0 to 40 μM).

Zn(II) transmetallation experiments were performed by adding 40 μM $ZnCl_2$ to a 40 μM solution of either $CuCl_2$ or $GdCl_3$ in the presence of 1 equivalent of peptide trimer (40 μM peptide trimer, which corresponds to 120 μM peptide monomer) in 100 mM HEPES buffer pH 7.0. Control samples were prepared using the same procedure without the addition of $ZnCl_2$. ^{1}H-NMR experiments were performed 1 h after sample preparation.

In studies using serum, concentrate human serum was diluted 10% in PBS buffer pH 7.4. Experiments were conducted for $CuCl_2$ and $GdCl_3$, in the absence and presence of MB1-2 (1 or 5 equivalents peptide trimer per equivalent of metal). r_1 and r_2 relaxivities were determined from plots of relaxation rate ($1/T_1$ and $1/T_2$) as a function of $GdCl_3$ concentration (0, 30 and 40 μM). $CuCl_2$ or $GdCl_3$ were mixed with the peptide at least 20 minutes prior to addition to serum to allow metallopeptide formation.

3.2.8 Relaxivity simulations

MATLAB R2021b software was used to simulate inner-sphere r_1 relaxivity as function of water residence time τ_m and distance r_{MH} using Equations 3-5.

$$r_1^{IS} = \frac{q/[H_2O]}{T_{1M} + \tau_M} \tag{3}$$

$$\frac{1}{T_{1M}} = \frac{2}{15}\left(\frac{\mu_0}{4\pi}\right)^2 \frac{\hbar^2 \gamma_S^2 \gamma_H^2}{r_{MH}^6} S(S+1)\left(\frac{3\tau_c}{1 + \omega_H^2 \tau_c^2}\right) \tag{4}$$

$$\frac{1}{\tau_c} = \frac{1}{\tau_m} + \frac{1}{\tau_R} + \frac{1}{\tau_s} \tag{5}$$

where S is the spin quantum number, r_{MH} is the ion-proton distance, ω_H is the Larmor frequency of the proton, γ_H is the proton gyromagnetic ratio, g_e is the electronic g-factor ($g_e = 2$), μ_B is the Bohr magneton and μ_0 is the permittivity of vacuum. Static magnetic field B_0 was set to 1.4 T and 7 T and rotational correlation time τ_R to 6.9 ns.

3.3 Results

3.3.1 Peptide design

Peptide sequences named MB1-2 and MB1C (Table 3.2), were previously designed by Berwick and co-workers.[20, 21] They are based on five heptad repeats of the sequence IAAIEQK,

with the first isoleucine (Ile, I) in ***a*** position.[20, 21] Ile residues were incorporated into the hydrophobic interior of the coil (Figure 3.1), glutamic acid (Glu, E) and lysine (Lys, K) were introduced to form salt bridges between strands and glutamine (Gln, Q) and alanine (Ala. A) to improve solubility and helical formation, respectively. The Gln residue near the metal binding site, was replaced by one tryptophan (Trp, W) to allow determination of peptide concentration in solution. The binding site in MB1-2 was introduced into the hydrophobic interior by substituting asparagine (Asn, N) and aspartic acid (Asp, D) residues in ***d*** and ***a*** position, respectively. The Asp layer provides six potential oxygen donor atoms for Ln(III) coordination, and the Asn layer, located above, potential three additional oxygen donors to generate an overall nine-coordinate site (Figure 3.2a). It was shown that upon Ln(III) addition, the peptide folds in to a parallel three-stranded coiled-coil with the metal buried in the designed cavity forming an overall neutrally-charged coordination site.[20, 21, 24] The substitution of Ln(III) with Cu(II) in this binding site (Figure 3.2a) could lead to the formation of a six-coordinated octahedral complex (Figure 3.2b).

Table 3.2: Peptides used in this chapter. The amino acids forming the copper binding site are underlined.

MB1-2	Ac- G IAAIEQK IAA<u>N</u>EWK <u>D</u>AAIEQK IAAIEQK IAAIEQK G – NH_2
MB1C	Ac- G IAAIEQK IAAIEWK IAAIEQK IAAIEQK IAAIEQK G – NH_2

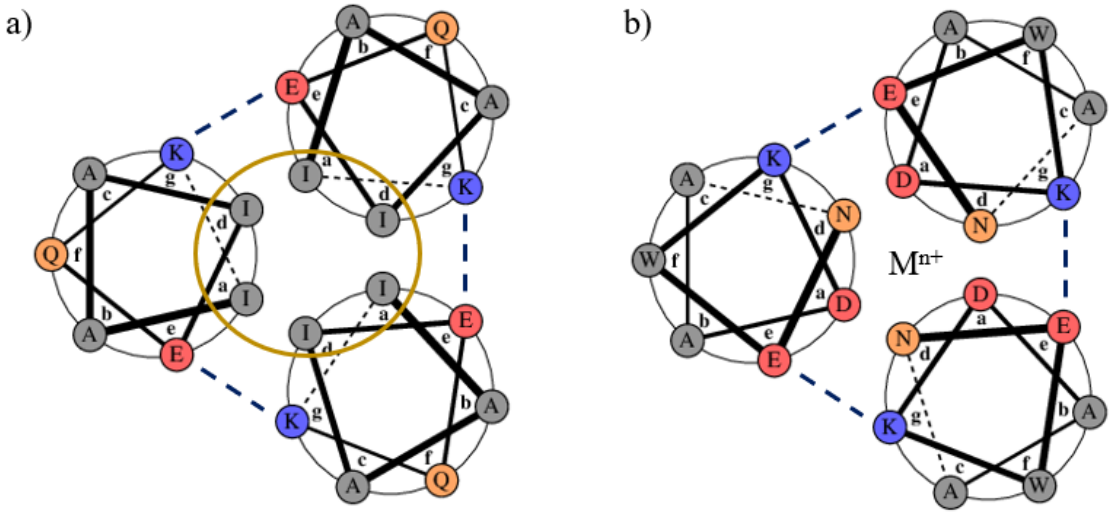


Figure 3.1: Helical wheel diagrams showing the design of the metal binding site by Ile substitution a) to Asn or Asp b) in the core of the MB1-2 trimer. Salt-bridges between the strands are shown as dashed lines.

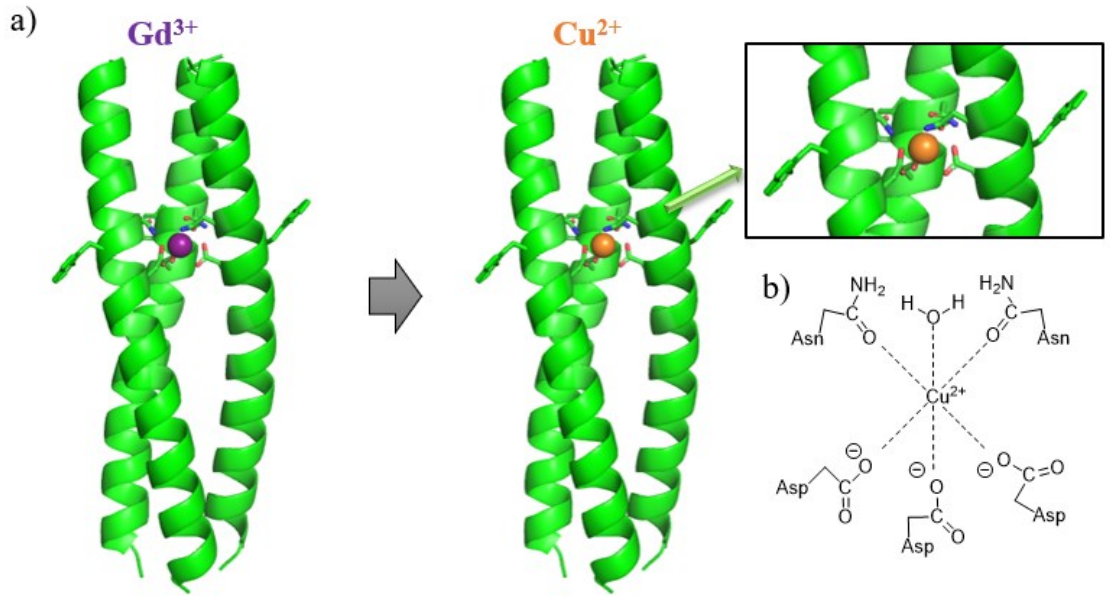


Figure 3.2: a) Cartoon representing Gd^{3+} to Cu^{2+} replacement in the MB1-2 binding site with magnification on the putative copper binding site. Peptide backbone shown as a helical ribbon and side chains shown as sticks, with oxygen in red and nitrogen in blue. Gd(III) and Cu(II) ions shown as purple and orange sphere, respectively. b) Cu(II) shown in a hypothetical octahedral complex.

3.3.2 Determining copper binding and complex stoichiometry

CD data, recorded by Dr. Anbu Sellamuthu, show that, in the absence of Cu(II), MB1-2 is a random-coil at pH 7.0 as its strands, with negative charges on the Asp residues, repel each other, preventing the formation of a folded coiled-coil structure (Figure 3.3a). The intensity of the signal at 222 nm becomes more negative on addition of $CuCl_2$ which is indicative of coiled-coil formation (Figure 3.3a). The plateau is reached only after addition of high excess of copper (>10 equivalents $CuCl_2$ per equivalent of peptide trimer, which correspond to 30 equivalents $CuCl_2$ per equivalent of peptide monomer), suggesting low affinity of copper to the binding site (Figure 3.3b). The fitting was made in accordance with a binding model of $L + 1/3M \leftrightarrow 1/3ML_3$ (M: metal ion and L: peptide monomer, Figure 3.3a,b) using Dynafit.[25] The binding constant (log K_a) was calculated to be 4.7 ± 0.1. Tryptophan fluorescence quenching following Cu(II) addition was used to verify copper binding (Figure 3.3c). Similarly, a high excess of copper was used to achieve relevant quenching (Figure 3.3d). A titration of water into MB1-2 was performed as control. Data were fitted and $\log K_a = 4.9 \pm 0.1$ was calculated confirming the binding constant calculated using CD.

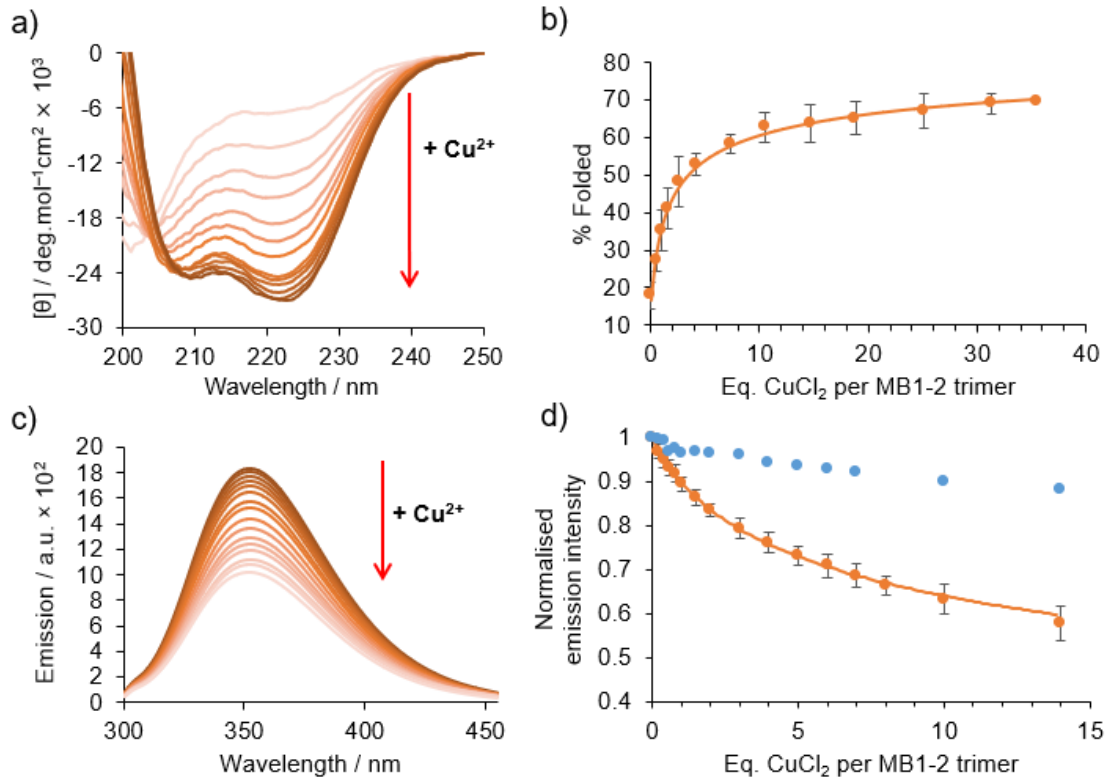


Figure 3.3: a) CD spectra and b) CD folding titration of $CuCl_2$ titration into 30 μM of MB1-2 peptide monomer solution, c) Tryptophan emission spectra d) plot of normalized tryptophan emission intensity at 293 K, λ_{ex} = 280 nm after copper (orange) and water (blue) addition into a 30 μM of MB1-2 peptide monomer solution. Data are results of average of three independent repeats and error bars derives from their standard deviation. The fitting was made with a $1/3M + L \rightarrow 1/3ML_3$ model using DynaFit[25]. All samples were recorded in 10 mM HEPES pH 7.0 buffer at 293 K.

By comparing this result with the binding constant of Tb(III)MB1-2 (log K_a = 5.5 ± 0.2), determined by using Tb(III) luminescence titrations,[21] Cu(II) has lower affinity than Tb(III) to MB1-2. Cu(II) binding is weaker than Tb(III) binding because the latter is a harder acceptor compared to Cu(II) and, therefore, more inclined to bind to Asp hard donors. Moreover, trivalent ions, such as Tb(III) or Gd(III), are able to compensate for the negative charge in the binding site and form more flexible coordination geometries than Cu(II).

It should be noted that the binding constants determined so far are apparent binding affinities, since Cu(II) binding, coiled-coil assembly and folding are coupled processes. Therefore, CD titrations were performed to elucidate the dependence of peptide folding on concentration. Results, reported in Figure 3.4, show that binding appears tighter as the concentration of MB1-2 monomer increases from 30 μM to 90, 120 and 150 μM. Oppositely, it becomes weaker as the concentration decreases to 17 μM.

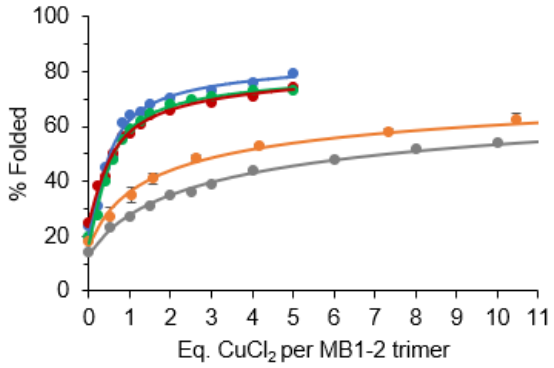


Figure 3.4: CD folding titration of $CuCl_2$ into a 17 µM (grey ●), 30 µM (orange ●), 90 µM (green ●), 120 µM (red ●) and 150 µM (blue ●) of MB1-2 peptide monomer solution. Data at 30 µM are results of average of three independent repeats and error bars derives from their standard deviation. The fitting were made with a $1/3M + L \rightarrow 1/3ML_3$ model using DynaFit[22]. Samples were recorded in pH 7.0 HEPES buffer with concentration either 10 mM (for 17 and 30 µM peptide monomer solution) or 50 mM (90, 120 and 150 µM peptide monomer solution) at 293 K..

A Job's plot analysis using CD spectroscopy (performed by Margaux Verdu and me) was conducted to determine the stoichiometry of the metallopeptide and to confirm the validity of the fittings made previously (Figure 3.5). The results show a maximum, at a ratio of 0.75 monomer to Cu(II), suggesting that a 3:1 monomer to Cu(II) complex is formed and that fitting to the binding model of $L + 1/3M \leftrightarrow 1/3ML_3$ (M: metal ion and L: peptide monomer), to determine the affinity constants, is reliable.

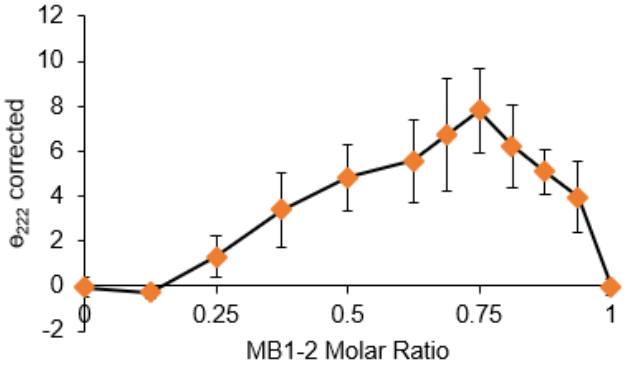


Figure 3.5: Job's continuous variation plot for MB1-2 and $CuCl_2$ in 10 mM HEPES buffer pH 7.0, with total concentration constant and equal to 40 µM. The plot shows MB1-2 monomer molar ration versus CD ellipticity at 222 nm corrected for the contribution from MB1-2 in the absence of Cu(II). Data are results of average of three independent repeats and error bars derives from their standard deviation.

3.3.3 UV-Visible spectroscopy of *d-d* transitions

Electronic transitions arising from electrons in *d*-orbitals were monitored to gain insights into the nature of ligands around Cu(II) in the Cu(MB1-2)$_3$ complex.[26, 27] As reference, a $CuCl_2$ solution in HEPES buffer was analysed and showed a broad absorption at 745 nm (Figure 3.6). In the presence of equimolar concentration of peptide trimer, a red shift to 776 nm was recorded, suggesting a replacement of H_2O ligands to the negatively charged oxygen donors provided by Asp, which are weaker ligands than water. This supports the hypothesis that only oxygen residues are involved in copper binding,[28] as nitrogen donors would have shifted the absorption to shorter wavelengths. Previously, Pecoraro and co-workers reported for a series of peptides containing a His layer for Cu(II) binding to λ_{max} between 600-700 nm.[29, 30]

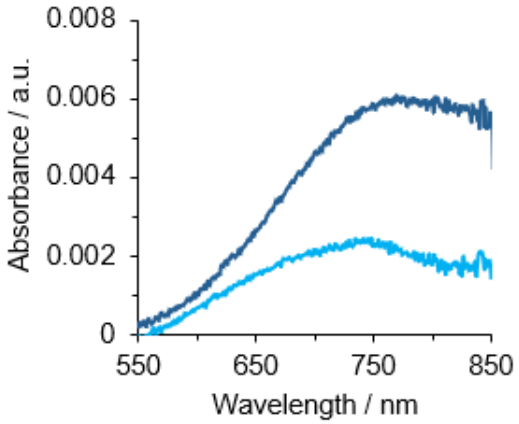


Figure 3.6: UV-Visible spectra in the wavelength range of 550-850 nm for a solution of 450 µM MB1-2 peptide monomer and 150 µM $CuCl_2$ (dark blue) compared to a solution of 150 µM $CuCl_2$ (light blue) in 100 mM HEPES buffer pH 7.0.

3.3.4 Folding kinetics and thermal stability

A kinetic study was performed by monitoring molar ellipticity at 222 nm over time as indication of MB1-2 folding. This study was conducted by comparing the folding kinetics at 30 µM (apo-peptide folding 16%) and 150 µM (apo-peptide folding 28%) upon the addition of 1 equivalent of $CuCl_2$ per equivalent of peptide trimer (which corresponds to 10 or 50 µM $CuCl_2$, respectively). At 30 µM (Figure 3.7a), the plot reveals clearly that kinetics are fast, but over the next 15 minutes the peptide gets unfolded. The same behaviour is observed when the concentration of the peptide monomer is 150 µM (Figure 3.7b). Here, the kinetics are even faster since after 5 minutes no change in folding was detected. Both plots suggest that, in the presence of 1 equivalent of $CuCl_2$, a more folded kinetic product is formed, while over time a less folded thermodynamic product is favoured.

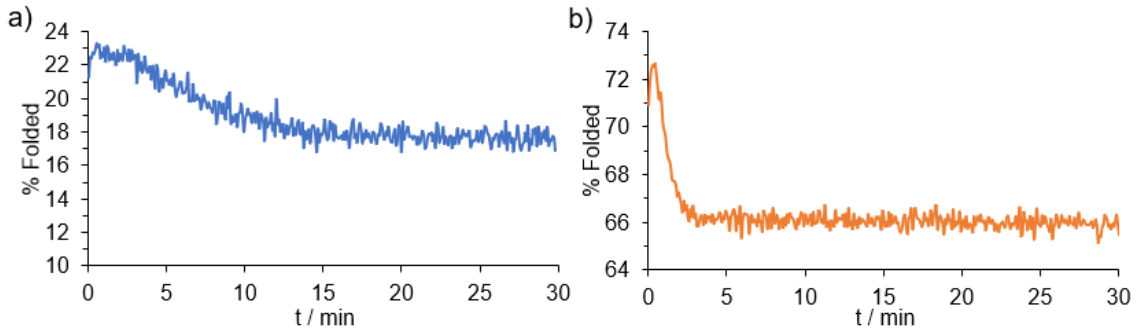


Figure 3.7: Plots showing variation over time of % folding of a) 30 μM (apo peptide folding 16%) and b) 150 μM (apo peptide folding 28%) MB1-2 monomer in the presence of 1 equivalent of $CuCl_2$ per peptide trimer. Samples prepared in pH 7.0 HEPES buffer a) 10 mM, b) 50 mM.

A variable temperature CD experiment (Figure 3.8) was performed to determine the stability of the copper coiled-coil over a range of temperature, including physiological (37°C) temperature. As shown in Figure 3.8, the apo form remains largely unfolded over the full temperature range. Oppositely, a higher variation was determined in the metalated form. The folding is maximum in a temperature range of 20-25°C and decreases from 62 to 46% with higher temperature. At 37°C the peptide is 50% folded. Tanaka and co-workers reported melting temperatures (T_m) values for Cu(II) binding to helical bundles (AM2D and AM2E) to be 66°C and 75°C.[31] This notable difference can be, for instance, attributed to the presence of a bundle instead of a coiled-coil being more able to stabilise Cu(II) binding over increasing temperatures. Gd(III) binding to MB1-2 has been reported by Berwick and co-workers to be more stable at temperatures up to 40°C.[21] For Gd(III) binding to MB1-2, T_m was estimated to be about 60°C.[32] This means that, compared to Gd(III), Cu(II) results in a less stable complex at increasing temperature.

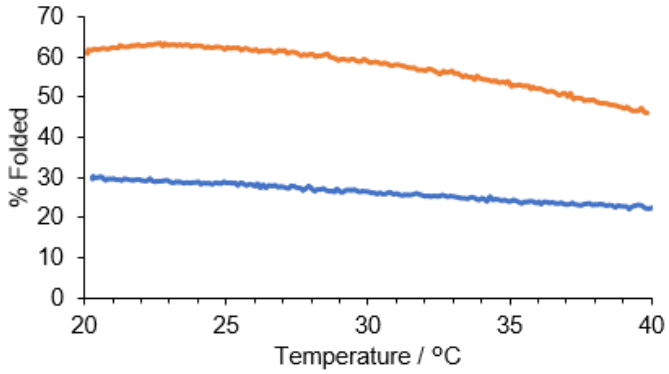


Figure 3.8: Plot showing variation between 20-40°C in % folding of 150 μM MB1-2 monomer in the absence (blue line) and in the presence of 1 equivalent of $CuCl_2$ per peptide trimer (orange line). Samples were prepared in 50 mM HEPES buffer pH 7.0.

3.3.5 Evaluation of the required amount of peptide to ensure Cu(II) complexation

Before measuring relaxivity, the ratio between metal and peptide trimer necessary to bind Cu(II) completely was determined. Calculations using ChemEQL[33] were performed to determine speciation of 40 and 10 μM $CuCl_2$ solutions in the presence of an increasing number of equivalents of peptide trimer, according to the experimental apparent log K_a values. From these values, plots were made to evaluate concentration of residual Cu(II) (Cu_{free}) in solution (Figure 3.9a,b), the formation of the complex CuL_3 (Figure 3.9c,d) and the presence of the non-bound ligand L (Figure 3.9e,f) as a function of the number of peptide trimer equivalents, where 1 equivalent of trimer correspond to 3 equivalents of monomer. Moreover, a comparison was made to assess the impact of increasing log K_a values. At 40 μM $CuCl_2$ concentration, for log $K_a > 4.5$, 3 equivalents of peptide trimer are sufficient to form a stoichiometric amount of metallo-trimer (for CuMB1-2 log $K_a = 4.9$). When Cu(II) is 10 μM, at least 5 equivalents of peptide trimer (15 equivalents of peptide monomer), are needed to ensure full complexation.

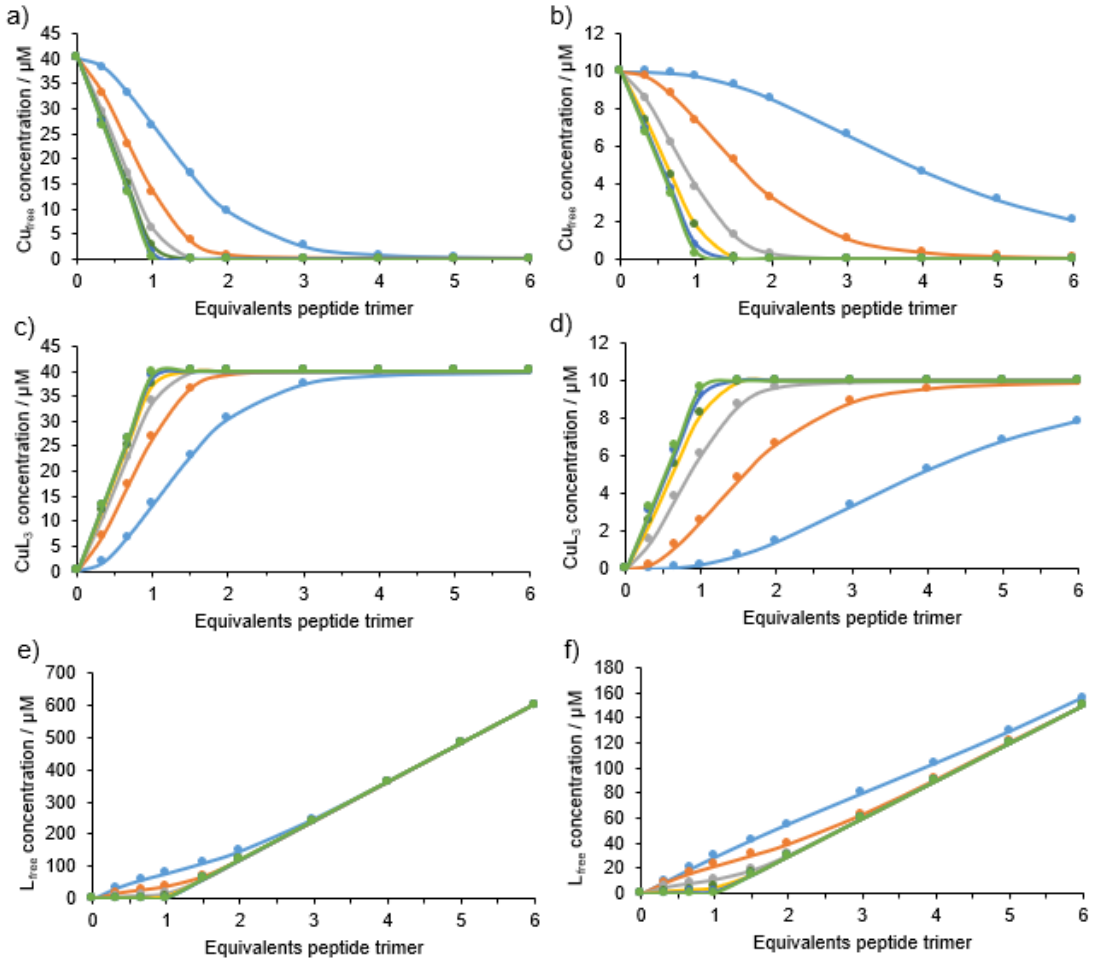


Figure 3.9: Binding plots showing Cu_{free}, CuL_3 or L_{free} for a), c), e) 40 µM or b), d), f) 10 µM $CuCl_2$ in the presence of increasing number of peptide trimer equivalents calculating using Chem EQL using log K_a = 4 (light blue ●), 4.5 (orange ●), 5 (grey ●), 5.5 (yellow ●), 6 (blue ●) and 6.5 (green ●).

To monitor metallopeptide formation, NMR T_1 and T_2 relaxation times were determined as function of peptide trimer equivalents (Figure 3.10) added to a solution of 40 µM $CuCl_2$. The graph shows that after 5 equivalents of peptide trimer there is no significant reduction of relaxation times, which is indication of metallopeptide formation. At higher equivalents, T_1 and T_2 relaxation times are not further reduced because of no additional metallopeptide formation.

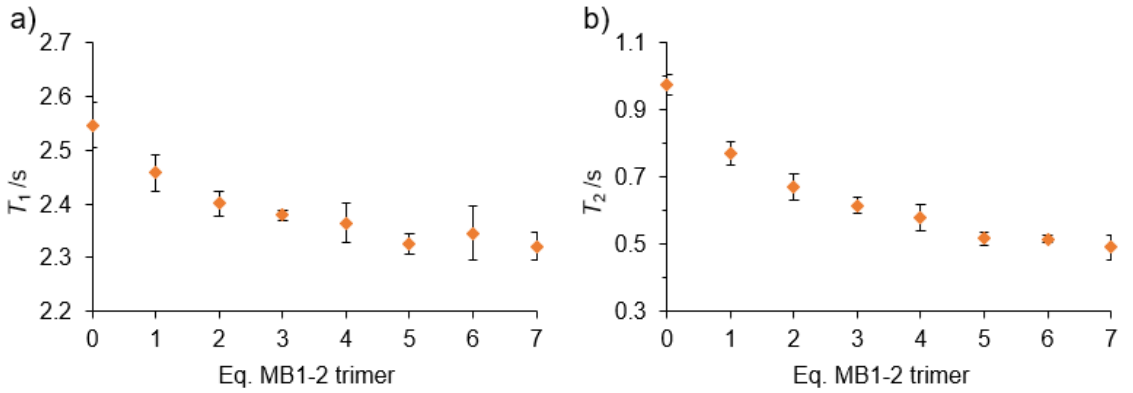


Figure 3.10: Plots of ^{1}H-NMR a) T_1 and b) T_2 relaxation times for solutions of 40 μM $CuCl_2$ in 100 mM HEPES buffer pH 7.0, as a function of increasing equivalents MB1-2 peptide. Samples recorded at 293 K on a 300 MHz NMR spectrometer. Error bars determined from standard deviation of three independent repeat experiments.

3.3.6 Relaxivity measurement

After having established Cu(II) binding and the required conditions to ensure full Cu(II) complexation, MRI relaxivity measurements were conducted to determine the efficiency of the Cu(II) compound as a contrast agent. As introduced in Section 2.7.2, MRI relaxivity can be measured experimentally using the linear relationship existing between the NMR $1/T_1$ and $1/T_2$ relaxation rates and the relative concentrations of paramagnetic contrast agent. Relaxation rates were determined at two different magnetic fields, 1.4 T (Figure 3.11) and 7 T (Figure 3.12), to evaluate the impact of the presence of a slow tumbling system (MB1-2 peptide) on the relaxivity at low, and clinically more relevant, magnetic field (1.4 T). As an excess of peptide was used, the r_1 and r_2 relaxivities of the apo peptide were also measured. No significant contribution from the excess of apo peptide to r_1 is reported, while some contribution to r_2 was found, especially at high field (7 T) (Table 3.3). The metallopeptide relaxivity was then corrected for the free peptide contribution to transversal T_2 relaxation. Moreover, relaxation times at a higher concentration of $CuCl_2$ (80 μM $CuCl_2$, 1.2 mM peptide monomer) were measured to prove that a linear trend still exist at higher peptide concentrations and peptide aggregation does not occur (Figure 3.13).[34]

The relaxivity values for CuMB1-2 (Table 3.3) were determined to be comparable or even higher than the Gd(III) analogue, despite the difference in spin quantum number (S = 1/2 for Cu(II) compared to S = 7/2 for Gd(III). This suggests that Cu(II) and Gd(III) coordination into MB1-2 binding site is different. Overall, this result is important because it is the highest relaxivity reported for a Cu(II) compound, to our knowledge, challenging the common belief that Cu(II) is unsuitable for use in MRI contrast agents. To further demonstrate that the high relaxivity is as a result of Cu(II) binding to the designed binding site, relaxivity values for Cu(II) in the presence

of the MB1C control peptide were determined (Table 3.3). The MB1C sequence is the exact same sequence but lacks the binding site (meaning that only Ile are located in the hydrophobic core). The resulting longitudinal relaxivity r_1 corresponds to free Cu(II) while the transversal relaxivity r_2 reflects the presence of Cu(II) and of the free peptide which provides a diamagnetic contribution to relaxivity.

Table 3.3: ^{1}H-MRI relaxivity data. Samples prepared in 100 mM HEPES buffer pH 7.0 at 293 K. Error determined from standard deviation of three independent repeats.

	1.4 T		7 T	
	r_1 / $mM^{-1}s^{-1}$	r_2 / $mM^{-1}s^{-1}$	r_1 / $mM^{-1}s^{-1}$	r_2 / $mM^{-1}s^{-1}$
$GdCl_3$	12.3	14.6	13.0	19.4
$CuCl_2$	0.6 ± 0.2	0.5 ± 0.3	0.5 ± 0.2	0.7 ± 0.4
$Gd(MB1\text{-}2)_3$	15.3 ± 0.6	18.9 ± 0.1	5.4 ± 0.1	19.8 ± 0.5
$Cu(MB1\text{-}2)_3$	14.2 ± 0.2	32.7 ± 0.4	1.3 ± 0.3	17.6 ± 0.7
Apo MB1-2	0.02 ± 0.01	0.09 ± 0.01	0.00 ± 0.00	0.48 ± 0.01
MB1C + $CuCl_2$	0.6 ± 0.2	1.6 ± 0.4	nd	nd

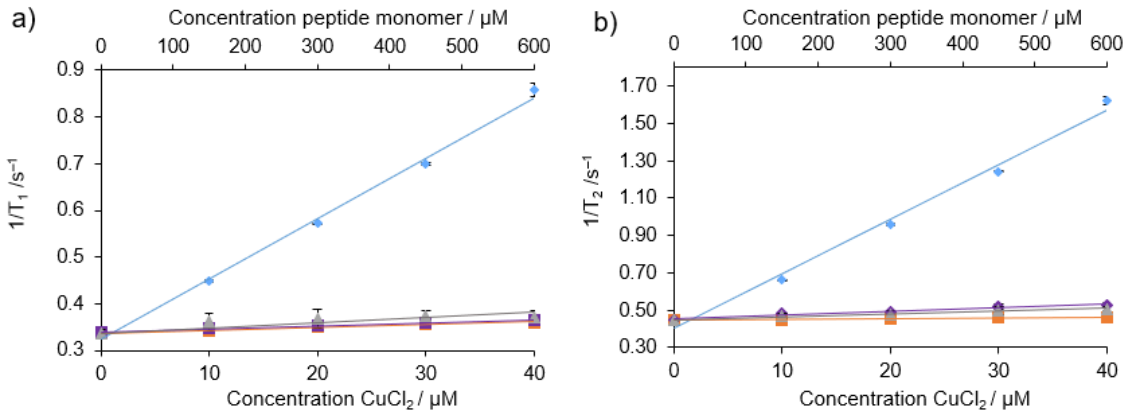


Figure 3.11: 60 MHz a) T_1 and b) T_2 ^{1}H-MRI relaxivity plots, showing the reciprocal of NMR relaxation times as a function of concentration for $CuCl_2$ (orange squares ■), apo MB1-2 (grey triangles ▲), $Cu(MB1\text{-}2)_3$ (blue diamonds ♦) and MB1C in the presence of $CuCl_2$ (purple diamonds ♦). Peptide samples prepared for Cu(II) in the presence of 5 equivalents MB1-2/MB1C peptide trimer. Samples recorded at 293-294 K, in the presence of 100 mM HEPES buffer pH 7.0. Error bars determined from standard deviation from three independent repeat experiments.

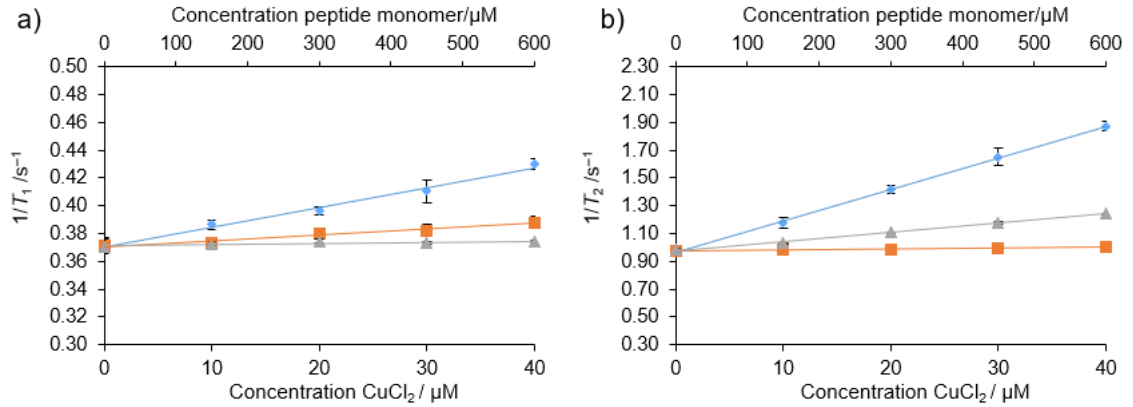


Figure 3.12: 300 MHz a) T_1 and b) T_2 ^{1}H-MRI relaxivity plots, showing the reciprocal of ^{1}H-NMR relaxation times as a function of concentration for $CuCl_2$ (orange squares ■), apo MB1-2 (grey triangles ▲) and $Cu(MB1\text{-}2)_3$ (blue diamonds ♦). $Cu(MB1\text{-}2)_3$ samples prepared for Cu(II) in the presence of 5 equivalents MB1-2 peptide trimer. Samples recorded at 293 K, in the presence of 100 mM HEPES buffer pH 7.0. Error bars determined from standard deviation from three independent repeat experiments.

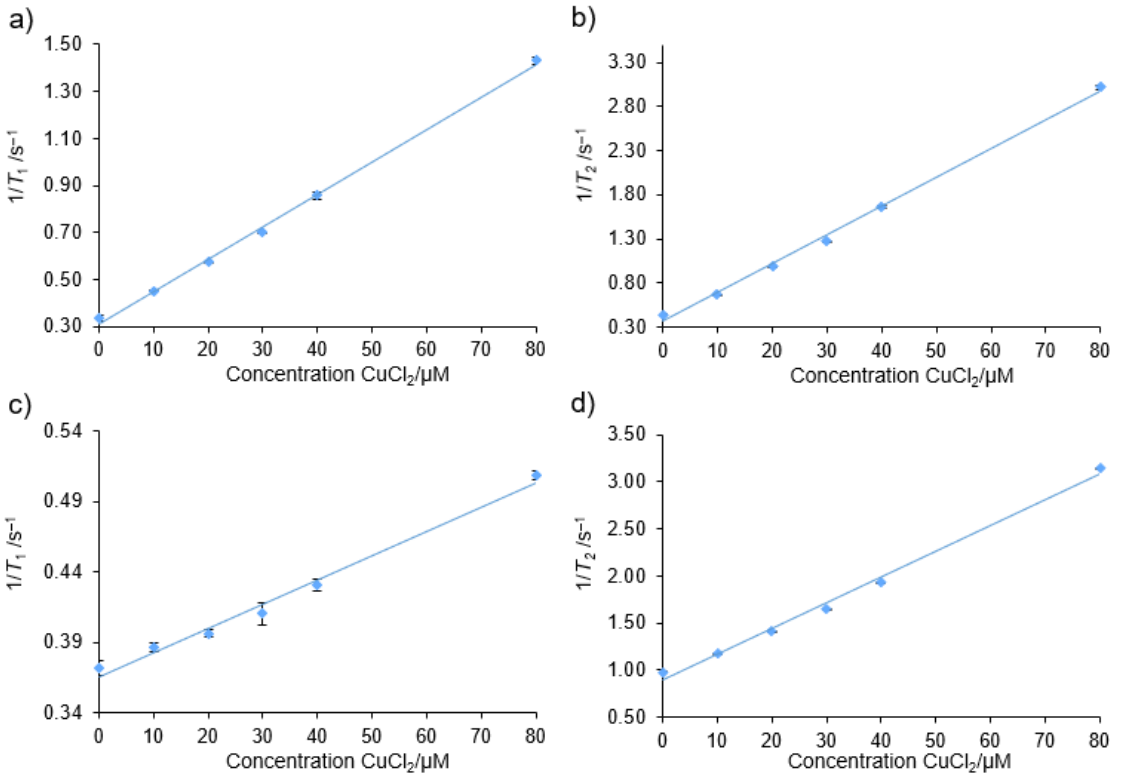


Figure 3.13: a), b) 60 and c), d) 300 MHz ^{1}H-MRI relaxivity plots showing the reciprocal of a), c) T_1 and b), d) T_2 ^{1}H-NMR relaxation times as a function of concentration of $Cu(MB1\text{-}2)_3$. Samples prepared for Cu(II) in the presence of 5 equivalents MB1-2 peptide trimer. Samples recorded at 293-294 K, in the presence of 100 mM HEPES buffer pH 7.0. Error bars determined from standard deviation from three independent repeat experiments.

Gd(MB1-2)$_3$ was initially reported by Berwick and co-workers, but relaxivity was only determined at 7 T, with values comparable to here (r_1 = 4.2 ± 1.2 mM^{-1}s^{-1} and r_2= 21.3 ± 2.6 mM^{-1}s^{-1}).[20, 21] The inner-sphere hydration value q of Gd(III) was determined experimentally to be 0,[21] meaning that no water is directly coordinated to Gd(III). Here, a field dependence of Gd(MB1-2)$_3$ relaxivity was found, suggesting that the dominant contribution derives from second-sphere water. Second-sphere water can be constituted by water hydrogen-bonded to Asp or Asn amino acid residues, which could be sufficiently close to the metal ion to be efficiently relaxed.[24] Alternatively, water can be coordinated to Lys or Glu in proximity to the binding site or to carbonyl or amide groups on peptide backbone at relatively short distance to Gd(III). Moreover, relaxation from outer-sphere water molecules contributes at both magnetic fields.

The second- and outer-sphere relaxation can be assumed to operate similarly in the Cu(MB1-2)$_3$ system, as they are more dependent on the primary and secondary structure of the peptide. However, because Gd(III) is more paramagnetic than Cu(II), high relaxation is likely to derive from the presence of inner-sphere water directly coordinated to Cu(II). This is further explored with simulations in Section 3.3.7. The presence of inner-sphere water molecules is consistent with the binding site being buried within the MB1-2 trimer, leading to limited flexibility. Gd(III) coordination can be more easily distorted than rigid Cu(II) coordination as in the lanthanide ions only steric effect determines coordination, while in transition metal complexes electronic effects are taken in account.[35] This leads to Gd(III) fitting more easily into the binding site, with less distortion of the peptide structure than Cu(II). In the Cu(II) system, the distortion of the peptide enables water molecule to coordinate to Cu(II), to complete Cu(II) coordination sphere.

3.3.7 Prediction of parameters influencing relaxivity

The reasons behind the exceptional high relaxivity of Cu(MB1-2)$_3$ were investigated. Firstly, reducing molecular tumbling is an efficient method to enhance relaxivity at low magnetic fields. However, there needs to a mechanism by which Cu(II) allows efficient relaxation of bulk water. EPR measurements, performed by the group of Janet Lovett (St. Andrews University) have shown that two water molecules are directly bound to Cu(II), with no evidence of water in axial positions.[28] This means that inner-sphere water does not occupy elongated axial positions in a hypothetical Jahn-Teller distorted coordination (typical in complex of d^9 metal ions, such as Cu(II)).[28] EXAFS studies performed by Iuliia Mikulska (Diamond Light Source, UK) showed that two oxygen shells are present with Cu-O bond lengths ranging from 1.93 to 1.96 Å and 2.30-2.35 Å within trigonal pyramidal, square pyramidal or Jahn-Teller distorted octahedral geometries.[28] Taken together, these results suggests that the presence of two water molecules in close proximity to Cu(II) is the main reason for the higher relaxivity reported for Cu(MB1-2)$_3$ at

both magnetic fields. Moreover, the very low relaxivities reported for q = 0 complexes[36-39] suggests that in Cu(II) systems, second-sphere and outer-sphere contributions are generally negligible.

MATLAB was used to simulate r_1 relaxivity as function of different parameters, using equations introduced in Chapter 1 for a S = 1/2 system and assuming that the major contribution to relaxation derives from dipolar relaxation.[40-42] To determine the impact of the metal ion distance to the water protons (r) and of water residence time τ_m, a plot was generated (Figure 3.14). This simulation shows that, for distances longer than 3.5-4 Å (which are related to second-sphere water molecules,), the contribution of one water molecule at these distances (shown in black in Figure 3.14) is negligible even in a slow rotating system such as a Cu(II)-peptide (with rotational correlation time τ_r = 6.9 ns)[43] at magnetic fields as low as 1.4 T.

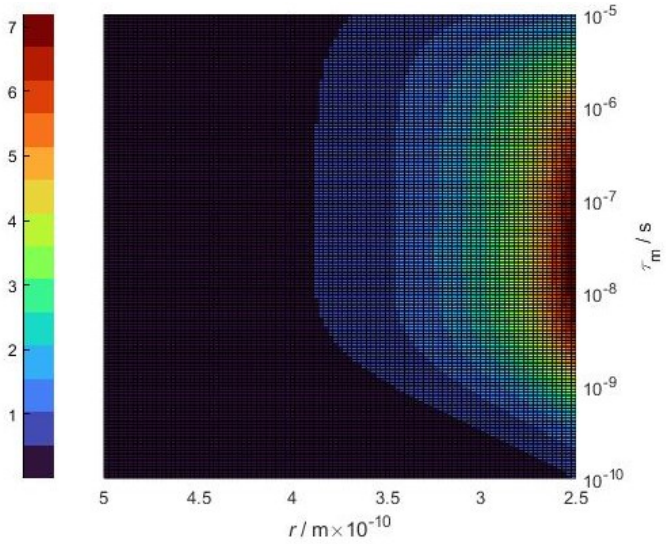


Figure 3.14: Simulation of ^{1}H-MRI r_1 relaxivity (shown on colour bar) at 1.4 T, for one water molecule (q = 1) in a Cu(II) compound with rotational correlation time τ_R = 6.9 ns and Cu(II) electron relaxation time τ_s = 5 ns, as function of variable water residence time τ_m and water proton-metal ion distance r.

Inner-sphere relaxivity was simulated using the same equation as second-sphere (see Chapter 1) and providing more details on shorter distances (2.5-3.1 Å). As first approximation, electron relaxation time of Cu(II) was estimated to be 5 ns, which is a reasonable value for Cu(II) proteins.[15, 44-46] A comparison was made for simulated relaxivity at 1.4 T and 7 T as shown in Figure 3.15. Simulated relaxivity matches experimental relaxivity (r_1= 14.2 ± 0.2 mM^{-1} s^{-1} at 1.4 T and r_1= 1.3 ± 0.3 mM^{-1} s^{-1} at 7 T) in the orange region in plot **a** (1.4 T) and in the light blue region in plot **b** (7 T). The intersection between these regions enables to estimate the distance r Cu-H between the metal ion and the water protons as around 2.6 Å, which supports the hypothesis that water molecules are located close to the metal.

Water residence time τ_m was estimated to be about 10 ns, longer than in the Cu(II)-aquo complex where $\tau_m = 4.4 \pm 0.1$ ns.[13, 14] This is reasonable since water accessibility to Cu(II) is reduced when the metal is located within the hydrophobic core of the coiled-coil, compared to the aquo complex. However, this value is only a prediction that should be confirmed by variable-temperature ^{17}O-NMR experiments.

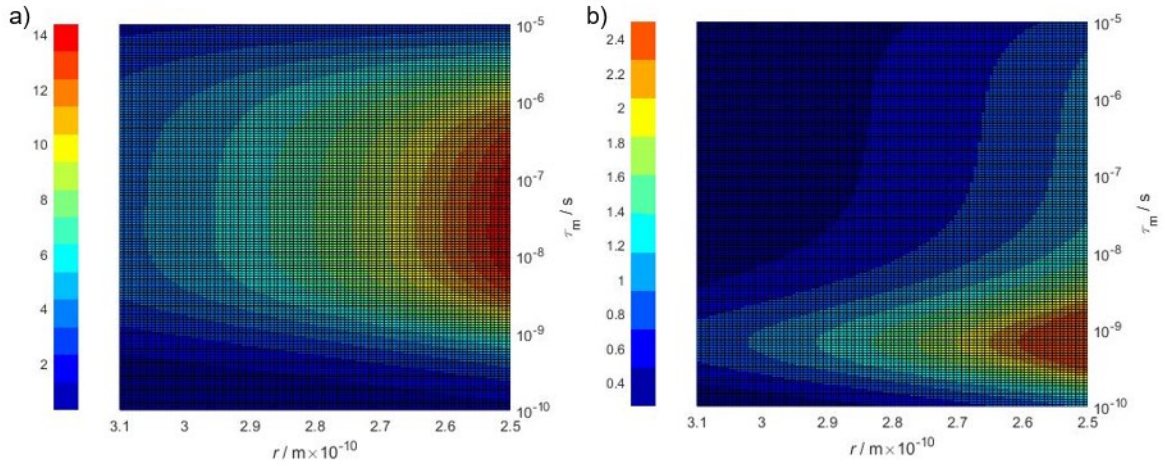


Figure 3.15: Simulation of ^{1}H-MRI r_1 relaxivity (shown on colour bar) at a) 1.4 T and b) 7 T for two water molecules (q = 2) in a Cu(II) compound with rotational correlation time τ_R = 6.9 ns and Cu(II) electron relaxation time τ_s = 5 ns, as function of variable water residence time τ_m and water proton-metal ion distance r.

In macromolecular Cu(II) complexes, electron relaxation strongly influences correlation time and, consequently, relaxivity, while in small complexes rotational correlation time has the major contribution on overall correlation time (Equation 6).[15] Simulations using different electron relaxation times (τ_s = 1 or 0.5 ns) were performed (Figure 3.16). At low magnetic fields (1.4 T), shorter electron relaxation times lead to a more drastic reduction of correlation time (Equation 6) and relaxivity than at higher fields (7 T), where a broader range of water residence times allows to reach high relaxivities.

$$\frac{1}{\tau_c} = \frac{1}{\tau_m} + \frac{1}{\tau_R} + \frac{1}{\tau_s} \qquad (6)$$

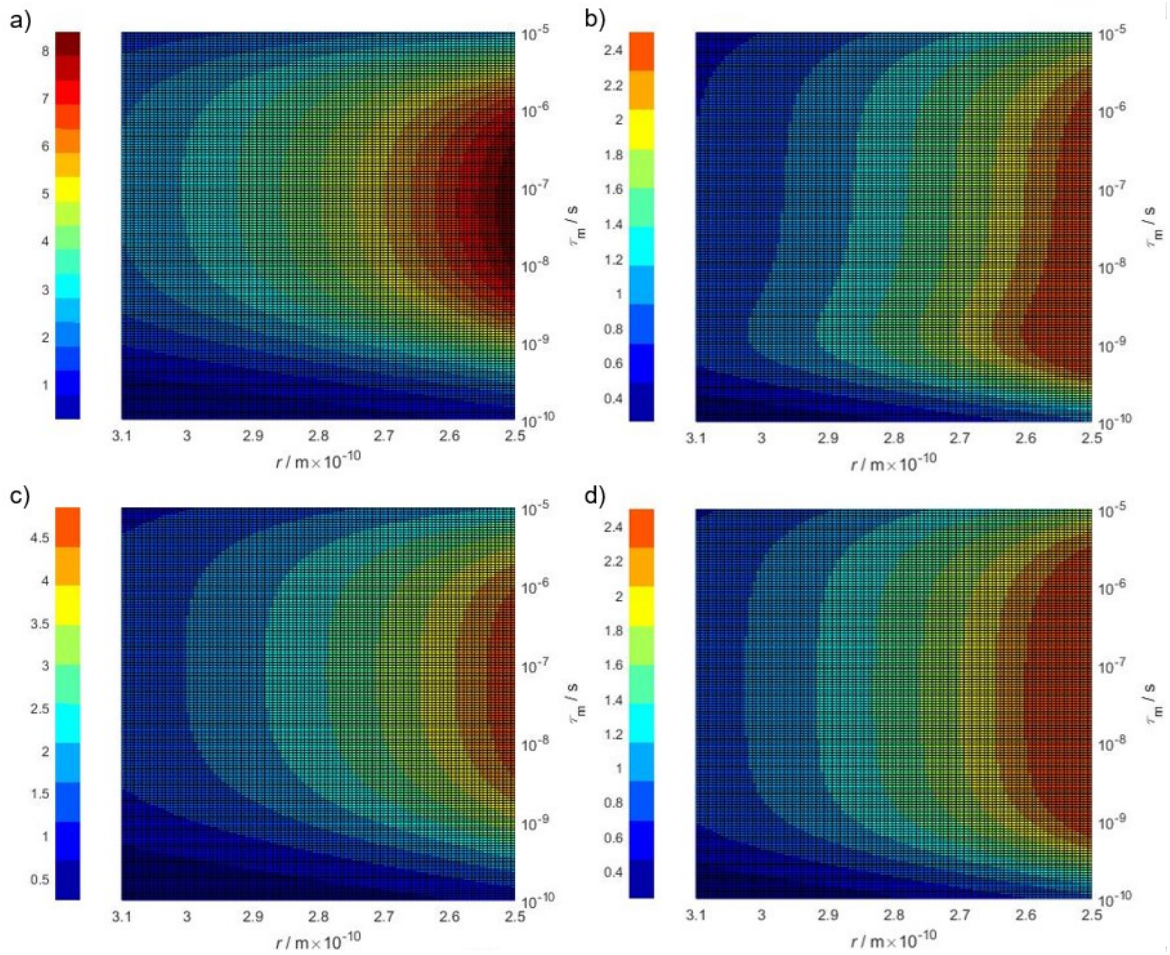


Figure 3.16: Simulation of ^{1}H-MRI r_1 relaxivity (shown on colour bar) at a), c) 1.4 T and b), d) for two water molecules ($q = 2$) in a Cu(II) compound with rotational correlation time $\tau_R = 6.9$ ns and Cu(II) electron relaxation time τ_s= a), b) 1 ns or c), d) 0.5 ns as function of variable water residence time τ_m and water proton-metal ion distance r.

3.3.8 Influence of HEPES buffer on relaxation times and relaxivities

Relaxivity measurements reported in Section 3.3.6 were conducted in HEPES buffer. Although there are conflicting reports about the use of this buffer with copper,[47-49] it was assumed that in the presence of a stronger ligand such as a peptide, such weak interaction is negligible. However, the impact of HEPES buffer was assessed by measuring T_1 and T_2 relaxation times in water pH 7.0 (manually adjusted) and comparing the relaxivities (Figure 3.17). r_1 plot shows that there is a negligible impact of HEPES on relaxation times and relaxivity of both the metallopeptide and $CuCl_2$. On the other hand, T_2 relaxation times are influenced by the presence of the buffer. However, the slope of the fitting line (relaxivity), is the same. This means that the presence of HEPES results in a translation of the line and not in a change in its slope (relaxivity).

It is apparent that HEPES buffer provide the same diamagnetic contribution to transversal $1/T_2$ relaxation rate in all samples (Equation 7) and not to longitudinal $1/T_1$ relaxation rate.

$$\frac{1}{T_{2,\ total}} = \frac{1}{T_{2,\ water}} + \frac{1}{T_{2,\ CuMB1-2}} + \frac{1}{T_{2,\ HEPES}} \tag{7}$$

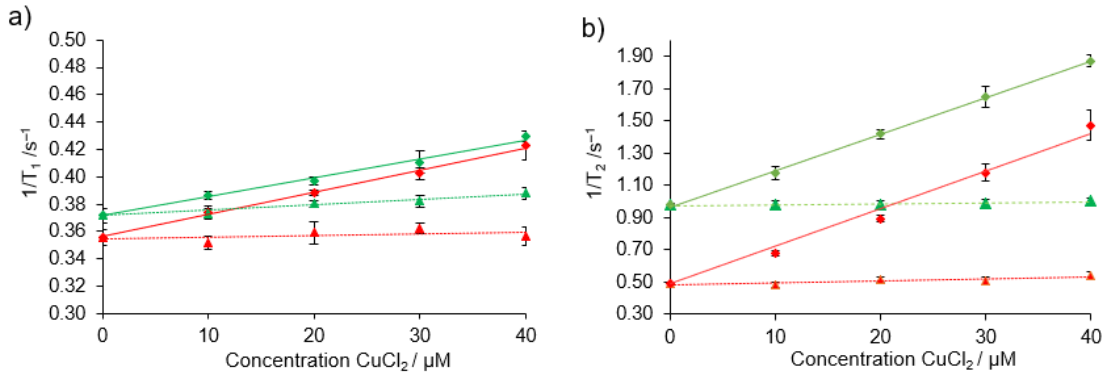


Figure 3.17: a) T_1 and b) T_2 ^{1}H-MRI relaxivity plots, showing the reciprocal of ^{1}H-NMR relaxation times as a function of Cu(II) concentration, recorded at pH 7.0, where samples were either manually adjusted (red) or prepared in 100 mM HEPES buffer (green), in the absence (triangles) and presence of 5 equivalents MB1-2 trimer (diamonds). Samples were recorded at 293 K on a 300 MHz NMR spectrometer. Error bars were determined from the standard deviation of three independent repeat experiments.

3.3.9 Influence of pH on relaxation times and relaxivity

Peptide folding in the Cu(II) system was monitored as function of pH (Figure 3.18). Peptide folding is increased from pH 3 to pH 5-6 with Glu side-chain deprotonation ($pK_a = 4.25$) and formation of salt-bridges with Lys. When all Glu carboxyl side chains are deprotonated (pH 5-6), peptide folding reaches its maximum. This is consistent with results reported by Pecoraro and co-workers for a series of similar peptides.[30] Above pH 6 folding slightly decreases up to pH 7.0 and more consistently at higher pH, indicating the formation of copper hydroxide. The formation of copper hydroxide in this system could arise from the weak affinity of Cu(II) to MB1-2.

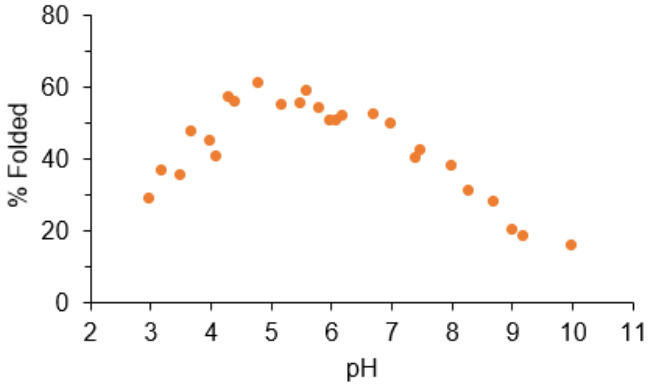


Figure 3.18: Plot with comparison between the variance of %folding of MB1-2 in water in the presence of $CuCl_2$ (5:1 $CuCl_2$: MB1-2 peptide trimer) as function of variable pH.

It was of interest to understand the effect of pH on the metallopeptide relaxation times, since they can be due to variation within the coordination chemistry. These could be structural changes leading to different number of inner-sphere water, protonation/deprotonation, formation of hydrogen bonds), modulation of water exchange rate and/or formation of hydroxide species at high pH, with slower exchange rates.[50-54] NMR T_1 and T_2 relaxation times were measured at pH varying from 5 to 8 (including pH 7.4, the physiological pH of blood). Data were recorded for the metallopeptide and for water, and the relaxation rates relative to the paramagnetic system were determined as the difference of experimental values at a given pH. No substantial variation in relaxation rates was reported, apart from a slight increase from pH 5 to pH 6.4 and a decrease above pH 7.4. The first rise could be attributed to a change in proton exchange mechanism as consequence of Glu deprotonation (for free Glu amino acid, $pK_a = 4.25$) while the reduction in relaxation rates at higher pH, likely reflects peptide unfolding (Figure 3.19) and copper precipitation as hydroxide.

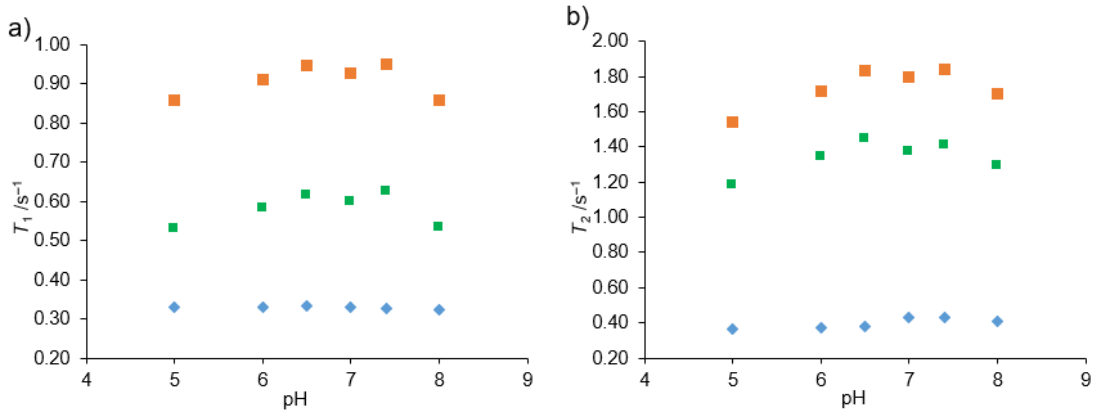


Figure 3.19: a) T_1 and b) T_2 plots, showing the ^{1}H-NMR relaxation times of CuMB1-2 (orange ■), $CuCl_2$ (blue ♦) and relative difference (green ■) as a function pH concentration. pH manually adjusted using NaOH/HCl. Samples were recorded at 293 K on a 60 MHz NMR spectrometer.

To further assess relaxivity pH dependency, a relaxivity plot was produced for Cu(MB1-2)$_3$ in water at pH 6.0 and compared with pH 7.0 in manually adjusted water (Figure 3.20). Such comparison demonstrates no influence of pH on relaxivity in the considered pH range.

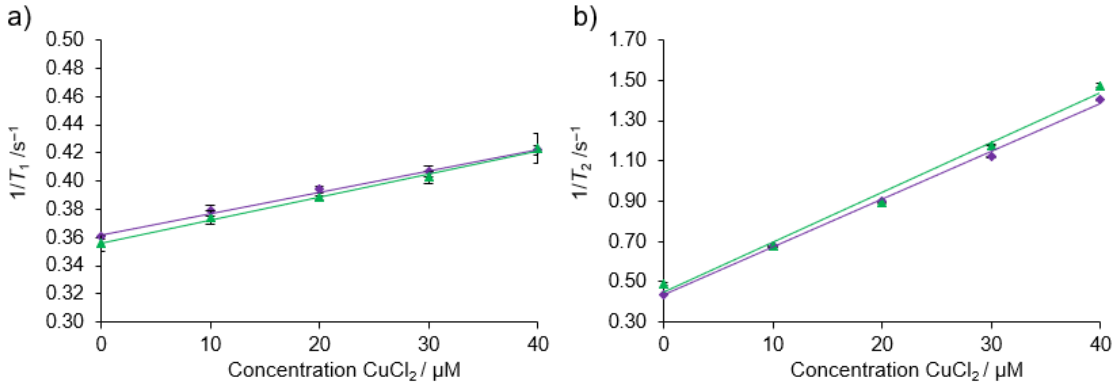


Figure 3.20: a) T_1 and b) T_2 ^{1}H-MRI relaxivity plots, showing the reciprocal of ^{1}H-NMR relaxation times as a function of Cu(MB1-2)$_3$ concentration, recorded at pH 7.0 (green ▲) and pH 6.0 (purple ♦), manually adjusted using NaOH/HCl. Samples were recorded at 293 K on a 300 MHz NMR spectrometer. Error bars were determined from the standard deviation of three independent repeat experiments.

3.3.10 Cu(II) displacement in the presence of Zn(II)

It should be noted that the apparent affinity constant is too low for *in vivo* application of the Cu(MB1-2)$_3$ complex (in clinically approved contrast agents, log K_{GdL}~ 20).[4] However, the high relaxivity determined for this metallopeptide shows that Cu(II) compounds can be efficient MRI contrast agents once metal affinity to the complex is optimised. For *in vivo* applications, transmetallation is an event that should be considered. The presence of endogenous metals such as Zn(II) (around 50 μM in serum)[55] can lead to partial or total substitution of the metal ion in the complex.[56] Here, longitudinal relaxation rates were determined to evaluate transmetallation of complexes in the presence of Zn(II) (Figure 3.21). For MB1-2 in the presence of 40 μM $ZnCl_2$ (1:1 Zn(II) : trimer ratio), $1/T_1$ relaxation rate was determined to be similar to a solution of the MB1-2 peptide at the same concentration. This is because Zn(II) is diamagnetic, so Zn(II) complexes do not induce an increase in either $1/T_1$ or $1/T_2$ relaxation rates. When 40 μM $ZnCl_2$ was added to a solution of CuMB1-2 (with a total ratio of 1 equivalent of $CuCl_2$, 1 equivalent of peptide trimer and 1 equivalent of $ZnCl_2$), after 1 h, a reduction in $1/T_1$ relaxation rate was found as consequence of partial transmetallation of the copper compound to form the Zn(II) analogue (estimated 80% residual CuMB1-2). The same experiment was performed on the relative Gd(III)

compound, showing that the Gd(III) analogue undergoes transmetallation to a lesser extent than the Cu(II) compound (estimated 95% residual GdMB1-2).

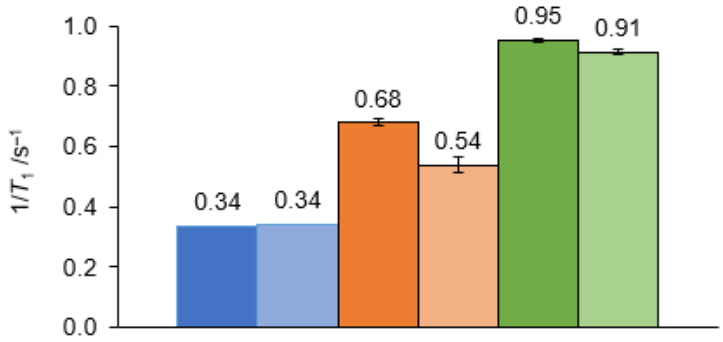


Figure 3.21: Diagram showing ^{1}H-NMR $1/T_1$ relaxation rate for a solution of HEPES 100 mM pH 7.0 (blue), 40 μM $ZnCl_2$ in HEPES 100 mM pH 7.0 (light blue), 40 μM $CuCl_2$ and 5 equivalents peptide trimer without (orange) and with (light orange) 40 μM $ZnCl_2$, 40 μM $GdCl_3$ and 5 equivalents peptide trimer without (green) and with (light green) 40 μM $ZnCl_2$ in HEPES 100 mM pH 7.0. Samples were recorded at 293 K on a 60 MHz NMR spectrometer. Error bars were determined from the standard deviation of three independent repeat experiments.

3.3.11 Stability in Phosphate Buffer Saline (PBS) and in human serum

Relaxivity in PBS (Phosphate Buffer Saline) was determined for $Cu(MB1\text{-}2)_3$, $CuCl_2$ and $Gd(MB1\text{-}2)_3$ (Figure 3.22 and Table 3.4), where PBS buffer is an aqueous salt solution of 137 mM NaCl, 2.7 mM KCl, 10 mM Na_2HPO_4 and 1.8 mM KH_2PO_4 at pH 7.4. For $Cu(MB1\text{-}2)_3$, relaxivity was found to be comparable to the values in HEPES buffer, suggesting that PBS does not alter the Cu(II) speciation. On the other hand, for the most concentrated sample of GdMB1-2, the relaxation rates deviates from linearity, indicating a change in Gd(III) speciation, most likely due to metal precipitation as the phosphate complex,[55] occurring preferentially over metal binding to the peptide. The other samples show quite a good linear fit, providing comparable relaxivities to HEPES.

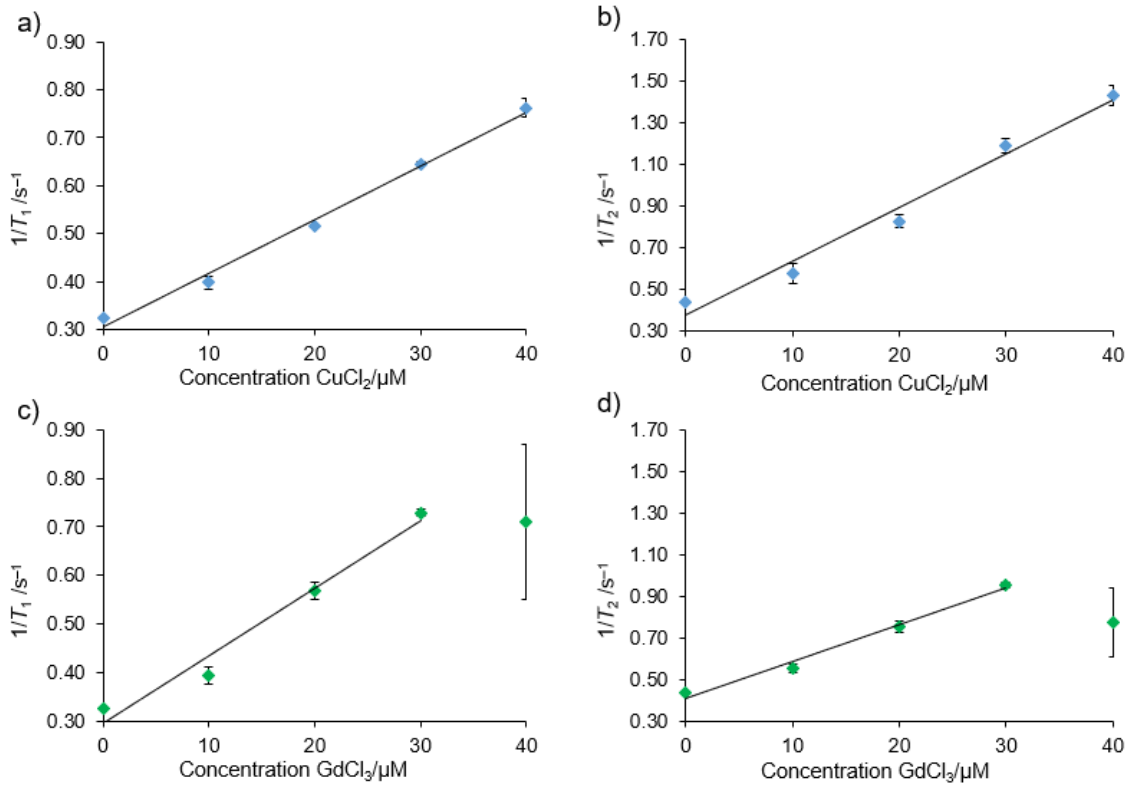


Figure 3.22: 60 MHz a), c) T_1 and b), d) T_2 ^{1}H-MRI relaxivity plots, showing the reciprocal of ^{1}H-NMR relaxation times as a function of concentration for a), b) Cu(MB1-2)$_3$ and c), d) Gd(MB1-2)$_3$. Samples prepared in the presence of 5 equivalents MB1-2 peptide trimer. Samples recorded at 293-294 K on a 60 MHz NMR spectrometer, in the presence of PBS buffer pH 7.4. Error bars determined from standard deviation error of three independent repeat experiments.

Table 3.4: ^{1}H-MRI relaxivity values for Cu(MB1-2)$_3$, $CuCl_2$, Cu(MB1-2)$_3$, $GdCl_3$ in either 100 mM HEPES pH 7.0 or PBS pH 7.4 buffer. Samples recorded at 293-294 K on a 60 MHz NMR spectrometer, in the presence of 100 mM HEPES buffer pH 7.0. Error determined from standard deviation error of three independent repeat experiments. Values for Gd(MB1-2)$_3$ in PBS obtained by fitting only samples with 0-30 μM $GdCl_3$.

Peptide	Buffer	r_1 / mM^{-1}s^{-1}	r_2 / mM^{-1}s^{-1}
Cu(MB1-2)$_3$	HEPES	14.2 ± 0.2	32.7 ± 0.4
	PBS	12.2 ± 1.0	29.2 ± 2.7
$CuCl_2$	HEPES	0.6 ± 0.2	0.5 ± 0.3
	PBS	0.2	0.6
Gd(MB1-2)$_3$	HEPES	15.3 ± 0.6	18.9 ± 0.1
	PBS	13.9 ± 0.5	21.8 ± 1.5
$GdCl_3$	HEPES	12.3	14.6
	PBS	4.9	7.0

Stability over time for $Cu(MB1\text{-}2)_3$ and $Gd(MB1\text{-}2)_3$ in PBS was assessed and confirmed previous observations (Figure 3.23). The Cu(II) complex seems not to undergo dechelation and change in metal speciation after 6 h, while in the Gd(III) analogue show progressive $1/T_1$ and $1/T_2$ reduction as a consequence of Gd(III)-phosphate complexation and precipitation.

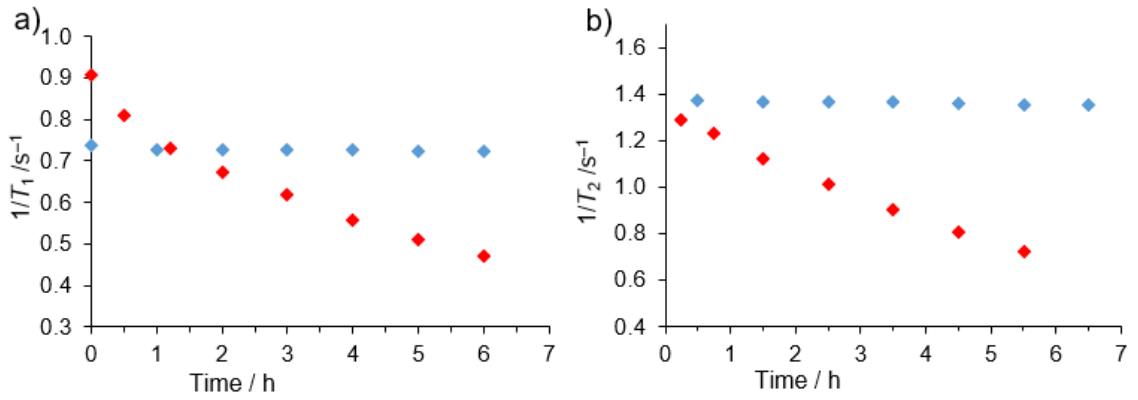


Figure 3.23: Plots of ^{1}H-NMR a) $1/T_1$ and b) $1/T_2$ relaxation rates for a solution of either 40 μM $CuCl_2$ (blue diamonds ♦) or 40 μM $GdCl_3$ (red diamonds ♦) in the presence of 5 equivalents of MB1-2 trimer in PBS buffer pH 7.4, as a function of time. Samples recorded at 293-294 K on a 60 MHz NMR spectrometer.

The presence of MB1-2 apo peptide in a solution of human serum in PBS, was found to predominantly shorten T_2 relaxation time (Figure 3.24). The presence of PBS buffer instead of HEPES had no impact on $CuCl_2$ relaxation rates, as also shown earlier (Figure 3.25). When $CuCl_2$ was added to a solution of human serum in PBS, a reduction in both T_1 and T_2 relaxation times was found, reflecting that Cu(II) undergoes partial complexation by serum proteins which possess K_d dissociation constants in pM-fM range.[17] As previously shown, $Cu(MB1\text{-}2)_3$ is quite stable in PBS solution, so no copper phosphate is proposed to form in solution under these conditions. However, when the metallopeptide was prepared and then added to serum, both relaxation times were found to be longer. This can be explained with a stronger affinity of Cu(II) to serum proteins (for human serum albumin apparent $\log K_a = 13.02 \pm 0.05$ at pH 7.4)[18] than to MB1-2 trimer. This result further underlines the need for metal affinity improvement to allow Cu(II) to bind preferentially to the peptide rather than to serum proteins.

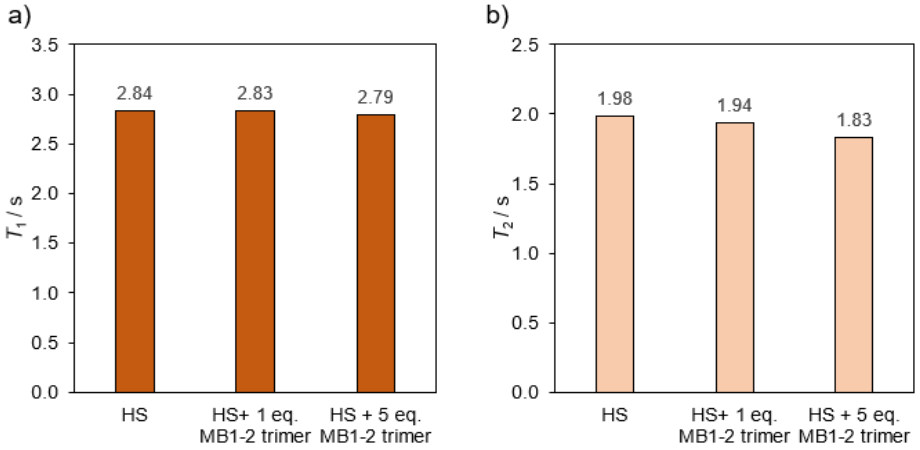


Figure 3.24: Diagram showing ^{1}H-NMR a) T_1 and b) T_2 relaxation times for solutions of 10% Human Serum (HS) in PBS buffer pH 7.4 in the absence or in the presence of 1 or 5 equivalents of MB1-2 trimer (relative to 40 μM $CuCl_2$, leading to concentrations of 120 and 600 μM peptide monomer, respectively). Samples recorded at 293-294 K on a 60 MHz NMR spectrometer.

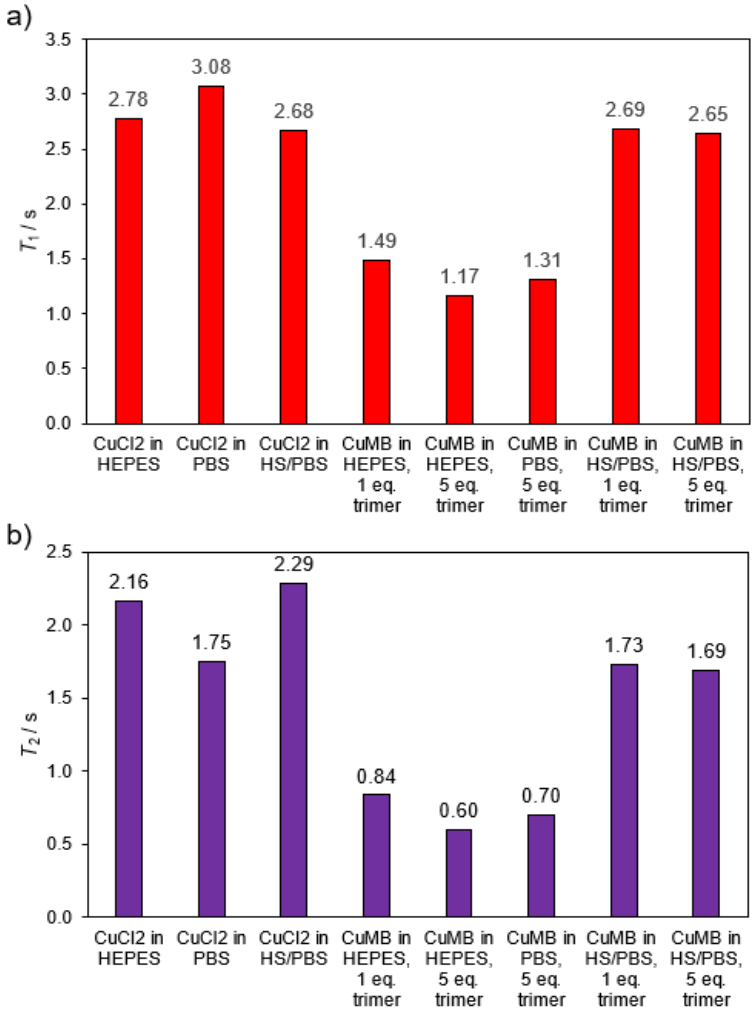


Figure 3.25: Diagram showing ^{1}H-NMR a) T_1 and b) T_2 relaxation times for solutions of 40 μM $CuCl_2$ in 100 mM HEPES buffer pH 7.0, PBS buffer pH 7.4 and 10% human serum (HS) in PBS buffer pH 7.4 in the absence or in the presence of 1 or 5 equivalents of MB1-2 trimer. Samples recorded at 293-294 K on a 60 MHz NMR spectrometer.

As shown earlier, $GdCl_3$ is more prone to phosphate complexation, as demonstrated by the longer relaxation times of $GdCl_3$ in PBS than in HEPES buffer (Figure 3.26). The presence of human serum in a $GdCl_3$ solution resulted in shortening relaxation times, as consequence of high Gd(III) affinity to serum proteins such as albumin.[4] Relaxation times of $Gd(MB1\text{-}2)_3$ in PBS or in human serum/PBS, were found to be comparable to both $GdCl_3$ in human serum and $Gd(MB1\text{-}2)_3$ in PBS, leading to difficult interpretation of data. Gd(III) could be bound MB1-2 or to serum proteins or both. Relaxivity measurements at 1.4 T (Figure 3.27a,d and Table 3.5) were still not informative, as relaxivities were still comparable.

Since relaxivity of $GdCl_3$ is more significantly different than that of $Gd(MB1\text{-}2)_3$ at higher fields (Table 3.4), the same experiment was conducted at 7 T (Figure 3.27b,d and Table 3.5). Lower relaxivity was determined for $GdCl_3$ in serum than for $GdCl_3$ in HEPES. This decrease in relaxivity suggests the metal binds preferentially to serum proteins, where the number of inner-sphere water molecules is much lower than 6 (as in Gd aquo-complex). r_1 relaxivity for $Gd(MB1\text{-}2)_3$ in serum was measured to be intermediate between $Gd(MB1\text{-}2)_3$ in HEPES and $GdCl_3$ in human serum, confirming a possible competition between serum proteins and the peptide. r_2 relaxivity is more difficult to decipher. In serum, it is higher for the $Gd(MB1\text{-}2)_3$ than for $GdCl_3$, more than what one could expect from the presence of free peptide. Therefore, some interactions may occur between Gd(III) and the proteins as well as some retention of the metal on the peptide. Ternary compounds (serum protein-peptide-metal) could also be present, forming larger macro-molecular adducts that lead to high relaxivity at 1.4 T.

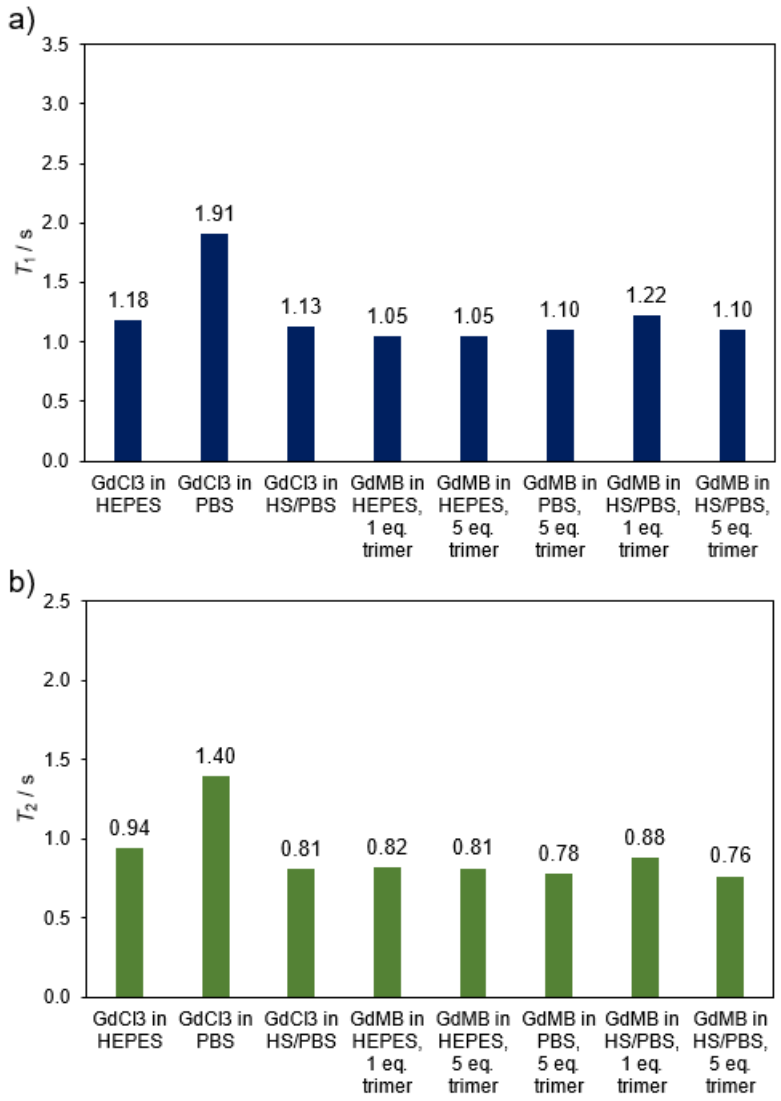


Figure 3.26: Diagram showing ^{1}H-NMR a) T_1 and b) T_2 relaxation times for solutions of 40 μM $GdCl_3$ in 100 mM HEPES buffer pH 7.0, PBS buffer pH 7.4 and 10% human serum (HS) in PBS buffer pH 7.4 in the absence or in the presence of 1 or 5 equivalents of MB1-2 trimer. Samples recorded at 293-294 K on a 60 MHz NMR spectrometer.

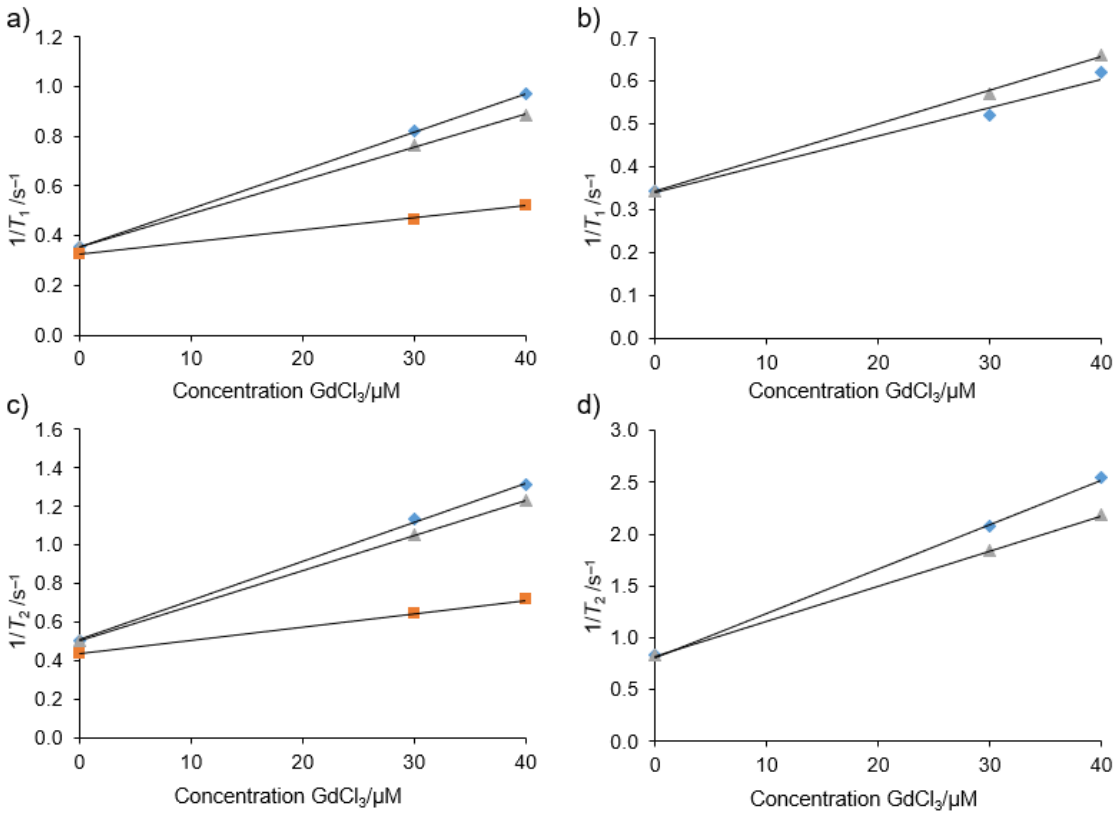


Figure 3.27: a), b) T_1 and c), d) T_2 ^{1}H-MRI relaxivity plots, showing the reciprocal of ^{1}H-NMR relaxation times for $GdCl_3$ (grey triangles ▲) and $Gd(MB1\text{-}2)_3$. (blue diamonds ♦) in 10% human serum in PBS buffer pH 7.4, $GdCl_3$ in PBS buffer pH 7.4 (orange squares ■). Samples prepared in the presence of 5 equivalents MB1-2 peptide trimer. Samples recorded on a a), c) 60 MHz or b), d) 300 MHz spectrometer at 293-294 K. Error bars determined from standard deviation error of three independent repeat experiments.

Table 3.5: ^{1}H-MRI relaxivity values for $Gd(MB1\text{-}2)_3$ and $GdCl_3$ in 100 mM HEPES pH 7.0, PBS pH 7.4 buffer, 10% human serum in PBS buffer pH 7.4 at 1.4 or 7 T. Values for $Gd(MB1\text{-}2)_3$ in PBS obtained by fitting only samples with 0-30 μM $GdCl_3$.

		1.4 T		7 T	
Peptide	Buffer	r_1 / mM^{-1}s^{-1}	r_2 / mM^{-1}s^{-1}	r_1 / mM^{-1}s^{-1}	r_2 / mM^{-1}s^{-1}
$Gd(MB1\text{-}2)_3$	HEPES	15.3 ± 0.6	18.9 ± 0.1	5.4 ± 0.1	19.8 ± 0.5
	PBS	13.9 ± 0.5	21.8 ± 1.5	-	-
	HS/PBS	15.5	20.3	6.6	42.7
$GdCl_3$	HEPES	12.3	14.6	13.0	19.4
	PBS	4.9	7.0	-	-
	HS/PBS	13.4	18.3	7.8	33.9

Relaxation times of $CuCl_2$ and $Cu(MB1\text{-}2)_3$ in PBS in the absence or presence of human serum were found to be comparable after 2 hours suggesting that the species are stable (Figure

3.28a and Figure 3.28b). On the other hand, after 2 hours, Gd(III) systems showed longer relaxation times (Figure 3.28c and Figure 3.28d)., especially in the presence of no excess of peptide trimer (in samples with 1 equivalent of peptide trimer). This suggests that precipitation occurs for the metal salt and for the metallo-complex in PBS and dechelation/precipitation lead to longer relaxation times of solutions of $Gd(MB1\text{-}2)_3$ in human serum.

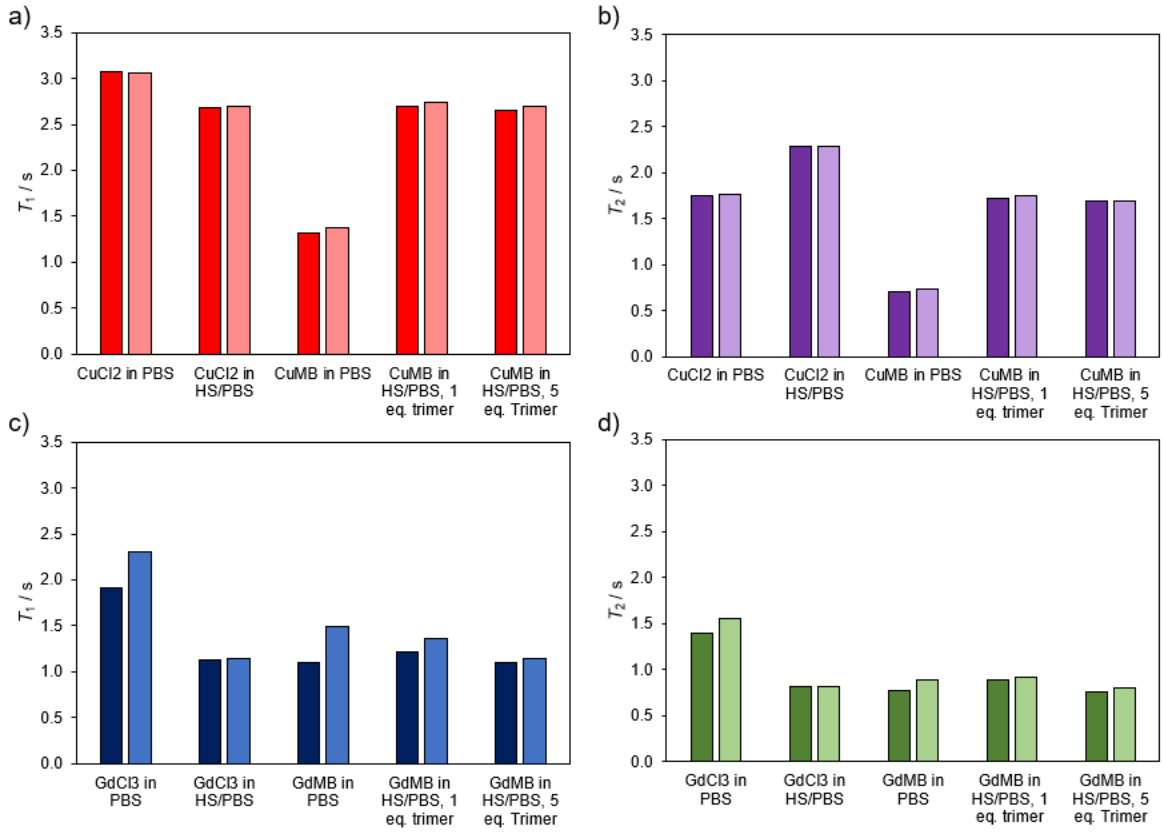


Figure 3.28: Diagram showing ^{1}H-NMR a),c) T_1 and b),d) T_2 relaxation times for solutions of a), b) $CuCl_2$ c), d) $GdCl_3$ in 100 mM HEPES buffer pH 7.0, PBS buffer pH 7.4 and 10% human serum (HS) in PBS buffer pH 7.4 in the absence or in the presence of 1 or 5 equivalents of MB1-2 trimer. Samples recorded after sample preparation (dark colour) and after 2 hours (light colour) at 293-294 K on a 60 MHz NMR spectrometer.

3.4 Discussion

In this chapter, a new Cu(II) coiled-coil was investigated in terms of metal binding and efficiency as MRI contrast agent. It was shown that Cu(II) binds to a designed peptide, forming a folded trimeric structure. The metal binding is unusual for Cu(II) binding, since it is constituted exclusively by oxygen donors.[28] In a trimer, three Asp are hypothesised to be involved in Cu(II) binding at pH 7.0, generating overall –1 charge. Copper coordination is completed with water molecules and possibly with carboxylic oxygen of Asn.[28] The novelty of this type of coordination

is the presence of exclusively oxygen donors,[28] whereas Cu(II) binding in biology is dominated by nitrogen or sulphur donors, or mixtures, sometimes with oxygen donors. The presence of two water molecules bound to Cu(II) is one of the main reasons for the high relaxivity of this compound, compared with the saturated Gd(III) analogue, where only second-sphere and outer-sphere water molecules contributes to relaxivity. However, the presence of an unsaturated and relatively unstructured Cu(II) binding site, leads to a weaker interaction between Cu(II) and the peptide compared to the Gd(III) analogue. This is also reflected on Zn(II) binding competition studies, where the Cu(II) complex is more prone to transmetallation than the Gd(III) analogue. On the other hand, studies in PBS showed that in these systems, Gd(III) phosphate precipitation is more likely to occur than with Cu(II). Relaxation measurements in human serum, have further highlighted the need of improving the binding constants.

3.5 Conclusions

This study demonstrates for the first time that the presence of a single unpaired electron on Cu(II) is not a limiting factor within the development of copper-based contrast agents. High relaxivities can be achieved especially at clinically relevant magnetic fields (such as 1.4 T), by optimising molecular parameters such as hydration state and molecular tumbling. This means that under optimised conditions, the use Cu(II) in MRI contrast agents offers a valuable alternative to the use of Gd(III).

Future work should focus on enhancing Cu(II) affinity for instance by pre-organising the binding site to reduce the free energy associated with Cu(II) binding. This could be achieved by covalently liking the peptide monomers using helical bundles or cross-linked strands. Moreover, variable temperature ^{17}O-NMR studies should be conducted to experimentally confirm the predicted water residence time for Cu(MB1-2)$_3$, hoping to gain insight into the water exchange mechanism.

References

1. A. S. Merbach, L. Helm and É. Tóth, *The chemistry of contrast agents in medical magnetic resonance imaging*, John Wiley & Sons, 2013.
2. D. Gaynor and D. M. Griffith, *Dalton Trans.*, 2012, **41**, 13239-13257.
3. J. Wahsner, E. M. Gale, A. Rodríguez-Rodríguez and P. Caravan, *Chem. Rev.*, 2018, **119**, 957-1057.
4. P. Caravan, J. J. Ellison, T. J. McMurry and R. B. Lauffer, *Chem. Rev.*, 1999, **99**, 2293-2352.
5. S. Aime and P. Caravan, *J. Magn. Reson. Imaging*, 2009, **30**, 1259-1267.
6. J. Ramalho, R. Semelka, M. Ramalho, R. Nunes, M. AlObaidy and M. Castillo, *Am. J. Neuroradiol.*, 2016, **37**, 1192-1198.
7. D. R. Roberts, S. M. Lindhorst, C. T. Welsh, K. R. Maravilla, M. N. Herring, K. A. Braun, B. H. Thiers and W. C. Davis, *Invest. Radiol.*, 2016, **51**, 280-289.
8. N. Murata, L. F. Gonzalez-Cuyar, K. Murata, C. Fligner, R. Dills, D. Hippe and K. R. Maravilla, *Invest. Radiol.*, 2016, **51**, 447-453.
9. N. Karabulut, *Diagn. Interv. Radiol.*, 2015, **21**, 269.
10. G. Bourne and J. Trifaró, *Neuroscience*, 1982, **7**, 1615-1622.
11. L. M. Gaetke and C. K. Chow, *Toxicology*, 2003, **189**, 147-163.
12. A. Pasquarello, I. Petri, P. S. Salmon, O. Parisel, R. Car, É. Tóth, D. H. Powell, H. E. Fischer, L. Helm and A. E. Merbach, *Science*, 2001, **291**, 856-859.
13. D. H. Powell, P. Furrer, P.-A. Pittet and A. E. Merbach, *J. Phys. Chem.*, 1995, **99**, 16622-16629.
14. D. H. Powell, L. Helm and A. E. Merbach, *J. Chem. Phys.*, 1991, **95**, 9258-9265.
15. I. Bertini, C. Luchinat, R. D. Brown III and S. H. Koenig, *J. Am. Chem. Soc.*, 1989, **111**, 3532-3536.
16. I. Bertini and R. Pierattelli, *Pure Appl. Chem.*, 2004, **76**, 321-333.
17. T. Kirsipuu, A. Zadorožnaja, J. Smirnova, M. Friedemann, T. Plitz, V. Tõugu and P. Palumaa, *Sci. Rep.*, 2020, **10**, 1-11.
18. K. Bossak- Ahmad, T. Frączyk, W. Bal and S. C. Drew, *ChemBioChem*, 2020, **21**, 331-334.
19. M. Z. Köylü, S. Asubay and A. Yilmaz, *Molecules*, 2009, **14**, 1537-1545.
20. M. R. Berwick, D. J. Lewis, A. W. Jones, R. A. Parslow, T. R. Dafforn, H. J. Cooper, J. Wilkie, Z. Pikramenou, M. M. Britton and A. F. Peacock, *J. Am. Chem. Soc.*, 2014, **136**, 1166-1169.
21. M. R. Berwick, L. N. Slope, C. F. Smith, S. M. King, S. L. Newton, R. B. Gillis, G. G. Adams, A. J. Rowe, S. E. Harding and M. M. Britton, *Chem. Sci.*, 2016, **7**, 2207-2216.
22. W. Chan and P. White, *Fmoc solid phase peptide synthesis: a practical approach*, OUP Oxford, 1999.
23. J. K. Myers, C. N. Pace and J. M. Scholtz, *PNAS*, 1997, **94**, 2833-2837.

24. L. N. Slope, O. J. Daubney, H. Campbell, S. A. White and A. F. Peacock, *Angew. Chem.*, 2021, **133**, 24678-24682.
25. P. Kuzmic, *Anal. Bioch.*, 1996, **237**, 260-273.
26. E. Prenesti, P. G. Daniele, M. Prencipe and G. Ostacoli, *Polyhedron*, 1999, **18**, 3233-3241.
27. E. Prenesti, P. G. Daniele, S. Berto and S. Toso, *Polyhedron*, 2006, **25**, 2815-2823.
28. A. Shah, M. J. Taylor, G. Molinaro, S. Anbu, M. Verdu, L. Jennings, I. Mikulska, S. Diaz-Moreno, H. El Mkami and G. M. Smith, *PNAS*, 2023, **120**, e2219036120.
29. M. Tegoni, F. Yu, M. Bersellini, J. E. Penner-Hahn and V. L. Pecoraro, *PNAS*, 2012, **109**, 21234-21239.
30. F. Yu, J. E. Penner-Hahn and V. L. Pecoraro, *J. Am. Chem. Soc.*, 2013, **135**, 18096-18107.
31. T. Tanaka, T. Mizuno, S. Fukui, H. Hiroaki, J.-i. Oku, K. Kanaori, K. Tajima and M. Shirakawa, *J. Am. Chem. Soc.*, 2004, **126**, 14023-14028.
32. M. R. Berwick, University of Birmingham, 2016.
33. D. Titrations and B. Müller.
34. K. L. Zapadka, F. J. Becher, A. Gomes dos Santos and S. E. Jackson, *Interface focus*, 2017, **7**, 20170030.
35. S. A. Cotton, *Encyclopedia of Inorganic and Bioinorganic Chemistry*, 2011.
36. J. Oakes and E. G. Smith, *J. Chem. Soc., Faraday Transactions 1*, 1983, **79**, 543-552.
37. J. Oakes and C. G. van Kralingen, *J. Chem. Soc., Dalton Trans.*, 1984, 1133-1137.
38. M. L. Blackwell, C. T. Farrar, B. Fischl and B. R. Rosen, *NeuroImage*, 2009, **46**, 382-393.
39. R. B. Lauffer, *Chem. Rev.*, 1987, **87**, 901-927.
40. A. Nolle and L. Morgan, *J. Chem. Phys.*, 1957, **26**, 642-648.
41. L. Morgan, J. Murphy and P. Cox, *J. Am. Chem. Soc.*, 1959, **81**, 5043-5047.
42. N. Bloembergen and L. Morgan, *J. Chem. Phys.*, 1961, **34**, 842-850.
43. S. L. Newton, University of Birmingham, 2018.
44. I. Bertini, F. Briganti, S. Koenig and C. Luchinat, *Biochemistry*, 1985, **24**, 6287-6290.
45. I. Bertini, F. Briganti, C. Luchinat, M. Mancini and G. Spina, *J. Magn. Reson. (1969)*, 1985, **63**, 41-55.
46. I. Bertini, C. Luchinat, M. S. Viezzoli, L. Banci, S. H. Koenig, H. T. Leung and J. E. Coleman, *Inorg. Chem.*, 1989, **28**, 352-358.
47. C. M. Ferreira, I. S. Pinto, E. V. Soares and H. M. Soares, *RSC Adv.*, 2015, **5**, 30989-31003.
48. M. Sokołowska and W. Bal, *J. Inorg. Biochem.*, 2005, **99**, 1653-1660.
49. K. Hegetschweiler and P. Saltman, *Inorg. Chem.*, 1986, **25**, 107-109.
50. S. Aime, S. G. Crich, M. Botta, G. Giovenzana, G. Palmisano and M. Sisti, *Chem. Comm.*, 1999, 1577-1578.
51. S. Aime, D. Delli Castelli and E. Terreno, *Angew. Chem. Int. Ed.*, 2002, **41**, 4334-4336.

52. C. Charpentier, J. Salaam, A. Nonat, F. Carniato, O. Jeannin, I. Brandariz, D. Esteban-Gomez, C. Platas- Iglesias, L. J. Charbonnière and M. Botta, *Chem. Eur. J.*, 2020, **26**, 5407-5418.

53. J. Wahsner, E. M. Gale, A. Rodriguez-Rodriguez and P. Caravan, *Chem. Rev.*, 2019, **119**, 957-1057.

54. K. Dutta, A. Alexandrov, H. Huang and S. M. Pascal, *Protein Sci.*, 2001, **10**, 2531-2540.

55. A. D. Sherry, P. Caravan and R. E. Lenkinski, *J. Magn. Reson. Imaging*, 2009, **30**, 1240-1248.

56. V. C. Pierre and M. J. Allen, Eds., *Contrast agents for MRI: experimental methods*, Royal Society of Chemistry, 2017.

CHAPTER 4

TRANSLATION OF THE COPPER(II) BINDING SITE

4.1 Introduction

Copper compounds generally show very poor MRI relaxivities, because of Cu(II) single unpaired electron, even though they have fast water exchange kinetics and Cu(II) possesses long electron relaxation times.[1-7] This belief was challenged in Chapter 3 and here is further explored. Aiming to establish the structural origin of their relaxivity and to determine what solvent access is required, the MB1-2 binding site is translated along the coiled-coil.

Berwick and co-workers have shown that translating the binding site along the coil is a strategy to allow more water molecules into Gd(III) inner-sphere coordination, with a corresponding increase in their relaxivities (Table 4.1).[8, 9] More specifically, when the binding site is located at the extremities of the coil, two or three water molecules are found in the Gd(III) inner-sphere. Moreover, Slope and co-workers report that the presence of bulky aromatic second coordination sphere amino acid residues, such as phenylalanine (Phe, F) or tryptophan (Trp, W), prevents water access to the binding site, thus reducing Ln(III) hydration, and in turn the relaxivity.[10]

Table 4.1: Gd(III) hydration state q and ^{1}H-MRI r_1 and r_2 relaxivities at 7 T reported for a series of Gd peptides.[9, 10]

	q	r_1 / $mM^{-1}\,s^{-1}$	r_2 / $mM^{-1}\,s^{-1}$	Ref.
MB1-1	3.1 ± 0.2	10.0 ± 1.5	89.3 ± 16.8	9
MB1-2	0.0 ± 0.1	4.2 ± 1.2	21.3 ± 2.6	9
MB1-3	0.0 ± 0.1	4.0 ± 1.0	20.9 ± 1.0	9
MB1-4	1.8 ± 0.4	7.5 ± 4.1	37.9 ± 4.0	9
MB1-1 2F	2.1 ± 0.2	nd	nd	10
MB1-1 2W	0.2 ± 0.1	3.9 ± 0.4	24.2 ± 2.4	10
MB1-4 37W	0.1 ± 0.2	nd	nd	10

In this chapter, the impact on Cu(II) coordination properties and MRI relaxivities of binding site location and of mutation of Cu(II) second sphere residues is explored. The aim is to determine if the relaxivity of the resulting Cu(II) complex can be tuned as consequence, for instance, of variation of Cu(II) hydration state.

CD spectroscopy is used to assess peptide folding of a series of peptides upon Cu(II) complexation. In addition, quenching of tryptophan emission, as consequence of Cu(II) binding, is determined to assess Cu(II) binding, especially in the case of peptides which are already well-structured in their apo form. Affinity constants are determined by fitting CD and fluorescence data. The electronic *d-d* transitions of Cu(II) ion are monitored using UV-Vis spectroscopy to gain insights into Cu(II) coordination. As introduced in Section 2.4, oxygen donors in amino acid residues shift maximum absorbance to longer wavelength, while nitrogen donors move the peak to shorter wavelengths. This is because the energy splitting determined by the presence of oxygen donors (weaker ligands) is smaller than that of nitrogen donors (stronger ligands). Finally, MRI relaxivities are measured and simulations are undertaken to predict Cu-water proton distances r_{Cu-H} and water residence times τ_m.

4.2 Experimental

Materials, peptide synthesis and purification as in Chapter 3.

4.2.1 UV-Visible spectroscopy

UV-Vis experiments, to determine peptide concentration, were recorded on a Cary 50 UV Spectrophotometer, recorded in single beam mode with a medium scan speed, slit width 1.0 nm, data interval of 1.0 nm and scan range 800-200 nm using a 1 cm pathway quartz cuvette.

The concentrations of freshly prepared peptide stock solutions (obtained by dissolving pure peptide in MQ water) were measured using the absorption of tryptophan at 280 nm (ε = 5690 L mol^{-1} cm^{-1}). A blank aqueous solution of 7 M urea was recorded, and solutions prepared by adding 10 µl of freshly prepared peptide stock solution to 690 µl 7 M urea. The peptide stock solution was then diluted to the desired concentration in a 10 mM HEPES pH 7.0. The concentration of the peptide solution was calculated again by UV-Vis avoiding the dilution in 7 M urea. All measurements were performed in triplicate.

Cu(II) electronic *d-d* transition were monitored on a Cary 5000 UV Spectrophotometer, recorded in single beam mode with a medium scan speed, slit width 1.0 nm, data interval of 1.0 nm and scan range 850-200 nm using a 1 cm pathway quartz cuvette.

4.2.2 Circular Dichroism (CD) spectroscopy

CD spectra were recorded on a Jasco J-715 Spectropolarimeter. The optical chamber was purged with nitrogen and kept under a nitrogen atmosphere throughout the duration of the experiments. A 1 mm pathlength, 300 µl quartz cuvette was used with three scans recorded from 400-200 nm using a 100-200 nm min^{-1} scan rate with 1 nm bandwidth and a 1 s response.

A pH 7.0 HEPES buffer solution was recorded as a blank before $CuCl_2$ was titrated into a solution of peptide monomer with concentration previously determined by UV-Vis analysis. All solutions were left to equilibrate for 15 mins before scanning. The ellipticity (θ_{obs}) data collected in millidegrees (mdeg). The molar ellipticity was calculated through Equation 1.

$$[\theta] = \frac{\theta_{\text{obs}}}{10\ lcN} \tag{1}$$

where θ_{obs} is the measured ellipticity at 222 nm in mdeg, c is the concentration in M, N is the number if amino acids in the sequence and l is the pathlength in cm, was used to convert ellipticity at 222 nm (mdeg) to molar ellipticity per residue, $[\theta]$ (deg $dmol^{-1}$ cm^2).

The helical content was then calculated as the percentage folded using Equation 2, where the denominator represents the molar ellipticity for a fully folded coiled-coil.[11]

$$\%\ \text{Folded} = \frac{[\theta_{222}] - 640}{\left(-42500 \times \left(1 - {}^{3}/_{N}\right)\right) - 640} \tag{2}$$

4.2.3 Emission spectroscopy

Emission spectra were recorded using a 1 cm pathlength quartz cuvette on a Jasco FP-8500 fluorescence spectrometer. Aliquots of a 1 mM stock solution of $CuCl_2$ were titrated into a 30-35 µM solution of peptide monomer in 10 mM HEPES buffer pH 7.0, and the emission profile recorded after 20 mins equilibration. Solutions were excited at 280 nm and the emission was scanned from 300-455 nm (Trp emission peak region) using an excitation slit width of 2.5 nm and bandwidth of 2.5 nm.

4.2.4 Nuclear magnetic resonance

^{1}H-NMR measurements, at high magnetic field (7 T), were performed on a Bruker Avance III HD spectrometer, operating at proton resonance frequency of 300.13 MHz. All measurements were performed at 20 ± 0.2°C. Data were acquired using 5 mm ^{1}H coil in a Bruker Diff30 probe. A 90° pulse duration calibrated for each sample was used for the experiments. For T_1 NMR relaxation measurements, a Saturation Recovery sequence (described in Section 2.7.3) was used. A series of 8 spectra were collected with logarithmically spaced recovery delays from 0.01 s to a maximum of 12-15 s, with 8 signal averages, 8k data points and spectral width of 10 kHz. For T_2 NMR relaxation measurements the Carr-Purcell-Meiboom-Gill (CPMG) pulse sequence (described in Section 2.7.3) was used with a repetition time > $5T_1$ (≥ 10 s), 8 signal averages, 16k data points and spectral width of 10 kHz. The variable counter list for the CPMG experiments consisted of 10 values logarithmically spaced from 2 to 1024, with a CPMG echo time value of 2 ms.

^{1}H-NMR measurements at low magnetic fields (1.4 T) were performed on a Spinsolve benchtop NMR (Magritek, Aachen, Germany), operating at proton resonance frequency of 61 MHz. Data were acquired at 21.0 ± 0.5°C (controlled room temperature) using 3 mm NMR tubes and a automated 90° pulse width of 7 μs. For T_1 NMR relaxation measurements, an Inversion Recovery sequence (described in Section 2.7.3) was used with a repetition time > $5T_1$ (≥ 10 s). A series of 11 spectra were collected with delays linearly spaced from 0.001 s to a maximum of 5-10 s, 8 signal averages and 32k points. For T_2 NMR relaxation measurements a CPMG pulse sequence was used with a repetition time > $5T_1$ (≥ 10 s). A series of 10 spectra were recorded with a 2 ms CPMG echo time and final echo time of 5 s, 8 signal averages and 32k data points. All data were analysed using Prospa (Magritek, Aachen, Germany). Signal intensity curves were fitted in KaleidaGraph (Synergy, USA).

Binding of Cu(II) by peptide trimers was monitored by measuring the ^{1}H T_1 and T_2 magnetic resonance relaxation times of solutions of 40 μM $CuCl_2$ in the presence of increasing concentrations of peptide monomer, in 100 mM HEPES buffer pH 7.0. The r_1 and r_2 relaxivities were calculated from the gradients of plots of the average, based on three independent repeats, ^{1}H magnetic resonance relaxation rates ($1/T_1$ and $1/T_2$ respectively), as a function of $CuCl_2$ concentration. A range of solutions were measured, containing 0, 10, 20, 30, 40 μM $CuCl_2$ and 15 equivalents of peptide monomer (5 equivalents peptide trimer), to drive Cu(II) complexation. Analogous control experiments were performed for solutions of peptide in the absence of $CuCl_2$. The r_2 relaxivity of the apo peptide was used to correct $1/T_2$ and relative r_2 for the Cu(II) complexes, by accounting for the contribution of excess unbound peptide.

4.2.5 Relaxivity simulations

MATLAB R2021b software was used to simulate inner-sphere r_1 relaxivity as function of water residence time τ_m and distance r_{MH} using Equations 3-5.

$$r_1^{IS} = \frac{q/[H_2O]}{T_{1M} + \tau_M} \tag{3}$$

$$\frac{1}{T_{1M}} = \frac{2}{15}\left(\frac{\mu_0}{4\pi}\right)^2 \frac{\hbar^2 \gamma_S^2 \gamma_H^2}{r_{MH}^6} S(S+1)\left(\frac{3\tau_c}{1 + \omega_H^2 \tau_c^2}\right) \tag{4}$$

$$\frac{1}{\tau_c} = \frac{1}{\tau_m} + \frac{1}{\tau_R} + \frac{1}{\tau_s} \tag{5}$$

where S is the spin quantum number, r_{MH} is the ion-proton distance, ω_H is the Larmor frequency of the proton, γ_H is the proton gyromagnetic ratio, g_e is the electronic g-factor ($g_e = 2$), μ_B is the Bohr magneton and μ_0 is the permittivity of vacuum. Static magnetic field B_0 was set to 1.4 T and 7 T and rotational correlation time τ_R to 6.9 ns.

4.3 Results

4.3.1 Peptide design

To determine the impact on MRI relaxivities of the accessibility of the Cu(II) binding site to water, and, therefore, Cu(II) hydration states (Figure 4.1), the MB1-2 binding site was translated along the coil to the N-terminus (MB1-1) and to the C-terminus (MB1-4) (Figure 4.2 and Table 4.2). Moreover, for the binding site located at the N-terminus MB1-1, the effect of second coordination sphere mutation (MB1-1 2F and MB1-1 2W) on MRI relaxivities was explored (Figure 4.3 and Table 4.2).

Table 4.2: Sequences of peptides used in this chapter. Residues designed for Cu(II) binding underlined and coloured red (Asp) and in blue (Asn).

MB1-2	Ac-G IAAIEQK IAANEWK DAAIEQK IAAIEQK IAAIEQK G-NH_2
MB1-1	Ac-G IAANEWK DAAIEQK IAAIEQK IAAIEQK IAAIEQK G-NH_2
MB1-4	Ac-G IAAIEQK IAAIEQK IAAIEQK IAANEWK DAAIEQK G-NH_2
MB1-1 2F	Ac-G FAANEWK DAAIEQK IAAIEQK IAAIEQK IAAIEQK G-NH_2
MB1-1 2W	Ac-G WAANEQK DAAIEQK IAAIEQK IAAIEQK IAAIEQK G-NH_2

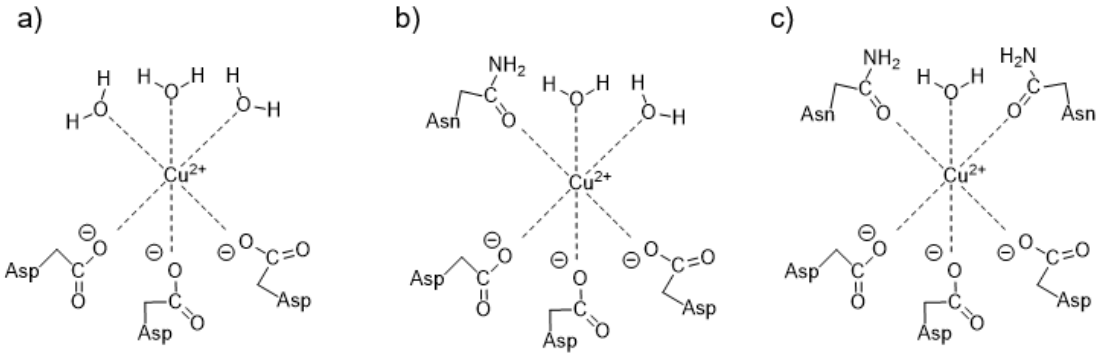


Figure 4.1: Potential Cu(II) binding sites in a) $q = 3$ and b) $q = 2$, as $Cu(MB1\text{-}2)_3$ and c) $q = 1$ octahedral complexes.

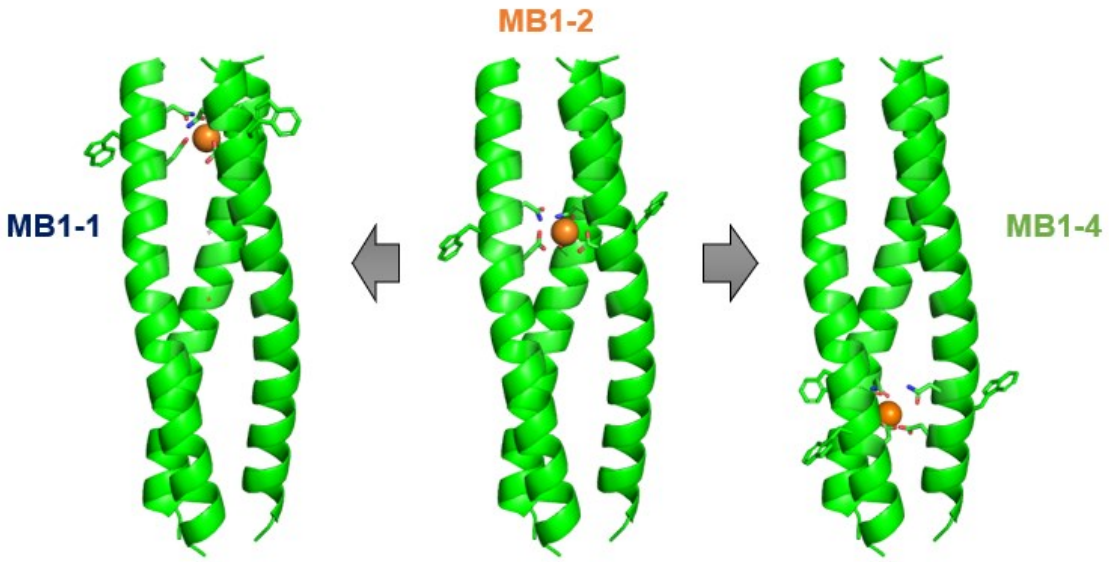


Figure 4.2: Cartoon representing translation of the MB1-2 binding site towards the N-terminus (MB1-1) and the C-terminus (MB1-4). Peptide backbone shown as a helical ribbon and side chains shown as sticks, with oxygen in red and nitrogen in blue. Cu(II) ion shown as orange sphere.

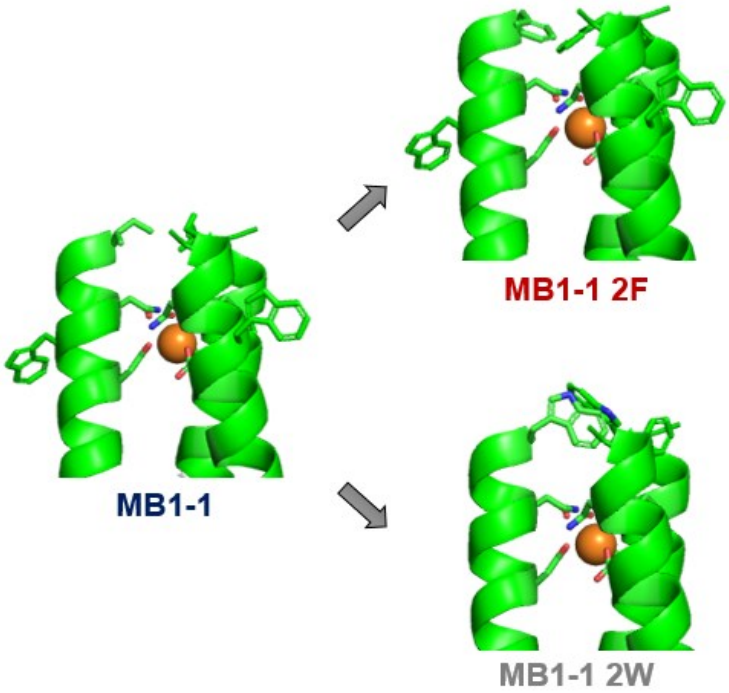


Figure 4.3: Cartoon representing second-sphere mutation of the MB1-1 binding site replacing Ile (MB1-1) to Phe (MB1-1 2F) or to Trp (MB1-1 2W). Peptide backbone shown as a helical ribbon and side chains shown as sticks, with oxygen in red and nitrogen in blue. Cu(II) ion shown as orange sphere.

4.3.2 Copper binding: peptide folding, quenching of Trp fluorescence and log K_a determination

Peptide folding was monitored using CD spectroscopy by performing titrations of $CuCl_2$ in a peptide monomer solution (Figure 4.4, Figure 4.5 and Table 4.3). MB1-1, MB1-4, MB1-1 2F and MB1-1 2W are all well folded in both apo and metallo form because of the presence of adjacent Ile layers within the hydrophobic core. In MB1-4, the folding was found to be 63% compared to 76% in MB1-1, suggesting the presence of a more distorted structure in MB1-4.

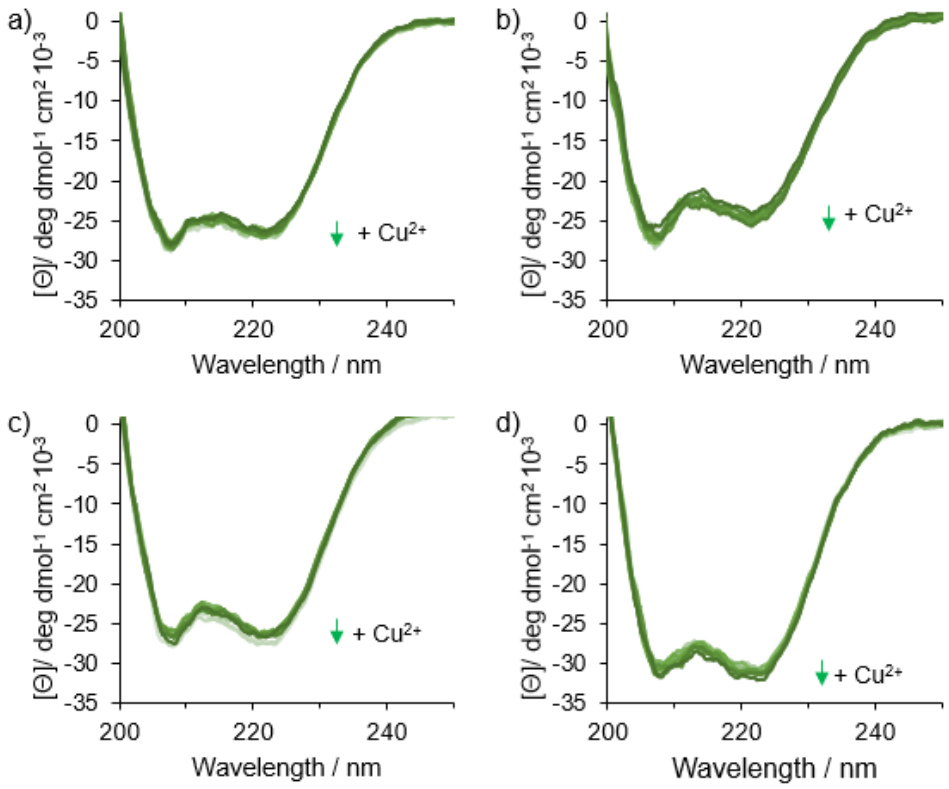


Figure 4.4: Representative CD spectra of $CuCl_2$ titration into 30 µM a) MB1-1, b) MB1-4, c) MB1-1 2F and d) MB1-1 2W peptide monomer in 10 mM HEPES buffer pH 7.0 at 293 K.

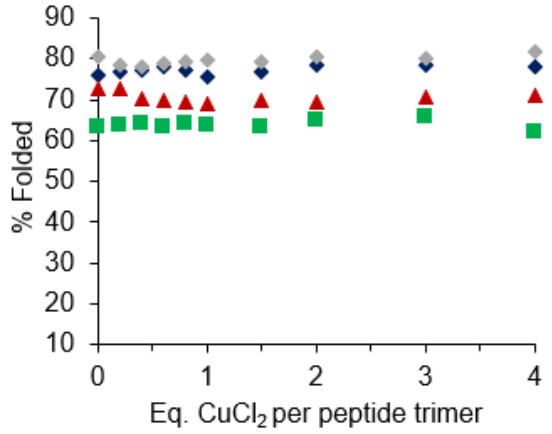


Figure 4.5: CD binding curves showing $CuCl_2$ titration into 30 µM MB1-1 (blue diamonds ♦), MB1-4 (green squares ■), MB1-1 2F (red triangles ▲) and MB1-1 2W (grey diamonds ♦) peptide monomer in 10 mM HEPES buffer pH 7.0.

Quenching of the tryptophan fluorescence emission on addition of $CuCl_2$ was monitored (

Figure **4.6** and Figure 4.7) to determine binding constants, which were calculated to be the same within error as MB1-2 (Table 4.3).

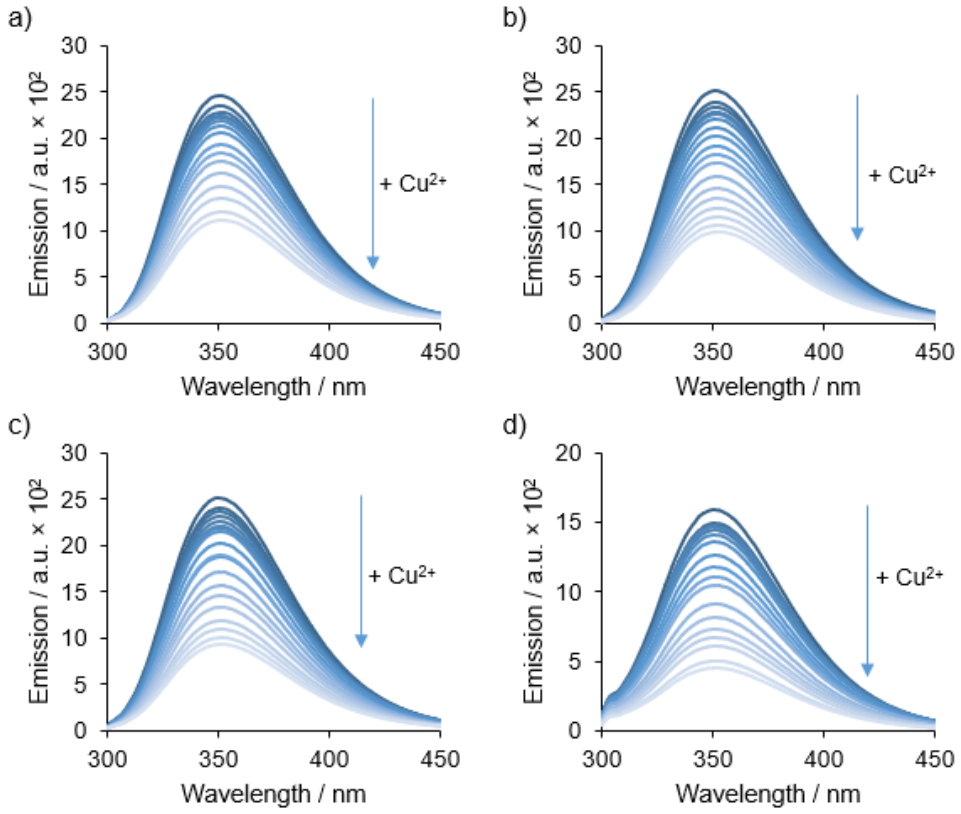


Figure 4.6: Representative tryptophan emission spectra showing titration of $CuCl_2$ into 30 μM a) MB1-1, b) MB1-4, c) MB1-1 2F and d) MB1-1 2W peptide monomer in 10 mM HEPES buffer pH 7.0 at 293 K, λ_{ex} = 280 nm.

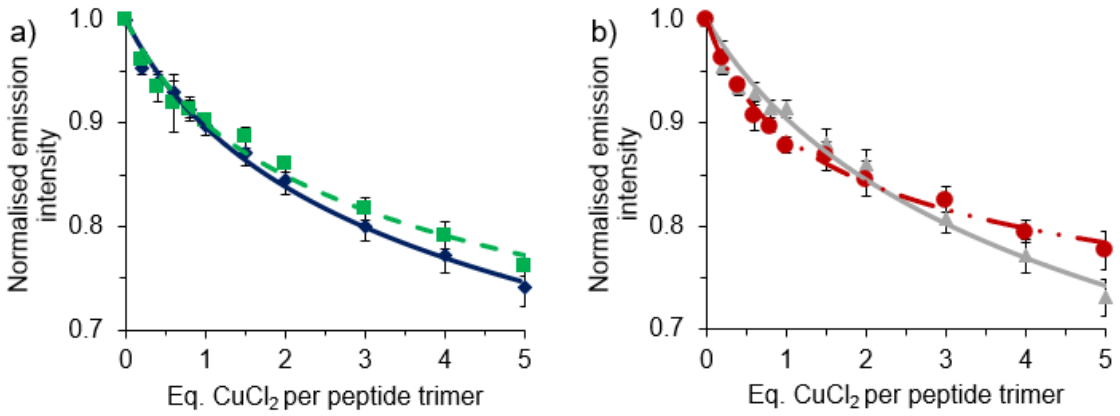


Figure 4.7: Normalised integrated emission following $CuCl_2$ titration into 30 μM a) MB1-1 (blue diamonds ♦, full line) , MB1-4 (green squares ■, dashed line) and b) MB1-1 2W (grey triangles ▲, full line) and MB1-1 2F (red circles ●, dashed-dotted line) peptide monomer in 10 mM HEPES buffer pH 7.0 at 293 K, λ_{ex} = 280 nm, λ_{em} integrated between 300 and 455 nm. Data fitted using DynaFit[12] to a nonlinear least-squares fitting based on 1/3M + L ↔ 1/3ML_3 model. Error bars determined from standard deviation of three independent experiments.

Table 4.3: % folding of the apo peptides compared to the metallo form (end of titration) for 30 μM peptide monomer in 10 mM HEPES buffer pH 7.0, monitored by CD. Values of log K_a determined from fitting CD and fluorescence data in 10 mM HEPES buffer pH 7.0. Data fitted using DynaFit[12] to a nonlinear least-squares fitting based on $1/3M + L \leftrightarrow 1/3ML_3$ model. Error determined from standard deviation of three independent experiments.

	% Folding apo	% Folding metallo	log K_a
MB1-2	18 ± 4% (21 ± 3% from ref. [9])	69 ± 1%	4.9 ± 0.1
MB1-1	76 (77 ± 1% from ref. [9])	78	4.9 ± 0.1
MB1-4	63 (55 ± 6% from ref. [9])	64	4.9 ± 0.1
MB1-1 2F	73 (73 ± 1% from ref. [10])	69	5.1 ± 0.1
MB1-1 2W	80 (82 ± 1% from ref. [10])	80	4.9 ± 0.0

4.3.3 Copper binding: UV-visible spectroscopy of *d-d* transitions

UV-Visible spectroscopy was used to probe electronic *d-d* transitions to investigate the nature of Cu(II) coordination to the peptides (Figure 4.8).[13, 14] Table 4.4 reports the wavelength of maximum absorption (λ_{max}) and extinction coefficient values (ε) of the peak in 550-850 nm range.

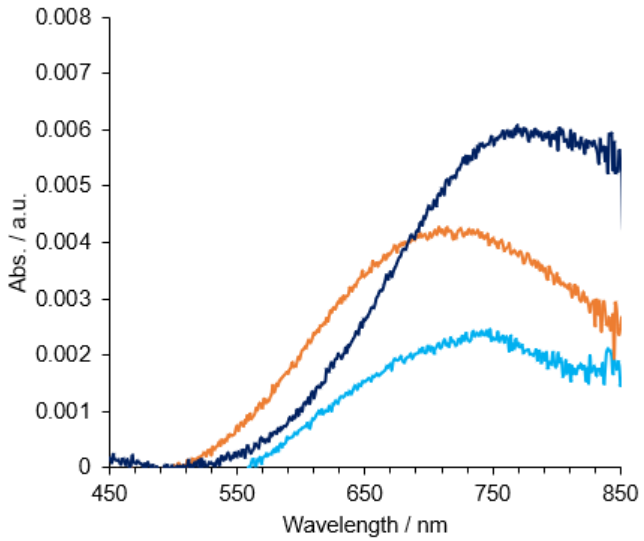


Figure 4.8: UV-Visible spectra of a solution of 150 μM $CuCl_2$ in the absence (light blue) and presence of 450 μM MB1-2 (dark blue) and MB1-1 (orange) monomer, in 100 mM HEPES buffer pH 7.0.

Table 4.4: Wavelength of maximum absorbance (λ_{max}) for Cu(II) *d-d* transitions recorded in the wavelength range 550-850 nm for a solution of 450 µM peptide monomer and 150 µM $CuCl_2$ compared to a solution of 150 µM $CuCl_2$ in 100 mM HEPES buffer pH 7.0.

	λ_{max} / nm	ε / M^{-1} cm^{-1}
$CuCl_2$	745	16
MB1-2	776	40
MB1-1	725	27

$CuCl_2$ solution in buffer was used as control and showed a broad absorption at 745 nm. In the presence of equimolar concentration of peptide trimer, a red shift to 776 nm was reported for MB1-2 (see Chapter 3) and was attributed to H_2O ligands in the aqua complex partially substituted by negatively charged oxygen donors provided by Asp. MB1-1, which was designed to present the same potential Asn and Asp coordination residues, shows a blue shift to 725 nm, suggesting a different coordination compared to MB1-2. Given that the coiled-coil is more flexible at the extremities, it is likely that the structure can become distorted and allow nitrogen in Asn or the NH of the backbone to coordinate Cu(II).

4.3.4 NMR relaxation times at increasing peptide trimer equivalents and in the absence of Cu(II)

T_1 relaxation times were measured for 40 µM $CuCl_2$ in the presence of an increasing number of equivalents of peptide trimer (Figure 4.9). Compared to MB1-2, the absence of a clear trend suggests that, for MB1-1 and MB1-4, Cu(II) binding does not further shorten the T_1 relaxation times of a $CuCl_2$ solution in bulk water at 7 T.

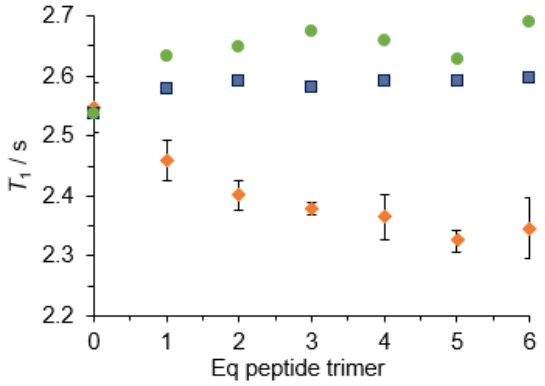


Figure 4.9: Plots of ^{1}H-NMR T_1 relaxation times for solutions of 40 µM $CuCl_2$ in 100 mM HEPES buffer pH 7.0, as a function of increasing equivalents MB1-2 (orange diamonds ♦, data from Chapter 3) MB1-1 (blue squares ■) and MB1-4 (green circles ●) peptide trimer. Samples recorded at 293 K on a 300 MHz NMR spectrometer. Error bars determined from standard deviation of three independent repeat experiments.

T_1 and T_2 relaxation times for apo peptide solutions were recorded at both 1.4 and 7 T and compared to the relaxation times determined for MB1-2 in Chapter 3. As expected[15, 16], the presence of these apo peptides has no significant influence on T_1, while there is some contribution to T_2. (Table 4.5).

Table 4.5: ^{1}H-NMR T_1, T_2 relaxation times, ^{1}H-NMR $1/T_1$,$1/T_2$ relaxation rates and ^{1}H-MRI r_1 and r_2 relaxivities for a series of apo peptides. Samples prepared in 100 mM HEPES buffer pH 7.0 Samples recorded at 293 K on either a 60 (1.4 T) or 300 MHz (7 T) NMR spectrometer. Error determined from standard deviation of three independent repeat experiments.

	1.4 T						7 T	
Apo peptide	T_1 / s	T_2 / s	$1/T_1$ / s^{-1}	$1/T_2$ / s^{-1}	r_1 /mM^{-1} s^{-1}	r_2 /mM^{-1} s^{-1}	r_1 /mM^{-1} s^{-1}	r_2 /mM^{-1} s^{-1}
MB1-1	2.88	2.06	0.35	0.48	n.d.	n.d.	n.d.	n.d.
MB1-2	2.91	2.09	0.34	0.48	0.02 ± 0.01	0.09 ± 0.01	0.00 ± 0.00	0.48 ± 0.01
MB1-4	2.93	2.12	0.34	0.47	n.d.	n.d.	n.d.	n.d.

4.3.5 MRI relaxivities

Copper binding affinity to this series of peptides has been determined in Section 4.3.2 through the log K_a values, with comparable values to MB1-2. Based on calculations performed in Chapter 3, in this range of log K_a, the use of five equivalents of peptide trimer per equivalent of metal in NMR experiments to determine MRI relaxivity was estimated to be sufficient to enable complete Cu(II) binding.

Table 4.6 reports the metallopeptides r_1 and r_2 relaxivities (Figure 4.10 shows the relative relaxivities plots), calculated after $1/T_2$ correction, and the number of water molecules directly coordinated to Cu(II) (q values, measured using EPR spectroscopy by Michael Taylor and Dr. Janet Lovett, St. Andrews University). Since only one measurement was conducted to determine the number of inner-sphere water q for each peptide, these values should be taken with caution.

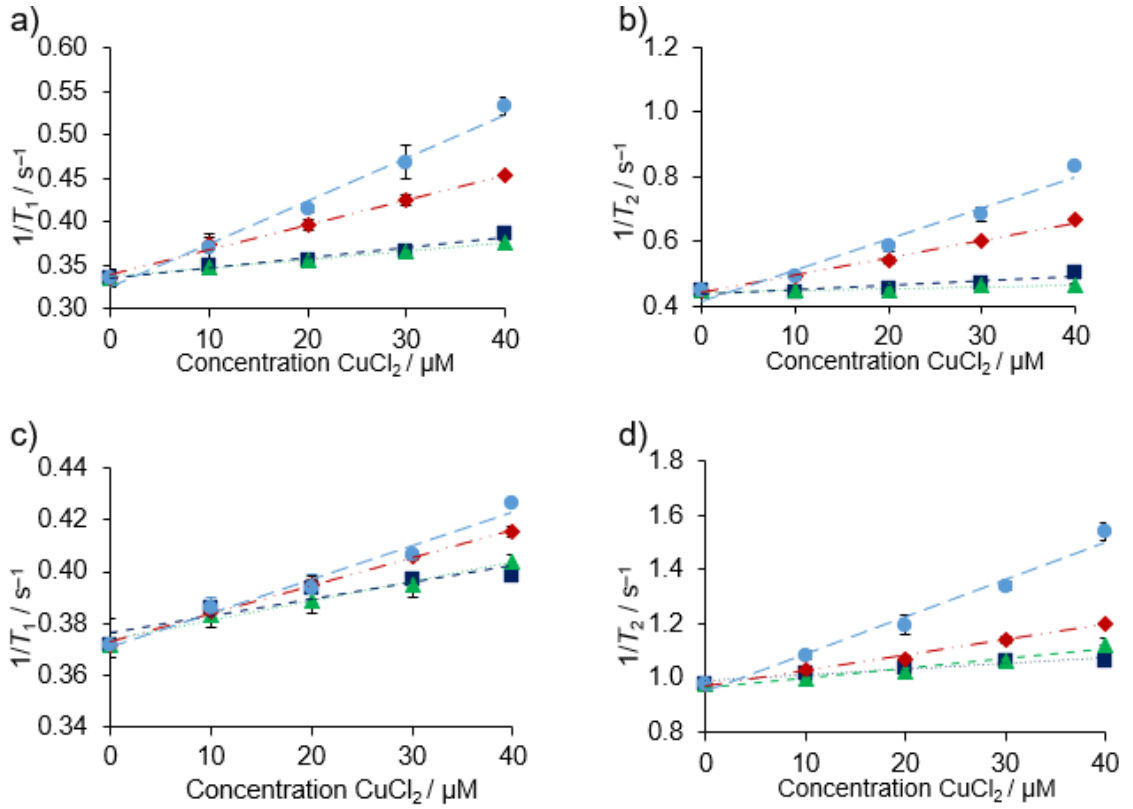


Figure 4.10: ^{1}H-NMR T_1 (a,c) and T_2 (b,d) relaxivity plots, showing reciprocal of relaxation time as a function of $CuCl_2$ concentration for relaxation rates recorded of samples at pH 7.0 in 100 mM HEPES buffer of $CuCl_2$ in the presence of 5 equivalents MB1-1 (dark blue squares ■, short dashed line), MB1-4 (green triangles ▲, dotted line), MB1-1 2F (red diamonds ♦, dashed-dotted-dotted line) and MB1-1 2W (light blue circles ●, long dashed line) trimer. Samples recorded at 293 K either on a 60 MHz, 1.4 T (a,b) and on a 300 MHz, 7 T (c,d) NMR spectrometer. Error bars determined from standard deviation of three independent repeat experiments.

Table 4.6: ^{1}H-MRI r_1 and r_2 relaxivities for the metallopeptides and relative number of inner-sphere water molecules. NMR samples prepared in 100 mM HEPES buffer pH 7.0 Samples recorded at 293 K on either a 60 (1.4 T) or 300 MHz (7 T) NMR spectrometer. Error determined from standard deviation of three independent repeat experiments.

	r_1 / mM^{-1} s^{-1}		r_2 / mM^{-1} s^{-1}		q inner-sphere water
Cu(II) complex of:	1.4 T	7 T	1.4 T	7 T	
MB1-2	13.5 ± 0.5	1.4 ± 0.1	31.7 ± 0.5	18.1 ± 1.3	2
MB1-1	1.2 ± 0.3	0.4 ± 0.2	2.0 ± 0.2	1.6 ± 1.0	1
MB1-4	0.9 ± 0.1	0.7 ± 0.1	0.7 ± 0.1	4.2 ± 1.1	2
MB1-1 2F	2.6 ± 0.2	1.0 ± 0.1	4.8 ± 0.8	5.9 ± 0.3	1 or 2
MB1-1 2W	5.2 ± 0.2	1.3 ± 0.1	11.2 ± 0.7	15.0 ± 0.3	1 or 2

Table 4.6 shows that when the binding site is translated to the extremities of the coil, the relaxivities are reduced. The number of inner-sphere water molecules (q) bound to Cu(II) was measured to be 2 when coordinated to MB1-2 but found to be lower, only 1, when coordinated to MB1-1. This suggests that the translation of the binding site to the N-terminus results in enhanced flexibility and distortions within the binding site, leading to better accommodation of the binding site in the MB1-1 coiled-coil than in the rigid MB1-2 structure. Alternatively, structural flexibility could lead to a local disruption of the peptide structure, leading more donor ligands to be able to bind Cu(II), thereby preventing as much water as in MB1-2 binding. Moreover, the translation may also impact the Cu(II)-water protons distance and the water residence time. When Cu(II) is coordinated to MB1-4, two water molecules were measured to be bound to Cu(II), reflecting a similar binding site as MB1-2 at the N-terminus. The low relaxivities could be explained in terms of water residence times becoming too fast to provide efficient relaxation as a consequence of improved water accessibility to the binding site. This is further explored in Section 4.3.6.

The peptides designed to modulate water access to the binding site (MB1-1 2F and MB1-1 2W), show improved relaxivities compared to MB1-1. This was attributed to the presence of bulky Phe and Trp residues that impose rigidity in the structure, preventing the local unfolding and potential backbone coordination, and allowing more water to coordinate to Cu(II) (1 to 2 water molecules calculated to be coordinated to Cu(II). Moreover, steric hindrance of the aromatic residues could lead to reduced access to the binding site with exchange rates shifting from a fast regime (as MB1-1) to an optimised regime (as MB1-2) and, finally, to shorter Cu-water proton distances. These hypotheses are explored in Section 4.3.6.

4.3.6 Prediction of parameters influencing relaxivity

Simulations were performed to investigate the variance of r_1 relaxivity as function of variable molecular parameters. The main assumption was to consider electron relaxation time to be the same within the MB1 group (MB1-1, MB1-2, MB1-4, MB1-1 2F and MB1-1 2W), being the coordination and electron environment similar within the series. This value was set to be τ_s = 5 ns as estimated for Cu(MB1-2)$_3$ (Chapter 3). As shown in the previous chapter, in Cu(MB1-2)$_3$ (Figure 4.11a,b), two water molecules were determined to be bound in the Cu(II) inner-sphere coordination, with water residence time around 10 ns and at Cu-H distance of 2.6 Å. In Section 4.3.5, the translation of the binding site to the extremities resulted in lower relaxivities. It is possible to explain these experimental differences with different Cu(II) coordination and the presence of a single inner-sphere water molecule when bound at the N-terminus. Figure 4.11c and Figure 4.11d show simulated relaxivity of one inner-sphere water molecule as is proposed for Cu(MB1-1)$_3$.

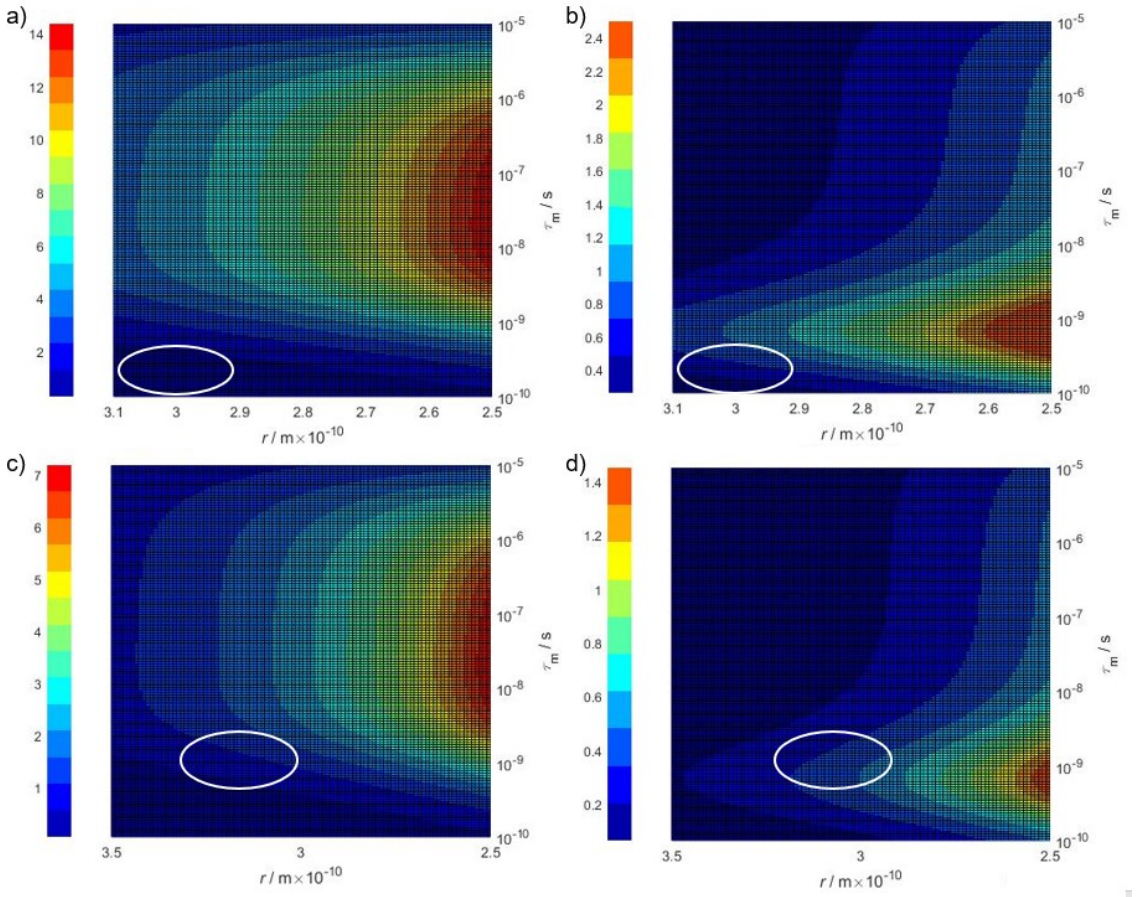


Figure 4.11: Simulation of ^{1}H-MRI r_1 relaxivity (shown on colour bar) at a), c) 1.4 T and b), d) 7 T for a), b) q = 2, as in Cu(MB1-2)$_3$ and Cu(MB1-4)$_3$ and c), d) q = 1, as in Cu(MB1-1)$_3$, for a Cu(II) compound with rotational correlation time τ_R = 6.9 ns and Cu(II) electron relaxation time τ_s = 5 ns, as function of variable water residence time τ_m and water proton-metal ion distance r. Region of overlay in white circle according to r_1 relaxivity of a), b) Cu(MB1-4)$_3$ and c), d) Cu(MB1-1)$_3$.

In Cu(MB1-1)$_3$ r_1 was measured to be 1.2 ± 0.3 mM^{-1} s^{-1} at 1.4 T and 0.4 ± 0.2 mM^{-1} s^{-1} at 7 T, which correspond to the blue region in the simulated plots (Figure 4.11c and d). The overlay of the region in the two plots gives a good estimation of the distance between Cu(II) and the water protons, which is estimated to be longer than in Cu(MB1-2)$_3$ (> 2.9 Å). This could be a possible consequence of the rearrangement of the donor residues. The presence of different coordination environment around Cu(II) is also confirmed by the different λ_{max} in Cu(II) *d-d* absorption, as shown in Section 4.3.3. Moreover, water residence time is predicted to be shorter than in Cu(MB1-2)$_3$, with values around 1 ns.

In Cu(MB1-4)$_3$ (r_1 = 0.9 ± 0.1 mM^{-1} s^{-1} at 1.4 T and 0.7 ± 0.1 mM^{-1} s^{-1} at 7 T), two inner-sphere water molecules were found, similarly to Cu(MB1-2)$_3$. The reason behind the dramatic reduction in relaxivity could be attributed to water residence time being too short to allow efficient

relaxation. From Figure 4.11a and b, τ_m can be estimated to be around 0.1 ns, with Cu-H distances around 3 Å.

4.4 Discussion

This chapter explores the impact on relaxivity of altering the relative position of a Cu(II) binding site along the coiled-coil and the identity of the second coordination sphere. These alterations were found to have no significant impact on Cu(II) affinity.

The relationship between relaxivity and molecular parameters (number of inner-sphere water molecules q, water residence time τ_m and distance Cu(II) - water proton $r_{Cu\text{-}H}$) was investigated, and important conclusions were drawn. In Chapter 3, it was shown that when the binding site is designed in a buried position, but still accessible to water, such as MB1-2, the systems are characterised by high relaxivities. This could be due to optimised water exchange or to a partially structured binding site that allows the presence of water molecules for Cu(II) complexation (Figure 4.12a). Since Asp residues can be bound either monodentate (through one carboxylate O) or bidentate (through both carboxylate O), therefore, their coordination cannot be easily predicted.

When the binding site is in a position highly accessible by water such as in MB1-1, relaxivity is reduced. This is attributed to the high accessibility of the binding site accompanied by an increase in flexibility or local disruption of the peptide structure at the N-terminus which allows the formation of a copper complex with ligands provided by amino acids residues and only one inner-sphere water molecule (Figure 4.12b,c). Moreover, simulations show that the inner-sphere water could be located at longer distances to Cu(II) and that water exchange rate could be in a fast-exchange regime. This means that water molecules exchange too rapidly so that their water protons cannot undergo efficient relaxation.

When amino acids with residues of high steric hindrance are introduced as second-sphere residues, the relaxivities are improved. The reason for that is hypothesised to be consequence of the presence of more water molecules in closer proximity to Cu(II) compared MB1-1, with longer residence times, more comparable to MB1-2. The impact of water residence time is emphasised in MB1-4 where, despite the presence of two inner-sphere water molecules as in MB1-2, the relaxivities are drastically reduced as possible consequence of water exchange rate shifting towards a fast-exchange limit.

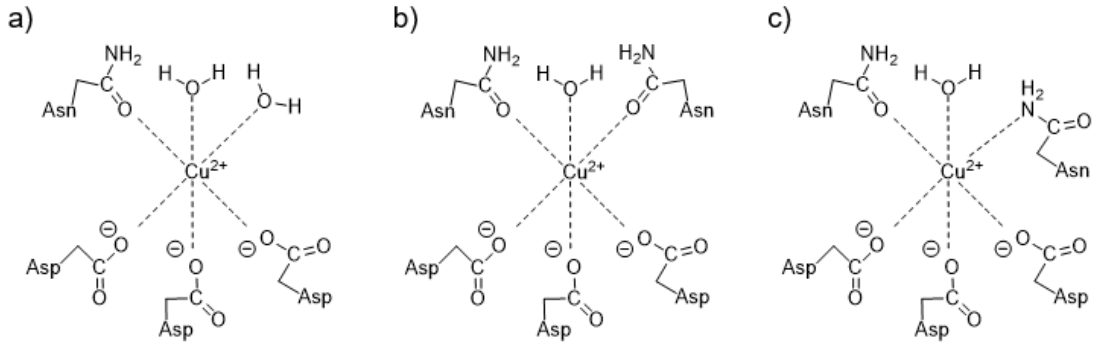


Figure 4.12: Based on the results presented in this chapter, potential Cu(II) binding sites in a) Cu(MB1-2)$_3$, q = 2 and b), c) Cu(MB1-1)$_3$, q = 1 coordinated through Asn oxygen or nitrogen, respectively. Cu(II) binding sites in MB1-1 2F and MB1-1 2W are hypothesised to be a dynamic interchange between the two hydration states.

Taken together, these results suggest that in these Cu(II) complexes the translation of the binding site to the extremities is not an efficient method to improve relaxivities, as in the analogous Gd(III) complexes,[9] where the translation to the extremities allows more water to bind Gd(III). The translation to the N-terminus in Cu(MB1-1)$_3$ leads to a reduction in the inner-sphere water molecules of Cu(II), which negatively impacts the relaxivity. Moreover, the water molecule is estimated to be at a longer distance to Cu(II) and exchanging with bulk water at a faster rate. The introduction of amino acids with residues of high steric hindrance results in an enhancement in the relaxivities. The reason for that is hypothesised to be due to one or two water molecules in closer proximity to Cu(II) compared to Cu(MB1-1)$_3$, with longer and more optimised residence times.

4.5 Conclusions

This chapter has provided important insights into some of the factors that governs the MRI efficiency of this class of contrast agents. These factors were found to be the water accessibility to the metal binding site governed by its location in the sequence and eventual second-sphere mutations which affect the sterics around the metal.

To confirm all these assumptions, variable temperature ^{17}O-NMR experiments are needed to determine water residence times of peptides and confirm the negative impact on relaxivity of the shift towards a fast exchange limit when a Cu(II) binding site is exposed to solvent. Finally, NMRD (Nuclear Magnetic Relaxation Dispersion) experiments can determine the variation of relaxivity at different proton Larmor frequencies and provide essential parameters to characterise the metal binding site such as hydration state q, distance metal-water proton $r_{Cu\text{-}H}$, water residence time τ_m, rotational correlation time τ_R, hyperfine interactions $A/\hbar$.

References

1. E. L. Que, E. Gianolio, S. L. Baker, A. P. Wong, S. Aime and C. J. Chang, *J. Am. Chem. Soc.*, 2009, **131**, 8527-8536.
2. R. B. Lauffer, *Chem. Rev.*, 1987, **87**, 901-927.
3. D. H. Powell, L. Helm and A. E. Merbach, *J. Chem. Phys.*, 1991, **95**, 9258-9265.
4. D. H. Powell, P. Furrer, P.-A. Pittet and A. E. Merbach, *J. Phys. Chem.*, 1995, **99**, 16622-16629.
5. A. Pasquarello, I. Petri, P. S. Salmon, O. Parisel, R. Car, É. Tóth, D. H. Powell, H. E. Fischer, L. Helm and A. E. Merbach, *Science*, 2001, **291**, 856-859.
6. I. Bertini and R. Pierattelli, *Pure Appl. Chem.*, 2004, **76**, 321-333.
7. I. Bertini, C. Luchinat, R. D. Brown III and S. H. Koenig, *J. Am. Chem. Soc.*, 1989, **111**, 3532-3536.
8. M. R. Berwick, D. J. Lewis, A. W. Jones, R. A. Parslow, T. R. Dafforn, H. J. Cooper, J. Wilkie, Z. Pikramenou, M. M. Britton and A. F. Peacock, *J. Am. Chem. Soc.*, 2014, **136**, 1166-1169.
9. M. R. Berwick, L. N. Slope, C. F. Smith, S. M. King, S. L. Newton, R. B. Gillis, G. G. Adams, A. J. Rowe, S. E. Harding and M. M. Britton, *Chem. Sci.*, 2016, **7**, 2207-2216.
10. L. N. Slope, M. G. Hill, C. F. Smith, P. Teare, F. J. de Cogan, M. M. Britton and A. F. Peacock, *Chem. Comm.*, 2020, **56**, 3729-3732.
11. J. K. Myers, C. N. Pace and J. M. Scholtz, *PNAS*, 1997, **94**, 2833-2837.
12. P. Kuzmic, *Anal. Bioch.*, 1996, **237**, 260-273.
13. E. Prenesti, P. G. Daniele, M. Prencipe and G. Ostacoli, *Polyhedron*, 1999, **18**, 3233-3241.
14. E. Prenesti, P. G. Daniele, S. Berto and S. Toso, *Polyhedron*, 2006, **25**, 2815-2823.
15. H. T. Edzes and E. T. Samulski, *Nature*, 1977, **265**, 521-523.
16. J. Wahsner, E. M. Gale, A. Rodríguez-Rodríguez and P. Caravan, *Chem. Rev.*, 2018, **119**, 957-1057.

CHAPTER 5

MUTATION OF THE RESIDUES IN COPPER(II) FIRST COORDINATION SPHERE

5.1 Introduction

In Chapter 3, a Cu(II) metallopeptide complex which exhibits high MRI relaxivities is presented, overcoming the limitation of the presence of a single unpaired electron in Cu(II) ion.[1-6] In Chapter 4, these relaxivities were modulated by translating the binding site along the coiled-coil. In this chapter, different copper binding sites are designed to determine the impact of first-sphere mutations on Cu(II) coordination chemistry and on the MRI relaxivities of the relative complexes.

As discussed in Chapter 1, copper coordination in natural proteins can occur through exclusive nitrogen coordination (Type 3 and Type B) or exclusive sulfur coordination (Cu-S_{Cys}), with the latter being more common for coordination of the softer metal Cu(I). The majority of Cu(II) complexes are generated by mixed donor sites, $CuO_xN_yS_z$ (Type 1, Type 2, Type 1.5, Type A, Type B, Type Z and Type 0).[7, 8] Type 1, Type 2 and mixed donor copper sites have been successfully included within coiled-coils and helical bundles,[9-19] with the goal to structurally and functionally reproduce natural copper sites or to design new functionalities. Whereas the MB1-2 design presents an abundance of potential oxygen donors, the impact on copper binding affinities and MRI relaxivities of introducing histidine (His, H) residues, a common amino acid found coordinated to Cu(II) is explored in this chapter. In fact, His is estimated to be involved in copper binding in 65% of natural proteins, while Glu and Asp only in 7 and 6%, respectively.[20]

In this chapter, CD spectroscopy is used to assess peptide folding of variable concentration of peptide monomer upon Cu(II) complexation. In addition, quenching of tryptophan emission as a consequence of Cu(II) binding is determined to confirm Cu(II) binding, especially in the case of peptides which are already well-structured in their apo form. Affinity constants are determined from fitting of binding data. Electronic *d-d* transitions of Cu(II) ion are monitored using UV-Vis spectroscopy to gain insights into Cu(II) coordination. As explained in Chapter 2, oxygen donors on amino acid residues shift maximum absorbance to longer wavelength, while nitrogen donors move the peak to shorter wavelengths. MRI relaxivities are measured and the impact of pH

variation on Cu(II) coordination and relaxivity is determined. Finally, transmetallation in the presence of Zn(II) is explored to gain more insight into the kinetic stability of Cu(II) binding.

5.2 Experimental

Materials, peptide synthesis and purification as in Chapter 3.

5.2.1 UV-Visible spectroscopy

UV-Vis experiments to determine peptide concentration and electronic Cu(II) *d-d* transitions were conducted as described in Chapter 4.

5.2.2 Circular Dichroism (CD) spectroscopy

CD spectra were recorded on a Jasco J-715 Spectropolarimeter and peptide folding was determined as described in Chapter 4.

Kinetic folding data were recorded by monitoring the ellipticity at 222 nm (θ_{obs}) of either 40 or 150 μM solution of peptide monomer (13.33 or 50 μM peptide trimer, respectively) in 10 or 50 mM HEPES buffer pH 7.0 (respectively) in the absence and presence of 1 equivalent $CuCl_2$ per equivalent of peptide trimer (13.33 or 50 μM $CuCl_2$, respectively), at 20°C. Data were collected ~3 seconds after $CuCl_2$ addition. θ_{obs} was converted to % folding using Equations 1 and 2 of Chapter 4. Thermal unfolding was determined by monitoring the ellipticity at 222 nm of a 150 μM solution of peptide monomer in 50 mM HEPES buffer pH 7.0 in the absence and presence of 50 μM $CuCl_2$, using a Jasco Peltier Type PTC-4235 temperature controller ramping from 20°C to 40°C.

5.2.3 Emission spectroscopy

Emission spectra were recorded over a range 300-455 nm (Trp emission peak region) on a Jasco FP-8500 fluorescence spectrometer as described in Chapter 4.

5.2.4 Nuclear magnetic resonance

^{1}H-NMR measurements, at high magnetic field (7 T), were performed on a Bruker Avance III HD spectrometer, operating at a proton resonance frequency of 300.13 MHz. All measurements were performed at 20 ± 0.2°C. Data were acquired using 5 mm ^{1}H coil in a Bruker Diff30 probe. A 90° pulse duration calibrated for each sample was used for the experiments. For T_1 NMR relaxation measurements, a Saturation Recovery sequence (described in Section 2.7.3)

was used. A series of 8 spectra were collected with logarithmically spaced recovery delays from 0.01 s to a maximum of 12-15 s, with 8 signal averages, 8k data points and spectral width of 10 kHz. For T_2 NMR relaxation measurements the Carr-Purcell-Meiboom-Gill (CPMG) pulse sequence (described in Section 2.7.3) was used with a repetition time > $5T_1$ (≥ 10 s), 8 signal averages, 16k data points and spectral width of 10 kHz. The variable counter list, for the CPMG experiments, consisted of 10 values logarithmically spaced from 2 to 1024, with a CPMG echo time value of 2 ms.

^{1}H-NMR measurements, at low magnetic fields (1.4 T), were performed on a Spinsolve benchtop NMR (Magritek, Aachen, Germany), operating at proton resonance frequency of 61 MHz. Data were acquired at 21.0 ± 0.5°C (controlled room temperature) using 3 mm NMR tubes and automated 90° pulse width of 7 µs. For T_1 NMR relaxation measurements, an Inversion Recovery sequence (described in Section 2.7.3) was used with a repetition time > $5T_1$ (≥ 10 s). A series of 11 spectra were collected with delays linearly spaced from 0.001 s to a maximum of 5-10 s, 8 signal averages and 32k points. For T_2 NMR relaxation measurements a CPMG pulse sequence was used with a repetition time > $5T_1$ (≥ 10 s). A series of 10 spectra were recorded with a 2 ms CPMG echo time and final echo time of 5 s, 8 signal averages and 32k data points. All data were analysed using Prospa (Magritek, Aachen, Germany). Signal intensity curves were fitted in KaleidaGraph (Synergy, USA).

Binding of Cu(II) by peptide trimers was monitored by measuring the ^{1}H T_1 and T_2 magnetic resonance relaxation times of solutions of 40 µM $CuCl_2$ in the presence of increasing concentrations of peptide monomer, in 100 mM HEPES buffer pH 7.0. The r_1 and r_2 relaxivities were calculated from the gradients of plots of the average, based on three independent repeats, ^{1}H magnetic resonance relaxation rates ($1/T_1$ and $1/T_2$ respectively), as a function of $CuCl_2$ concentration. A range of solutions were measured, containing 0, 10, 20, 30, 40 µM $CuCl_2$ and 15 equivalents of peptide monomer (5 equivalents of peptide trimer), to drive Cu(II) complexation. The r_2 relaxivity of the apo peptide was used to correct $1/T_2$ and relative r_2 for the Cu(II) complexes, by accounting for the contribution of excess unbound peptide.

Zn(II) transmetallation experiments were performed by adding 40 µM $ZnCl_2$ to a 40 µM solution of $CuCl_2$ in the presence of 1 equivalent of peptide trimer, corresponding to 40 µM peptide trimer or 120 µM peptide monomer, in 100 mM HEPES buffer pH 7.0. Control samples were prepared using the same procedure without the addition of $ZnCl_2$. ^{1}H-NMR experiments were performed 1 h after sample preparation.

5.3 Results

5.3.1 Peptide design

From the native MB1-2 sequence, the design of this group of peptides involved the mutation of the first coordination sphere of Cu(II) (Table 5.1 and Figure 5.1). This was achieved by replacing Asn with His (LS4-2) or Ile (CS1-2) or by modifying the binding site to have only His donors (GM3) in *a* position and one additional Asp layer above His (GM4) (Figure 5.2). GM4 potentially provide the same residues for Cu(II) binding as LS4-2 (Asp and His) but in reverse position.

Table 5.1: Sequences of peptides used in this chapter. Residues designed for Cu(II) binding underlined and coloured red (Asp), blue (Asn) and in green (His).

MB1-2	Ac-G IAAIEQK IAANEWK DAAIEQK IAAIEQK IAAIEQK G-NH_2
LS4-2	Ac-G IAAIEQK IAAHEWK DAAIEQK IAAIEQK IAAIEQK G-NH_2
CS1-2	Ac-G IAAIEQK IAAIEWK DAAIEQK IAAIEQK IAAIEQK G-NH_2
GM3	Ac-G IAAIEQK IAAIEWK HAAIEQK IAAIEQK IAAIEQK G-NH_2
GM4	Ac-G IAAIEQK IAADEWK HAAIEQK IAAIEQK IAAIEQK G-NH_2

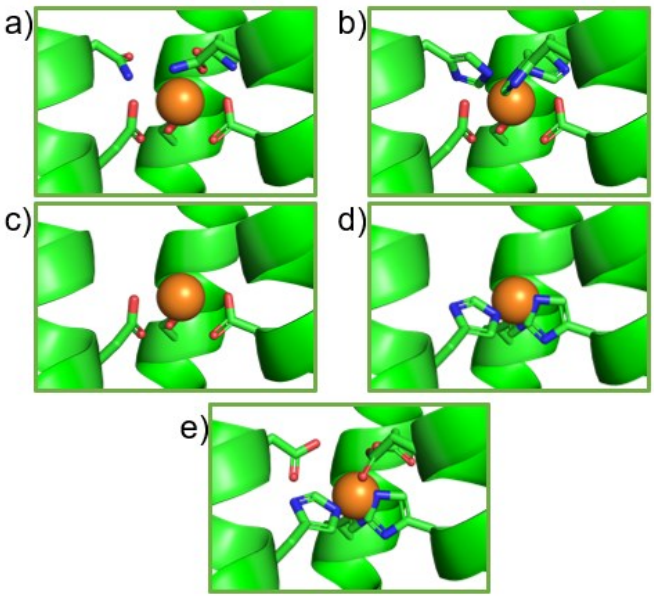


Figure 5.1: Cartoons of designed copper binding sites in a) $Cu(MB1\text{-}2)_3$, b) $Cu(LS4\text{-}2)_3$, c) $Cu(CS1\text{-}2)_3$, d) $Cu(GM3)_3$, and e) $Cu(GM4)_3$. Peptide backbone shown as a helical ribbon and side chains shown as sticks, with oxygen in red and nitrogen in blue. Cu(II) ion shown as orange sphere.

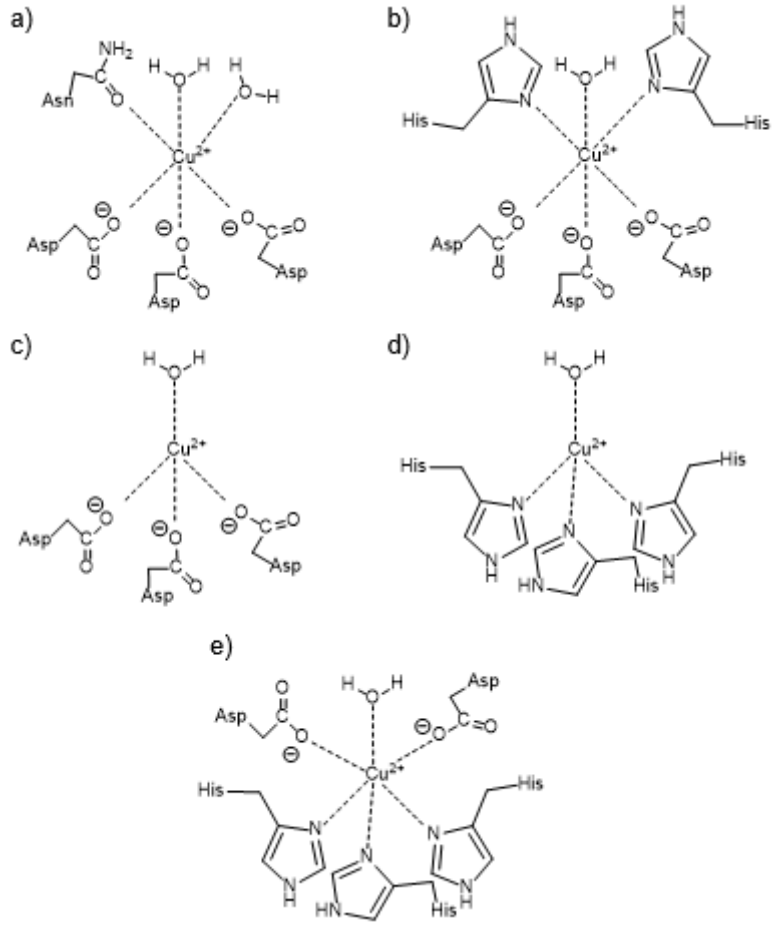


Figure 5.2: Hypotethical Cu(II) binding sites in a) $Cu(MB1\text{-}2)_3$ and b) $Cu(LS4\text{-}2)_3$ and e) $Cu(GM4)_3$ featuring octahedral geometry (due to the abundance of potential donors); c) $Cu(CS1\text{-}2)_3$ and d) $Cu(GM3)_3$, featuring tetrahedral geometry.

5.3.2 Copper binding: peptide folding, quenching of Trp fluorescence and log K_a determination

Peptide folding was monitored using CD spectroscopy by performing titrations of $CuCl_2$ in a 30 μM peptide monomer solution (Figure 5.3, Figure 5.4 and Table 5.2). CD titrations for LS4-2 were performed by Dr. Louise Slope, University of Birmingham.[21] Similar to MB1-2, LS4-2 and GM4 are unfolded in their apo form. This can be attributed to the presence of destabilising, negatively charged Asp residues in the hydrophobic core. After addition of Cu(II), CD spectra in all three peptides showed increase in negative ellipticity at 222 nm, as a consequence of forming an α-helical structure, and improvement in folding. In contrast, the remaining peptides were already well structured in their apo form: the replacement of one single layer of donor residues by a Ile layer, allows GM3 and CS1-2 to be structured even without the addition of Cu(II).

Moreover, CS1-2 is less folded than GM3, but displays a modest improvement after Cu(II) addition due to the presence of negative Asp residues.

The fittings for LS4-2, CS1-2 and GM3 were made in accordance with a binding model of $L + 1/3M \leftrightarrow 1/3ML_3$ (M: metal ion and L: peptide monomer, Figure 5.4), while for GM4 only the model $L + 1/3M \leftrightarrow 1/3ML_3 + 1/3M \leftrightarrow 1/3M_2L_3$ allowed a good fitting, suggesting that two copper ions are able to bind to the designed binding site with two different log K_a (Figure 5.5 and Table 5.2).

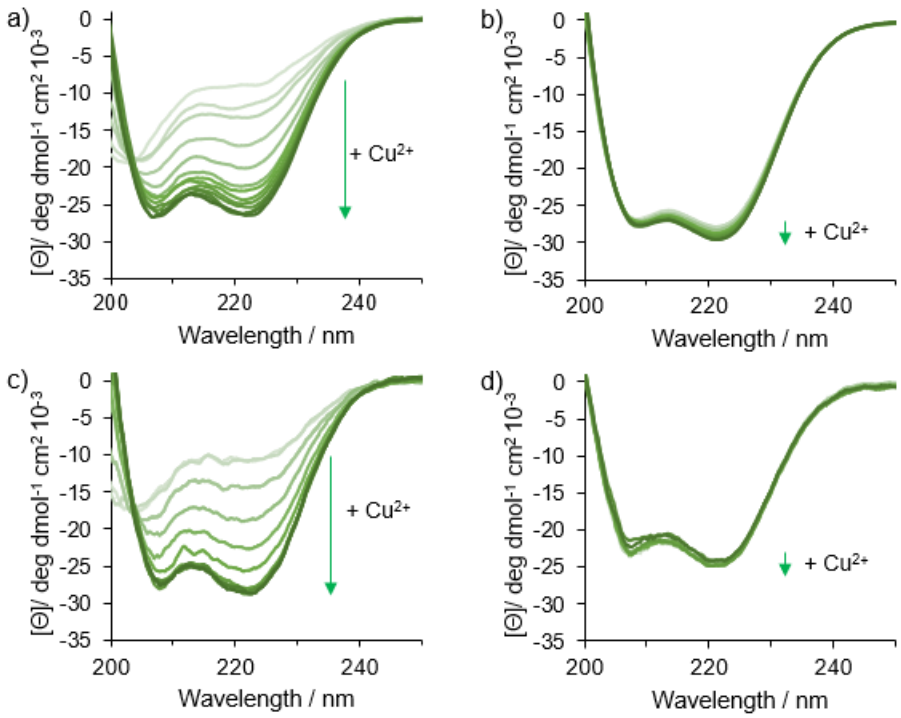


Figure 5.3: Representative CD spectra of $CuCl_2$ titration into 30 μM a) LS4-2, b) CS1-2, c) GM4 and d) GM3 peptide monomer in 10 mM HEPES buffer pH 7.0.

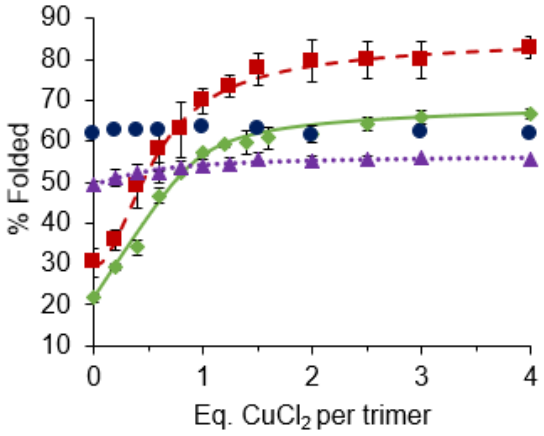


Figure 5.4: CD binding curves showing $CuCl_2$ titration into 30 μM LS4-2 (green diamonds ♦, full line), CS1-2 (purple triangles ▲, dotted line), GM4 (red squares ■, dashed line) and GM3 (blue circles ●) peptide monomer in 10 mM HEPES buffer pH 7.0. The plot of % folded, based on the molar ellipticity at 222 nm, as a function of $CuCl_2$ concentration, is shown fit to a nonlinear least-squares fitting based on $1/3M + L \leftrightarrow 1/3ML_3$ and $1/3M + 3L \leftrightarrow 1/3ML_3 \leftrightarrow 1/3M_2L_3$ (GM4) binding models (a). Error bars determined from standard deviation of three independent experiments.

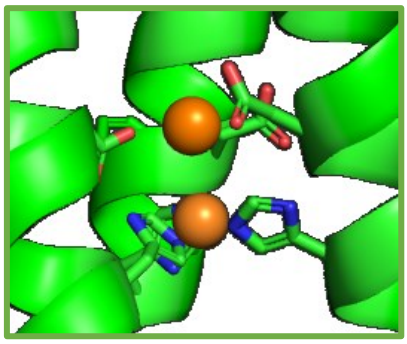


Figure 5.5: Cartoon of proposed for a dicopper binding site in GM4 . Peptide backbone shown as a helical ribbon and side chains shown as sticks, with oxygen in red and nitrogen in blue. Cu(II) ions shown as orange sphere.

Quenching of the tryptophan fluorescence emission following the addition of $CuCl_2$ was monitored to determine (Figure 5.6 and Figure 5.7) binding constants. This is useful especially for well-structured peptides even in the absence of Cu(II) for which CD titrations could not be used to extract binding constants. For the remaining peptides, the affinity constants $\log K_a$ measured using data from fluorescence quenching experiments are in good agreement with the ones determined using CD experiments (Table 5.2).

Compared to MB1-2 ($\log K_a$ around 4.8), the introduction of His within the sequence in LS4-2, GM3 and GM4, leads to general increase of binding constants. LS4-2, where His replaced Asn in ***d*** position, showed a modest improvement ($\log K_a$ around 5.1), while in GM4, where His replaced Asp in ***a*** position, the binding constants where enhanced by two orders of magnitude

(log K_{a1} around 7.5). Moreover, a second constant for another Cu(II) binding was determined in GM4 (log K_{a2} around 6.6). Therefore, fitting of GM4 data suggests that two copper ions are able to bind to the designed binding site, probably one for each amino acid layer (Figure 5.5).

GM3 and CS1-2, featuring His and Asp, respectively, in ***a*** position were found to have binding constants similar and higher than MB1-2 (log K_a around 5.5, corresponding to K_d = 3.16 ± 1.16 μM). This could be due to the presence of a Ile layer which determines a pre-organised structure, favouring Cu(II) binding. For a peptide similar to GM3, featuring a 3 His binding site, Pecoraro and co-workers[11] reported K_d = 40 ± 8 at pH 5.9 and 8.7 ± 1.1 nM at pH 7.4 from fitting of tryptophan fluorescence data. However, they also showed that modification of amino acids in proximity to the Cu(II) binding site has an impact on the K_d value, with values increasing to 0.7 μM at pH 5.8.[18] Another similar peptide was reported by Tanaka and co-workers,[15] who determined K_d = 10 μM using CD spectroscopy data and the same binding model as here.

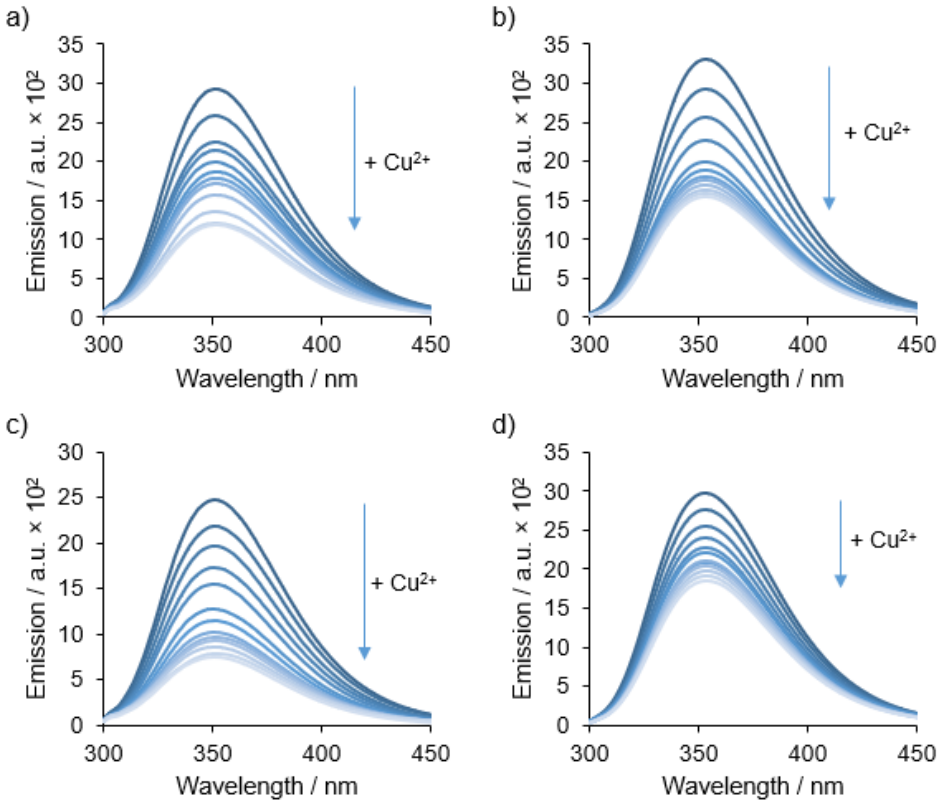


Figure 5.6: Representative tryptophan emission spectra showing titration of $CuCl_2$ into 30 μM a) LS4-2, b) CS1-2, c) GM4 and d) GM3 peptide monomer in 10 mM HEPES buffer pH 7.0 at 293 K, λ_{ex} = 280 nm.

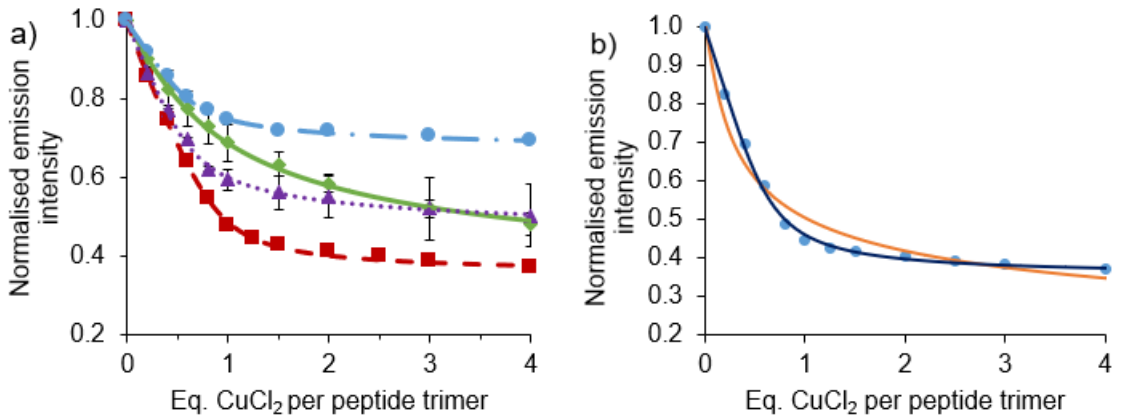


Figure 5.7: Plot a): Normalised integrated emission following $CuCl_2$ titration into 30 μM LS4-2 (green diamonds ♦, full line), GM3 (blue circles ●, dashed-dotted line), CS1-2 (purple triangles ▲, dotted line) and GM4 (red squares ■, dashed line) peptide monomer in 10 mM HEPES buffer pH 7.0 at 293 K, λ_{ex} = 280 nm, λ_{em} integrated between 300 and 455 nm. Data fitted using DynaFit[22] to a nonlinear least-squares fitting based on 1/3M + L ↔ $1/3ML_3$ and 1/3M + L ↔ $1/3ML_3$ ↔ $1/3M_2L_3$ (GM4) models. Plot b): normalised integrated emission following $CuCl_2$ titration into 30 μM GM4 in 10 mM HEPES buffer pH 7.0 at 293 K, λ_{ex} = 280 nm, λ_{em} integrated between 300 and 455 nm. Data fitted using DynaFit[22] to a nonlinear least-squares fitting based on 1/3M + L ↔ $1/3ML_3$ (orange) and 1/3M + L ↔ $1/3ML_3$ ↔ $1/3M_2L_3$ (blue) models. Error bars determined from standard deviation of three independent experiments.

Table 5.2: % folding of the apo peptides compared to the metallo form (end of titration) for 30 μM peptide monomer in 10 mM HEPES buffer pH 7.0, monitored by CD and log K_a values determined from fitting CD and fluorescence data in 10 mM HEPES buffer pH 7.0. Data fitted using DynaFit[22] to a nonlinear least-squares fitting based on 1/3M + L ↔ $1/3ML_3$ and 1/3M + L ↔ $1/3ML_3$ ↔ $1/3M_2L_3$ (GM4) models. Error determined from standard deviation of three independent experiments.

	CD folding		log K_a	
	% Folding apo	% Folding metallo	CD	Fluorescence
MB1-2	18 ± 4% (21 ± 3% from ref. [23])	69 ± 1%	4.7 ± 0.1	4.9 ± 0.1
LS4-2	23 ± 1%	60 ± 2%	5.2 ± 0.0	5.0 ± 0.2
GM3	62	62	5.5 ± 0.3	5.5 ± 0.3
CS1-2	49 ± 1%	54 ± 1%	-	5.5 ± 0.2
GM4	30 ± 4%	70 ± 3% (1 eq.)	7.3 ± 0.3	7.6 ± 0.1
		80 ± 5% (2 eq.)	6.5 ± 0.1	6.8 ± 0.3

5.3.3 Copper binding: peptide folding at higher concentration of peptide monomer

In Chapter 3, it was shown that the peptide folding is a process related to peptide concentration. Here, the same analysis was conducted on three peptides (Figure 5.8). At 30 μM, CS1-2 is well folded in the apo form and does not become significantly more folded with Cu(II) addition. At 150 μM, the apo peptide is significantly more folded and even more folded in the metallo form (Table 5.3). At 30 μM peptide monomer GM4 and LS4-2 are mostly unfolded in the absence of any metal and become more folded after Cu(II) addition. At 150 μM the apo forms of both peptides are more folded than at 30 μM. The addition of $CuCl_2$ to GM4 leads to enhanced folding. After the addition of around 1 equivalent of metal per equivalent of trimer, this becomes comparable to folding at 30 μM. $CuCl_2$ addition to LS4-2 is able to promote folding, forming a structure that is more folded at higher concentration of peptide, 73% at 150 μM monomer concentration compared to 60% at 30 μM.

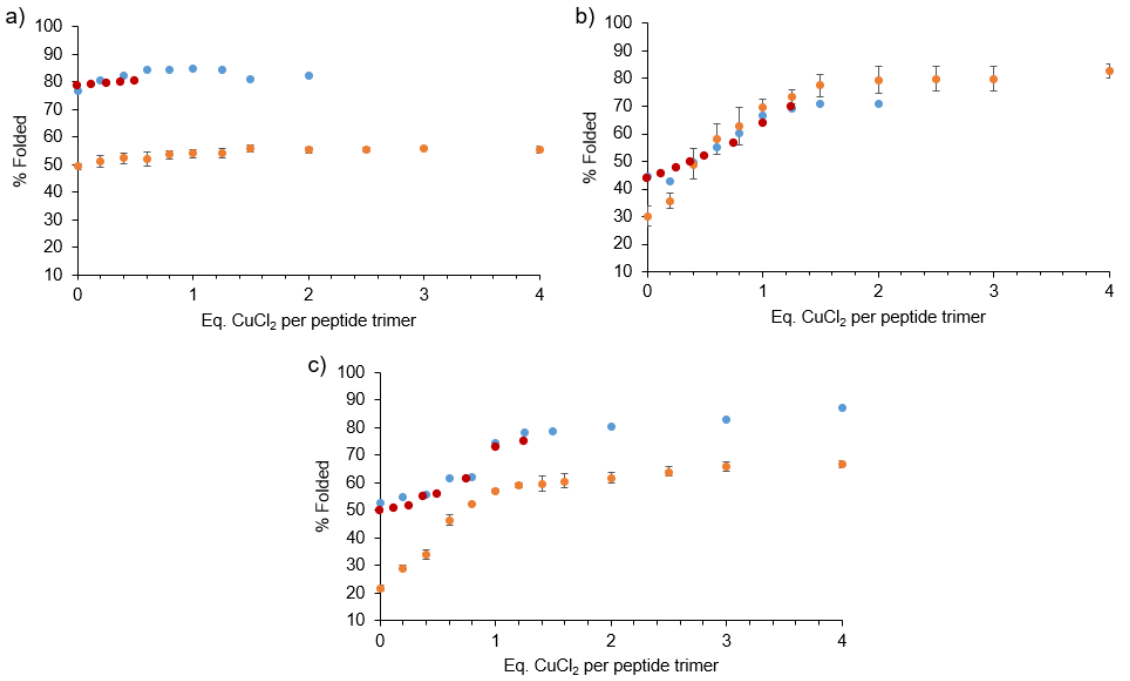


Figure 5.8: CD binding curves showing $CuCl_2$ titration into 30 μM (orange) and 150 μM (repeat 1 in red and repeat 2 in blue) a) CS1-2 b) GM4 and c) LS4-2 in 50 mM HEPES buffer pH 7.0, monitored by CD. Error bars determined from standard deviation of three independent experiments.

Table 5.3: % folding of the apo peptides compared to the metallo form for 30 μM and 150 μM peptide monomer in 10 mM HEPES buffer pH 7.0, monitored by CD. Error determined from standard deviation of three independent experiments.

	30 μM		150 μM	
	% Folding apo	% Folding metallo	% Folding apo	% Folding metallo
LS4-2	23 ± 1%	60 ± 2%	50%	73%
CS1-2	49 ± 1%	54 ± 1%	78%	86%
GM4	30 ± 4%	70 ± 3% (1 eq), 80 ± 5% (2 eq)	44%	64% (1 eq), 73% (2 eq)

5.3.4 Copper binding: UV-Visible spectroscopy of *d-d* transitions

UV-Visible spectroscopy was used to gain insights into Cu(II) coordination ligands in the peptides (Figure 5.9).[24, 25] Table 5.4 reports the wavelength of maximum absorption (λ_{max}) and extinction coefficient values (ε) of the peak in 550-850 nm range.

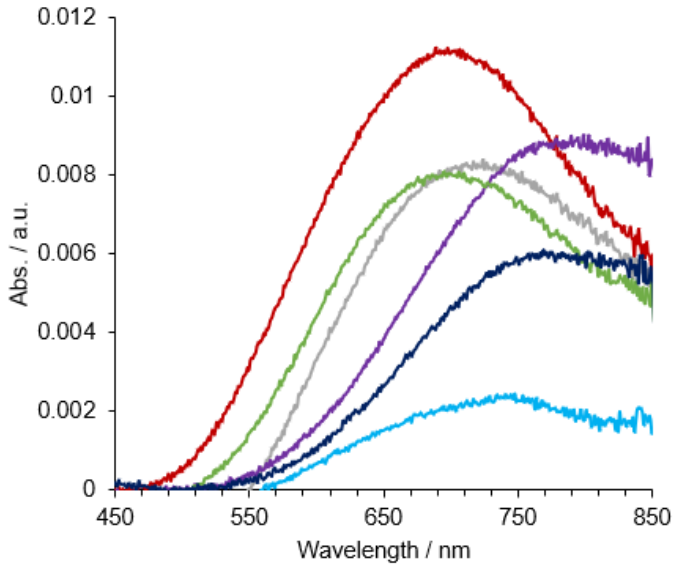


Figure 5.9: UV-Visible spectra of a solution of 150 μM $CuCl_2$ in the absence (light blue) and presence of 450 μM MB1-2 (dark blue), LS4-2 (green), CS1-2 (purple). GM3 (grey) and GM4 (red) monomer, in 100 mM HEPES buffer pH 7.0.

Table 5.4: Wavelength of maximum absorbance (λ_{max}) for Cu(II) *d-d* transitions recorded in the wavelength range 550-850 nm for a solution of 450 μM peptide monomer and 150 μM $CuCl_2$ compared to a solution of 150 μM $CuCl_2$ in 100 mM HEPES buffer pH 7.0.

	λ_{max} / nm	ε / M^{-1} cm^{-1}
$CuCl_2$	745	16
MB1-2	776	40
LS4-2	698	46
CS1-2	779	59
GM3	723	55
GM4	700	73

A $CuCl_2$ solution, in buffer, was used as control and showed a broad absorption at 745 nm and compared to a solution consisting of equimolar concentration of MB1-2 peptide trimer in the presence of $CuCl_2$, in which a red shift to 776 nm was reported (see Chapter 3). This red shift was attributed to H_2O ligands in the aqua complex partially substituted by negatively charged oxygen donors provided by Asp.

Here, LS4-2 shows a blue shift to 698 nm, suggesting the presence of at least one nitrogen, provided by a His, binding to Cu(II). GM4, featuring the same amino acid residues as LS4-2 in reverse order, presents a similar λ_{max} (700 nm), which is slightly shifted to shorter wavelengths (692 nm), after the addition of more equivalents of Cu(II) per peptide trimer (Figure 5.10). CS1-2, which presents only one Asp layer, a similar to MB1-2 red shift to 779 nm was recorded due to a comparable oxygen-rich Cu(II) coordination environment. Finally, GM3 presents a blue shift to 723 nm. When compared to $\lambda_{max} \sim 650$ nm, as reported in literature for similar peptides,[11, 18] the value reported here is quite high. This is further explored in Section 5.3.8.

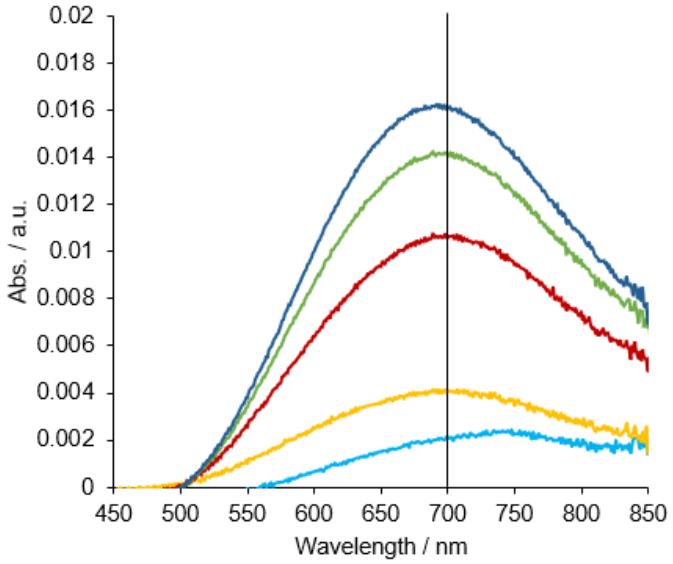


Figure 5.10: UV-Visible spectra of a solution of 150 μM $CuCl_2$ in the absence of peptide (light blue) compared with 450 μM GM4 monomer in the presence of 0.5 (yellow), 1 (red), 1.5 (green) and 2 (blue) equivalents of $CuCl_2$ per trimer, in 100 mM HEPES buffer pH 7.0.

5.3.5 Copper binding: folding kinetics and thermal stability

Folding kinetics for Cu(II) binding were established for LS4-2 and CS1-2. Folding kinetics for LS4-2 at 40 μM peptide monomer are very rapid since the apo peptide is 22% folded and at the beginning of the measurement (~3 seconds later) 54% folding is measured (Figure 5.11a). After 5 minutes, a further 6% increase is detected. At 150 μM monomer, kinetics are even faster, since the % folding reaches the maximum from 50% apo peptide within the timeframe of setting up the experiment (~3 seconds) so folding cannot be detected and no additional increment happens within the next 30 minutes (Figure 5.11c). The same concentration-dependent behaviour was observed for MB1-2 (see Section 3.3.4), but, in LS4-2, there is no evidence of the formation of a kinetic product. In CS1-2, the apo peptides are 50% and 78% folded at 40 and 150 μM peptide monomer concentration, and 55% and 86% in the metallo form. At 40 μM the kinetics are slower since the increase in folding can be detected (Figure 5.11b). At 150 μM the kinetics become faster, with a slight increase detectable (Figure 5.11d).

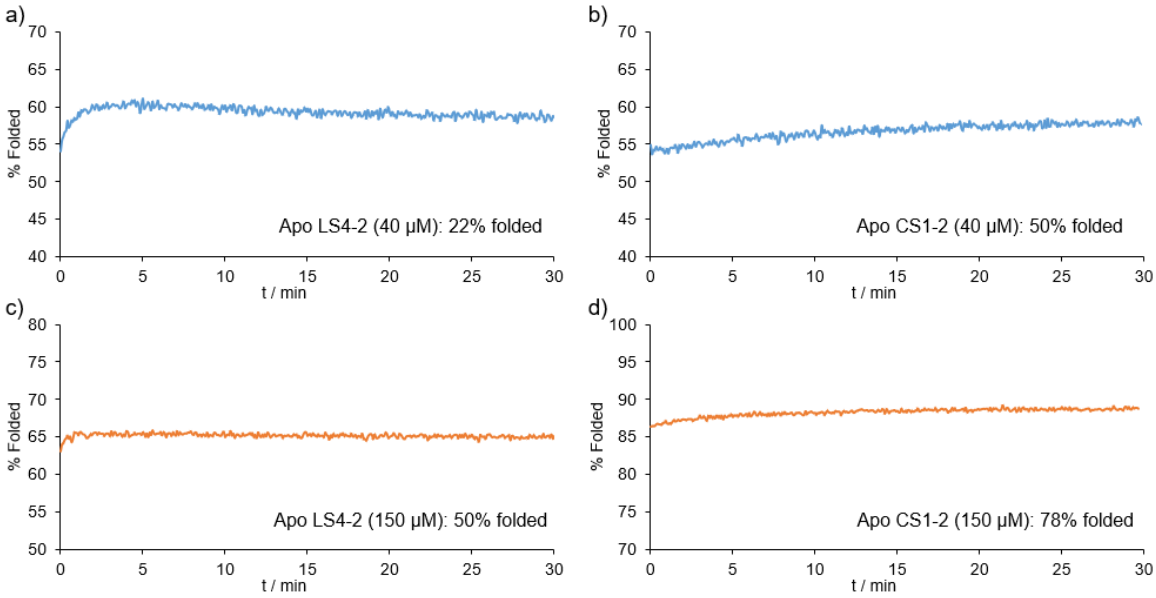


Figure 5.11: Plots showing variation over time (~3 s. mixing time) of % folding of a), b) 30 μM c), d) 150 μM a), c) LS4-2 and b), d) CS1-2 monomer in the presence of 1 equivalent of $CuCl_2$ per peptide trimer. Samples prepared in pH 7.0 HEPES buffer a), b) 10 mM, c), d) 50 mM.

Thermal stability experiments were performed between 20 to 40°C, range which includes the physiological temperature of 37°C. LS4-2 and MB1-2 (which both needs the presence of the metal ion to fold) were compared to CS1-2, which is well structured in its apo form. Overall, all three peptides are generally stable within this temperature range, so their melting temperature T_m cannot be determined.

LS4-2 folding is reduced as consequence of temperature increase, but its thermal stability appears improved compared to MB1-2, which showed a more pronounced temperature-dependent unfolding (Figure 5.12a). Cu(II) binding to CS1-2 allows to stabilise folding at increasing temperatures (Figure 5.12b). Moreover, its stability in the presence of Cu(II) is higher compared to LS4-2 and MB1-2, suggesting that the additional Ile layer can further stabilise folding at higher temperatures.

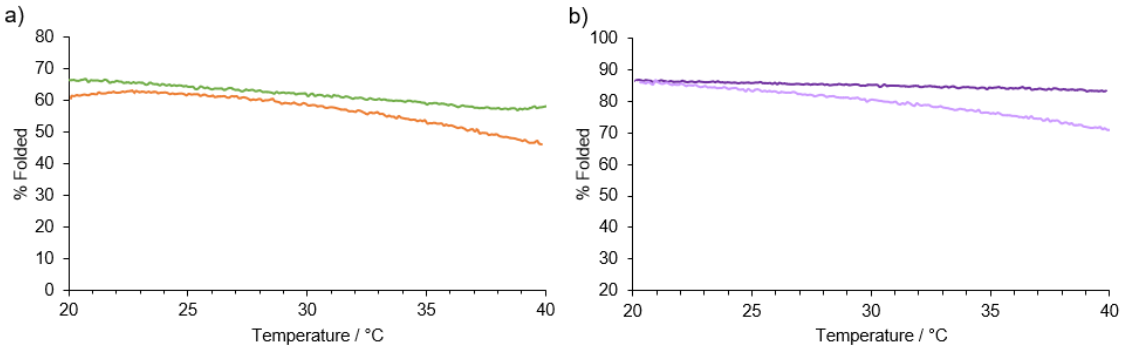


Figure 5.12: Plots showing variation between 20-40°C of % folding of a) 150 μM MB1-2 (orange) and LS4-2 (green) monomer and b) 150 μM CS1-2 monomer in the absence (light purple line) and in the presence of 1 equivalent of $CuCl_2$ per peptide trimer (purple line). Samples prepared in 50 mM HEPES buffer pH 7.0.

5.3.6 NMR relaxation times at increasing peptide trimer equivalents and in the absence of Cu(II)

T_1 relaxation times were measured for 40 μM $CuCl_2$ with increasing number of peptide trimer (Figure 5.13). Most of T_1 variation takes place between 0 and 1 equivalents in LS4-2 and CS1-2, reflecting the increased log K_a compared to MB1-2. For the remaining peptides, GM3 and GM4, there is no clear trend, suggesting that for these peptides, Cu(II) binding does not further shorten the T_1 relaxation times of a $CuCl_2$ solution in bulk water at 7 T.

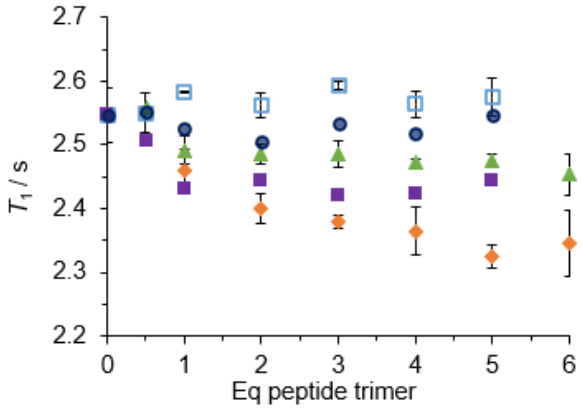


Figure 5.13: Plots of ^{1}H-NMR T_1 relaxation times for solutions of 40 μM $CuCl_2$ in 100 mM HEPES buffer pH 7.0, as a function of increasing equivalents MB1-2 (orange diamonds ♦, data from Chapter 3), CS1-2 (purple squares ■), LS4-2 (green triangles ▲), GM4 (blue circles ●), GM3 (empty blue squares □) peptide trimer. Samples recorded at 293 K on a 300 MHz NMR spectrometer. Error bars determined from standard deviation of three independent repeat experiments.

T_1 and T_2 relaxation times and r_1 and r_2 relaxivities of apo peptides were recorded at either 1.4 or 7 T. The presence of these apo peptides has no significant influence on T_1 and r_1, while there is some contribution to T_2 and r_2, especially at 7 T (Table 5.5). Moreover, no relationship between relaxivity values and the variation of the peptide sequence (and relative folding) was found.

Table 5.5: ^{1}H-NMR T_1, T_2 relaxation times, ^{1}H-NMR $1/T_1$,$1/T_2$ relaxation rates and ^{1}H-MRI r_1 and r_2 relaxivities for a series of apo peptides. Samples prepared in 100 mM HEPES buffer pH 7.0 Samples recorded at 293 K on either a 60 (1.4 T) or 300 MHz (7 T) NMR spectrometer. Error determined from standard deviation of three independent repeat experiments.

	1.4 T						7 T	
Apo peptide	T_1 / s	T_2 / s	$1/T_1$ / s^{-1}	$1/T_2$ / s^{-1}	r_1 /mM^{-1} s^{-1}	r_2 /mM^{-1} s^{-1}	r_1 /mM^{-1} s^{-1}	r_2 /mM^{-1} s^{-1}
MB1-2	2.91	2.09	0.34	0.48	0.02 ± 0.01	0.09 ± 0.01	0.00 ± 0.00	0.48 ± 0.01
CS1-2	2.87	2.08	0.35	0.48	n.d.	n.d.	n.d.	n.d.
LS4-2	2.89	2.07	0.35	0.48	0.01 ± 0.01	0.09 ± 0.03	0.01 ± 0.00	0.65 ± 0.03
GM3	2.89	2.07	0.34	0.48	0.00 ± 0.01	0.05 ± 0.01	0.00 ± 0.01	0.60 ± 0.01
GM4	2.88	2.07	0.35	0.48	0.02 ± 0.01	0.07 ± 0.01	0.03 ± 0.01	0.59 ± 0.01

5.3.7 MRI relaxivities

Copper binding affinity to this series of peptides has been determined in Section 5.3.2 through the log K_a values. Based on calculations performed in Chapter 3, in this range of log K_a, the use of five equivalents of peptide trimer in NMR experiments to determine MRI relaxivity, was estimated to be sufficient to enable complete Cu(II) binding.

Table 5.6 reports the metallopeptides relaxivities r_1 and r_2 (Figure 5.14 shows the relative relaxivities plots), calculated after $1/T_2$ correction (Figure 5.15 and Figure 5.16), and the number of water molecules directly coordinated to Cu(II) (q values, measured using EPR spectroscopy by Michael Taylor and Dr. Janet Lovett, St. Andrews University). Since only one measurement was conducted to determine q for each peptide, these values should be taken with caution.

Table 5.6: ^{1}H-MRI r_1 and r_2 relaxivities for the metallopeptides and relative number of inner-sphere water molecules. NMR samples prepared in 100 mM HEPES buffer pH 7.0 Samples recorded at 293 K on either a 60 (1.4 T) or 300 MHz (7 T) NMR spectrometer. Error determined from standard deviation of three independent repeat experiments.

	r_1 / mM^{-1} s^{-1}		r_2 / mM^{-1} s^{-1}		q inner-sphere water
Cu(II) complex of:	1.4 T	7 T	1.4 T	7 T	
MB1-2	13.5 ± 0.5	1.4 ± 0.1	31.7 ± 0.5	18.1 ± 1.3	2
LS4-2	5.1 ± 0.5	0.8 ± 0.1	13.6 ± 0.8	11.8 ± 1.1	n.d.
CS1-2	7.3 ± 0.4	1.1 ± 0.1	18.2 ± 0.6	14.7 ± 0.8	1-2
GM3	2.2 ± 0.4	0.6 ± 0.1	6.0 ± 0.7	7.0 ± 0.5	n.d.
GM4	2.4 ± 0.1	1.0 ± 0.2	4.4 ± 0.7	5.0 ± 0.7	n.d.

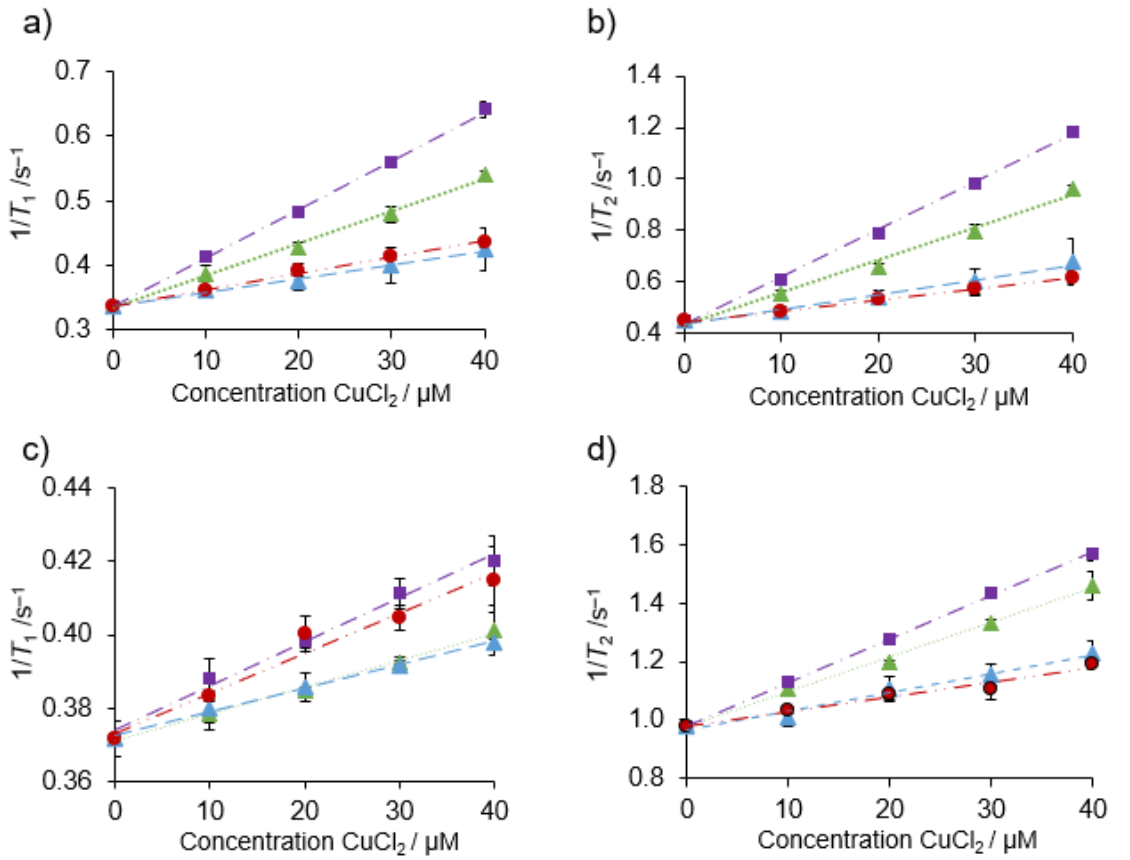


Figure 5.14: ^{1}H-NMR T_1 (a,c) and T_2 (b,d) relaxivity plots, showing reciprocal of relaxation time as a function of $CuCl_2$ concentration for relaxation rates recorded of samples at pH 7.0 in 100 mM HEPES buffer of $CuCl_2$ in the presence of 5 equivalents LS4-2 (green triangles ▲, dotted line), CS1-2 (purple squares ■, dashed-dotted line), GM3 (blue triangles ▲, dashed line) and GM4 (red circles ●, dashed-dotted-dotted line) trimer. Samples recorded at 293 K either on a 60 MHz, 1.4 T (a,b) and on a 300 MHz, 7 T (c,d) NMR spectrometer. Error bars determined from standard deviation of three independent repeat experiments.

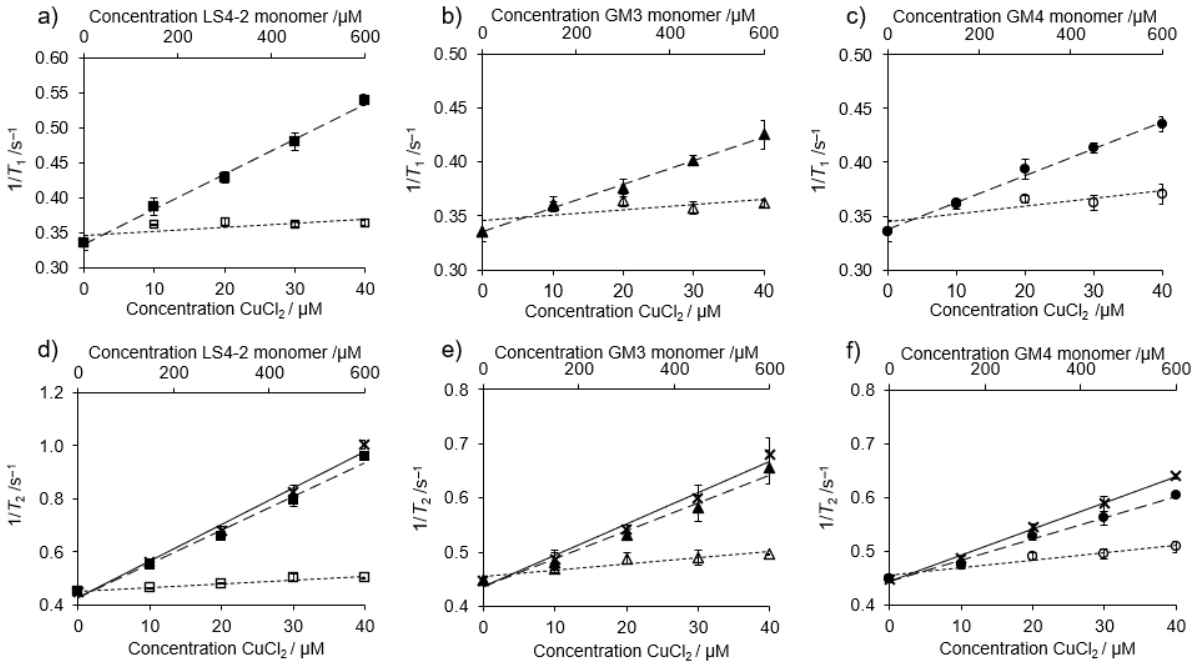


Figure 5.15: ^{1}H-NMR T_1 (a,b,c) and T_2 (d,e,f) relaxivity plots, showing reciprocal of relaxation time as a function of $CuCl_2$ concentration for relaxation rates recorded of samples at pH 7.0 in 100 mM HEPES buffer in the presence of 5 equivalents LS4-2 (a,d), GM3 (b,e) and GM4 (c.f) peptide trimer compared to the relaxation rates of the same concentration of peptide monomer without any metal (empty data points – LS4-2 □, GM3 Δ and GM4 ○). $1/T_1$ relaxation rates (a,b,c) are shown as full data points (LS4-2 ■, GM3 ▲ and GM4 ●) and $1/T_2$ relaxation rates (d,e,f) as crosses × (before correction) and as full data points (after correction, LS4-2 ■, GM3 ▲ and GM4 ●). Samples recorded at 293 K on a 60 MHz (1.4 T) NMR spectrometer. Error bars determined from standard deviation of three independent repeat experiments.

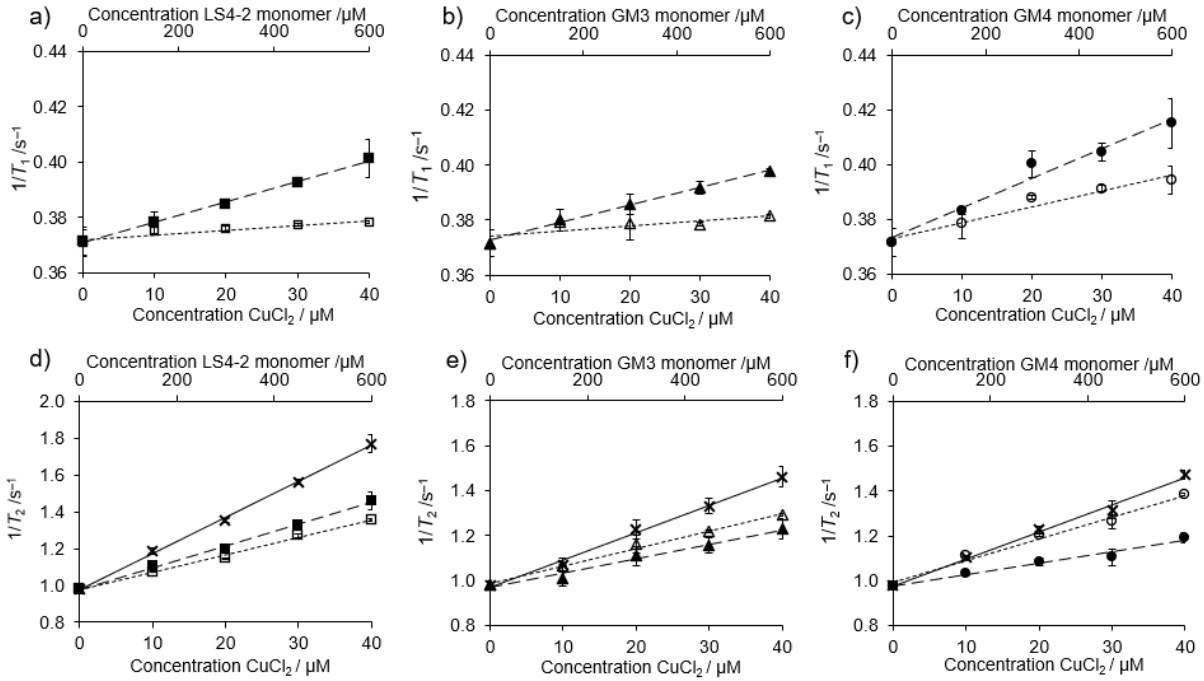


Figure 5.16: ^{1}H-NMR T_1 (a,b,c) and T_2 (d,e,f) relaxivity plots, showing reciprocal of relaxation time as a function of $CuCl_2$ concentration for relaxation rates recorded of samples at pH 7.0 in 100 mM HEPES buffer in the presence of 5 equivalents LS4-2 (a,d), GM3 (b,e) and GM4 (c.f) peptide trimer compared to the relaxation rates of the same concentration of peptide monomer without any metal (empty data points – LS4-2 □, GM3 Δ and GM4 ○). $1/T_1$ relaxation rates (a,b,c) are shown as full data points (LS4-2 ■, GM3 ▲ and GM4 ●) and $1/T_2$ relaxation rates (d,e,f) as crosses × (before correction) and as full data points (after correction, LS4-2 ■, GM3 ▲ and GM4 ●). Samples recorded at 293 K on a 300 MHz (7 T) NMR spectrometer. Error bars determined from standard deviation of three independent repeat experiments.

For all the peptides presented in this chapter, r_1 and r_2 relaxivities at 1.4 and 7 T were found to be reduced compared to MB1-2. Lower relaxivities suggest that the redesign of the binding site has influenced one or more important parameters, such as the Cu(II) hydration state, distance r_{MH} between the metal ion and the water protons, water residence times τ_m and electron relaxation times. GM3, with His_3 layer in ***a*** position, shows lower relaxivities ($r_1 = 2.2 \pm 0.4$ mM^{-1} s^{-1} and $r_2 = 6.0 \pm 0.7$ mM^{-1} s^{-1} at 1.4 T and $r_1 = 0.6 \pm 0.1$ mM^{-1} s^{-1} and $r_2 = 7.0 \pm 0.5$ mM^{-1} s^{-1} at 7 T). For a peptide with a similar His_3 binding site, Pecoraro and co-workers, determined 1 or 2 water molecules to be bound to Cu(II).[10, 11, 18]

For GM3 compared with CS1-2 ($r_1 = 7.3 \pm 0.4$ mM^{-1} s^{-1} and $r_2 = 18.2 \pm 0.6$ mM^{-1} s^{-1} at 1.4 T and $r_1 = 1.1 \pm 0.1$ mM^{-1} s^{-1} and $r_2 = 14.7 \pm 0.8$ mM^{-1} s^{-1} at 7 T), which are likely to have similar coordination geometry and, therefore, similar hydration state, the relaxivities are lower. This suggests an influence of water residence times and/or different electron relaxation time. In Section 5.3.4, LS4-2 and GM4 were hypothesised to have similar Cu(II) coordination in the presence of 1 equivalent of Cu(II) per peptide trimer. Here, they presented different relaxivities,

suggesting different features in Cu(II) coordination that influence relaxivity. These could be different number of inner-sphere and second-sphere water molecules, relative residence times and distances to the metal ion. In particular, hydrogen bonding network, which potentially includes second-sphere water molecules, could vary across the series due to differences in the amino acid residues in the hydrophobic core.

5.3.8 Influence of pH on metal binding and relaxivity

To gain insights into the effect of modifications in Cu(II) coordination in GM3, GM4 and LS4-2, which all feature His in their binding site, CD folding and tryptophan quenching were monitored at pH 7.4 (blood physiological pH) and were compared to pH 7.0. In free His, the pK_a of the NH hydrogen on the imidazolium ring is 6.0 and it is sensitive to the environment of the His. For example the close proximity of the aspartic acid carboxylate can stabilise the His protonated form.[26, 27]

At pH 7.4, GM3 and LS4-2 are more folded than at pH 7.0, with 90% folding and 80%, respectively (Figure 5.17a,e). Moreover, their quenching profile at pH 7.4 is different from pH 7.0 (Figure 5.17b,f), even though the log K_a determined from the fitting were comparable to relative compound at pH 7.0 (Table 5.7).

On the other hand, GM4 folding is the same as pH 7.0 (Figure 5.17c), but the Trp quenching is significantly different (Figure 5.17d). Data fitting for GM4 suggests that two Cu(II) ions can be bound at the binding site and the relative affinity constants are comparable, with log K_{a1} being slightly reduced from 7.6 ± 1 to 7.2. However, only one measurement was conducted at pH 7.4, therefore, this difference could be due to experimental error.

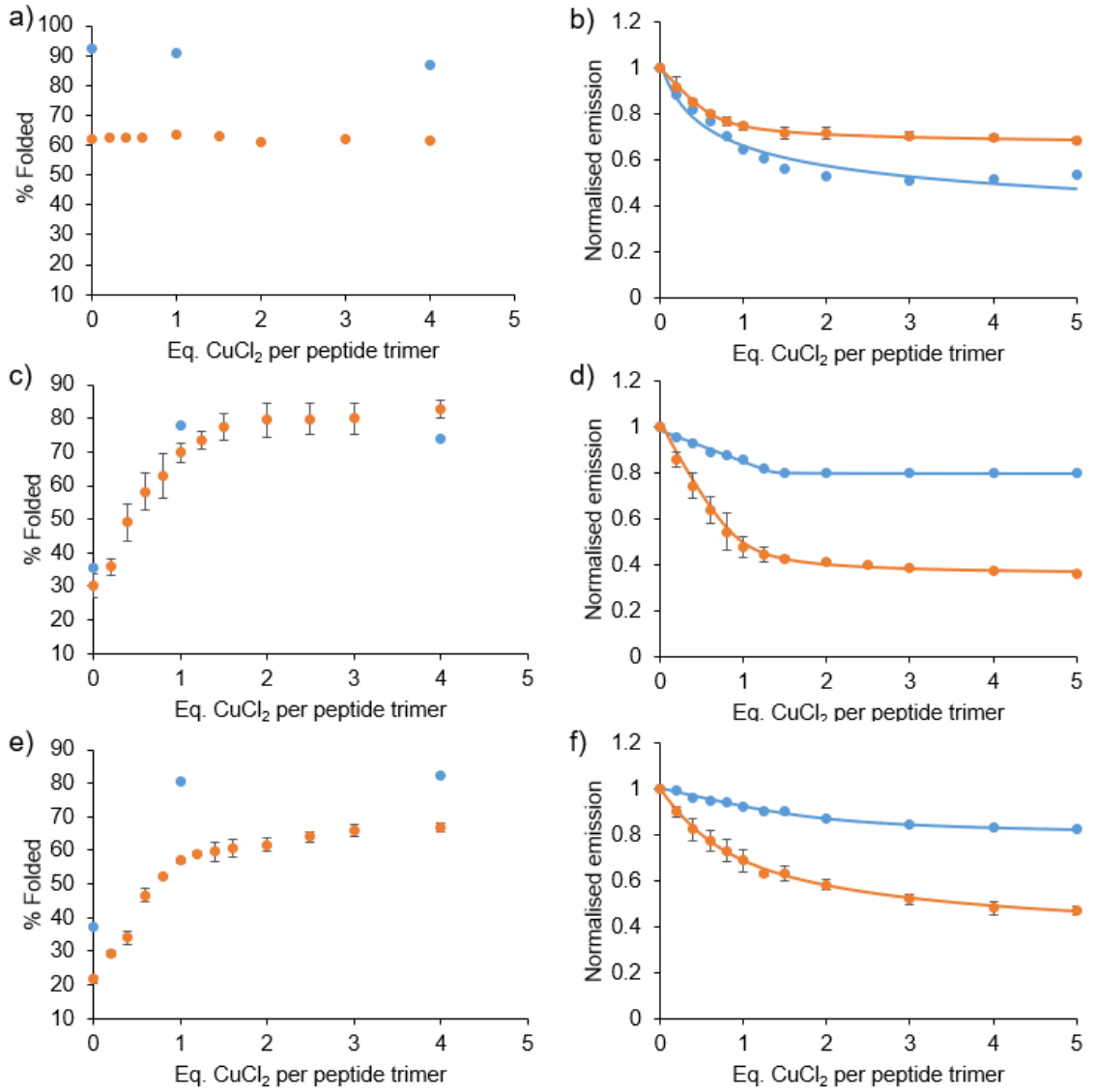


Figure 5.17: Binding curves of CD folding (a,c,e) and normalised emission intensity of tryptophan fluorescence (b,d,f) showing $CuCl_2$ titration into 30 mM CS1-2 (a,b), GM4 (c,d) and LS4-2 (e,f) peptide monomer in 10 mM HEPES buffer pH 7.0 (orange) or pH 7.4 (blue). Plot of % folded based on the molar ellipticity at 222 nm, as a function of $CuCl_2$ concentration. Fluorescence emission λ_{ex} = 280 nm, λ_{em} integrated between 300 and 455 nm. Data fitted using DynaFit[22] to a nonlinear least-squares fitting based on $1/3M + L \leftrightarrow 1/3ML_3$ and $1/3M + 3L \leftrightarrow 1/3ML_3 \leftrightarrow 1/3M_2L_3$ (GM4) models. Error bars determined from standard deviation of three independent experiments.

Table 5.7: Values of log K_a determined from CD and fluorescence data fitting. Samples prepared in 10 mM HEPES buffer pH 7.0 and pH 7.4. Data fitted using DynaFit[22] to a nonlinear least-squares fitting based on $1/3M + L \leftrightarrow 1/3ML_3$ and $1/3M + 3L \leftrightarrow 1/3ML_3 \leftrightarrow 1/3M_2L_3$ (GM4) models. Error determined from standard deviation of three independent experiments.

	pH 7.0	pH 7.4
LS4-2	5.0 ± 0.2	4.9
GM3	5.5 ± 0.2	5.5
GM4	7.6 ± 0.1	7.2
	6.8 ± 0.3	6.6

A UV-Visible experiment on GM3 was conducted to determine any variance of absorption for Cu(II) *d-d* transitions as a function of pH (Figure 5.18a). From pH 7.0, where λ_{max} = 723 nm, a reduction of pH from 7.0 to 6.4 resulted in a marginal red shift and an increase in absorption. When the pH was raised to 7.4 and 7.8, a shift to shorter wavelength was recorded and a reduction of absorption was observed, the latter being a consequence of the variation in molar extinction coefficient (Figure 5.18b,c).

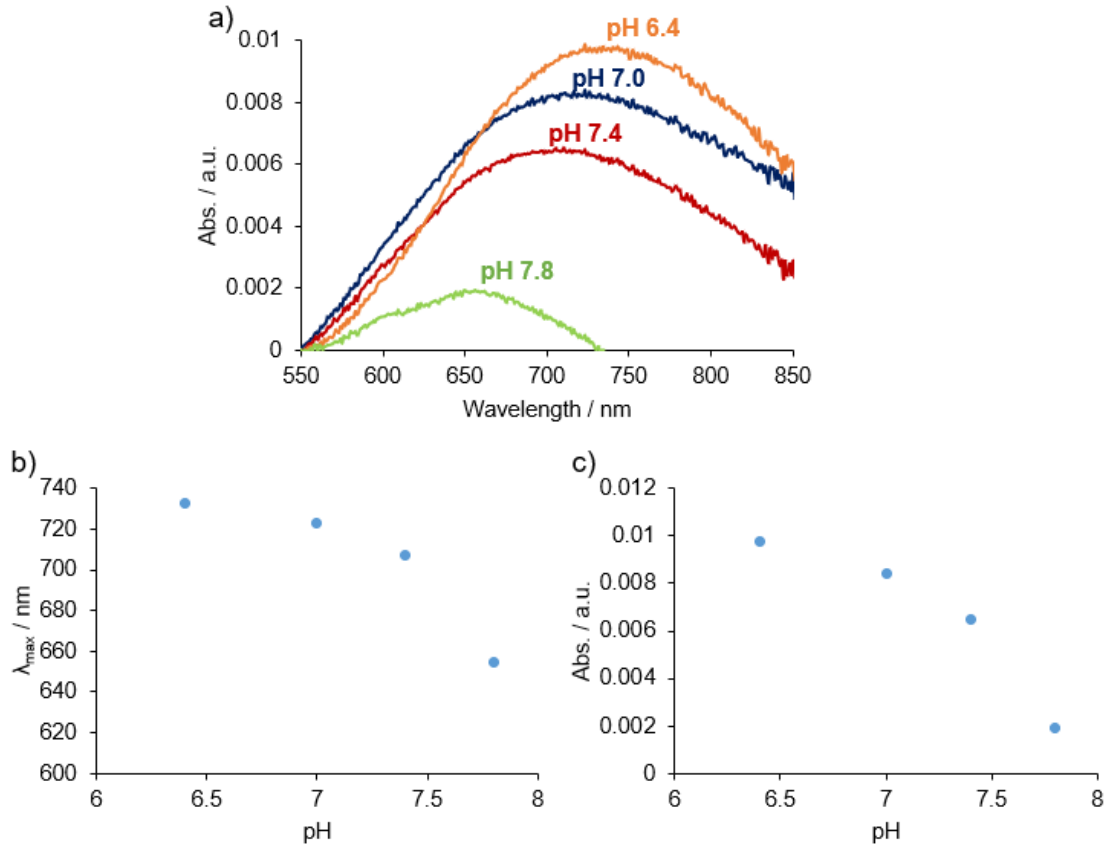


Figure 5.18: a) UV-Visible spectra in wavelength range 550-850 nm for a solution of GM3 450 µM peptide monomer and 150 µM $CuCl_2$) in 100 mM HEPES buffer pH 6.4 (orange), 7.0 (blue), 7.4 (red) and 8.0 (green); b) Relative wavelength of maximum absorbance (λ_{max}) and c) maximum absorbance (Abs.) for Cu(II) d-d transitions in GM3 recorded in the wavelength range 550-850 nm at different pH.

These results suggest that, in GM3 and LS4-2, Cu(II) coordination is different between pH 7.0 and 7.4. This could be a consequence of His deprotonation, when the pH is higher, which leads to Cu(II) coordination rearrangement. His deprotonation would also result in a less positive charge within the hydrophobic core, which would lead to higher folding in these two peptides. Moreover, the blue-shift in Cu(II) *d-d* transitions is consistent with more nitrogen donor(s) being

bound to Cu(II), such as that of His, and the reduction of absorption suggests an increase in Cu(II) coordination number as result of formation of a more centrosymmetric system such as a His_3 binding site.[28]

On the other hand, GM4 folding does not vary with different pH, suggesting that eventual His protonated residues can be better accommodated in ***a*** position rather than in ***d*** position as in LS4-2. However, the different quenching behaviour between the two pH, suggests a different coordination as was observed in GM3 and LS4-2. To support this, the log K_a determined for the complexation of the first Cu(II) ion is lower, suggesting that Cu(II) binds within a different environment.

Relaxivity measurements were conducted at pH 7.4 to better understand the variation in Cu(II) coordination for these peptides and subsequent implications to MRI relaxivity. The relaxivities at pH 7.4 are mostly the same to that at pH 7.0 within experimental error (Table 5.8). r_2 values appears slightly reduced. However, the experiment at pH 7.4 was conducted only once with only two samples to determine relaxivity, so r_2 variance could be attributed to experimental error. This implies that variation in Cu(II) coordination does not impact on the relaxivities, mainly as a consequence of an unvaried number of inner-sphere water molecule(s).

Table 5.8: ^{1}H-MRI r_1 and r_2 relaxivities for a series of peptides and number of inner-sphere water molecules. NMR samples prepared in 100 mM HEPES buffer pH 7.0 or 7.4. Samples recorded at 293 K on a 60 MHz (1.4 T) NMR spectrometer. Error determined from standard deviation of three independent repeat experiments (pH 7.0).

	pH 7.0		pH 7.4	
	r_1 / mM^{-1} s^{-1}	r_2 / mM^{-1} s^{-1}	r_1 / mM^{-1} s^{-1}	r_2 / mM^{-1} s^{-1}
LS4-2	5.1 ± 0.5	13.6 ± 0.8	4.7	12.5
GM3	2.2 ± 0.4	6.0 ± 0.7	2.5	5.0
GM4	2.4 ± 0.1	4.4 ± 0.7	2.6	4.3

5.3.9 Cu(II) displacement in the presence of Zn(II)

Zn(II) competition studies were undertaken and compared with results for $Cu(MB1\text{-}2)_3$, in which the addition of Zn(II) to the $Cu(MB1\text{-}2)_3$ led to a 20% decrease of the Cu(II) species. The extent of transmetallation was determined through reduction of $1/T_1$ relaxation rate after 1 h as consequence of formation of a non-paramagnetic Zn(II) metallopeptide. Here, 1 equivalent of $ZnCl_2$ (40 μM) was added to 1 equivalent of either $Cu(CS1\text{-}2)_3$ and $Cu(LS4\text{-}2)_3$ trimers, respectively. The contribution of the Zn(II) peptide is shown in Figure 5.19, with equivalence

between $1/T_1$ relaxation rate of HEPES buffer (dark blue) and that of Zn(II) in the presence of MB1-2 (light blue). In $Cu(CS1\text{-}2)_3$, after Zn(II) addition, $1/T_1$ relaxation rate was reduced from 0.63 to 0.46 s^{-1}, indicating that 27% displacement of Cu(II). In $Cu(LS4\text{-}2)_3$, reduction in $1/T_1$ relaxation rate was from 0.51 to 0.44 s^{-1}, corresponding to a 14% Cu(II) displacement and 86% residual $Cu(LS4\text{-}2)_3$. Taken together, these results, suggest that MB1-2, CS1-2 and LS4-2 are more selective for Cu(II) than Zn(II). CS1-2 showed the highest rate of transmetallation, that can be attributed to the lower number of potential donor atoms, and a site that presents lower coordination numbers which is more suitable for Zn(II) binding.

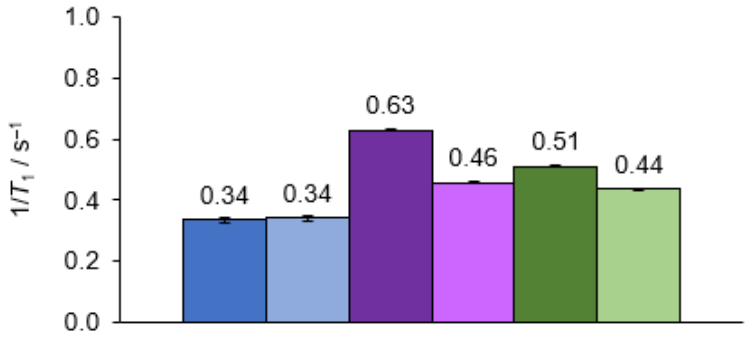


Figure 5.19: Diagram showing ^{1}H-NMR $1/T_1$ relaxation rate for a solution of HEPES 100 mM pH 7.0 (blue), 40 μM $ZnCl_2$ in HEPES 100 mM pH 7.0 (light blue), 40 μM $CuCl_2$ and 1 equivalent CS1-2 trimer without (purple) and with (light purple) 40 μM $ZnCl_2$ and 40 μM $CuCl_2$ and 1 equivalent LS4-2 trimer without (green) and with (light green) 40 μM $ZnCl_2$ in HEPES 100 mM pH 7.0. Samples were recorded at 293 K on a 60 MHz (1.4 T) NMR spectrometer. Error bars determined from standard deviation of three independent repeat experiments.

5.4 Discussion

This chapter explores the impact on relaxivity of Cu(II) coordination chemistry when bound within a coiled-coil. This is achieved by altering the identity of the first coordination ligand set. Affinity constants were found to be dependent on the nature of binding residues and generally increased in the presence of His, which is a common amino acid for Cu(II) binding to natural proteins.

This chapter further confirms that when the binding site is designed in a buried position in the coiled-coil hydrophobic core, but still accessible to water, such as could be the case for MB1-2,[29] CS1-2 and LS4-2, the systems are characterised by high relaxivities. This could be due to optimised water exchange or to a partially structured binding site that allows the presence of water molecule(s) for Cu(II) complexation (Figure 5.20a,b,c). GM3 and GM4 show low relaxivity, suggesting that the presence of His_3 layer in ***a*** position (Figure 5.20d) has an impact on Cu-H

distances, water residence time and/or electron relaxation. When the pH is raised from 7.0 to 7.4, Cu(II) coordination in the peptides containing His (GM3, GM4 and LS4-2) is modified without any impact on the relaxivities, implying no variance in the parameters that highly contribute to relaxivity, such as the number of inner-sphere water molecules. Since Asp residues can be bound either monodentate (through one carboxylate O) or bidentate (through both carboxylate O), therefore, their coordination cannot be easily predicted, but can be explored using infrared spectroscopy.

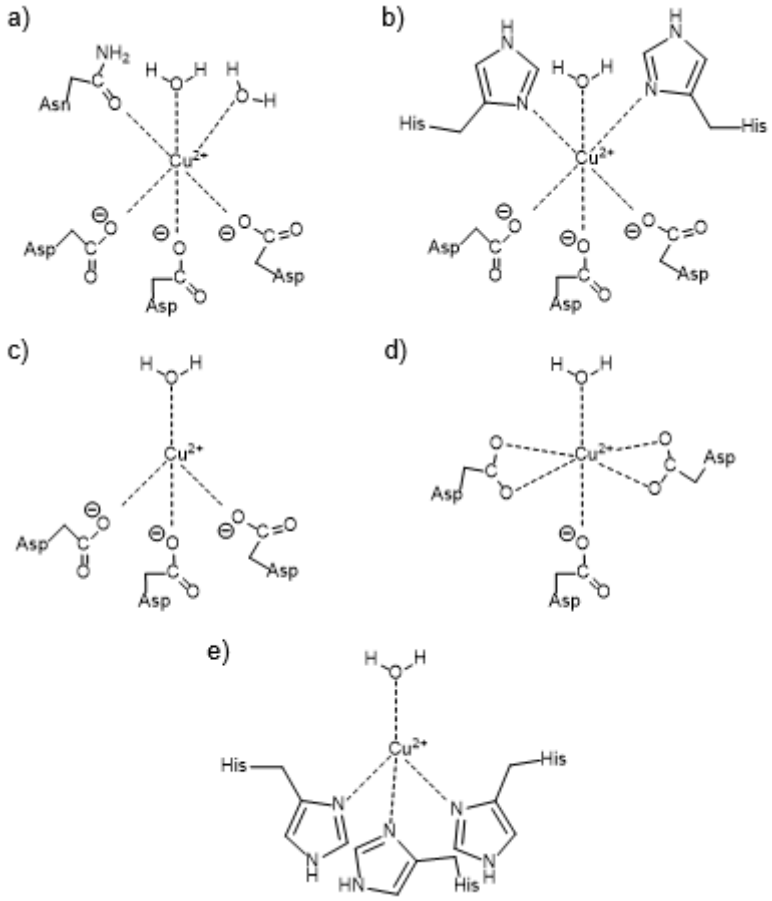


Figure 5.20: Based on the results presented in this chapter, potential Cu(II) binding sites in a) $Cu(MB1\text{-}2)_3$ and b) $Cu(LS4\text{-}2)_3$, featuring six-coordinated geometry; c) $Cu(CS1\text{-}2)_3$ and e) $Cu(GM3)_3$, featuring four-coordinated geometry. d) $Cu(CS1\text{-}2)_3$ in a six-coordinated geometry.

5.5 Conclusions

In this chapter, knowledge about the factors that governs Cu(II) coordination and the MRI efficiency of this class of contrast agents has been expanded from Chapter 3 and Chapter 4. Mutations of first coordination sphere residues, especially as consequence of introduction of His residues, have provided enhanced Cu(II) binding affinities. Moreover, such mutations offer a powerful method to tune MRI relaxivity, through variation of coordination geometries and, consequently, of the molecular parameters which influence relaxivity such as water residence time and Cu(II) hydration state.

EPR hyperfine studies are needed to elucidate the different modes of Cu(II) binding at different pH and to determine the presence of nitrogen donors and any difference with pH variation (UV-Visible spectroscopy presented here can offer only a qualitative analysis). Moreover, variable temperature ^{17}O-NMR experiments and NMRD (Nuclear Magnetic Relaxation Dispersion) experiments can determine the variation of relaxivity at different proton Larmor frequencies and provide essential parameters to characterise the metal binding site such as water residence time $\tau_{m,}$ hydration state q, distance metal-water proton $r_{Cu\text{-}H,}$, rotational correlation time $\tau_{R,}$ hyperfine interactions $A/\hbar$. Finally, crystallisation of the metallopeptides would be helpful to characterise the different Cu(II) binding sites and confirm the proposed binding modes.

References

1. D. H. Powell, L. Helm and A. E. Merbach, *J. Chem. Phys.*, 1991, **95**, 9258-9265.
2. D. H. Powell, P. Furrer, P.-A. Pittet and A. E. Merbach, *J. Phys. Chem.*, 1995, **99**, 16622-16629.
3. A. Pasquarello, I. Petri, P. S. Salmon, O. Parisel, R. Car, É. Tóth, D. H. Powell, H. E. Fischer, L. Helm and A. E. Merbach, *Science*, 2001, **291**, 856-859.
4. R. B. Lauffer, *Chem. Rev.*, 1987, **87**, 901-927.
5. E. L. Que, E. Gianolio, S. L. Baker, A. P. Wong, S. Aime and C. J. Chang, *J. Am. Chem. Soc.*, 2009, **131**, 8527-8536.
6. I. Bertini and R. Pierattelli, *Pure Appl. Chem.*, 2004, **76**, 321-333.
7. R. H. Holm, P. Kennepohl and E. I. Solomon, *Chem. Rev.*, 1996, **96**, 2239-2314.
8. J. T. Rubino and K. J. Franz, *J. Inorg. Biochem.*, 2012, **107**, 129-143.
9. D. Shiga, Y. Hamano, M. Kamei, Y. Funahashi, H. Masuda, M. Sakaguchi, T. Ogura and T. Tanaka, *J. Biol. Inorg. Chem.*, 2012, **17**, 1025-1031.
10. E. Mathieu, A. E. Tolbert, K. J. Koebke, C. Tard, O. Iranzo, J. E. Penner- Hahn, C. Policar and V. Pecoraro, *Chem. Eur. J.*, 2020, **26**, 249-258.
11. M. Tegoni, F. Yu, M. Bersellini, J. E. Penner-Hahn and V. L. Pecoraro, *PNAS*, 2012, **109**, 21234-21239.
12. M. L. Zastrow, A. F. Peacock, J. A. Stuckey and V. L. Pecoraro, *Nature Chem.*, 2012, **4**, 118.
13. K. J. Koebke, L. Ruckthong, J. L. Meagher, E. Mathieu, J. Harland, A. Deb, N. Lehnert, C. Policar, C. Tard and J. E. Penner-Hahn, *Inorg. Chem.*, 2018, **57**, 12291-12302.
14. O. A. Kharenko, D. C. Kennedy, B. Demeler, M. J. Maroney and M. Y. Ogawa, *J. Am. Chem. Soc.*, 2005, **127**, 7678-7679.
15. T. Kiyokawa, K. Kanaori, K. Tajima, M. Koike, T. Mizuno, J. I. Oku and T. Tanaka, *J. Pept. Res.*, 2004, **63**, 347-353.
16. T. Tanaka, T. Mizuno, S. Fukui, H. Hiroaki, J.-i. Oku, K. Kanaori, K. Tajima and M. Shirakawa, *J. Am. Chem. Soc.*, 2004, **126**, 14023-14028.
17. D. Shiga, D. Nakane, T. Inomata, H. Masuda, M. Oda, M. Noda, S. Uchiyama, K. Fukui, Y. Takano and H. Nakamura, *Biopolymers*, 2009, **91**, 907-916.
18. F. Yu, J. E. Penner-Hahn and V. L. Pecoraro, *J. Am. Chem. Soc.*, 2013, **135**, 18096-18107.
19. K. J. Koebke and V. L. Pecoraro, *ACS Catal.*, 2018, **8**, 8046-8057.
20. M. R. Gangula, *Struct. Chem.*, 2020, **31**, 1057-1064.
21. L. N. Slope, PhD, University of Birmingham, 2017.
22. P. Kuzmic, *Anal. Bioch.*, 1996, **237**, 260-273.
23. L. N. Slope, M. G. Hill, C. F. Smith, P. Teare, F. J. de Cogan, M. M. Britton and A. F. Peacock, *Chem. Comm.*, 2020, **56**, 3729-3732.
24. E. Prenesti, P. G. Daniele, M. Prencipe and G. Ostacoli, *Polyhedron*, 1999, **18**, 3233-3241.
25. E. Prenesti, P. G. Daniele, S. Berto and S. Toso, *Polyhedron*, 2006, **25**, 2815-2823.

26. T. Liu, M. Ryan, F. W. Dahlquist and O. H. Griffith, *Protein Sci.*, 1997, **6**, 1937-1944.

27. B. H. Pogostin, A. Malmendal, C. H. Londergan and K. S. Åkerfeldt, *Molecules*, 2019, **24**, 405.

28. S. Gómez-Salces, F. Aguado, R. Valiente and F. Rodríguez, *Angew. Chem.*, 2012, **124**, 9469-9472.

29. A. Shah, M. J. Taylor, G. Molinaro, S. Anbu, M. Verdu, L. Jennings, I. Mikulska, S. Diaz-Moreno, H. El Mkami and G. M. Smith, *PNAS*, 2023, **120**, e2219036120.

CHAPTER 6

MANGANESE(II) COILED-COILS

6.1 Introduction

Manganese is a crucial element for life as it is involved in essential hydrolytic and redox processes such as oxidation of water, during photosynthesis, and the disproportionation of superoxide in the manganese-based superoxide dismutase (SOD).[1] Moreover, it is important for medical use such as in SOD mimetics[2-4] and MRI contrast agents.[5-9] The use of Mn(II) in T_1-MRI contrast agents offers an efficient method to replace Gd(III) in patients with renal diseases.[10] This is because Mn(II) has 5 unpaired electrons (S = 5/2) in *d* orbitals in high-spin complexes which are also symmetric and spherical, providing long electron relaxation times. In addition, the inner-sphere water molecule(s) in Mn(II) complexes generally show exchange kinetics comparable to Gd(III) complexes but reduced Mn(II)-water protons distances (around 2.5-2.9 Å in Mn(II) complexes compared to around 3.1 Å in Gd(III) complexes), partially compensating for the lower number of unpaired electron on Mn(II).[11] Moreover, availability of the oxidised form Mn(III) which is sustainable under physiological conditions but is less paramagnetic, allows for the design of redox-responsive MRI contrast agents.[12-14]

As for Gd(III) complexes, it remains essential that Mn(II) complexes show high stability, kinetic inertness and selectivity from other essential elements such as Zn(II), Cu(II), Mg(II) and Ca(II). However, due to the relatively large ionic radius of Mn(II) and spherical distribution of the electrons in the *d* orbitals, Mn(II) complexes are generally liable and less stable than complexes with the same ligand and any other transition metals with 2+ charge because of the lack of ligand-field stabilisation energy. In the Irving-Williams series, which relates the octahedral complexes stability of the first-row transition metals, Mn(II) is the least stable Mn(II)<Fe(II)<Co(II)<Ni(II)<Cu(II)>Zn(II). Therefore, in the presence of endogenous metals such as Zn(II), transmetallation is likely to occur. Ligand design can be used to enhance Mn(II) *vs* Zn(II) selectivity such as introducing the binding site within a large and rigid cavity, since Mn(II) is about 10% larger than Zn(II).

In biological proteins, Mn(II) is predominantly bound to oxygen donors (81%), such as those from solvent water molecules, Asp, Glu or backbone carbonyl groups. Nitrogen donors can also be present (18%), mainly constituted by His.[15] Because of the lack of ligand field stabilization

energy, the geometry of Mn(II) complexes is difficult to be predicted, however, the octahedral geometry (sometimes distorted) appears to be the most prevalent in Mn(II) proteins.[15] Moreover, Mn-O (water) distances in natural proteins are very short, around 2.0 Å,[15] resulting in Mn-H (water) distances of about 2.5 Å.

This chapter reports of a class Mn(II) binding peptides designed to fold in three-stranded coiled-coils and determines for the first time their MRI relaxivity. Finally, transmetallation in the presence of Zn(II) is explored to gain more insight into the kinetic stability of Mn(II) to the designed peptides.

6.2 Experimental

Materials, peptide synthesis and purification as in Chapter 3. Manganese(II) chloride purchased from Sigma Aldrich and used as received.

6.2.1 UV-Vis spectroscopy

UV-Vis experiments to determine peptide concentration were conducted on a Cary 50 UV Spectrophotometer as described in Chapter 4.

6.2.2 Circular Dichroism (CD) spectroscopy

CD spectra were recorded on a Jasco J-715 Spectropolarimeter. The optical chamber was purged with nitrogen and kept under a nitrogen atmosphere throughout the duration of the experiments. A 1 mm pathlength, 300 µl quartz cuvette was used with three scans recorded from 400-200 nm using a 100-200 nm min^{-1} scan rate with 1 nm bandwidth and a 1 s response.

A 10 mM HEPES buffer solution pH 7.0 was recorded as a blank before $MnCl_2$ was titrated into a solution of peptide monomer with concentration previously determined by UV-Vis analysis. All solutions were left to equilibrate for 15 mins before scanning. The ellipticity (θ_{obs}) data collected in millidegrees (mdeg), was converted to molar ellipticity per residue, [θ] (deg $dmol^{-1}$ cm^2) using Equation 1.

$$[\theta] = \frac{\theta_{\text{obs}}}{10\ lcN} \tag{1}$$

where θ_{obs} is the measured ellipticity at 222 nm in mdeg, c is the concentration in M, N is the number if amino acids in the sequence and l is the pathlength in cm.

The helical content was then calculated as the percentage folded using Equation 2, where the denominator represents the molar ellipticity for a fully folded coiled-coil.[16]

$$\% \text{ Folded} = \frac{[\theta_{222}] - 640}{\left(-42500 \times \left(1 - {}^{3}/_{N}\right)\right) - 640} \quad (2)$$

Kinetic data were recorded by monitoring the ellipticity at 222 nm (θ_{obs}) of either 30 or 150 μM solution of peptide monomer (10 or 50 μM peptide trimer, respectively) in 10 or 50 mM HEPES buffer pH 7.0 (respectively) in the absence and presence of 1 equivalent $MnCl_2$ per equivalent of peptide trimer (10 or 50 μM $MnCl_2$, respectively), at 20°C. Data were collected ~3 seconds after $MnCl_2$ addition. θ_{obs} was converted to % folding using Equations 1 and 2.

Thermal unfolding data were recorded by monitoring the ellipticity at 222 nm for a 150 μM solution of peptide monomer in 50 mM HEPES buffer pH 7.0 in the absence and presence of 50 μM $MnCl_2$, using a Jasco Peltier Type PTC-4235 temperature controller ramping from 20°C to 40°C.

6.2.3 Nuclear magnetic resonance

^{1}H-NMR measurements, at high magnetic field (7 T), were performed on a Bruker Avance III HD spectrometer, operating at proton resonance frequency of 300.13 MHz. All measurements were performed at 20 ± 0.2°C. Data were acquired using 5 mm ^{1}H coil in a Bruker Diff30 probe. A 90° pulse duration calibrated for each sample was used for the experiments. For T_1 NMR relaxation measurements, a Saturation Recovery sequence (described in Section 2.7.3) was used. A series of 8 spectra were collected with logarithmically spaced recovery delays from 0.01 s to a maximum of 12-15 s, with 8 signal averages, 8k data points and spectral width of 10 kHz. For T_2 NMR relaxation measurements the Carr-Purcell-Meiboom-Gill (CPMG) pulse sequence (described in Section 2.7.3) was used with a repetition time > $5T_1$ (≥ 10 s), 8 signal averages, 16k data points and spectral width of 10 kHz. The variable counter list for the CPMG experiments was logarithmically spaced with 7 values from 2 to 512, with a CPMG echo time value of 2 ms.

^{1}H-NMR measurements at low magnetic fields (1 and 1.4 T) were performed on a Spinsolve benchtop NMR (Magritek, Aachen, Germany), operating at proton resonance frequency of 43 and 61 MHz, respectively. Data were acquired at 21.0 ± 0.5°C (controlled room temperature) using 3 mm NMR tubes and automated 90° pulse width of 7 μs. For T_1 NMR relaxation measurements, an Inversion Recovery sequence (described in Section 2.7.3) was used with a repetition time > $5T_1$ (≥ 10 s). A series of 11 spectra were collected with delays linearly spaced from 0.001 s to a maximum of 5-10 s, 8 signal averages and 32k points. For T_2 NMR relaxation measurements a CPMG pulse sequence was used with a repetition time > $5T_1$ (≥ 10 s). A series of 10 spectra were recorded with a 2 ms CPMG echo time and final echo time of 5 s, 8 signal averages and 32k data

points. All data were analysed using Prospa (Magritek, Aachen, Germany). Signal intensity curves were fitted in KaleidaGraph (Synergy, USA).

Binding of Mn(II) by peptide trimers was monitored by measuring the ^{1}H T_1 and T_2 magnetic resonance relaxation times of solutions of 40 μM $MnCl_2$ in the presence of increasing concentrations of peptide monomer, in 100 mM HEPES buffer pH 7.0. The r_2 relaxivity of the apo peptide was used to correct $1/T_2$ and relative r_2 for the Cu(II) complexes, by accounting for the contribution of excess unbound peptide.

The r_1 and r_2 relaxivities were calculated from the gradients of plots of the average, based on three independent repeats, ^{1}H magnetic resonance relaxation rates ($1/T_1$ and $1/T_2$ respectively), as a function of $MnCl_2$ concentration. For measurements at 1.4 T, a range of solutions were measured, containing 0, 10, 20, 30, 40 $MnCl_2$ and 15 equivalents of peptide monomer (5 equivalents peptide trimer), to drive Mn(II) complexation. For measurements at 1 and 7 T, relaxivity was measured using samples containing 0 and 40 μM $MnCl_2$ in the presence of 15 equivalents of peptide monomer. To eliminate any error due to sample preparation, the same solutions were analysed at 1, 1.4 and 7 T. Analogous control experiments were performed for solutions of peptide in the absence of $MnCl_2$. The r_2 relaxivity of the apo peptide (see Section 5.3.6) was used to correct $1/T_2$ and relative r_2 for the Mn(II) complexes, by accounting for the contribution of excess unbound peptide.

Zn(II) transmetallation experiments were performed by adding 40 μM $ZnCl_2$ to a 40 μM solution of $MnCl_2$ in the presence of 1 equivalent of peptide trimer (40 μM peptide trimer or 120 μM peptide monomer) in 100 mM HEPES buffer pH 7.0. Control samples were prepared using the same procedure without the addition of $ZnCl_2$. T_1 measurements were performed 15 minutes after sample preparation.

6.3 Results

6.3.1 Peptide design

The peptides in this study (Table 6.1 and Figure 6.1), named CS1-2, MB1-2, LS4-2 and GM4, were previously introduced in Chapter 3 and in Chapter 5 for Cu(II) binding. They all present Asp in their sequence, aiming to provide suitable ligands for Mn(II). Therefore, in this study, the peptides lacking oxygen donors, such as GM3 (His_3 site), are not considered.

CS1-2 is designed to have only Asp donors, although other ligands can participate in Mn(II) binding such as Glu, backbone carbonyl group or water molecules (Figure 6.2). In LS4-2, a His layer is introduced as a potential ligand. In MB1-2 the His layer is replaced by Asn, to elucidate the role of the His layer in LS4-2. GM4 presents the same binding residues as LS4-2 in reverse order. Finally, the MB1C control sequence (designed with no potential binding residues in the hydrophobic core of an assembled coiled-coil) was used to determine the presence on any non-specific binding.

Table 6.1: Peptides used in this chapter. The amino acids that could form the manganese binding site are underlined and coloured in red (Asp), green (His) and in blue (Asn).

CS1-2	Ac-G IAAIEQK IAAIEWK DAAIEQK IAAIEQK IAAIEQK G-NH_2
LS4-2	Ac-G IAAIEQK IAAHEWK DAAIEQK IAAIEQK IAAIEQK G-NH_2
MB1-2	Ac-G IAAIEQK IAANEWK DAAIEQK IAAIEQK IAAIEQK G-NH_2
GM4	Ac-G IAAIEQK IAADEWK HAAIEQK IAAIEQK IAAIEQK G-NH_2
MB1C	Ac-G IAAIEQK IAAIEWK IAAIEQK IAAIEQK IAAIEQK G-NH_2

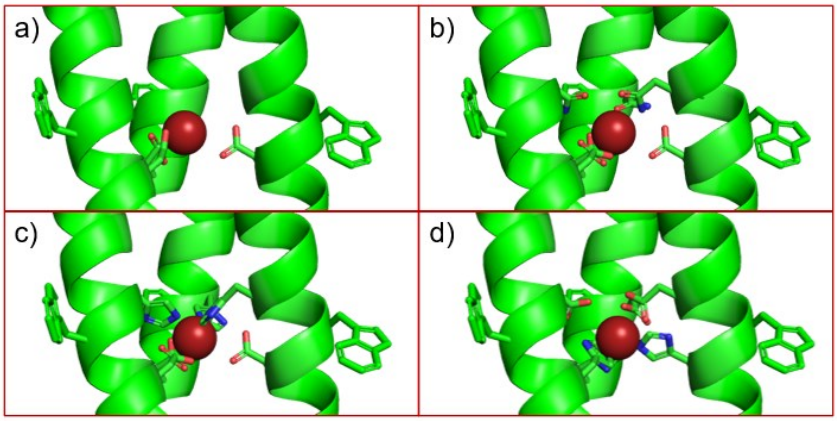


Figure 6.1: Cartoons representing theoretical manganese binding sites in a) $Mn(CS1\text{-}2)_3$, b) $Mn(MB1\text{-}2)_3$, c) $Mn(LS4\text{-}2)_3$, and c) $Mn(GM4)_3$. Peptide backbone shown as a helical ribbon and side chains shown as sticks, with oxygen in red and nitrogen in blue. Mn(II) ion shown as red sphere.

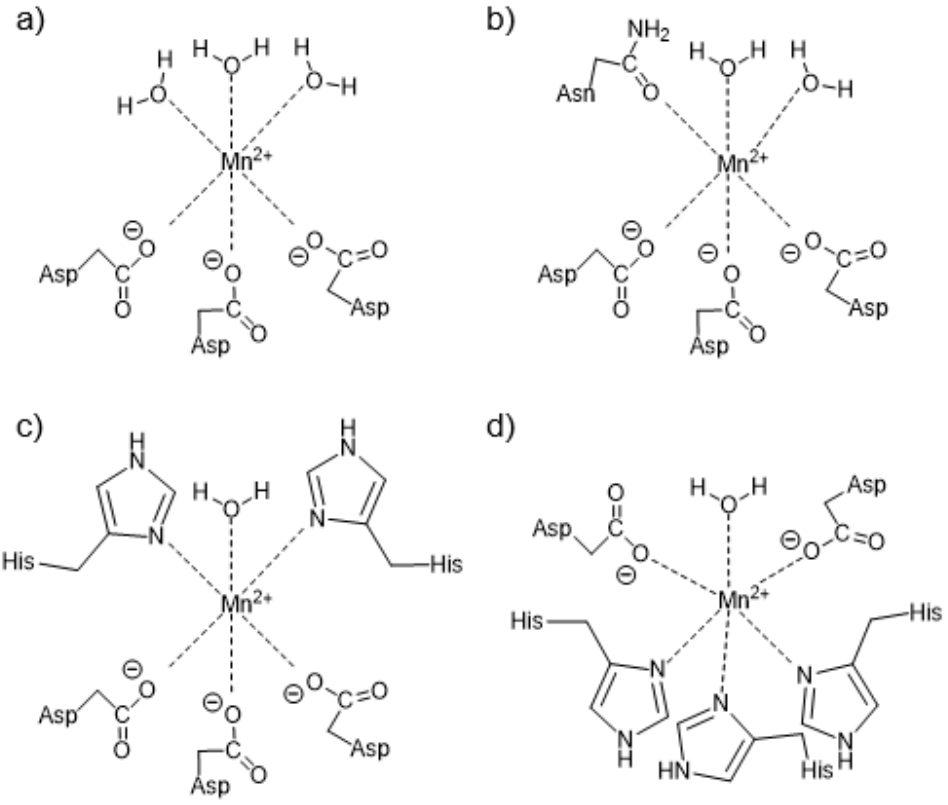


Figure 6.2: Hypothetical Mn(II) binding sites (Mn(II) hydration states generally based on relative Cu(II) complexes) in a) $Mn(CS1\text{-}2)_3$, b) $Mn(MB1\text{-}2)_3$, c) $Mn(LS4\text{-}2)_3$ and d) $Mn(GM4)_3$ in six-coordinated complexes.

6.3.2 Establishing peptide folding and log K_a determination for Mn(II) binding

CD studies were performed to assess Mn(II) binding through formation of an assembled folded structure starting from a 30 μM solution of peptide monomer. (Figure 6.3). As shown in Chapter 5, LS4-2 and GM4 are essentially unfolded in the absence of metal, while CS1-2 is more folded because of the presence of a Ile layer in place of the His (LS4-2) or Asp (GM4). After Mn(II) addition, LS4-2 and GM4 revealed a slight improvement in folding, while CS1-2 remained well folded throughout the experiment (Table 6.2).

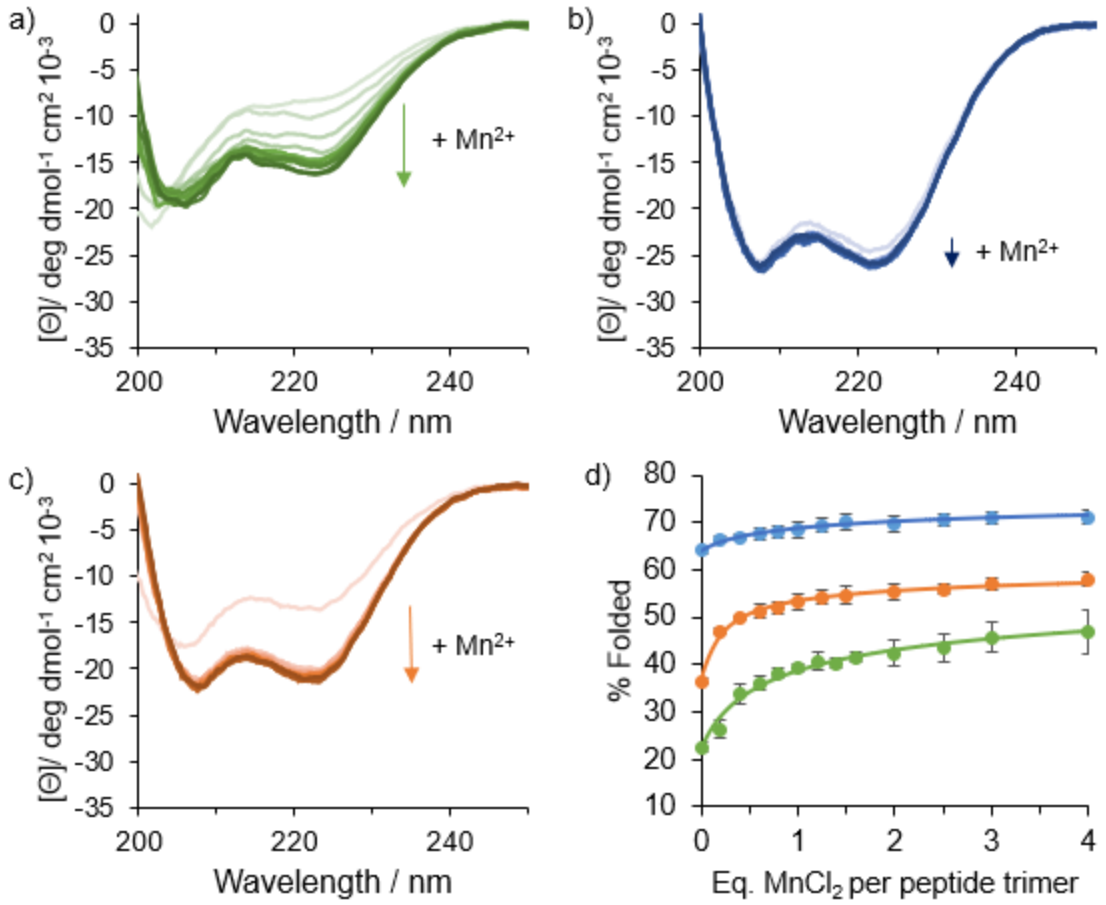


Figure 6.3: Representative CD spectra of $MnCl_2$ titration into 30 μM a) LS4-2, b) CS1-2 and c) GM4 peptide monomer solution and d) CD folding titration of $MnCl_2$ into 30 μM LS4-2 (green ●), CS1-2 (blue ●) and GM4 (orange ●) peptide monomer solution. Data are results of an average of three independent repeats and error bars derived from their standard deviation. The fitting was made with a 1/3M + L → $1/3ML_3$ model using DynaFit.[17] All samples were recorded in 10 mM HEPES pH 7.0 buffer at 293 K.

The fittings shown in Figure 6.4 to determine Mn(II) affinity to the peptides (log K_a) were made in accordance with a binding model of L + 1/3M ↔ $1/3ML_3$ (M: metal ion and L: peptide

monomer) with Dynafit.[17] The resulting log K_a values (Table 6.2) show that the three peptides have good affinities for Mn(II), in the same order of magnitude as Cu(II) compounds in Chapter 5 and Gd(III) complexes.[18] Because of the small variance of folding, caution should be taken when interpreting fitting results.

These values fall within the range observed for Mn(II) proteins and peptides.[19-22] However, they are 4-5 order of magnitude lower than those of Mn(II) complexes for use as MRI contrast agents (for MnEDTA log K_a = 9.17 and for MnPyC3A log K_a = 10.16 ± 0.02).[7, 23]

Table 6.2: % folding of the apo peptides compared to the metallo form (end of titration) and log K_a values determined from fitting CD data for 30 μM peptide monomer in 10 mM HEPES buffer pH 7.0, monitored by CD. Data fitted using DynaFit[17] to a nonlinear least-squares fitting based on $1/3M + L \leftrightarrow 1/3ML_3$ model. Error determined from standard deviation of three independent experiments.

	% Folding apo	% Folding metallo	log K_a
LS4-2	23 ± 1%	40 ± 2%	5.0 ± 0.3
CS1-2	50 ± 1%	54 ± 2%	5.2 ± 0.1
GM4	36 ± 4%	54 ± 3%	5.5 ± 0.1

6.3.3 Influence of peptide concentration on metal binding and peptide folding

The impact of higher concentrations of peptide monomer was evaluated for LS4-2, CS1-2, GM4 and MB1-2 (Figure 6.4). At 150 μM, LS4-2 and CS1-2 are more folded than at 30 μM (50 and 78%, respectively). No additional folding was determined at higher Mn(II) concentrations. At 150 μM, GM4 did not present higher folding in the apo form than at 30 μM (43%) and this remained essentially invariant during the titration.

At 30 μM, MB1-2 showed a very weak affinity for Mn(II) with log K_a = 2.5 ± 0.4 and a very slight improvement in folding, as reported by Dr. Anbu Sellamuthu and Dr. Sarah Newton.[24] Here, at 150 μM monomer concentration, the peptide becomes more folded, suggesting improved and concentration-dependent Mn(II) affinity to MB1-2. The low stability of MB1-2 compared to LS4-2 can be attributed to a preference for Mn(II) to bind to His (LS4-2) in ***d*** position over to Asn (MB1-2). This also suggests that the nature of the amino acid layer in ***d*** position is able to modulate Mn(II) stability.

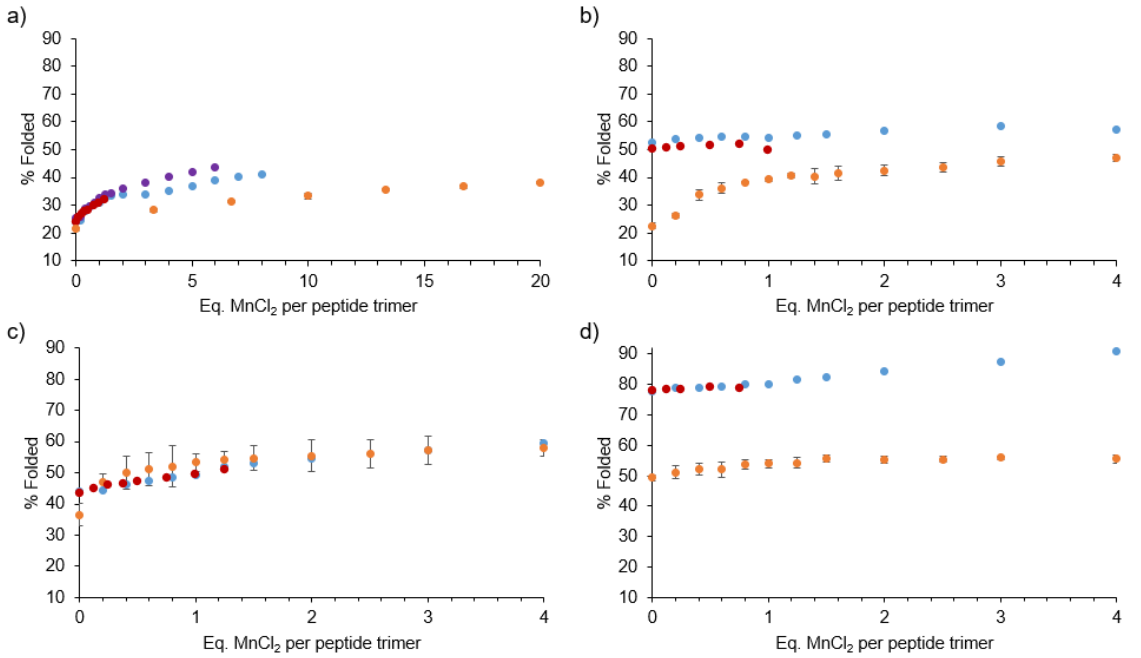


Figure 6.4: CD binding curves showing $CuCl_2$ titration into 30 μM (orange) and 150 μM (repeat 1 in red and repeat 2 in blue and purple) a) MB1-2 b) LS4-2 and c) GM4 and d) CS1-2 in 50 mM HEPES buffer pH 7.0 at 298 K, monitored by CD. Error bars determined from standard deviation of three independent experiments.

6.3.4 Folding kinetics and thermal stability

Folding kinetics of 30 μM (Figure 6.5a) and 150 μM (Figure 6.5b) MB1-2, LS4-2 and CS1-2 after addition of 1 equivalent $MnCl_2$ per peptide trimer (10 or 50 μM $MnCl_2$, respectively), revealed vary fast kinetics, with the folding occurring within the first 3-4 seconds after addition. Moreover, variation in peptide concentration was found not to affect binding kinetics.

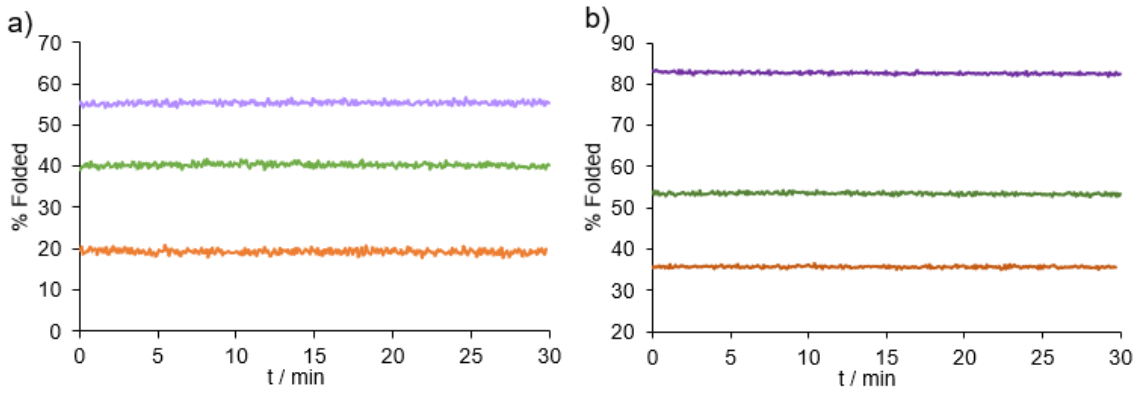


Figure 6.5: Plots showing variation over time at 298 K of % folding of a) 30 μM b) 150 μM LS4-2 (green), CS1-2 (purple) and GM4 (orange) monomer in the presence of 1 equivalent of $MnCl_2$ per peptide trimer. Samples prepared in pH 7.0 HEPES buffer a) 10 mM, b) 50 mM.

The thermal stability of $Mn(CS1\text{-}2)_3$, $Mn(LS4\text{-}2)_3$ and $Mn(MB1\text{-}2)_3$ was investigated over a biologically relevant temperature range 20 – 40°C, which include physiological temperature (37°C). MB1-2 and CS1-2 profiles in the presence of 1 equivalent of Mn(II) were compared with the respective apo peptide and Cu(II) complexes (which have already been reported in Chapter 3 and in Chapter 5). In MB1-2 (Figure 6.6a), the increase in temperature probably leads to nearly full Mn(II) decomplexation, as the folding at 40°C of the Mn complex is essentially the same as the apo peptide.

CS1-2 has similar folding at 20°C in the presence and in the absence of any metal, with no distinction, mainly due to a well-folded structure even in the apo form (Figure 6.6b). However, at higher temperatures, the profiles split, with the Cu(II) analogue being more stable at the increase of temperature and Mn(II) compound more prone to unfolding. Both Cu(II) and Mn(II) CS1-2 are more stable than the in apo form, suggesting that metal binding helps to prevent unfolding at higher temperatures. Because of the relative small variance between the folding of the apo peptide and of the Mn(II) complex, melting temperatures T_m were not possible to be determined in this temperature range.

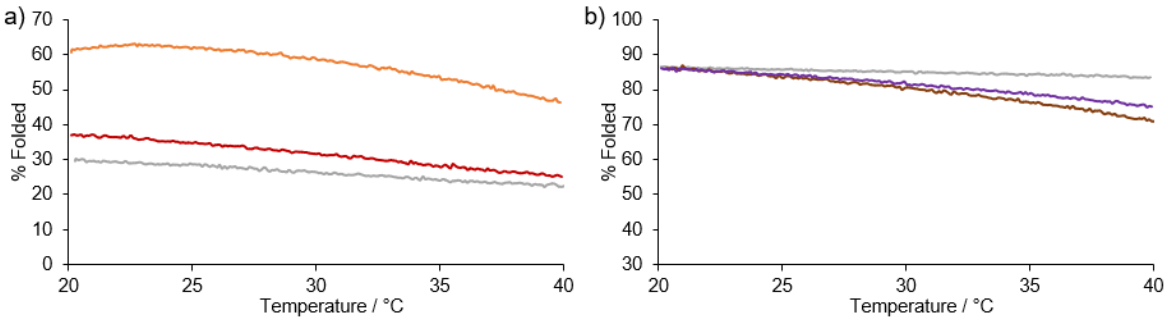


Figure 6.6: Plot showing variation between 20-40°C of % folding of 150 μM a) MB1-2 monomer in the absence (grey line) and in the presence of 1 equivalent of $CuCl_2$ (orange line) or $MnCl_2$ (red line) per peptide trimer and b) 150 μM CS1-2 monomer in the absence (brown line) and in the presence of 1 equivalent of $CuCl_2$ (grey line) or $MnCl_2$ (purple line), per peptide trimer. Samples prepared in 50 mM HEPES buffer pH 7.0.

6.3.5 MRI relaxivity at 1.4 T

In Chapter 3, the importance of working with an excess of peptide to ensure full metal complexation was introduced. NMR T_1 relaxation time can be used to monitor the formation of the metallopeptide system in a series of samples with increasing equivalents of peptide trimer (LS4-2, CS1-2 and GM4) per 40 μM $MnCl_2$ (Figure 6.7). The trends look almost identical for the three peptides and generally show that the most appreciable reduction in T_1 occurs between 0 and

2 equivalents of peptide trimer, and that 5 equivalents are sufficient to reach a plateau where no more metallopeptide is forming. These results are comparable with the trends for the Cu(II) complexes in Chapter 5, having similar log K_a values.

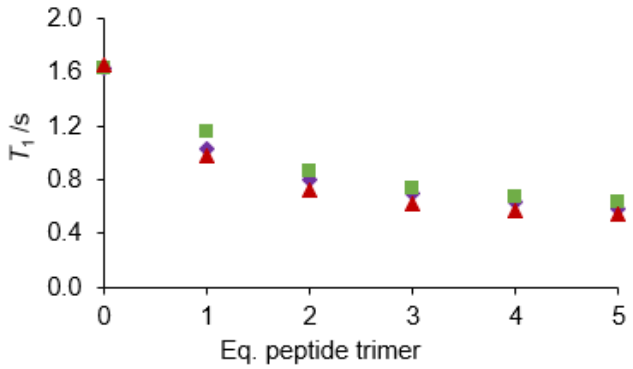


Figure 6.7: Plot of ^{1}H-NMR T_1 relaxation times for solutions of 40 μM $MnCl_2$ in 100 mM HEPES buffer pH 7.0, as a function of increasing equivalents LS4-2 (green squares ■), CS1-2 (purple diamonds ♦) and GM4 (red triangles ▲) of peptide trimer. Samples recorded at 293 K on a 60 MHz NMR spectrometer.

MRI relaxivities were determined at 1.4 T for all the peptides, for $MnCl_2$ and MB1C controls (Figure 6.8) and the results are reported on Table 6.3. r_1 values are around 7-fold higher when compared to $MnCl_2$, and this is due to Mn(II) binding to a slowly rotating system (the peptide) and probably to high number of inner-sphere water molecules in Mn(II) coordination. MB1C (a control with no binding site), in the presence of Mn(II), shows low relaxivities, comparable to $MnCl_2$. Short relaxation times compared to the controls further suggests that, in LS4-2, CS1-2 and GM4, Mn(II) binds to the designed binding sites located in the hydrophobic core. Finally, MB1-2 did not show the expected linear trend. This is probably due to the high dependence of Mn(II) binding to the concentration of the peptide, resulting in degree of metallopeptide formation dependent on monomer concentration. MB1-2 relaxivities can be estimated to be $r_1 = 56.7 \pm 1.2$ mM^{-1} s^{-1} and $r_2 = 137.6 \pm 5.8$ mM^{-1} s^{-1} at 1.4 T, suggesting the presence of even more inner-sphere water molecules bound to Mn(II) in MB1-2 than in LS4-2, CS1-2 and GM4, due to a highly unstructured $Mn(MB1\text{-}2)_3$ peptide.

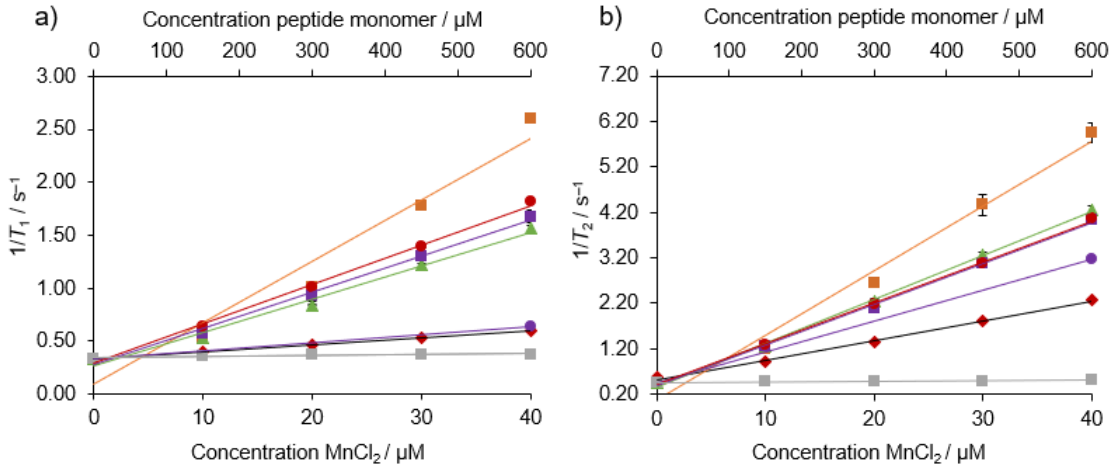


Figure 6.8: 60 MHz a) T_1 and b) T_2 ^{1}H-MRI relaxivity plots, showing the reciprocal of NMR relaxation times as a function of concentration for $MnCl_2$ (red diamonds ♦), apo MB1-2 (grey squares ■) or $MnCl_2$ in the presence of 5 equivalents of MB1C (purple circles ●), LS4-2 (green triangles ▲), CS1-2 (purple squares ■), GM4 (red circles ●) and MB1-2 (orange squares ■) peptide trimer in the presence of $MnCl_2$. Samples recorded at 293-294 K, in the presence of 100 mM HEPES buffer pH 7.0. Error bars determined from standard deviation error of three independent repeat experiments.

Table 6.3: ^{1}H-MRI r_1 and r_2 relaxivities for the Mn(II) peptides. NMR samples prepared in 100 mM HEPES buffer pH 7.0 Samples recorded at 293 K on a 60 MHz NMR spectrometer. Error determined from standard deviation of three independent repeat experiments.

	r_1 / mM^{-1} s^{-1}	r_2 / mM^{-1} s^{-1}
$MnCl_2$	6.8 ± 0.6	59.5 ± 7.5
LS4-2	31.4 ± 0.6	96.0 ± 2.2
CS1-2	34.2 ± 1.2	89.9 ± 2.4
GM4	37.2 ± 0.6	90.1 ± 1.1
MB1-2	56.7 ± 1.2	137.6 ± 5.8
MB1C	6.5 ± 0.2	68.6 ± 3.0

6.3.6 NMR relaxation times as a function of magnetic field

NMR T_1 and T_2 relaxation times and relative $1/T_1$ and $1/T_2$ relaxation rates were determined for samples with 40 μM $MnCl_2$ in the absence or in the presence of either LS4-2, CS1-2, GM4 or MB1C (Figure 6.9). In metallopeptide systems $1/T_1$ appears to be highly field-dependent with a decrease with increasing magnetic field strength from 1 T (43 MHz) to 1.4 T (60 MHz) and to

7 T (300 MHz). This clearly consistent with Mn(II) being bound to a system with long rotational correlation time. At 1 T, the estimated relaxivities for the Mn(II)-MB1-2 complex are $r_1 = 70.8 \pm 1.6$ mM^{-1} s^{-1} and $r_2 = 124.7 \pm 4.3$ mM^{-1} s^{-1}. Because the relaxivities at 1 T are higher than at 1.4 T (Table 6.3), this is evidence of interactions between Mn(II) to the slowly rotating MB1-2 system. This is because the inclusion of a paramagnetic ion within a macromolecular structure leads to enhanced relaxivities as the magnetic field is reduced.[25] On the other hand, relaxivity values for $MnCl_2$ in the presence of MB1C are field-independent and equal to $MnCl_2$ alone. This confirms that Mn(II) cannot bind this class of peptides in the absence of a designed binding site.

$1/T_2$ relaxation rate profiles are essentially the same for all the peptides. However, at 7 T, transversal $1/T_2$ relaxation rate in $Mn(GM4)_3$ are shorter. Moreover, $1/T_1$ relaxation rates in GM4 are slightly higher at 1 and 1.4 T. Compared to the other peptides, GM4 presents His in ***a*** position instead of Asp, which could possibly lead to different Mn(II) coordination compared with the other peptides with Asp in ***a*** position. Therefore, a change in coordination in GM4 can lead to variance in some molecular parameters, such as water residence time τ_m or the correlation time of electron spin relaxation time modulation τ_v.[26, 27]

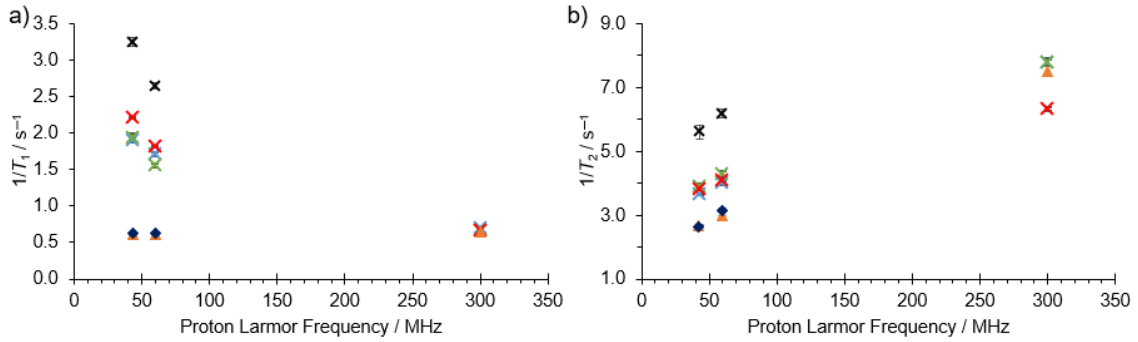


Figure 6.9: a) $1/T_1$ and b) $1/T_2$ plots, showing the reciprocal of NMR relaxation times as a function of Proton Larmor Frequency for $MnCl_2$ in the absence (orange triangles ▲) or in the presence of 5 equivalents of MB1C (blue diamonds ♦ – only values at 43 and 60 MHz), LS4-2 (green crosses ×), CS1-2 (blue crosses ×), GM4 (red crosses ×), MB1-2 (black crosses × – only values at 43 and 60 MHz) peptide trimer in the presence of $MnCl_2$. Samples recorded at 293-294 K, in the presence of 100 mM HEPES buffer pH 7.0. Error bars determined from standard deviation error of three independent repeat experiments.

6.3.7 Mn(II) displacement in the presence of Zn(II)

Zn(II) competition studies were undertaken to determine the extent of Zn(II) transmetallation of the Mn(II) peptides, using the decrease in longitudinal relaxation rate $1/T_1$ occurring due to formation of a diamagnetic Zn(II) complex (Figure 6.10). Samples of 100 mM HEPES buffer pH 7.0 in the absence and in the presence of 40 μM $MnCl_2$ were recorded and used as control. Peptide

samples were measured in the presence of 40 μM $MnCl_2$ before and 15 minutes after 40 μM $ZnCl_2$ addition. Data show that, following Zn(II) addition, the resulting $1/T_1$ relaxation rates of all the three peptides become comparable to that of free $MnCl_2$ $1/T_1$ relaxation rate in the absence of peptide. This suggests that Zn(II) completely replaces Mn(II) in the binding site, with the latter being completely hydrated. This leads to $1/T_1$ relaxation rate comparable to that of aqueous Mn(II). This result show that this class of coiled-coils is not able to provide selective binding for Mn(II), since complete substitution with Zn(II) occurs. The large degree of transmetallation also confirms that the Mn(II) peptides within the study are highly hydrated, leading to a Mn(II) binding site easily accessible by water molecules and Zn(II) ions.[11]

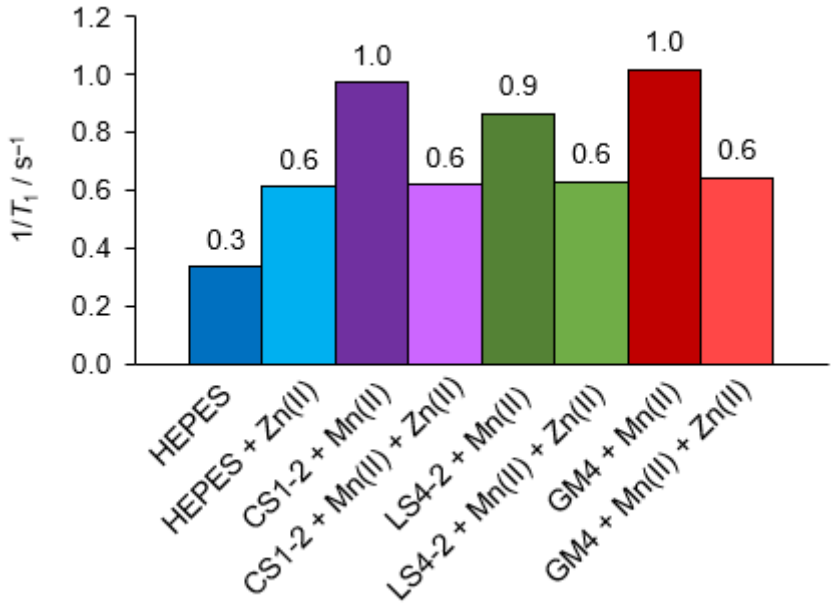


Figure 6.10: Diagram showing ^{1}H-NMR $1/T_1$ relaxation rate for a solution of HEPES 100 mM pH 7.0 (blue), 40 μM $ZnCl_2$ in HEPES 100 mM pH 7.0 (light blue), 40 μM $MnCl_2$ and 1 equivalent peptide CS1-2 (purple), LS4-2 (green) or GM4 (red) trimer without (dark colour) and with (light colour) 40 μM $ZnCl_2$ (data collected 15 minutes after $ZnCl_2$ addition), in HEPES 100 mM pH 7.0. Samples were recorded at 293 K on a 60 MHz NMR spectrometer.

6.4 Discussion

Results suggest that Mn(II) binding site is located within the hydrophobic core of the folded peptide. At 7 T, where the longer rotational correlation time of the peptides does not contribute significantly on correlation time and, therefore, on relaxivity,[25] r_1 relaxivities of all metallopeptides are around 7.5-8.4 mM^{-1} s^{-1}. These values are much higher than values reported in the literature for small Mn(II) complexes with 0 to 1 inner-sphere water molecules which are

about 1.1-3.7 mM^{-1} s^{-1}.[8, 28, 29] This further supports the hypothesis that a high number of inner-sphere water molecules (probably 2 or 3) are bound to Mn(II).

Because Mn(II) coordination is sometimes difficult to predict, different Mn(II) coordination geometries can be hypothesised (Figure 6.11). Moreover, Asp residues can be bound either monodentate (through one carboxylate O) or bidentate (through both carboxylate O): therefore, their coordination cannot be easily predicted, but can be explored using infrared spectroscopy.

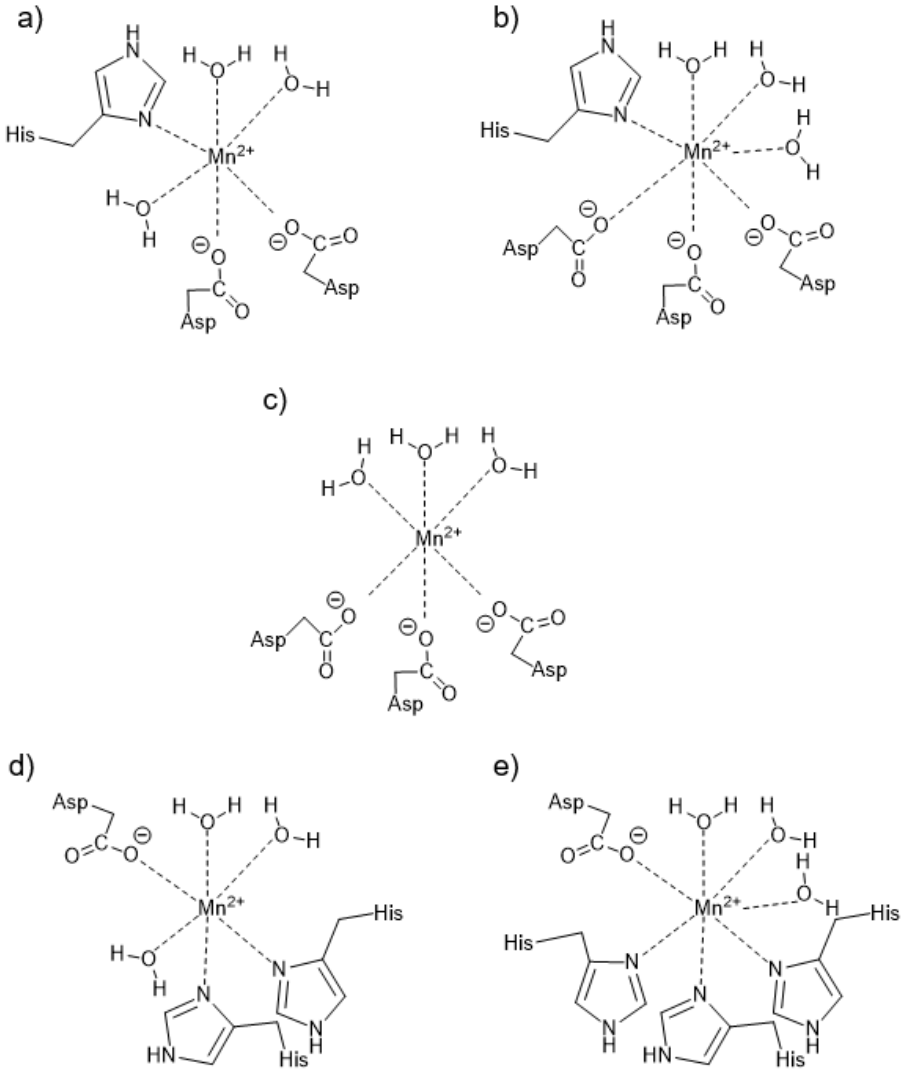


Figure 6.11: Based on the results presented in this chapter, potential Mn(II) binding sites in $Mn(LS4\text{-}2)_3$ (a,b) $Mn(CS1\text{-}2)_3$ (c) and $Mn(GM4)_3$ (d,e) featuring 6-coordinated geometry (a,c,d) or, alternatively, 7-coordinated geometry (b,d).

The introduction of a His layer in *d* position above an Asp layer in *a* position (LS4-2, Figure 6.11a,b) appears not to lead to variation of stability compared to when single Asp layer is present

(CS1-2). However, this results in the formation of a slightly less structured peptide, which can be due to the bulkiness of His residues. Mn(II) is probably bound to CS1-2 through Asp residues (Figure 6.11c), with water molecules (2 or 3) to complete its coordination, while in LS4-2, His residue(s) could be also involved in Mn(II) binding (Figure 6.11a,b).

When the layer in ***d*** position is replaced with Asn in MB1-2, the stability and folding are drastically reduced, indicating that Mn(II) cannot bind properly, whereas there is evidence of the metal bound to the slowly rotating system. The low stability of the complex could be due difficulty for the peptide to be distorted for accommodating the Mn(II) binding site. Therefore, MB1-2 coordination is even more difficult to predict. Even if Asp residues are present in ***a*** position (as in CS1-2 and LS4-2), the presence of Asn in ***d*** position appears to destabilise the coiled-coil structure, which could potentially lead to a more hydrated Mn(II) coordination site then the other peptides.

Mn(II) affinity constant to GM4 is almost comparable to LS4-2, meaning that the inversion of the two amino acid layers has no influence on Mn(II) affinity. However, different r_1 and r_2 dependence on different magnetic fields suggests distinct Mn(II) coordination environments. This could be due to Mn(II) being bound to GM4 mainly through His residues in ***a*** position (Figure 6.11d,e).

6.5 Conclusions

This chapter has provided evidence of Mn(II) binding to a class of peptides, leading to formation of coiled-coils with highly hydrated Mn(II) coordination sites. Because of the large number of inner-sphere water molecules, these systems show high relaxivities at high magnetic fields (7 T), which are even higher at low magnetic fields (1 and 1.4 T) as consequence of Mn(II) inclusion within a coiled-coil.

However, the affinity constants measured for all the peptides are 4-5 orders of magnitude lower than those of Mn(II) complexes for use as MRI contrast agents.[7, 23] Moreover, Zn(II) competition studies have revealed very labile and low kinetically stable Mn(II) coordination. These results suggest that efforts should be devoted to optimise both the thermodynamic and the kinetic inertness of these Mn(II) systems. For instance, the peptides can be designed to improve Mn(II) selectivity by introducing the binding site within a more rigid cavity, such as thought formation of covalent bonds between the strands and near the binding site. Moreover, a larger cavity could be beneficial for increase the selectivity to Mn(II) over Zn(II), to better accommodate

the larger Mn(II) ion. This could be achieved for instance by designing four-stranded coiled-coils or bundles.

As for Cu(II) compounds, fitting of NMRD (Nuclear Magnetic Relaxation Dispersion) profiles could help with determining parameters such as metal hydration state q, distance metal-water proton $r_{Cu\text{-}H}$, water residence time τ_m, rotational correlation time τ_R, hyperfine interactions $A/\hbar$ and the correlation time for electron relaxation τ_V. Variable temperature ^{17}O NMR experiments could also validate metal hydration and water residence times.[8, 30] In addition, other endogenous metals could be considered in transmetallation studies, such as Cu(II), Mg(II) and Ca(II).[8]

References

1. D. W. Christianson, *Prog. Biophys. Mol. Biol.*, 1997, **67**, 217-252.
2. D. P. Riley and R. H. Weiss, *J. Am. Chem. Soc.*, 1994, **116**, 387-388.
3. K. Barnese, E. B. Gralla, J. S. Valentine and D. E. Cabelli, *PNAS*, 2012, **109**, 6892-6897.
4. C. M. Weekley, I. Kenkel, R. Lippert, S. Wei, D. Lieb, T. Cranwell, J. L. Wedding, A. S. Zillmann, R. Rohr and M. R. Filipovic, *Inorg. Chem.*, 2017, **56**, 6076-6093.
5. M. Botta, F. Carniato, D. Esteban-Gomez, C. Platas-Iglesias and L. Tei, *Future Med. Chem.*, 2019, **11**, 1461-1483.
6. H. Su, C. Wu, J. Zhu, T. Miao, D. Wang, C. Xia, X. Zhao, Q. Gong, B. Song and H. Ai, *Dalton Trans.*, 2012, **41**, 14480-14483.
7. E. M. Gale, I. P. Atanasova, F. Blasi, I. Ay and P. Caravan, *J. Am. Chem. Soc.*, 2015, **137**, 15548-15557.
8. V. C. Pierre and M. J. Allen, Eds., *Contrast agents for MRI: experimental methods*, Royal Society of Chemistry, 2017.
9. J. S. Troughton, M. T. Greenfield, J. M. Greenwood, S. Dumas, A. J. Wiethoff, J. Wang, M. Spiller, T. J. McMurry and P. Caravan, *Inorg. Chem.*, 2004, **43**, 6313-6323.
10. J. Wahsner, E. M. Gale, A. Rodríguez-Rodríguez and P. Caravan, *Chem. Rev.*, 2018, **119**, 957-1057.
11. B. Drahoš, I. Lukeš and É. Tóth, *Eur. J. Inorg. Chem.*, 2012, **2012**, 1975-1986.
12. G. S. Loving, S. Mukherjee and P. Caravan, *J. Am. Chem. Soc.*, 2013, **135**, 4620-4623.
13. E. M. Gale, C. M. Jones, I. Ramsay, C. T. Farrar and P. Caravan, *J. Am. Chem. Soc.*, 2016, **138**, 15861-15864.
14. E. M. Gale, S. Mukherjee, C. Liu, G. S. Loving and P. Caravan, *Inorg. Chem.*, 2014, **53**, 10748-10761.
15. M. R. Gangula, *Struct. Chem.*, 2020, **31**, 1057-1064.
16. J. K. Myers, C. N. Pace and J. M. Scholtz, *PNAS*, 1997, **94**, 2833-2837.
17. P. Kuzmic, *Anal. Bioch.*, 1996, **237**, 260-273.
18. M. R. Berwick, L. N. Slope, C. F. Smith, S. M. King, S. L. Newton, R. B. Gillis, G. G. Adams, A. J. Rowe, S. E. Harding and M. M. Britton, *Chem. Sci.*, 2016, **7**, 2207-2216.
19. M. W. Brazier, P. Davies, E. Player, F. Marken, J. H. Viles and D. R. Brown, *J. Biol. Chem.*, 2008, **283**, 12831-12839.
20. B.-D. Hsu, J.-Y. Lee and R.-L. Pan, *Biochim. Biophys. Acta (BBA)-Bioenergetics*, 1987, **890**, 89-96.
21. J. A. Hayden, M. B. Brophy, L. S. Cunden and E. M. Nolan, *J. Am. Chem. Soc.*, 2013, **135**, 775-787.
22. M. Peana, E. Gumienna-Kontecka, F. Piras, M. Ostrowska, K. Piasta, K. Krzywoszynska, S. Medici and M. A. Zoroddu, *Inorg. Chem.*, 2020, **59**, 4661-4684.
23. F. K. Kálmán and G. Tircsó, *Inorg. Chem.*, 2012, **51**, 10065-10067.
24. S. L. Newton, University of Birmingham, 2018.
25. R. B. Lauffer, *Chem. Rev.*, 1987, **87**, 901-927.

26. P. Caravan, C. T. Farrar, L. Frullano and R. Uppal, *Contrast Media Mol. Imaging*, 2009, **4**, 89-100.

27. R. Uzal-Varela, L. Valencia, D. Lalli, M. Maneiro, D. Esteban-Gómez, C. Platas-Iglesias, M. Botta and A. Rodríguez-Rodríguez, *Inorg. Chem.*, 2021, **60**, 15055-15068.

28. G. A. Rolla, C. Platas-Iglesias, M. Botta, L. Tei and L. Helm, *Inorg. Chem.*, 2013, **52**, 3268-3279.

29. B. Phukan, C. Mukherjee, U. Goswami, A. Sarmah, S. Mukherjee, S. K. Sahoo and S. C. Moi, *Inorg. Chem.*, 2018, **57**, 2631-2638.

30. E. M. Gale, J. Zhu and P. Caravan, *J. Am. Chem. Soc.*, 2013, **135**, 18600-18608.

CHAPTER 7

MULTI METALLO COILED-COILS

7.1 Introduction

Besides optimising molecular parameters to achieve enhanced relaxivity, an alternative way to obtain high relaxivities is to design contrast agents with more than one paramagnetic metal ion bound. Furthermore, the addition of new moieties to the structure, to allow multiple metal binding, leads to a reduction of molecular tumbling and, potentially, to enhanced relaxivity. As shown in Chapter 1 and Chapter 2, relaxation times are the highest once the total correlation time τ_c is reciprocal of proton Larmor frequency,[1] meaning that their optimal values are varied at different magnetic fields. Since reciprocal correlations times are involved in Equation 1, the shortest correlation time is the factor that contributes to the overall correlation time more strongly. Moreover, when two of these parameters are optimised, the third plays a significant role in limiting or modulating the overall correlation time and relaxation rates. In the case of macromolecules, such as human serum albumin (HSA), the rotational correlation time (τ_R) becomes long enough not to influence relaxivity significantly (τ_R = 10.1 ± 2.6 ns for the Gd(III) complex MS-325 bound to HSA compared to 115 ps when the small complex is unbound).[2] This makes water residence time (τ_m) and electron relaxation time (T_e) limiting factors to the relaxivity.

$$\frac{1}{\tau_{ci}} = \frac{1}{\tau_m} + \frac{1}{\tau_R} + \frac{1}{T_{ie}} \; ; \; i = 1,2 \qquad (1)$$

Generally, the most common strategies to include multiple metal ions into a molecule, have been the conjugation of Gd(III) complexes to polymers,[3-6] dendrimers,[7-10] or biological molecules.[11-16] Moreover, single chelates have been linked to form dimers, trimers or tetramers.[17-19] The use of biological structures such as peptides, appears to be a relatively easy and powerful method to introduce more than one metal binding site within an assembled molecule. Tanaka and co-workers reported a 5 heptad peptide,[20] which can bind Ni(II) and Cu(II) in the hydrophobic core of a three-stranded α-helical coiled-coil. They also designed a peptide with 12 His residues in the hydrophobic core of a coiled-coil structure, folded in the presence of 2 equivalents of divalent metal ions.[21]

In this chapter, the approach is directed towards introducing more than one metal binding site within a coiled-coil, aiming to improve the relaxivity of the overall complex and possibly to

gain more insight into the relaxation properties of this class of contrast agents by translating the relative binding site position along the coil. These are based on binding sites formed by Asn-Asp or Asp layers[22, 23], allowing multiple Gd(III) or Cu(II) ions to bind.

CD spectroscopy is used to assess peptide folding for a series of peptides upon Gd(III) or Cu(II) complexation. In addition, sensitised terbium fluorescence emission and quenching of tryptophan emission are used to probe Tb(III) (which has a similar coordination to Gd(III)) and Cu(II) binding, respectively. Affinity constants are determined from fitting of binding data. Finally, MRI relaxivities are measured and simulations are undertaken to determine the impact of increasing rotational correlation times τ_R.on relaxivity in this series of peptides. At 1 T, Sarah Newton measured[24] $r_1 = 64.3 \pm 3.2$ mM^{-1} s^{-1} for Gd(MB1-1)$_3$ and $r_1 = 67.4 \pm 4.2$ mM^{-1} s^{-1} for the same peptide with one additional heptad, suggesting that rotational correlation time is not a limiting factor in this series of peptides.

7.2 Experimental

Materials, peptide synthesis and purification as in Chapter 3. Gadolinium(III) chloride hexahydrate and terbium(III) chloride hexahydrate were purchased from Sigma Aldrich and used as received.

7.2.1 UV-Vis spectroscopy

UV-Vis experiments to determine peptide concentration were conducted on a Cary 50 UV Spectrophotometer as described in Chapter 4.

7.2.2 CD spectroscopy

CD spectra were recorded on a Jasco J-715 Spectropolarimeter. The optical chamber was purged with nitrogen and kept under a nitrogen atmosphere throughout the duration of the experiments. A 1 mm pathlength, 300 µl quartz cuvette was used with three scans recorded from 400-200 nm using a 100-200 nm min^{-1} scan rate with 1 nm bandwidth and a 1 s response.

A 10 mM HEPES buffer solution pH 7.0 was recorded as a blank before either $CuCl_2$ or $GdCl_3$ was titrated into a solution of peptide monomer with concentration previously determined by UV-Vis analysis. All solutions were left to equilibrate for 15 mins before scanning. The ellipticity (θ_{obs}) data collected in millidegrees (mdeg), was converted to molar ellipticity per residue, [θ] (deg dmol^{-1} cm^2) using Equation 2.

$$[\theta] = \frac{\theta_{\text{obs}}}{10\ lcN} \tag{2}$$

where θ_{obs} is the measured ellipticity at 222 nm in mdeg, c is the concentration in M, N is the number if amino acids in the sequence and l is the pathlength in cm..

The helical content was then calculated as the percentage folded using Equation 3, where the denominator represents the molar ellipticity for a fully folded coiled-coil.[25]

$$\%\ \text{Folded} = \frac{[\theta_{222}] - 640}{\left(-42500 \times \left(1 - {}^{3}/_{N}\right)\right) - 640} \tag{3}$$

7.2.3 Emission spectroscopy

Emission spectra were recorded in a 1 cm pathlength quartz cuvette using a Jasco FP-8500 fluorescence spectrometer. For Tb(III) emission experiments, aliquots of $TbCl_3$ stock solution were titrated into a 30-35 μM solution of peptide monomer in 10 mM HEPES buffer pH 7.0 and the emission profile recorded after 20 minutes of equilibration. Solutions were excited at 280 nm and the emission was scanned from 455-660 nm (Tb(III) emission region) using an excitation slit width of 5 nm and bandwith of 5 nm.

For quenching experiments, aliquots of a 1 mM stock solution of $CuCl_2$ were titrated into a 30-35 μM solution of peptide monomer in 10 mM HEPES buffer pH 7.0 and the emission profile recorded after 20 minutes of equilibration. Solutions were excited at 280 nm and the emission was scanned from 300-455 nm (Trp emission region) using an excitation slit width of 2.5 nm and bandwith of 2.5 nm.

7.2.4 Nuclear magnetic resonance

^{1}H-NMR measurements were performed on a Spinsolve benchtop NMR (Magritek, Aachen, Germany), operating at proton resonance frequency of 61 MHz.. Data were acquired at 21.0 ± 0.5°C (controlled room temperature) using 3 mm NMR tubes and automated 90° pulse width of 7 μs. For T_1 NMR relaxation measurements, an Inversion Recovery sequence (described in Section 2.7.3) was used with a repetition time > $5T_1$ (≥ 5 s). A series of 11 spectra were collected with delays linearly spaced from 0.001 s to a maximum of 3-10 s, 8 signal averages and 32k points. For T_2 NMR relaxation measurements a CPMG pulse sequence (described in Section 2.7.3) was used with a repetition time > $5T_1$ (≥ 5 s). A series of 10 spectra were recorded with a 2 ms CPMG echo time and final echo time of 3 or 5 s, 8 signal averages and 32k data points. All data were analysed using Prospa (Magritek, Aachen, Germany). Signal intensity curves were fitted in KaleidaGraph (Synergy, USA).

The r_1 and r_2 relaxivities were calculated from the gradients of plots of the average, based on three independent repeats, ^{1}H magnetic resonance relaxation rates ($1/T_1$ and $1/T_2$ respectively), as a function of contrast agent concentration. For measurements at 1.4 T, a range of solutions were measured, containing 1 (CS1-1), 2 (LS2 peptides) or 3 (GM2) equivalents of either $GdCl_3$ or $CuCl_2$ per equivalent of peptide trimer (where 1 equivalent of peptide trimer, corresponds to 3 equivalents of peptide monomer).

7.2.5 Relaxivity simulations

MATLAB R2021b software was used to simulate inner-sphere r_1 relaxivity as function of water residence time τ_m and rotational correlation time τ_R using Equations 4-6.

$$r_1^{IS} = \frac{q/[H_2O]}{T_{1M} + \tau_M} \tag{4}$$

$$\frac{1}{T_{1M}} = \frac{2}{15}\left(\frac{\mu_0}{4\pi}\right)^2 \frac{\hbar^2 \gamma_S^2 \gamma_H^2}{r_{MH}^6} S(S+1)\left(\frac{3\tau_c}{1 + \omega_H^2 \tau_c^2}\right) \tag{5}$$

$$\frac{1}{\tau_c} = \frac{1}{\tau_m} + \frac{1}{\tau_R} + \frac{1}{\tau_s} \tag{6}$$

where S is the spin quantum number, r_{MH} is the ion-proton distance, ω_H is the Larmor frequency of the proton, γ_H is the proton gyromagnetic ratio, g_e is the electronic g-factor ($g_e = 2$), μ_B is the Bohr magneton and μ_0 is the permittivity of vacuum. Static magnetic field B_0 was set to 1.4 T and distance r_{MH} to 2.7 Å (Cu(II) complexes) and 3.1 Å (Gd(III) complexes).

7.3 Results

7.3.1 Peptide design

CS1-1 possesses the same binding site at the N-terminus (Table 7.1), as MB1-1. However, only one Asp layer is available for metal binding. Berwick and co-workers showed that the two peptides have similar Ln(III) binding properties, as in MB1-1 only the Asp layer was hypothesised to be involved in Ln(III) binding, with the remaining Ln(III) coordinating donors completed with water molecules.[23]

The LS2 series (Table 7.1 and Figure 7.1a,b,c) was designed by Louise Slope (as outlined in her PhD thesis)[26] to have two binding sites for lanthanide binding, translated along the coil. She provided evidence for Tb(III) binding, although no systematic study was conducted to determine the MRI relaxivities of the Gd(III) analogues. LS2-1,2 features two adjacent binding sites as a combination of CS1-1 (Asp) and MB1-2 (Asn-Asp) binding sites. The translation of the buried (Asn-Asp) binding site generates LS2-1,3 21W and the analogous peptide with Gln instead of Trp was named LS2-1,3 21Q. Finally, LS2-2,3 features by two adjacent buried Asn-Asp layers.

In this work, a new peptide is designed, named GM2 (Table 7.1 and Figure 7.1d), which presents three binding sites located at the N-terminus with an Asp layer and two consecutive Asn-Asp layers, in an effort to design a coiled-coil capable of binding three metal ions. For each additional binding site introduced, the coiled-coil was lengthened by one heptad to compensate for the introduction of polar, destabilising residues in the hydrophobic interior of the coiled-coil.[27]

Table 7.1: Sequences of peptides used in this chapter. Residues designed for metal binding underlined and coloured red (Asp), blue (Asn). In yellow the mutation of Trp (W) to Gln (Q).

CS1-1	Ac-G IAAIEWK DAAIEQK IAAIEQK IAAIEQK IAAIEQK G-NH_2
MB1-2	Ac-G IAAIEQK IAANEWK DAAIEQK IAAIEQK IAAIEQK G-NH_2
LS2-1,2	Ac-G IAAIEWK DAANEWK DAAIEQK IAAIEQK IAAIEQK IAAIEQK G-NH_2
LS2-1,3 21W	Ac-G IAAIEWK DAAIEQK IAANEWK DAAIEQK IAAIEQK IAAIEQK G-NH_2
LS2-1,3 21Q	Ac-G IAAIEWK DAAIEQK IAANEQK DAAIEQK IAAIEQK IAAIEQK G-NH_2
LS2-2,3	Ac-G IAAIEQK IAANEWK DAANEWK DAAIEQK IAAIEQK IAAIEQK G-NH_2
GM2	Ac-G IAAIEWK DAANEWK DAANEWK DAAIEQK IAAIEQK IAAIEQK IAAIEQK G-NH_2

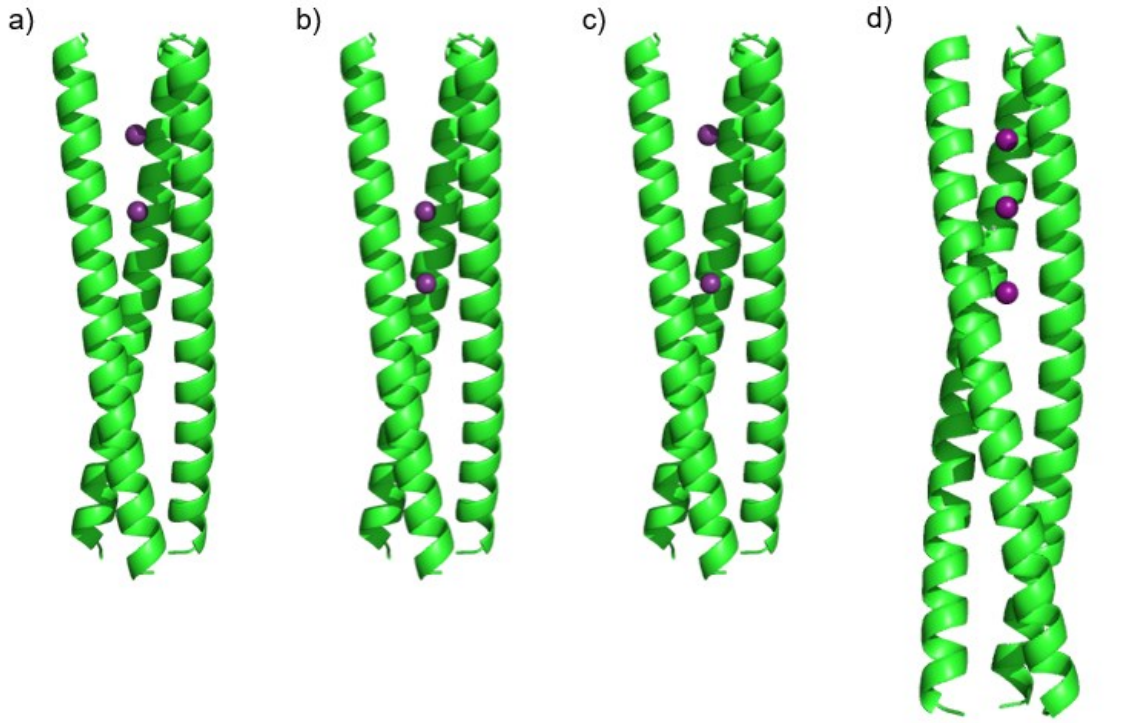


Figure 7.1: Cartoon representing the relative positions of the metal ions in a) LS2-1,2, b) LS2-2,3, c) LS2-1,3 and d) GM2. Only the peptide backbone is shown as a helical ribbon. Metal (either Gd(III) or Cu(II) ions shown as purple spheres.

7.3.2 Lanthanide binding

CD folding and fluorescence titrations were undertaken to assess Ln(III) binding to 30 μM of peptide monomer with either $GdCl_3$ (GM2) or $TbCl_3$ (remaining peptides) (Figure 7.2 and Table 7.2). The data reported here for Tb(III) binding to CS1-1 and to the LS2 series are taken from Louise Slope's PhD thesis for comparison,[26] while data fitting was done by me.

CS1-1 was reported to bind Tb(III) through the Asp layer forming a trimer with a log K_a of 4.6 ± 0.1.[23] In their apo form, CS1-1 and LS2-1,2 are well folded and the addition of Tb(III) results in modest improvement. In contrast, the remaining peptides (LS2-1,3-21W, LS2-1,3-21Q and LS2-2,3), which incorporate the binding sites more centrally within the coiled-coil, present unfolded structures in the apo form which become more folded with Tb(III) addition. It is worth noting that the substitution of Trp to Gln in LS2-1,3-21W and LS2-1,3-21Q did not influence the folding in the absence of metal, as the substitution was made in ***f*** position which is not involved in peptide folding. In fact, amino acid residues in ***f*** position, which point outside the coil, impact on the water solubility of the overall structure. The model which allowed best fitting for Tb(III) fluorescence experiments of LS2-1,2, LS2-1,3 21W and LS2-2,3 is based on stepwise addition of two equivalents of Tb(III) per peptide trimer. The log K_a values are reported on Table 7.2.

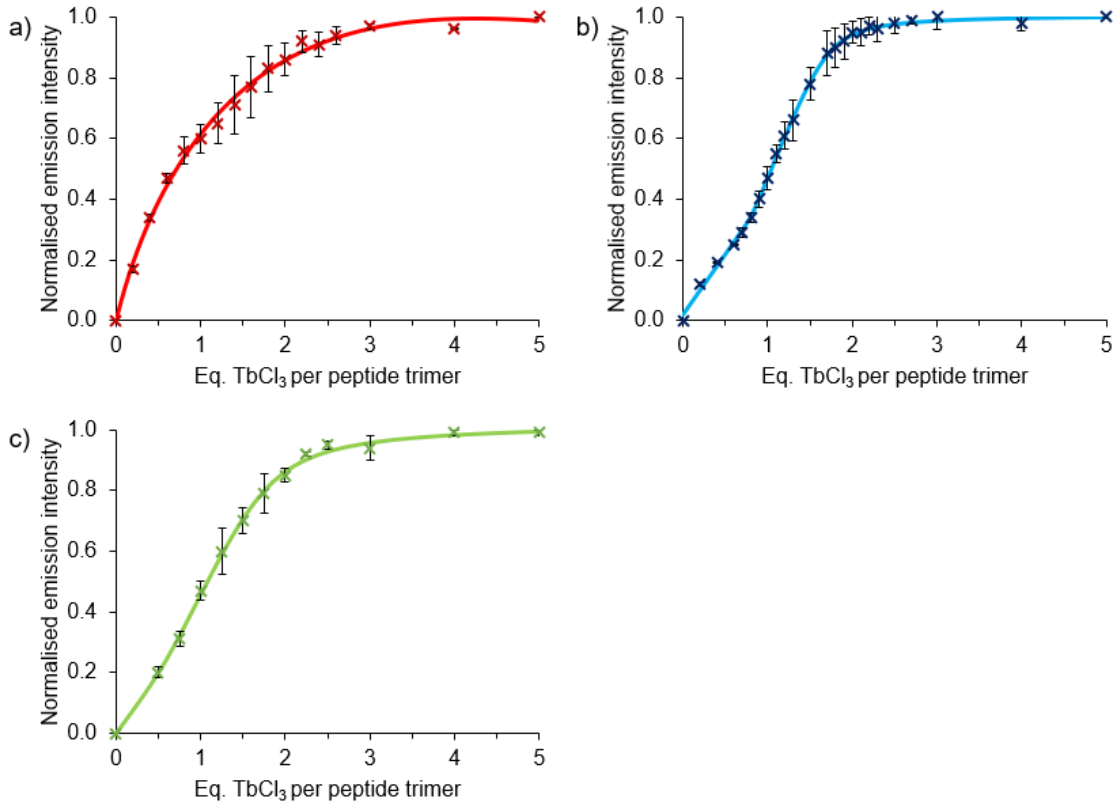


Figure 7.2: Plot of normalized Tb(III) emission intensity at 293 K, λ_{ex} = 280 nm after $TbCl_3$ addition into a 30 μM LS2-1,2 (red), LS2-1,3 21W (blue) and LS2-2,3 (green) peptide monomer in 10 mM HEPES buffer pH 7.0 at 293 K, λ_{ex} = 280 nm. Data, taken from Louise Slope's PhD thesis,[26] are results of average of three independent repeats and error bars derive from their standard deviation. The fitting was made with a $1/3M + L \rightarrow 1/3[ML_3] + 1/3M \rightarrow 1/3[M_2L_3]$ model using DynaFit[28]. All samples were recorded in 10 mM HEPES buffer pH 7.0 at 293 K.

With the presence of a high number of polar amino acids (Asn and Asp, with the latter being negatively charged at pH 7.0), at a concentration of 30 μM of peptide monomer, GM2 is only partially folded in its apo form. The addition of Gd(III) is able to promote folding, resulting in well-folded Gd(III) structure (Figure 7.3a,b and Table 7.2). Sensitised Tb(III) fluorescence (Figure 7.3c,d) further suggest Ln(III) binding, with a major increase up to 3 equivalents of Tb(III) per peptide trimer. CD and fluorescence data for Gd(III) and Tb(III) binding to GM2 were fitted with a $M + L \leftrightarrow 1/3M_3L_3$ model where three metal ions binds simultaneously to a trimer, producing a binding constant of $\log K_a = 6.1 \pm 0.2$ from CD data which compares with $\log K_a = 5.8 \pm 0.2$ from data obtained from fluorescence (Table 7.2).

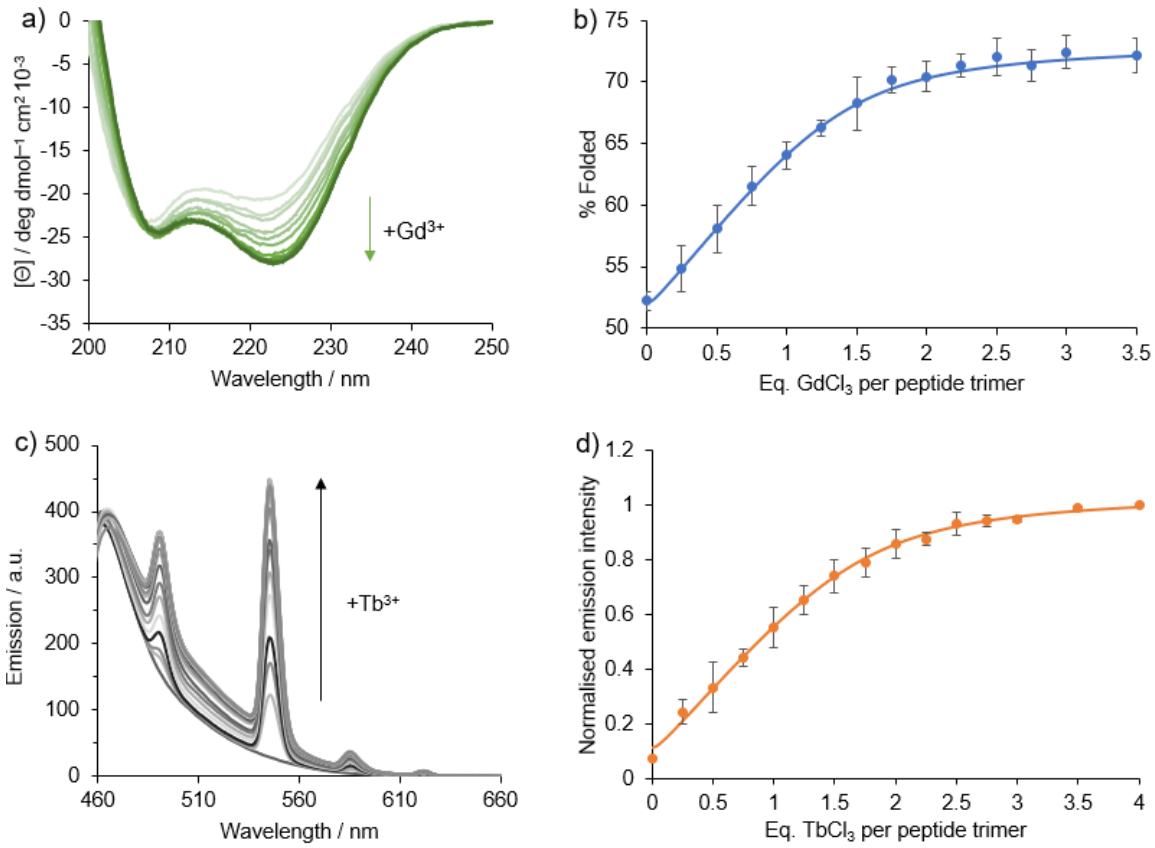


Figure 7.3: a) Representative CD spectra and b) CD folding titration of $GdCl_3$ titration into 30 μM GM2 peptide monomer solution; c) representative Tb(III) emission spectra and d) plot of normalized Tb(III) emission intensity at 293 K, λ_{ex} = 280 nm after $TbCl_3$ addition into a 30 μM GM2 peptide monomer solution. Data are results of average of three independent repeats and error bars derive from their standard deviation. The fitting was made with a M + L → 1/3[M_3L_3] model using DynaFit[28]. All samples were recorded in 10 mM HEPES buffer pH 7.0 at 293 K.

Table 7.2: % folding of the apo peptides compared to the metallo form after the addition of 1 or 2 equivalents of either $GdCl_3$ (GM2) or $TbCl_3$ (remaining peptides) per peptide trimer. The concentration was 30 μM peptide monomer, corresponding to 10 μM peptide trimer in 10 mM HEPES buffer pH 7.0. Values of log K_a determined from fitting fluorescence data (all peptides) and CD data (GM2) in 10 mM HEPES buffer pH 7.0. Data fitted using DynaFit[24] to a nonlinear least-squares fitting based on 1/3M + L ↔ 1/3[ML_3] (CS1-1), 1/3M + L → 1/3[ML_3] + 1/3M → 1/3[M_2L_3] (LS2 peptides) and M + L → 1/3[M_3L_3] (GM2) models. Error determined from standard deviation of three independent experiments.

	% Folding apo	% Folding Ln(III)	log K_{a1}	log K_{a2}
CS1-1	78 ± 2%	83 ± 1%	4.6 ± 0.1[23]	-
LS2-1,2	66 ± 1%	71 ± 1% (1 eq.)* 76 ± 1% (2 eq.)*	5.8 ± 0.2	5.1 ± 0.1
LS2-1,3-21W	14 ± 0%	40 ± 1% (1 eq.)* 52 ± 2% (2 eq.)*	7.0 ± 0.2	5.2 ± 0.0
LS2-1,3-21Q	14 ± 1%	40 ± 1% (1 eq.)* 52 ± 2% (2 eq.)*	-	-
LS2-2,3	14 ± 0%	40 ± 2% (1 eq.)* 48 ± 1% (2 eq.)*	6.2 ± 0.2	4.9 ± 0.3
GM2	52 ± 1%	64 ± 1% (1 eq.) 70 ± 1% (2 eq.) 72 ± 1% (3 eq.)	6.1 ± 0.2 (CD) 5.8 ± 0.2 (fluorescence)	-

*: as reported in Louise Slope's PhD thesis

To support the assignment of this binding ratio, a Job's plot analysis was conducted by Dr. Valentina Borghesani (unpublished results) on the system with Tb(III) binding to GM2 (Figure 7.4). Tb(III) fluorescence reaches its maximum at about 50% Tb(III) to monomer ratio, suggesting that 3 equivalents of Tb(III) bind to a peptide trimer.

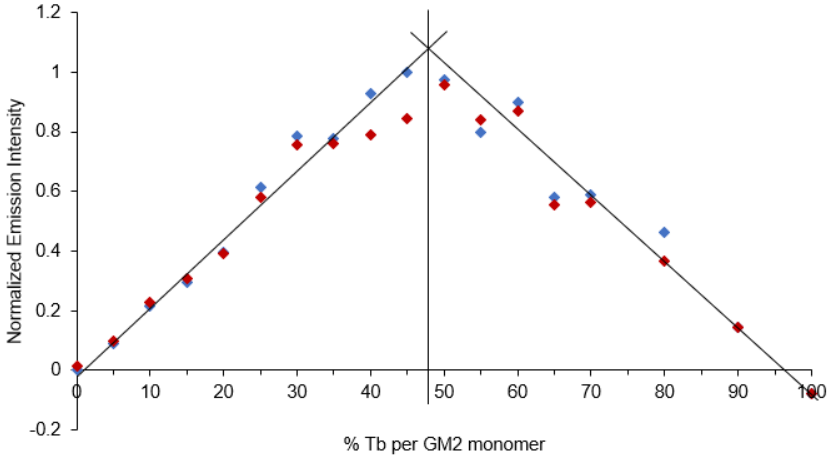


Figure 7.4: Job's continuous variation plot for GM2 and $TbCl_2$ in 10 mM HEPES buffer pH 7.0, with total concentration constant and equal to 40 μM. The plot shows GM2 monomer molar ratio versus Tb(III) emission. In blue and in red two independent repeats.

7.3.3 Copper binding

CD folding (Figure 7.5) and fluorescence experiments (Figure 7.6) were undertaken to monitor Cu(II) binding to 30 μM of peptide monomer. Since the addition of Cu(II) does not improve folding in CS1-1, LS2-1,2 and LS2-2,3, tryptophan quenching was used to assess Cu(II) binding. The fitting for CS1-1 binding to Cu(II) (Figure 7.7a) was made in accordance with a binding model of $L + 1/3M \leftrightarrow 1/3ML_3$ (M: metal ion and L: peptide monomer), determining $\log K_a$ of 4.6 ± 0.0. The model which allowed best fitting for LS2-1,2 and LS2-2,3 is based on stepwise addition of two equivalents of Cu(II) per equivalent of peptide trimer (Figure 7.7b,c). The $\log K_a$ values are reported on Table 7.3.

In the presence of Tb(III), the LS2-1,3-21W and LS2-1,3-21Q peptides showed similar folding improvement. In the presence of Cu(II), a different response is observed. LS2-1,3 21W does not increase its folding as much as LS2-1,3 21Q at two or even higher number of Cu(II) equivalents per peptide trimer. This unexpected behaviour is hypothesised to be due to peptide aggregation in LS2-1,3 21W, helped by the presence of Cu(II). This is further explored in Section 7.3.4. No fitting was made for LS2-1,3 21W and LS2-1,3 21Q, since a possible peptide aggregation in the first peptide and the presence of a single Trp in the second, leads to difficult interpretation of the results.

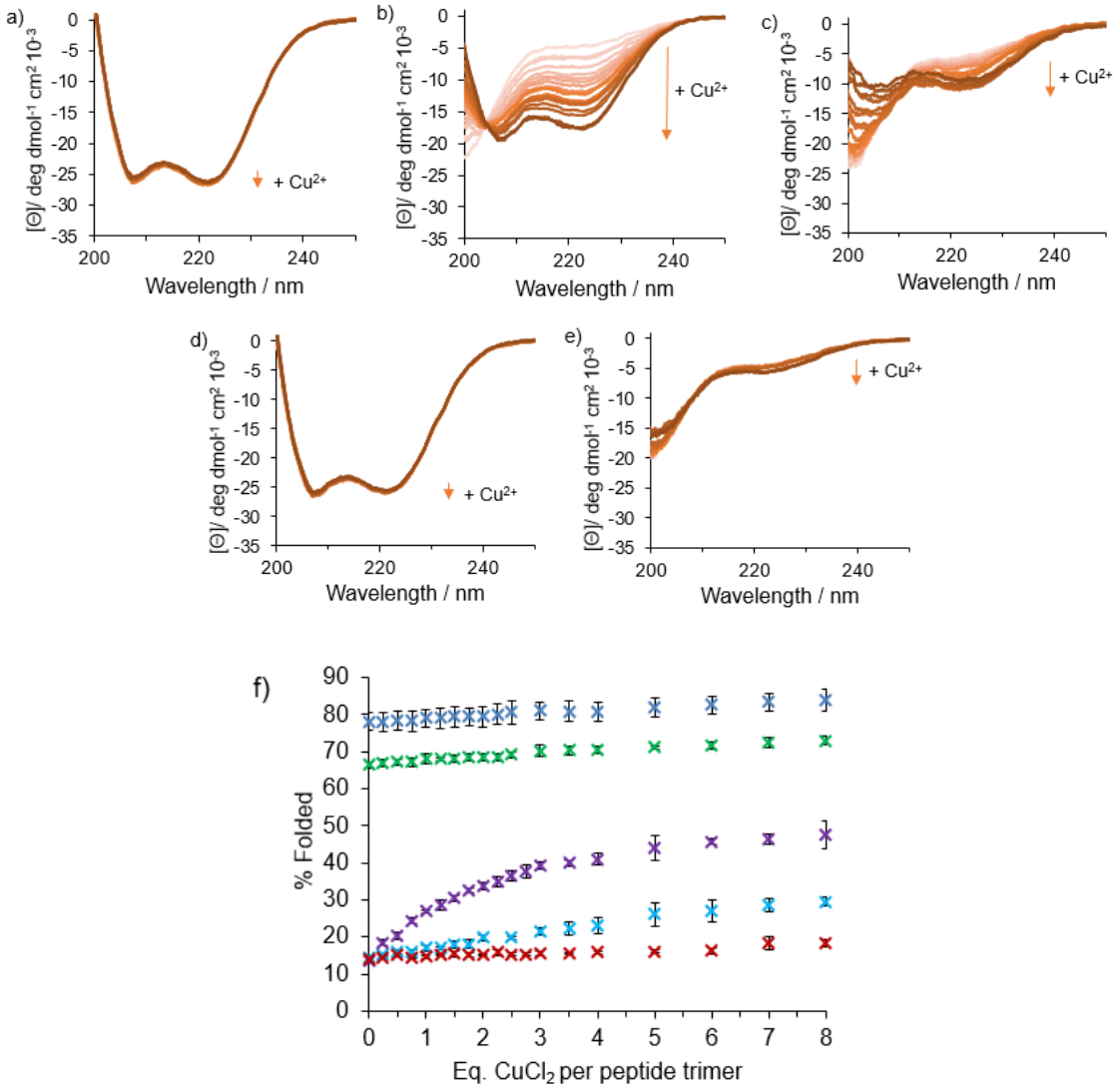


Figure 7.5: Representative CD spectra of $CuCl_2$ titration into 30 µM a) CS1-1, b) LS2-1,3 21Q, c) LS2-1,3 21W and d) LS2-2,3 peptide monomer and f) relative CD folding profiles showing $CuCl_2$ titration into CS1-1 (blue ×), LS2-1,2 (green ×), LS2-1,3 21Q (purple ×), LS2-1,2 21W (light blue ×) and LS2-2,3 (red ×) peptide monomer. Data are results of average of three independent repeats and error bars derive from their standard deviation. All samples were recorded in 10 mM HEPES buffer pH 7.0 at 293 K, $\lambda_{ex} = 280$ nm, λ_{em} integrated between 300 and 455 nm.

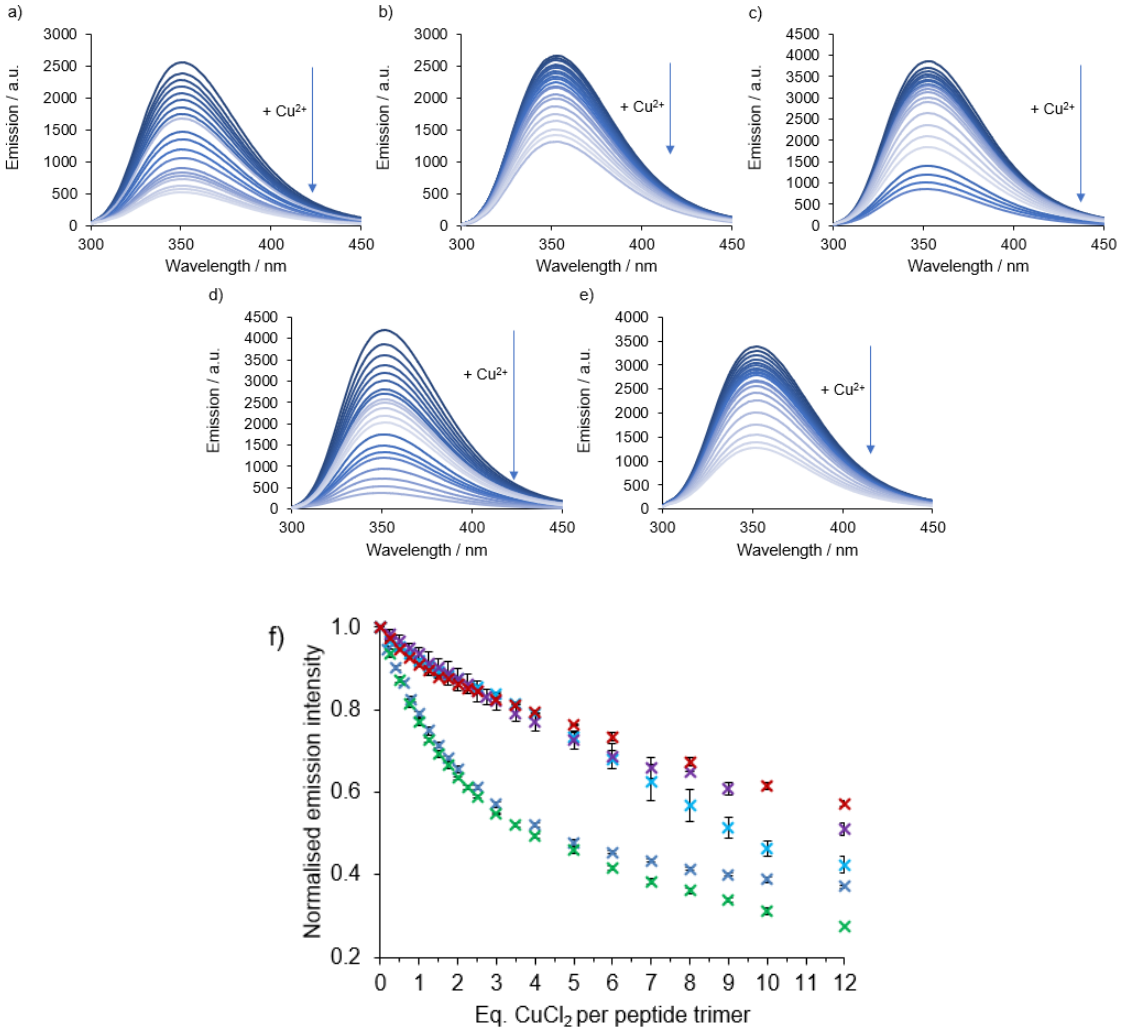


Figure 7.6: Representative tryptophan emission spectra showing titration of $CuCl_2$ into 30 µM a) CS1-1, b) LS2-1,3 21Q, c) LS2-1,3 21W and d) LS2-2,3 peptide monomer and f) relative normalised integrated emission showing $CuCl_2$ titration into CS1-1 (blue ×), LS2-1,2 (green ×), LS2-1,3 21Q (purple ×), LS2-1,2 21W (light blue ×) and LS2-2,3 (red ×) peptide monomer. Data are results of average of three independent repeats and error bars derive from their standard deviation. All samples were recorded in 10 mM HEPES buffer pH 7.0 at 293 K, λ_{ex} = 280 nm, λ_{em} integrated between 300 and 455 nm.

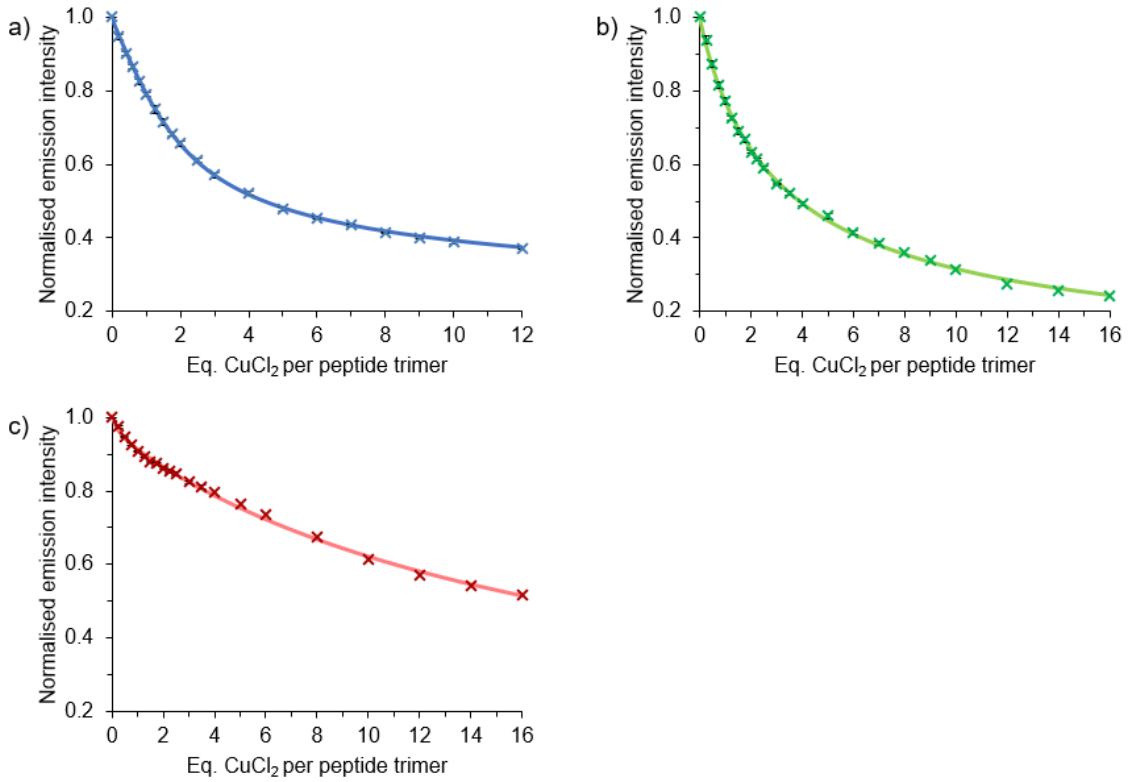


Figure 7.7: Normalised integrated emission showing $CuCl_2$ titration into 30 µM CS1-1 (blue), LS2-1,2 (green) and LS2-2,3 (red) peptide monomer in 10 mM HEPES buffer pH 7.0 at 293 K, λ_{ex} = 280 nm, λ_{em} integrated between 300 and 455 nm. Data fitted using DynaFit[24] to a nonlinear least-squares fitting based on $1/3M + L \rightarrow 1/3[ML_3] + 1/3M \rightarrow 1/3[M_2L_3]$ models. Error determined from standard deviation of three independent experiments. All samples were recorded in 10 mM HEPES buffer pH 7.0 at 293 K, λ_{ex} = 280 nm, λ_{em} integrated between 300 and 455 nm.

As introduced in Section 7.3.2, GM2 is only partially folded in its apo form. The addition of Cu(II) is able to partially promote folding, resulting in its marginal improvement, (Figure 7.8a,b and Table 7.3). Therefore, quenching of tryptophan fluorescence (Figure 7.8c,d) was used to confirm Cu(II) binding. Compared with CS1-1 and LS2-1,2, GM2 is less folded in the absence and in the presence of Cu(II). Data fitting for CuGM2 were not conclusive, since more than one model can fit the data. The best models were two Cu(II) bind sequentially or, firstly, one Cu(II) binds, followed by two Cu(II) ions binding simultaneously. However, this could be due to the aggregation during the experiment leading to difficult interpretations.

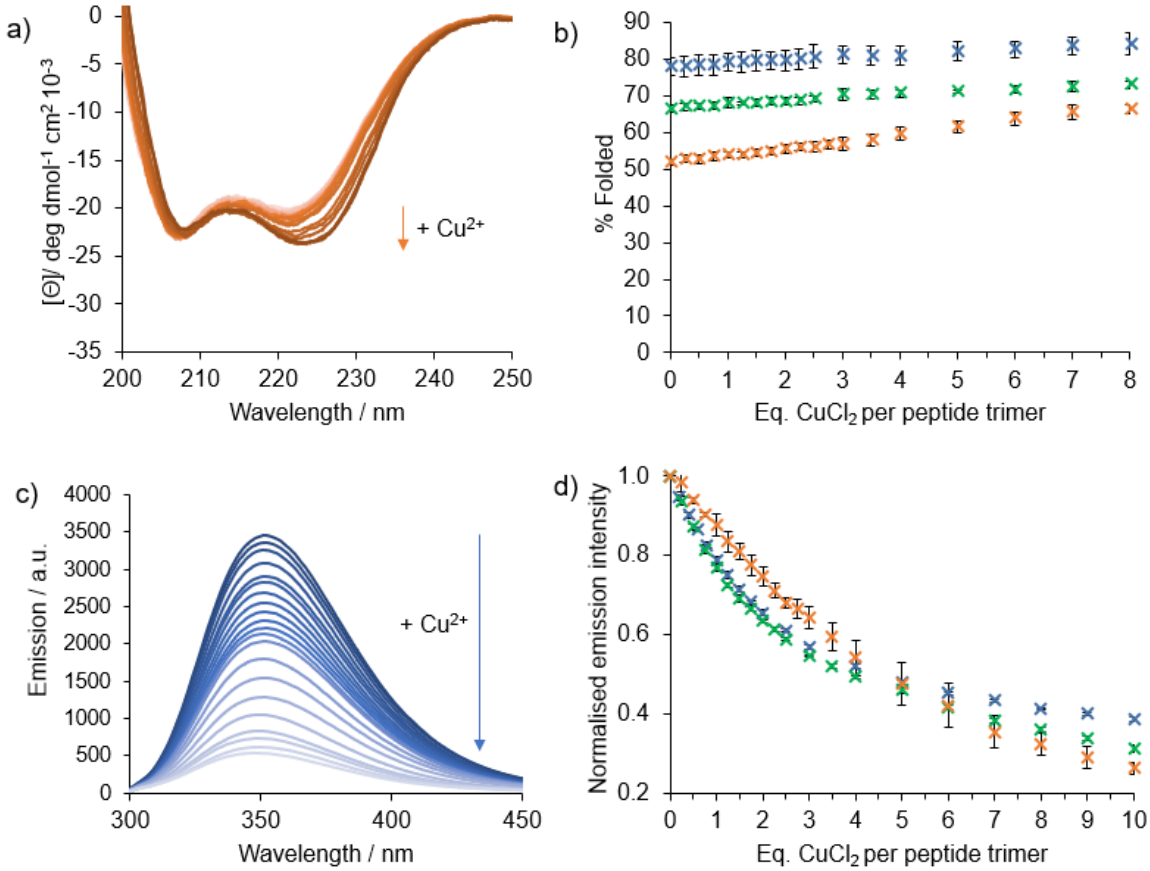


Figure 7.8: a) Representative CD spectra of GM2, b) CD folding titration of $CuCl_2$ titration into 30 µM peptide monomer solution of GM2 (orange ×) compared with CS1-1 (blue ×) and LS2-1,2 (green ×) c) representative Trp emission spectra of GM2 and d) plot of normalized tryptophan emission intensity at 293 K, λ_{ex} = 280 nm after Cu(II) addition into a 30 µM peptide monomer solution of GM2 (orange ×) compared with CS1-1 (blue ×) and LS2-1,2 (green ×). Data are results of average of three independent repeats and error bars derive from their standard deviation. All samples were recorded in 10 mM HEPES buffer pH 7.0 at 293 K.

Table 7.3: % folding of the apo peptides compared to the metallo form after the addition of 1, 2 or 3 equivalents of metal per peptide trimer. The concentration was 30 μM peptide monomer, corresponding to 10 μM peptide trimer) in 10 mM HEPES buffer pH 7.0, monitored by CD. Values of log K_a determined from fitting fluorescence data in 10 mM HEPES buffer pH 7.0. Data fitted using DynaFit[24] to a nonlinear least-squares fitting based on $1/3M + L \leftrightarrow 1/3[ML_3]$ (CS1-1) and $1/3M + L \rightarrow 1/3[ML_3] + 1/3M \rightarrow 1/3[M_2L_3]$ (LS2 peptides) models. Error determined from standard deviation of three independent experiments.

	% Folding apo	% Folding Cu(II)	log K_{a1}	log K_{a2}
CS1-1	78 ± 2%	79 ± 2%	4.6 ± 0.0	-
LS2-1,2	66 ± 1%	68 ± 1% (1 eq.) 68 ± 1% (2 eq.)	5.0 ± 0.0	4.3 ± 0.0
LS2-1,3-21W	14 ± 0%	17 ± 1% (1 eq.) 20 ± 1% (2 eq.)	-	-
LS2-1,3-21Q	14 ± 1%	27 ± 0% (1 eq.) 33 ± 1% (2 eq.)	-	-
LS2-2,3	14 ± 0%	15 ± 0% (1 eq.) 15 ± 0% (2 eq.)	5.6 ± 0.3	4.9 ± 0.3
GM2	52 ± 1%	54 ± 1% (1 eq.) 55 ± 1% (2 eq.) 57 ± 2% (3 eq.)	-	-

7.3.4 Precipitation

In Sections 7.2.2 and 7.3.3, the hypothesis of metal-dependent aggregation was introduced. Precipitation was observed at the end of titrations of 30 μM GM2 monomer with both Gd(III) and Tb(III), whereas the apo peptide solution was clear even at high concentrations (around 800 μM). On titration of GM2 with Cu(II) no precipitation was observed at the end of the titration, but after 24 h, the formation of precipitate was observed. Overnight precipitation occurred also with the LS2 series in the presence of both metals, except from LS2-1,3 21Q. This suggests that the inclusion of one Gln residue instead of one Trp improves the peptide solubility, which was notably compromised by the presence of a high excess of metal. Again, the apo peptide solutions were clear even after days.

7.3.5 Relaxivity

Relaxivities were determined at 1.4 T (Figure 7.9, Figure 7.10 and Table 7.4), aiming to verify the impact of the addition multiple metal ions on relaxivity and to investigate Gd(III) and Cu(II) coordination.

For $Gd_3(GM2)_3$, the use of the same concentration of metal and peptide, as in other relaxivity experiments reported in this thesis, leads to fast precipitation in the NMR tube. Relaxivity was then calculated using lower concentration of peptide trimer (0 to 8 μM $GdCl_3$). For the $Cu_3(GM2)_3$ complex an additional sample at higher concentration (20 μM $CuCl_2$) was used and no precipitation was observed, as in the Gd(III) complex. This observation further confirms a role of the metal on peptide precipitation.

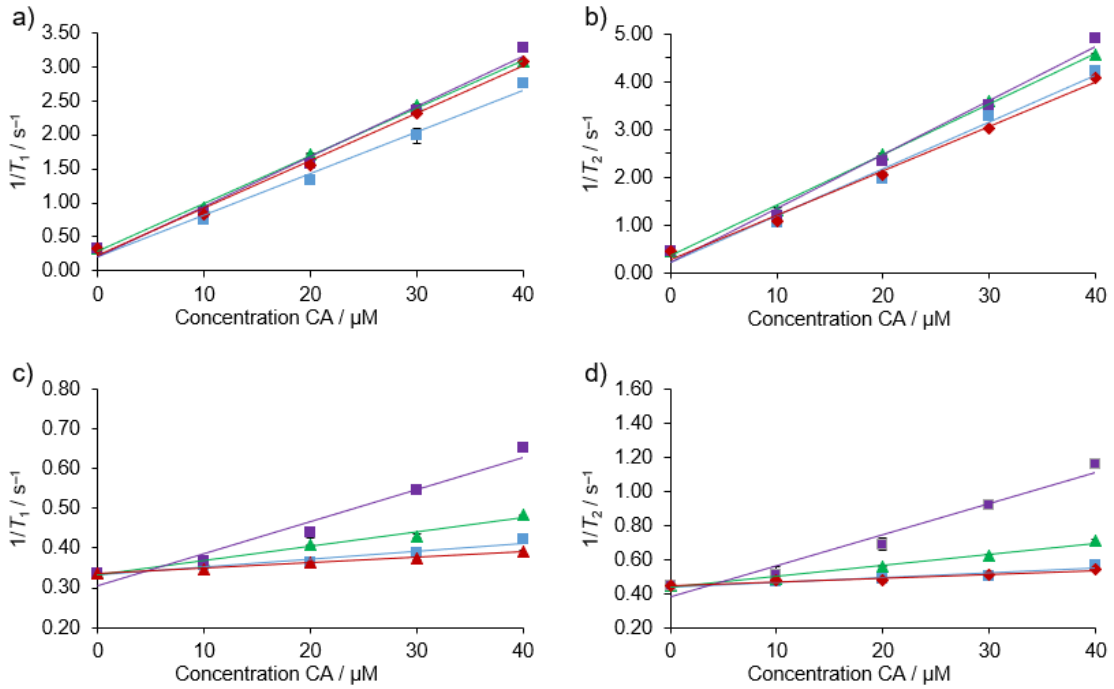


Figure 7.9: ^{1}H-NMR T_1 (a,c) and T_2 (b,d) relaxivity plots, showing reciprocal of relaxation time as a function of contrast agent (CA) concentration for relaxation rates recorded of samples at pH 7.0 in 100 mM HEPES buffer of either $GdCl_3$ (a,b) or $CuCl_2$ (c,d) in the presence CS1-1 (blue squares ■), LS2-1,2 (green triangles ▲), LS2-1,3 21Q (purple squares ■) and LS2-2,3 (red diamonds ♦) trimer. Samples recorded at 293 K on a 60 MHz, 1.4 T NMR spectrometer. Error bars determined from standard deviation error of three independent repeat experiments.

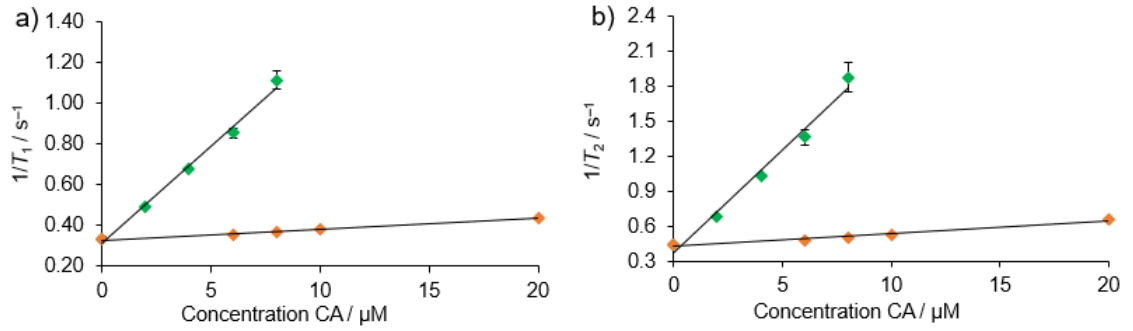


Figure 7.10: ^{1}H-NMR T_1 (a) and T_2 (b) relaxivity plots, showing reciprocal of relaxation time as a function of contrast agent (CA) concentration for relaxation rates recorded of samples at pH 7.0 in 100 mM HEPES buffer of either $GdCl_3$ (green diamonds ♦) or $CuCl_2$ (orange diamonds ♦) in the presence of GM2. Samples recorded at 293 K on a 60 MHz, 1.4 T NMR spectrometer. Error bars determined from standard deviation error of three independent repeat experiments.

Table 7.4: ^{1}H-MRI r_1 and r_2 relaxivities for Gd(III) and Cu(II) peptides compared with $Gd(MB1\text{-}2)_3$ and $Cu(MB1\text{-}2)_3$. NMR samples prepared using 1:1 (CS1-1), 1:5 (MB1-2), 2:1 (LS2 peptides) and 3:1 (GM2) metal:trimer ratio in 100 mM HEPES buffer pH 7.0. Samples recorded at 293 K on a 60 MHz (1.4 T) NMR spectrometer. Error determined from standard deviation of three independent repeat experiments.

	Gd(III)		Cu(II)	
	r_1 / mM^{-1} s^{-1}	r_2 / mM^{-1} s^{-1}	r_1 / mM^{-1} s^{-1}	r_2 / mM^{-1} s^{-1}
CS1-1	67.0 ± 1.5	108.8 ± 4.5	2.2 ± 0.2	3.1 ± 0.1
MB1-2	15.3 ± 0.6	18.9 ± 0.1	14.2 ± 0.2	32.7 ± 0.4
LS2-1,2	71.8 ± 0.4	109.1 ± 1.6	3.7 ± 0.1	7.2 ± 0.2
LS2-1,3 21Q	80.7 ± 1.5	119.6 ± 3.9	9.6 ± 0.4	21.7 ± 1.6
LS2-2,3	74.4 ± 0.9	100.6 ± 1.1	1.4 ± 0.3	2.2 ± 0.1
GM2	100.2 ± 9.9	191.8 ± 27.8	6.0 ± 0.5	12.8 ± 1.0

7.3.6 Impact of rotational correlation times

In the peptide design, the addition of multiple metal binding sites required lengthening the coiled-coil to compensate for the introduction of destabilising sites.[27] This leads to longer molecular tumbling along the *z*-axis and longer rotational correlation times which finally modulate relaxivity. Therefore, the impact of variable rotational correlation times on relaxivity was established.

In her PhD thesis, Sarah Newton estimated 6.9 ns as rotational correlation time for a peptide constituted by 5 heptads such as MB1-2 or CS1-1.[24] The addition of another heptad (as in the LS2

series) increased this up to 10 ns, extrapolating a further 3 ns increase for the addition of one heptad. Therefore, a rotational correlation time 13 ns can be estimated to characterise a 7-heptad system (GM2). Here, the impact of rotational correlation time was predicted for Gd(III) and Cu(II) complexes (Figure 7.11), with metal-water proton distance r_{MH} 3.1 Å and 2.7 Å, respectively, estimated for Gd(III) complexes[11] and for the Cu(II) compound shown in Chapter 3. For the Cu(II) complex, 5 ns was used as electron relaxation time, as in Cu(II) compounds it is not varied at different magnetic fields.[29] On the other hand, electron relaxation time becomes longer in Gd(III) complexes on increasing the magnetic field,[30, 31] resulting in a negligible contribution at the magnetic fields of interest.[1, 11, 31] A water residence time τ_m = 1.56 ns was measured for the Gd(MB1-1)$_3$ system.[24] For the Cu(II) system (Chapter 3 and Chapter 4) τ_m was predicted to be around 10 ns in a buried site (Cu(MB1-2)$_3$), while in a site located at the extremity of the coil (Cu(MB1-1)$_3$) around 1 ns. Oppositely, when the Gd(III) binding site was designed in the interior of the hydrophobic core, as in Gd(MB1-2)$_3$, no inner-sphere water molecules were found.[22, 23]

In both Gd(III) and Cu(II) compounds, when water residence time is around 0.1 ns, no influence of rotational correlation time (τ_R) is shown, reflecting water residence time being the limiting factor to relaxivity. When water residence time is increased up to about 1 ns (Cu(II) and Gd(III) sites at the extremity of the coil could be in this range), relaxivity increases with longer rotational correlation times (Figure 7.11), reaching a plateau at about τ_R = 5 ns. For water residence times above 10 ns, in Gd(II) compounds, relaxivity is reduced for rotational correlation times longer than 10 ns, while the Cu(II) compounds retained high relaxivities because of the impact of non-negligible electron relaxation time (a Cu(II) site in the interior of the coil could be in this range). Therefore, an independence on rotational correlation time can be assumed for the range of τ_R considered here (6.9 to 13 ns) in both Gd(III) and Cu(II) compounds.

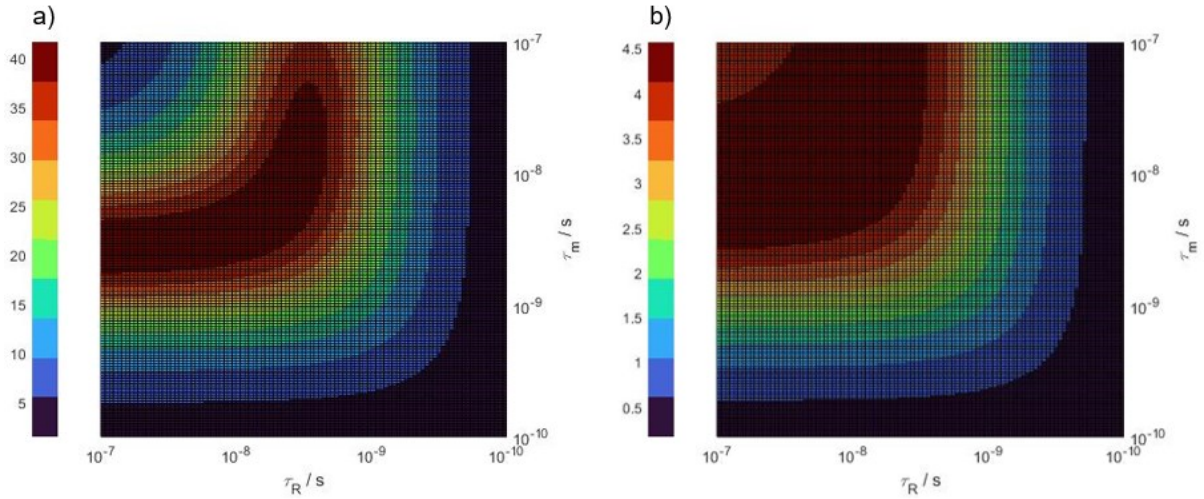


Figure 7.11: Simulation of ^{1}H-MRI r_1 relaxivity (shown on colour bar) at 1.4 T for one inner-sphere water molecule as a function of variable water residence time τ_m and rotational correlation times τ_R in a) Gd(III) complex with r_{MH} = 3.1 Å and $1/\tau_S$ negligible and b) Cu(II) complex with r_{MH} = 2.7 Å and τ_S = 5 ns.

7.4 Discussion

Cu(II) binding to the well-folded LS2-1,2 structure does not result in improvement in folding even in high excess of Cu(II), suggesting that Cu(II) is less capable than Tb(III) to further template the pre-assembled structure. A similar behaviour was observed in LS2-2,3: Tb(III) is able to induce peptide folding, while Cu(II) is not, resulting in a unstructured form even if Cu(II) is bound. However, Cu(II) binding was successfully assessed by quenching of tryptophan fluorescence emission.

In the presence of Tb(III), the LS2-1,3-21W and LS2-1,3-21Q peptides show similar folding improvement, while, in the presence of Cu(II), a different response is observed, where only LS2-1,3 21Q is able to enhance its folding in the presence of Cu(II). This unexpected behaviour is hypothesised to be due to peptide aggregation in LS2-1,3 21W, helped by the presence of Cu(II).

The high relaxivity in Gd(CS1-1)$_3$ reflects the presence of a high number of inner-sphere water molecules (q = 3.6 ± 0.1, for the Tb(III) analogue)[23] due to the position of the binding site at the N-terminus. In the Cu(II) complex, a low relaxivity was measured when compared to Cu(CS1-2)$_3$ (r_1 = 7.3 ± 0.4 mM^{-1} s^{-1} and r_2 = 18.2 ± 0.6 mM^{-1} s^{-1} at 1.4 T, as shown in Chapter 5), where the binding site was located in a buried position. A detrimental impact of fast water exchange rates can explain this behaviour, as observed in Chapter 4. The difference to MB1-1 can be due to a more hydrated complex, since in CS1-1 there are no Asn are present to provide more coordination sites for Cu(II). Moreover, similarly to MB1-1, inner-sphere water molecules can be predicted to exchange with bulk water in a fast-exchange regime.

Gd_2(LS2-1,2)$_3$ and Cu_2(LS2-1,2)$_3$ relaxivities cannot be explained by the addition of a top binding site similar to CS1-1 with one additional buried site (similar to MB1-2). This second, buried site (Asn-Asp), is located just below the CS1-1-like binding site (Asp), in a position that prevents the water to enter into the hydrophobic core and get in proximity to the binding site in either the Gd(III) complex or the Cu(II) complex (behaviour observed in the MB1-2 system). This means that relaxivity in LS2-1,2 is not the result of the addition of the relaxivities of CS1-1 and MB1-2.

This hypothesis is confirmed in LS2-1,3 21Q, where the relaxivities were found to be higher for both Gd_2(LS2-1,3 21Q)$_3$ and Cu_2(LS2-1,3 21Q)$_3$, than the relative LS2-1,2 systems. The presence of a translated MB1-2 binding site, allows water to enter into the hydrophobic core and interacting with Gd(III) and Cu(II). This finally leads to enhanced relaxivities than LS2-1,2.

In the Cu_2(LS2-2,3)$_3$, low relaxivity was measured. This can be explained by the presence of an almost unstructured system, with water being able to easily access to Cu(II) as in the CS1-1 and MB1-1 systems. The relative Gd(III) complex presents high relaxivity, higher than the simple addition of two buried binding sites (MB1-2 like), suggesting that a similar open structure is found in the Gd(III) system as well as in the Cu(II) complex. This proposed open structure allows the presence of high number of inner-sphere water molecules in rapid exchange with bulk water.

The same observation as in the LS2-1,2 system can be translated to GM2 binding to Gd(III). The presence of an additional metal ion can explain the higher relaxivity than the Gd_2(LS2-1,2)$_3$ complex. This increment in r_1 appears to be due to an additional Gd(III) binding site with water molecules (probably second-sphere as MB1-2). This could be due to the GM2 trimer being less folded than LS2-1,2 in the presence of Ln(III). However, the high r_1 and r_2 values in Gd_3(GM2)$_3$, can be a consequence of formation of aggregates/precipitate as observed in Section 7.3.2.

Finally, fitting of fluorescence data for GM2 binding to Cu(II) could not provide information about Cu(II) binding, therefore, interpretation of relaxivity data is more difficult. The best fitting models were two Cu(II) binding stepwise or binding of one Cu(II), followed by two Cu(II) binding simultaneously. In the first case, the interpretation of Cu_2(GM2)$_3$ relaxivity is difficult because of the presence of one equivalent of excess $CuCl_2$ per trimer. Alternatively, if three Cu(II) ions bind to GM2, the same observation as in the Cu_2(LS2-1,2)$_3$ complex can be made: an additional Cu(II) ion in Cu_3(GM2)$_3$, can explain the higher relaxivity, although the lack of water accessibility determines only in a modest increment.

7.5 Conclusions

In this chapter, the inclusion of more than one metal within a single coiled-coil and the relative impact on MRI relaxivities were explored. An important consideration should be made about the assessment of the number of metal ions that effectively bind within a coil. No results presented here unequivocally confirm the binding of more than one metal ion within a three stranded coiled-coil. More clear evidence suggests three Gd(III) ions binding to GM2. Other techniques such as Native MS and Job's plot analyses could be used. However, here, MRI relaxivities showed an increase in relaxivity, especially in the series constituted by CS1-1, LS2-1,2 and GM2 in the presence of either metal. This series was designed by adding a buried binding site progressively on the heptad below and a negligible impact on relaxivity was shown as a consequence of increase in rotational correlation time.

Important design features can be extrapolated: the reduction in solubility of the peptides with increasing the length of the sequence should be taken into account and one should consider adding polar residues in ***b*** and ***c*** positions, which are not involved in the coiled-coil folding. In Chapter 3 and Chapter 4 it was shown that optimised MRI relaxivities of this class of Cu(II) complexes are achieved if the binding site is located in a buried position, but still accessible by water, while when it is designed at the extremities, the relaxivities are drastically reduced also because a shift of water exchange towards the fast-exchange limit. Here, similar conclusions can be made. In the presence of more binding sites, when located on adjacent heptads (LS2-1,2 and GM2), water is prevented from entering into the hydrophobic core to get in proximity (in the Gd(III) compounds) or to coordinate to the metal (in the Cu(II) peptides). This was confirmed, in both Gd(III) and Cu(II) systems, when the buried binding site was translated one heptad along the coil (LS2-1,3) as the relaxivities rise again as consequence of water entering close to the metal site. Finally, results confirms that when a peptide is almost unstructured (therefore the metal is probably highly hydrated), as in LS2-2,3, the relaxivities are high in Gd(III) compound, while they are low in the Cu(II) system.

References

1. P. Caravan, *Chem. Soc. Rev.*, 2006, **35**, 512-523.
2. P. Caravan, N. J. Cloutier, M. T. Greenfield, S. A. McDermid, S. U. Dunham, J. W. Bulte, J. C. Amedio, R. J. Looby, R. M. Supkowski and W. D. Horrocks, *J. Am. Chem. Soc.*, 2002, **124**, 3152-3162.
3. P. F. Sieving, A. D. Watson and S. M. Rocklage, *Bioconjugate Chem.*, 1990, **1**, 65-71.
4. A. Bogdanov Jr, R. Weissleder, H. Frank, A. Bogdanova, N. Nossif, B. Schaffer, E. Tsai, M. Papisov and T. Brady, *Radiology*, 1993, **187**, 701-706.
5. É. Tóth, L. Helm, K. E. Kellar and A. E. Merbach, *Chem. Eur. J.*, 1999, **5**, 1202-1211.
6. V. P. Torchilin, *Curr. Pharm. Biotechnol.*, 2000, **1**, 183-215.
7. A. Gossmann, Y. Okuhata, D. M. Shames, T. H. Helbich, T. P. Roberts, M. F. Wendland, S. Huber and R. C. Brasch, *Radiology*, 1999, **213**, 265-272.
8. J. Bremerich, M. F. Wendland, H. Arheden, R. Wyttenbach, D. W. Gao, J. P. Huberty, M. W. Dae, C. B. Higgins and M. Saeed, *J. Am. Coll. Cardiol.*, 1998, **32**, 787-793.
9. H. Kobayashi, S. Kawamoto, T. Saga, N. Sato, T. Ishimori, J. Konishi, K. Ono, K. Togashi and M. W. Brechbiel, *Bioconjugate Chem.*, 2001, **12**, 587-593.
10. T. Barrett, G. Ravizzini, P. L. Choyke and H. Kobayashi, *IEEE Eng. Med. Biol. Mag.*, 2009, **28**, 12.
11. P. Caravan, J. J. Ellison, T. J. McMurry and R. B. Lauffer, *Chem. Rev.*, 1999, **99**, 2293-2352.
12. Q. Xu, L. Zhu, M. Yu, F. Feng, L. An, C. Xing and S. Wang, *Polymer*, 2010, **51**, 1336-1340.
13. B. Sitharaman, K. R. Kissell, K. B. Hartman, L. A. Tran, A. Baikalov, I. Rusakova, Y. Sun, H. A. Khant, S. J. Ludtke and W. Chiu, *Chem. Comm.*, 2005, 3915-3917.
14. J. J. Yang, J. Yang, L. Wei, O. Zurkiya, W. Yang, S. Li, J. Zou, Y. Zhou, A. L. W. Maniccia and H. Mao, *J. Am. Chem. Soc.*, 2008, **130**, 9260-9267.
15. S. R. Bull, M. O. Guler, R. E. Bras, P. N. Venkatasubramanian, S. I. Stupp and T. J. Meade, *Bioconjugate Chem.*, 2005, **16**, 1343-1348.
16. S. R. Bull, M. O. Guler, R. E. Bras, T. J. Meade and S. I. Stupp, *Nano Lett.*, 2005, **5**, 1-4.
17. V. V. Martin, W. H. Ralston, M. R. Hynes and J. F. Keana, *Bioconjugate Chem.*, 1995, **6**, 616-623.
18. B. Jebasingh and V. Alexander, *Inorg. Chem.*, 2005, **44**, 9434-9443.
19. D. H. Powell, O. M. N. Dhubhghaill, D. Pubanz, L. Helm, Y. S. Lebedev, W. Schlaepfer and A. E. Merbach, *J. Am. Chem. Soc.*, 1996, **118**, 9333-9346.
20. T. Tanaka, T. Mizuno, S. Fukui, H. Hiroaki, J.-i. Oku, K. Kanaori, K. Tajima and M. Shirakawa, *J. Am. Chem. Soc.*, 2004, **126**, 14023-14028.
21. T. Mizuno, K. Murao, Y. Tanabe, M. Oda and T. Tanaka, *J. Am. Chem. Soc.*, 2007, **129**, 11378-11383.

22. M. R. Berwick, D. J. Lewis, A. W. Jones, R. A. Parslow, T. R. Dafforn, H. J. Cooper, J. Wilkie, Z. Pikramenou, M. M. Britton and A. F. Peacock, *J. Am. Chem. Soc.*, 2014, **136**, 1166-1169.

23. M. R. Berwick, L. N. Slope, C. F. Smith, S. M. King, S. L. Newton, R. B. Gillis, G. G. Adams, A. J. Rowe, S. E. Harding and M. M. Britton, *che*, 2016, **7**, 2207-2216.

24. S. L. Newton, University of Birmingham, 2018.

25. J. K. Myers, C. N. Pace and J. M. Scholtz, *PNAS*, 1997, **94**, 2833-2837.

26. L. N. Slope, PhD, University of Birmingham, 2017.

27. D. Ghosh, K.-H. Lee, B. Demeler and V. L. Pecoraro, *Biochemistry*, 2005, **44**, 10732-10740.

28. P. Kuzmic, *Anal. Bioch.*, 1996, **237**, 260-273.

29. I. Bertini, C. Luchinat, R. D. Brown III and S. H. Koenig, *J. Am. Chem. Soc.*, 1989, **111**, 3532-3536.

30. R. B. Lauffer, *Chem. Rev.*, 1987, **87**, 901-927.

31. P. Caravan, C. T. Farrar, L. Frullano and R. Uppal, *Contrast Media Mol. Imaging*, 2009, **4**, 89-100.

CHAPTER 8

EXPLORING THE USE OF LANTHANIDE COILED-COILS AS PARACEST CONTRAST AGENTS

8.1 Introduction

In the previous chapters, the use of Cu(II) and Mn(II) as safer alternatives to Gd(III) to induce NMR T_1 and T_2-shortening, was explored. The choice of a macromolecular ligand (*de novo* designed coiled-coils) allowed to obtain high relaxivities, especially at low magnetic fields (1.4 T). Moreover, the impact of introducing more Gd(III) and Cu(II) metal ions within the same coiled-coil was investigated.

As an alternative to the use of T_1 and T_2-shortening contrast agents, another technique, named chemical exchange saturation transfer (CEST) is able to provide negative contrast by selectively saturating the resonance frequencies of proton pools in exchange with bulk water (as shown in Section 2.7.4). The main advantage of CEST over relaxation agents, is the ability to switch on and off the contrast by turning on and off the selective saturation of the exchangeable proton pools. This leads to a better identification of the region where the contrast agent is distributed.

The use of diamagnetic molecules as diaCEST (diamagnetic-CEST) contrast agents, offers limited advantages. Firstly, the small chemical shifts ω of their exchangeable protons (around 5 ppm) limit the exchange rates k_{ex} range which satisfy the slow-to-intermediate exchange condition for giving rise to CEST effect, $\Delta\omega > k_{ex}$ (where $\Delta\omega$ is the resonance frequency difference between the protons on the molecule and bulk water).[1] Moreover, selectively saturating protons at resonance frequencies near to water can be difficult without partially saturating bulk water.[2]

The use of lanthanide complexes as paraCEST (paramagnetic-CEST) contrast agents enables to generate large proton chemical shifts, also called hyperfine shifts, leading to resonances ranging from around +100 ppm in Eu(III) compounds to around –50 ppm in Nd(III) complexes. In these complexes, in addition to the exchangeable protons on the molecule, also water molecule(s) bound to the metal can be used. The molecular exchange of metal-bound water with bulk water can be more easily modulated than proton exchange of the protons on the ligand.[3] This enables to tune the CEST effect more efficiently.

An important feature for paraCEST contrast agents is the presence of exchangeable protons in a moderate-to-slow exchange regime.[1] This can be achieved by using paramagnetic metal ions that shift proton resonance frequencies far from that of bulk water, and, at the same time, leading to slow exchange rates of the bound water, such as Eu(III) and Nd(III).[3]

A way to slow down water exchange is to introduce the metal binding site within a hydrophobic cavity,[4] which could be the hydrophobic core of a coiled-coil. The MB1-2 peptide (Table 8.1) is known to form a well folded coiled-coil in the presence of lanthanides.[5-7] The use of molecular modelling helped to identify the presence of a water channel which leads the water molecules in close proximity to the Ln(III) ion.[8] Experimentally, this has been confirmed by the presence of second-sphere water molecules in the Gd(III) binding site of the $Gd(MB1\text{-}2)_3$ complex (see Chapter 3).

Table 8.1: Sequence of the MB1-2 peptide used in this chapter. Residues designed for Ln(III) binding underlined and coloured red (Asp) and blue (Asn).

MB1-2	Ac-G IAAIEQK IAANEWK DAAIEQK IAAIEQK IAAIEQK G-NH_2

The amino acids in the MB1-2 sequence present a large number of exchangeable protons as shown in Figure 8.1. Each amino acid contributes one proton from the NH amide on the backbone (as shown in red). In addition, the NH amide on Asn and Gln could possibly be in exchange as well as the NH proton on the indole ring on Trp. Finally, Lys presents an ammonium proton, positively charged at the pH 7.0, resulting in faster proton exchange rates (around 4000 s^{-1} compared to 100 s^{-1} for NH and NH_2 amide proton(s) and Trp NH indole proton).[9]

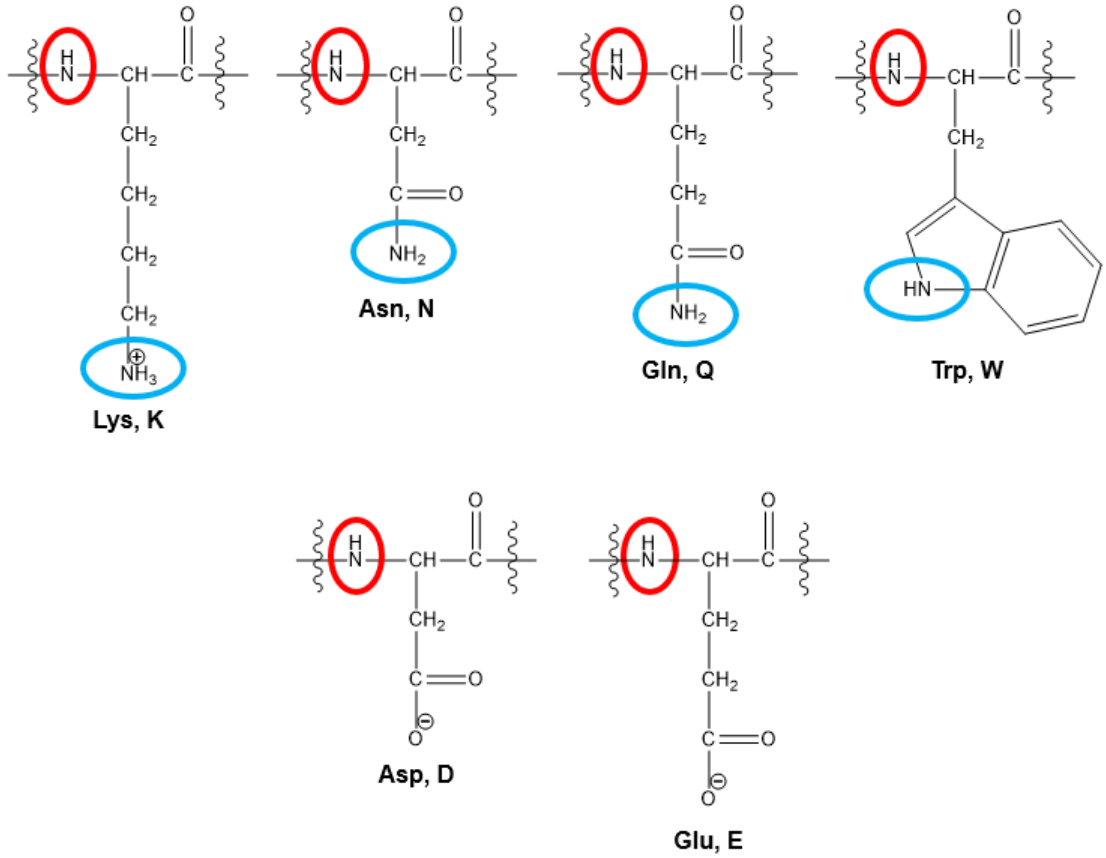


Figure 8.1: Chemical structure of the amino acids in MB1-2 with identification of exchangeable protons: in red NH amide backbone and in blue amine (Lys), amide (Asn and Gln) and NH indole Trp.

Based on these considerations, this chapter focuses on evaluating for the first time the use of Ln(MB1-2)$_3$ complexes as potential paraCEST contrast agents. The presence of shifted peaks in the presence of Ln(III) is also studied by collecting the NMR spectrum of the Nd(MB1-2)$_3$ complex outside the conventional 0-10 ppm range, aiming to identify resonances from water bound/in proximity to Nd(III) and/or exchangeable protons. Finally, the CEST efficiency of the Nd(III) complex is determined by recording its Z-spectrum.

8.2 Experimental

8.2.1 Materials

Chemicals were used as received and purchased from: Sigma Aldrich (deuterium oxide (D_2O), neodymium(III) choride hexahydrate, terbium(III) choride hexahydrate, sodium trimethylsilylpropanesulfonate (DSS), Acros Organics (lanthanum(III) choride heptahydrate

europium (III) choride hexahydrate). Water was ultrapure grade obtained from a Millipore Elix-Gradient A10 system.

8.2.2 Sample preparation

NMR samples were prepared by diluting freshly prepared peptide stock solutions in D_2O to a concentration of 1.2 mM of peptide monomer (peptide stock solutions left at 40°C for 48h to allow H-D exchange). Aliquots of 10 mM $LaCl_3$ or $NdCl_3$ stock solution prepared in D_2O was added to have a final metal concentration of 0.4 mM. The pH of the sample was adjusted to 6.6 (resulting in pD = 7.0)[10] by adding small volumes of either NaOH or HCl (1, 0.1 or 0.01 M). The same procedure was followed for NMR samples prepared in 90:10 H_2O:D_2O, with the difference that the Ln(III) solutions were prepared in H_2O and the pH was adjusted to 7.0. The peptide sample was transferred to a 3 mm tube, which was then put inside a 5 mm tube with 70 μM DSS in D_2O as reference.

8.2.3 NMR spectra

^{1}H-NMR experiments were performed on a 9.39 T Bruker ultrashield magnet spectrometer operating at a proton resonance frequency of 400.13 MHz. 1D-NMR spectra were recorded using 512 scans and 64k data points. For CEST experiments, a zgpr sequence (described in Section 2.7.4) was used, using 64 scans and 64k data points. The power of the presaturation pulse (PLW9) was set to 8.174 10^{-5} W and its length (D1) to 18 s. The Z-spectrum was generated by plotting on *y*-axis M/M_0%, where M and M_0 are the integration of the water peak in the presence (M) or in the absence (M_0) of the presaturation pulse. On *x*-axis the difference of the frequency of the presaturation pulse compared to bulk water (frequency offset, $\Delta\omega$).

8.3 Results

8.3.1 Identification of exchangeable protons

^{1}H-NMR spectra of MB1-2 in D_2O the absence and presence of either La(III) or Nd(III) were recorded and the peaks were assigned to groups of protons (Figure 8.2). The peaks between 0 and 3 ppm can be assigned to aliphatic CH_2 or CH_3 protons, while around 4 ppm the peaks of the protons bound to the chiral C can be identified (αCH). Finally, around 7 ppm there are the aromatic protons on the Trp indole ring. A comparison between the La(III) and the Nd(III) spectra was made to identify any influence derived from the presence of a paramagnetic ion, Nd(III),

rather than a diamagnetic ion, La(III). However, it was not possible to identify unequivocally the shift of non-exchangeable proton resonances due to the presence of the paramagnetic ion.

A comparison between the spectra of $Nd(MB1\text{-}2)_3$ in D_2O compared to H_2O enabled the identification of exchangeable protons. In H_2O, peaks appeared around 8 ppm from NH amide backbone, the Lys protonated amine NH_3^+, and the NH of the Trp indole ring (10 ppm). Because of the broad water peak, it was difficult to identify exchangeable protons around 4 ppm. This derives from Gln and Asn amide protons. It was hypothesised that the amide proton on Asn was susceptible to parashift due to its proximity to the metal. The two peaks were found at negative frequencies in the $Nd(MB1\text{-}2)_3$ spectrum. Because they were absent in D_2O, as a result, they were assigned to exchangeable protons.

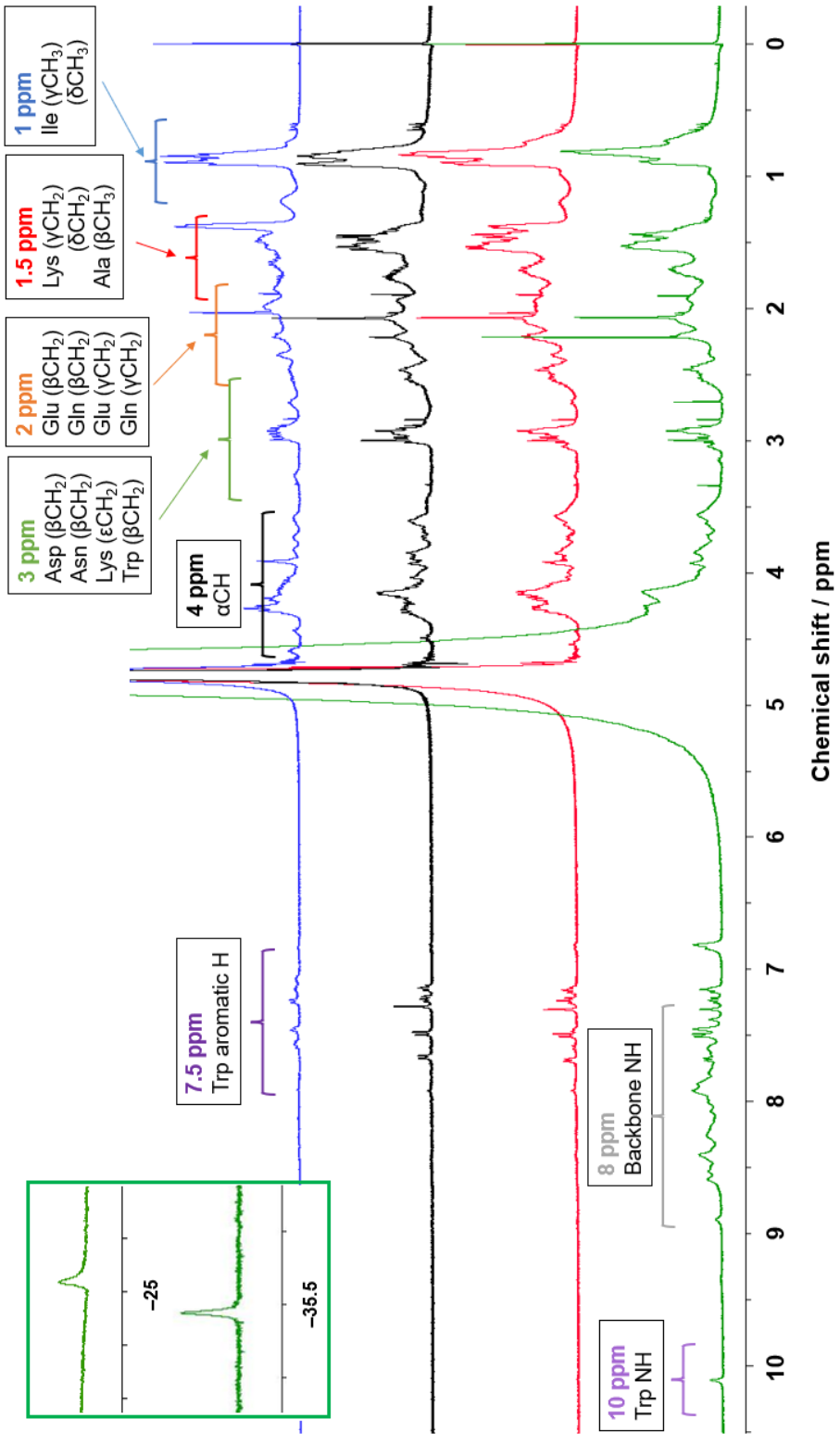


Figure 8.2: ^{1}H-NMR spectra of apo MB1-2 in D_2O (blue), La(MB1-2)$_3$ in D_2O (black), Nd(MB1-2)$_3$ in D_2O (red) and in 90:10 H_2O:D_2O (green) in the region 0-10 ppm. In the insert, peaks at shifted negative frequencies in the Nd(MB1-2)$_3$ spectrum (in 90:10 H_2O:D_2O). Samples prepared in either D_2O, pD 7.0 or 90:10 H_2O:D_2O, pH 7.0. DSS used as reference (0 ppm).

8.3.2 Z-spectrum

The Z-spectrum of Nd(MB1-2)$_3$ showed many peaks, probably arising from exchangeable protons and/or water molecules in the hydration sphere of the peptide (Figure 8.3). One broad peak centred at $\Delta\omega$ = –27 ppm respect to bulk water (for bulk water, $\Delta\omega$ = 0), is probably due to water in proximity or bound to Nd(III). The peak at $\Delta\omega$ ~ 4 ppm can be attributed to the backbone amide protons. This peak presents a shoulder at 5.4 ppm, corresponding to Trp NH proton.

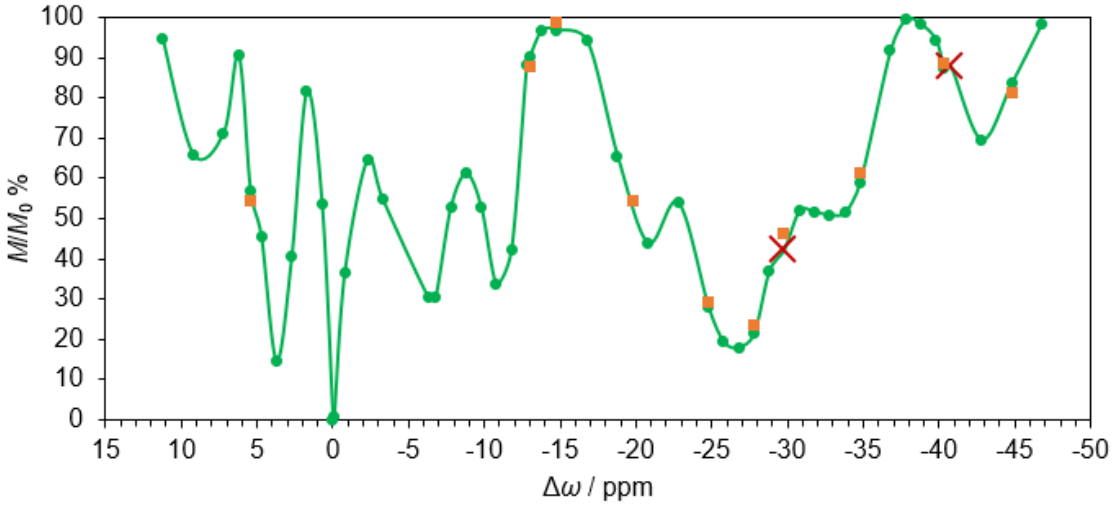


Figure 8.3: Z-spectrum showing M/M_0% of Nd(MB1-2)$_3$ in 90:10 H_2O:D_2O, pH 7.0 at different saturation frequencies relative to bulk water (for bulk water $\Delta\omega$= 0 ppm). In orange and in green two independent repeats. Red crosses show the values relative to the peaks identified in NMR spectra (see Section 8.3.1).

8.4 Discussion

Z-spectrum analysis enabled the identification of different pools in exchange with bulk water in the Nd(MB1-2)$_3$ system. These are mainly constituted by NH backbone amide protons at 8.3 ppm relative to frequency offset of 4 ppm. A broad peak was found, centred at frequency offset of −27 ppm, which was attributed to water bound to Nd(III) or at least in close proximity (second-sphere water). This is in good agreement with a previous report where a Nd(III) complex showed chemical shift of the water bound to the metal at –32 ppm.[11] In NMR spectra only 2 peaks were found to be shifted, at negative frequencies, due to the presence of Nd(III). These peaks were attributed to exchangeable protons. However, these peaks do not correspond to regions of maximum CEST effect, suggesting that they may derive from protons exchanging from bulk water at a rate too low to provide good CEST effect (which also is consistent with the relative sharpness of the peaks, as consequence of slow exchange rates). The lack of other detectable shifted peaks in NMR spectra was attributed to protons exchanging with bulk water at a rate fast

enough to provide CEST, but resulting in large peak broadening, as consequence of slow-to-intermediate exchange rates.

8.5 Conclusions and future work

A lanthanide-binding coiled-coil capable of giving rise to CEST effect was reported for the first time. This result opens to further studies on this system, such as the identification of the shifted peaks, for instance using 2D-NMR experiments (NOESY, COSY or heteronuclear experiments). Moreover, studies devoted to optimising instrument parameters (for example the power and the duration of the saturation pulse) could possibly lead to enhanced CEST effect.

In addition, other systems could be evaluated, such as the analogue Eu(III) complex, which has been shown to be folded in its metallo-form.[6] A preliminary study to identify shifted peaks has already been conducted (Figure 8.4) and a peak resonating at 104 ppm was identified and attributed to exchangeable protons, since no signal was detected in D_2O.

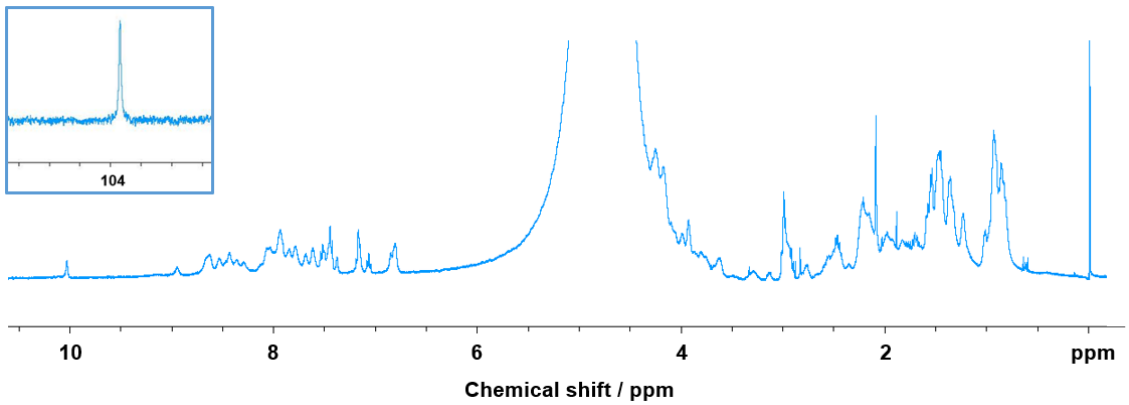


Figure 8.4: ^{1}H-NMR spectrum of Eu(MB1-2)$_3$. In the insert, peak at shifted positive frequencies. Sample prepared in 90:10 H_2O:D_2O, pH 7.0, DSS used as reference (0 ppm).

References

1. I. Hancu, W. T. Dixon, M. Woods, E. Vinogradov, A. D. Sherry and R. E. Lenkinski, *Acta Radiol.*, 2010, **51**, 910-923.
2. V. C. Pierre and M. J. Allen, Eds., *Contrast agents for MRI: experimental methods*, Royal Society of Chemistry, 2017.
3. S. Zhang, M. Merritt, D. E. Woessner, R. E. Lenkinski and A. D. Sherry, *Acc. Chem. Res.*, 2003, **36**, 783-790.
4. O. Vasalatiy, P. Zhao, M. Woods, A. Marconescu, A. Castillo-Muzquiz, P. Thorpe, G. E. Kiefer and A. D. Sherry, *Bioorg. Med. Chem.*, 2011, **19**, 1106-1114.
5. M. R. Berwick, D. J. Lewis, A. W. Jones, R. A. Parslow, T. R. Dafforn, H. J. Cooper, J. Wilkie, Z. Pikramenou, M. M. Britton and A. F. Peacock, *J. Am. Chem. Soc.*, 2014, **136**, 1166-1169.
6. L. N. Slope, PhD, University of Birmingham, 2017.
7. L. N. Slope, O. J. Daubney, H. Campbell, S. A. White and A. F. Peacock, *Angew. Chem.*, 2021, **133**, 24678-24682.
8. S. L. Newton, PhD, University of Birmingham, 2018.
9. E. Liepinsh and G. Otting, *Magn. Reson. Med.*, 1996, **35**, 30-42.
10. K. Mikkelsen and S. O. Nielsen, *J. Phys. Chem.*, 1960, **64**, 632-637.
11. S. Zhang and A. D. Sherry, *J. Solid State Chem.*, 2003, **171**, 38-43.

CHAPTER 9

CONCLUSIONS, FUTURE WORK AND APPLICATIONS

9.1 Conclusions

In this work, the potential use of *de novo* designed coiled-coils as MRI contrast agents has been explored, aiming to provide alternatives to Gd(III)-based contrast agents which could give rise to safety and environmental concerns. Moreover, the application of CEST as imaging technique was preliminary explored. This offers multiple advantages, for instance, the ability to turn on and off the contrast when needed.

The first part of this work was devoted to the establish for the first time that Cu(II) is suitable for use as relaxation agent, despite the limitation arising from the presence of a single unpaired electron (which has led to a general low interest in developing Cu(II) based contrast agents).[1] However, fast water exchange kinetics,[2] long Cu(II) electron relaxation times[3] and the lower potential toxicity than Gd(III), stimulates the exploration of its coordination compounds as MRI contrast agents. In this work, to overcome the intrinsic low efficiency of Cu(II) compounds as relaxation agents, the strategy was to include the metal within *de novo* designed coiled-coils. This generates a complex with slower molecular tumbling, leading to an increase in MRI relaxivity at low, clinically relevant magnetic fields. In Chapter 3, a new Cu(II)-based three stranded coiled-coil was developed, named $Cu(MB1\text{-}2)_3$, and NMR experiments showed that the complex can generate high relaxivities. Further investigation determined that, in the complex, molecular parameters, such as rotational correlation time, water residence time and the number of inner-sphere water molecules are optimised, leading to high relaxivities. These are, to the best of our knowledge, the highest ever reported for a Cu(II) compound.

In Chapter 4 and Chapter 5 new Cu(II) coiled-coils were explored, in an attempt to develop structure-performance/activity relationships and to gain more insight into the mechanisms which lead to high relaxivity of the $Cu(MB1\text{-}2)_3$ complex. Moreover, it was established that the peptide design rules that enhance relaxivity for the Gd(III) coiled-coils complexes do not translate to the Cu(II) systems. Water accessibility to Cu(II) was modulated by translating the binding site to the extremities of the coiled-coil (generating $Cu(MB1\text{-}1)_3$ and $Cu(MB1\text{-}4)_3$). In the analogous Gd(III) coiled-coils, this determined enhanced hydration of Gd(III), leading to improved relaxivities.[4]

In contrast, translation of the Cu(II) site to the N-terminus (top of the CC) led to a reduction in relaxivity. This was attributed to the presence of a single inner-sphere water molecule, as a consequence of a more flexible and/or less folded peptide structure at the N-terminus. Moreover, simulations were consistent with the single inner-sphere water molecule located at longer distances to Cu(II) and it being in a fast-exchange regime with bulk water. This means that, in this complex, water molecules exchange too quickly to allow efficient proton relaxation. The impact of water residence time was even more evident in Cu(MB1-4)$_3$: despite the presence of two inner-sphere water molecules (similar to MB1-2), the relaxivities were found to be drastically reduced, hypothesised to be due to the water exchange rate again shifting towards a fast-exchange limit.

Residues with high steric hindrance were positioned at the entrance of the binding site to further tune water coordination (Cu(MB1-1 2F)$_3$ and Cu(MB1-1 2W)$_3$). These showed improved relaxivity than their parent Cu(MB1-1)$_3$ complex. The reason for that was hypothesised to be consequence of the bulky aromatic residues which impose rigidity and distortions to the structure, leading to the presence of more water molecules in closer proximity to Cu(II). In addition, these water molecules could have with longer residence times, more comparable to Cu(MB1-2)$_3$. This was found to be in contrast with the analogous Gd(III) coiled-coils, in which the presence of the aromatic residues led to reduced hydration and, consequently, reduced relaxivity.[5]

The Cu(II) first-coordination sphere residues were mutated in an effort to establish the relationship between the Cu(II) coordination chemistry, stability constants and relaxivity. The introduction of His residues within the sequence was shown to yield Cu(II) complexes with higher thermodynamic stability, but with no clear improvement on kinetic inertness over Zn(II) transmetallation. Such mutations are, however, a powerful method to modulate MRI relaxivity. In the presence of Asp in ***a*** position and Ile or His in ***d*** position, for binding sites buried within the interior of the coiled-coils, relaxivity are only slightly lower than Cu(MB1-2)$_3$. This was attributed either to optimised water exchange, or to the presence of a partially structured binding site that enables the presence of water molecules for Cu(II) complexation. Cu(II) complexes of both coiled-coils with His in ***a*** position and Ile or Asp in ***d*** position, only displayed low relaxivity, suggesting that the replacement of Asp$_3$ layer to a His$_3$ layer in ***a*** position has a detrimental impact on Cu-water proton distances, water residence times and/or Cu(II) electron relaxation times.

A series of coiled-coils designed to bind to Mn(II) were developed in Chapter 6, in an effort develop a new class of Mn(II) based contrast agents, which are currently investigated as safer alternatives to Gd(II).[6-8]. Mn(II) binding was determined to be very weak and dynamic, leading to marginal folding improvement. For future applications, this needs to be overcome.

However, it was shown that high MRI relaxivities at 1.4 T can be accessed for the metallopeptides with designed Mn(II) binding sites (r_1 ~35 mM^{-1} s^{-1} and r_2 ~ 92 mM^{-1} s^{-1}). These values were found to be higher or comparable to a small Mn(II) complex in the presence of human serum albumin (r_1 = 27.2 mM^{-1} s^{-1} and r_2 = 96.4 mM^{-1} s^{-1}).[9] Relaxivities of the control peptide in the presence of $MnCl_2$, were determined to be comparable to $MnCl_2$ alone (r_1 = 6.8 ± 0.6 mM^{-1} s^{-1} and r_2 = 59.5 ± 7.5 mM^{-1} s^{-1}), suggesting lack of Mn(II) binding in the absence of a designed binding site. Moreover, magnetic field dependence of $1/T_1$ and $1/T_2$ relaxation rates, suggests Mn(II) interacting with a peptide which possesses long rotational correlation time. Overall, the high relaxivities were attributed to a large number of water molecules in the Mn(II) inner-sphere (around two), probably due to inefficacy for the peptides to be distorted to generate a saturated Mn(II) binding site. Despite their high relaxivities, the Mn(II) peptides in this study showed very fast Zn(II) transmetallation, meaning low kinetic inertness.

A strategy to enhance relaxivity was explored in Chapter 7 by increasing the number of paramagnetic metals in one complex. Two and three metal binding sites were introduced into the same scaffold, aiming to generate scaffolds able to bind to multiple paramagnetic metal ions (e.g. Gd(III) or Cu(II)), in an effort to generate high relaxivities per complex. CD and fluorescence experiments are consistent with two or three Ln(III) ions binding, but Cu(II) binding data was more difficult to interpret. Relaxivity experiments revealed that when the binding sites are located at the N-terminus and on the adjacent heptad, water is prevented from entering into the hydrophobic core to get in proximity (in the Gd(III) compounds) or to coordinate to the metal (in the Cu(II) peptides) in the buried site.

In contrast, when the buried Gd(III)/Cu(II) binding site is separated by one heptad from the binding site at the N-terminus, the relaxivities are improved. Finally, it was shown that when a peptide is almost unstructured (therefore the metal is probably highly hydrated) the relaxivities are high in Gd(III) compound (as shown by Berwick and co-workers[4]) while they are low in the Cu(II) system. In the Cu(II) complex, this could be due to very fast water exchange kinetics (as shown in Chapter 4) and/or dynamic Cu(II) binding.

From this work, important design features were identified. The reduction in solubility of the peptides with increasing the length of the sequence should be taken into account and one should consider adding polar residues in ***b*** and ***c*** positions, which are not involved in coiled-coil folding.

Finally, the potential use of Nd(MB1-2)$_3$ coiled-coil as paraCEST contrast agent was preliminary explored in Chapter 8. Different proton pools, in exchange with bulk water at a rate suitable for providing CEST effect, were identified. This stimulates more studies on the use of

this class of peptides as paraCEST agents, which potentially offers multiple advantages, such as a high number of exchangeable protons as well as relatively easy tunability of water exchange.

9.2 Future work and applications

Despite the promising relaxivities displayed for almost all the Cu(II), Mn(II) and Gd(III)-binding coiled-coils reported in this work, both apparent thermodynamic stability constants and kinetic inertness towards Zn(II) transmetallation were found to be too low for the use of these complexes as MRI contrast agents without further improvement.[10] One method for binding constant enhancement, is to cross-link peptides at either termini, or in proximity of the binding site. This should generate preorganised peptide structures, which do not have the same entropic penalty due to the self-assembly (and disassembly) of three separate peptide strands. This could be achieved by generating amide bonds between Lys and Glu residues of different strands.[11] Moreover, by covalently linking the strands near the binding site, metal binding geometry could be potentially more controlled to enhance metal specificity and, therefore, improve kinetic inertness. Moreover, helical bundles could be designed to bind metals by self-assembly of a single strand.

Measurements of water residence time τ_m (through ^{17}O-NMR variable temperature experiments), and metal hydration state q (using EPR), along with nuclear magnetic resonance dispersion (NMRD) experiments, would gain crucial insights into the metal coordination of the Cu(II) and Mn(II) species. These are, for instance, electron relaxation time τ_s and/or its correlation time τ_v.[8] EPR experiments would be also beneficial to better elucidate the presence of N-donors (His or NH_2-Asn), through the presence or absence of Cu(II)-^{14}N coupling.[12]

In terms of applications of this class of peptide-based contrast agents, electrochemistry measurements could be performed for Cu(II) and Mn(II) complexes using cyclic voltammetry. Using this technique, reduction potentials (CuI/CuII and MnII/MnIII) and the reversibility of the measure would determine if the complexes can be used as redox-sensitive MRI contrast agents. The reduction potentials of such complexes should be compared, for instance, with the redox buffers of the intracellular and/or extracellular spaces.[13] For example, the cysteine/cystine couple (CySH/CySSCy) is the dominant buffer in the extracellular matrix (values typically –80 mV vs. NHE - normal hydrogen electrode - in healthy systems, and –62-20 mV in pathologic systems). The glutathione/glutathione disulfide (GSH/GSSG) couple is the dominant buffer inside cells (with values typically −220 mV vs. NHE in healthy cells, and more reducing in proliferating cells, −260 mV).[13]

Redox-sensitive MRI contrast agents can be developed because Cu(I) is diamagnetic (whereas Cu(II) is paramagnetic) and Mn(III) less paramagnetic than Mn(II), giving rise, potentially, to relaxivities dependent of the redox state of the metal. Moreover, the relative flexibility of the peptide could be beneficial to generate high affinities to both reduced and oxidised forms (mandatory for redox-sensitive contrast agents)[14] or could potentially stabilise only one redox form. Finally, peptide-based contrast agents offer the unique advantage for conjugating MRI contrast enhancement with target specificity. This could be achieved by designing specific amino acids sequences able to bind to DNA, proteins or enzymes.[15-17]

This thesis provides important design strategies and perspectives for developing more stable, potentially less toxic and possibly more efficient peptide-based MRI contrast agents. These could find applications as blood-pool MRI contrast agents as well as redox-sensitive and targeting contrast agents.

References

1. R. B. Lauffer, *Chem. Rev.*, 1987, **87**, 901-927.
2. D. H. Powell, P. Furrer, P.-A. Pittet and A. E. Merbach, *J. Phys. Chem.*, 1995, **99**, 16622-16629.
3. I. Bertini, C. Luchinat, R. D. Brown III and S. H. Koenig, *J. Am. Chem. Soc.*, 1989, **111**, 3532-3536.
4. M. R. Berwick, L. N. Slope, C. F. Smith, S. M. King, S. L. Newton, R. B. Gillis, G. G. Adams, A. J. Rowe, S. E. Harding and M. M. Britton, *Chem. Sci.*, 2016, **7**, 2207-2216.
5. L. N. Slope, M. G. Hill, C. F. Smith, P. Teare, F. J. de Cogan, M. M. Britton and A. F. Peacock, *Chem. Comm.*, 2020, **56**, 3729-3732.
6. E. M. Gale, I. P. Atanasova, F. Blasi, I. Ay and P. Caravan, *J. Am. Chem. Soc.*, 2015, **137**, 15548-15557.
7. B. Drahoš, I. Lukeš and É. Tóth, *Eur. J. Inorg. Chem.*, 2012, **2012**, 1975-1986.
8. V. C. Pierre and M. J. Allen, Eds., *Contrast agents for MRI: experimental methods*, Royal Society of Chemistry, 2017.
9. P. Caravan, C. T. Farrar, L. Frullano and R. Uppal, *Contrast Media Mol. Imaging*, 2009, **4**, 89-100.
10. P. Caravan, J. J. Ellison, T. J. McMurry and R. B. Lauffer, *Chem. Rev.*, 1999, **99**, 2293-2352.
11. C. Wang, X. Li, F. Yu, L. Lu, X. Jiang, X. Xu, H. Wang, W. Lai, T. Zhang and Z. Zhang, *Sci. Rep.*, 2016, **6**, 32161.
12. A. Shah, M. J. Taylor, G. Molinaro, S. Anbu, M. Verdu, L. Jennings, I. Mikulska, S. Diaz-Moreno, H. El Mkami and G. M. Smith, *PNAS*, 2023, **120**, e2219036120.
13. P. B. Tsitovich, P. J. Burns, A. M. McKay and J. R. Morrow, *J. Inorg. Biochem.*, 2014, **133**, 143-154.
14. E. M. Gale, C. M. Jones, I. Ramsay, C. T. Farrar and P. Caravan, *J. Am. Chem. Soc.*, 2016, **138**, 15861-15864.
15. P. Caravan, J. M. Greenwood, J. T. Welch and S. J. Franklin, *Chem. Comm.*, 2003, 2574-2575.
16. P. Caravan, *Acc. Chem. Res.*, 2009, **42**, 851-862.
17. B. L. Oliveira and P. Caravan, *Dalton Trans.*, 2017, **46**, 14488-14508.

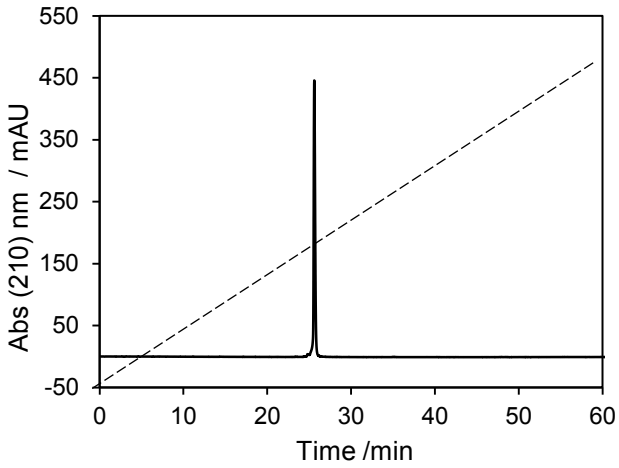
APPENDIX A

ANALYTICAL HPLC AND MASS SPECTRA OF PURE PEPTIDES

Table A.1: Sequences of peptides in this appendix.

MB1-2	Ac-G IAAIEQK IAANEWK DAAIEQK IAAIEQK IAAIEQK G-NH_2
LS4-2	Ac-G IAAIEQK IAAHEWK DAAIEQK IAAIEQK IAAIEQK G-NH_2
GM3	Ac-G IAAIEQK IAAIEWK HAAIEQK IAAIEQK IAAIEQK G-NH_2
CS1-2	Ac-G IAAIEQK IAAIEWK DAAIEQK IAAIEQK IAAIEQK G-NH_2
GM4	Ac-G IAAIEQK IAADEWK HAAIEQK IAAIEQK IAAIEQK G-NH_2
MB1-1	Ac-G IAANEWK DAAIEQK IAAIEQK IAAIEQK IAAIEQK G-NH_2
MB1-4	Ac-G IAAIEQK IAAIEQK IAAIEQK IAANEWK DAAIEQK G-NH_2
MB1-1 2F	Ac-G FAANEWK DAAIEQK IAAIEQK IAAIEQK IAAIEQK G-NH_2
MB1-1 2W	Ac-G WAANEQK DAAIEQK IAAIEQK IAAIEQK IAAIEQK G-NH_2
LS2-1,2	Ac-G IAAIEWK DAANEWK DAAIEQK IAAIEQK IAAIEQK IAAIEQK G-NH_2
LS2-1,3 21W	Ac-G IAAIEWK DAAIEQK IAANEWK DAAIEQK IAAIEQK IAAIEQK G-NH_2
LS2-1,3 21Q	Ac-G IAAIEWK DAAIEQK IAANEQK DAAIEQK IAAIEQK IAAIEQK G-NH_2
LS2-2,3	Ac-G IAAIEQK IAANEWK DAANEWK DAAIEQK IAAIEQK IAAIEQK G-NH_2
GM2	Ac-G IAAIEWK DAANEWK DAANEWK DAAIEQK IAAIEQK IAAIEQK IAAIEQK G-NH_2
CS1-1	Ac-G IAAIEWK DAAIEQK IAAIEQK IAAIEQK IAAIEQK G-NH_2

a)



b)

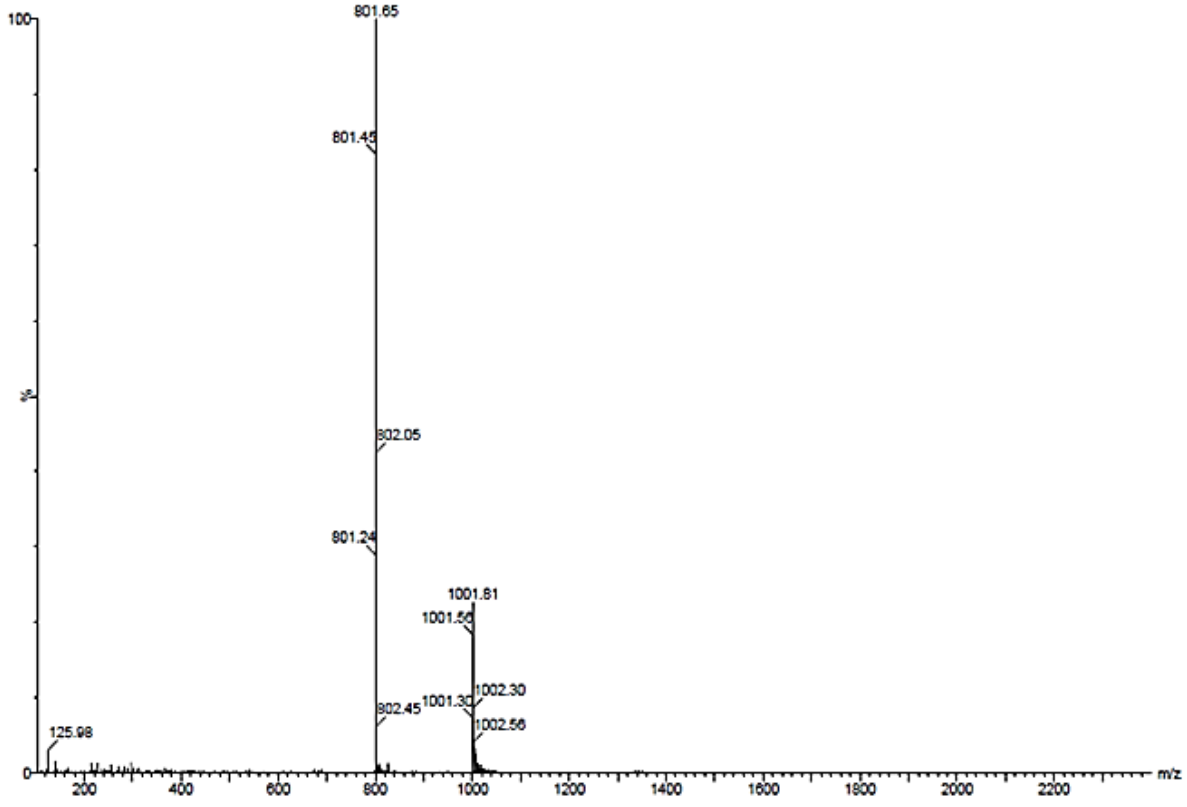
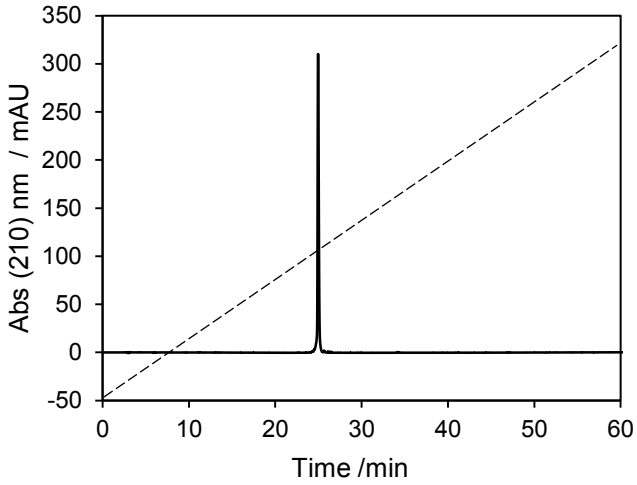


Figure A.1: a) Analytical HPLC trace of pure MB1-2 (retention time 25.6 min) using a linear 0 to 100% MeCN + 0.05% TFA gradient in H_2O + 0.05% TFA over 60 minutes. b) Electrospray mass spectrum of pure MB1-2 (MW 4003.6 g/mol).

a)



b)

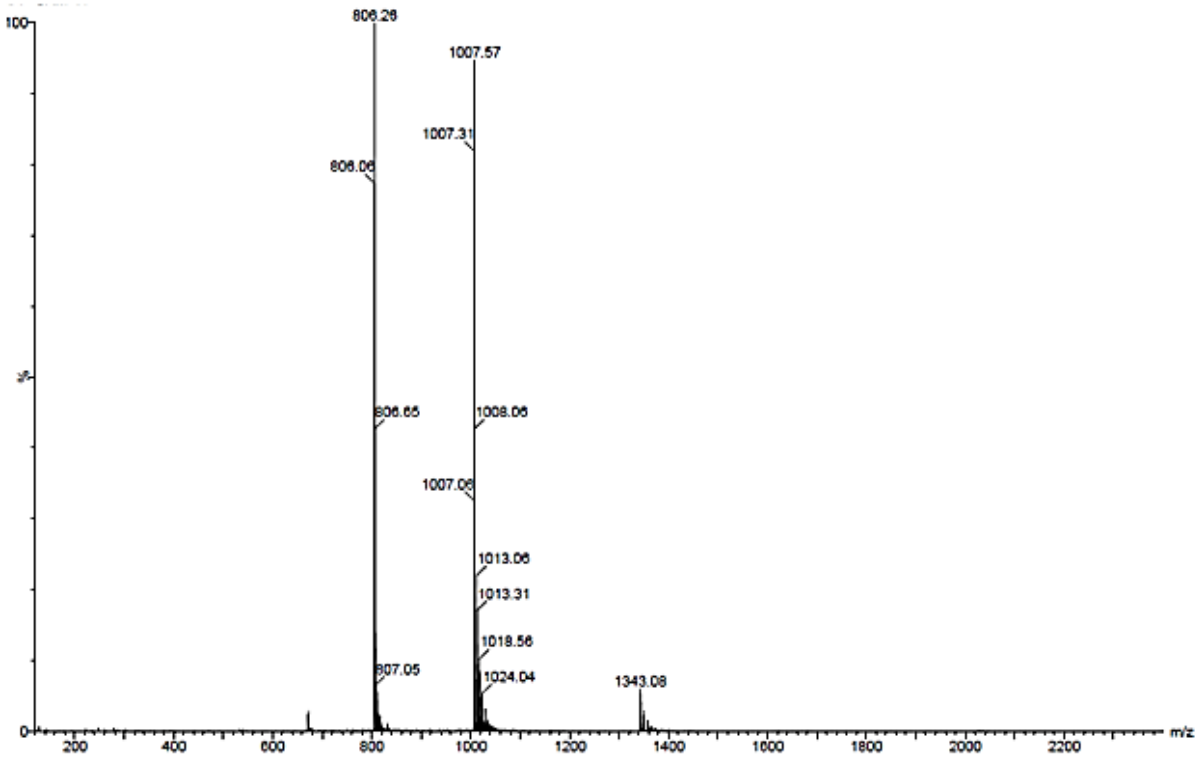
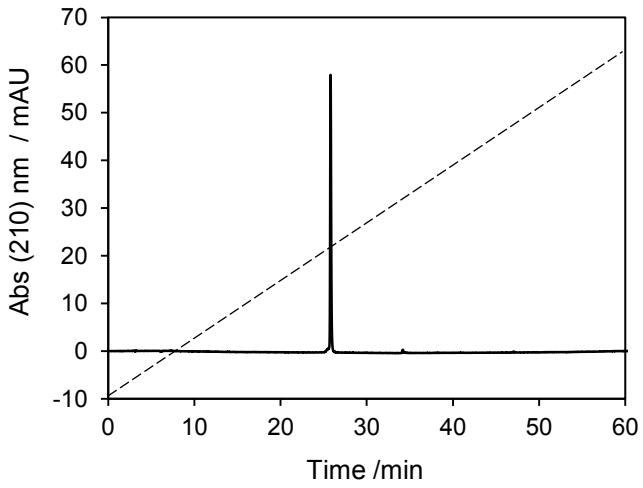


Figure A.2: a) Analytical HPLC trace of pure LS4-2 (retention time 24.9 min.) using a linear 0 to 100% MeCN + 0.05% TFA gradient in H_2O + 0.05% TFA over 60 minutes. b) Electrospray mass spectrum of pure LS4-2 (MW 4026.6 g/mol).

a)



b)

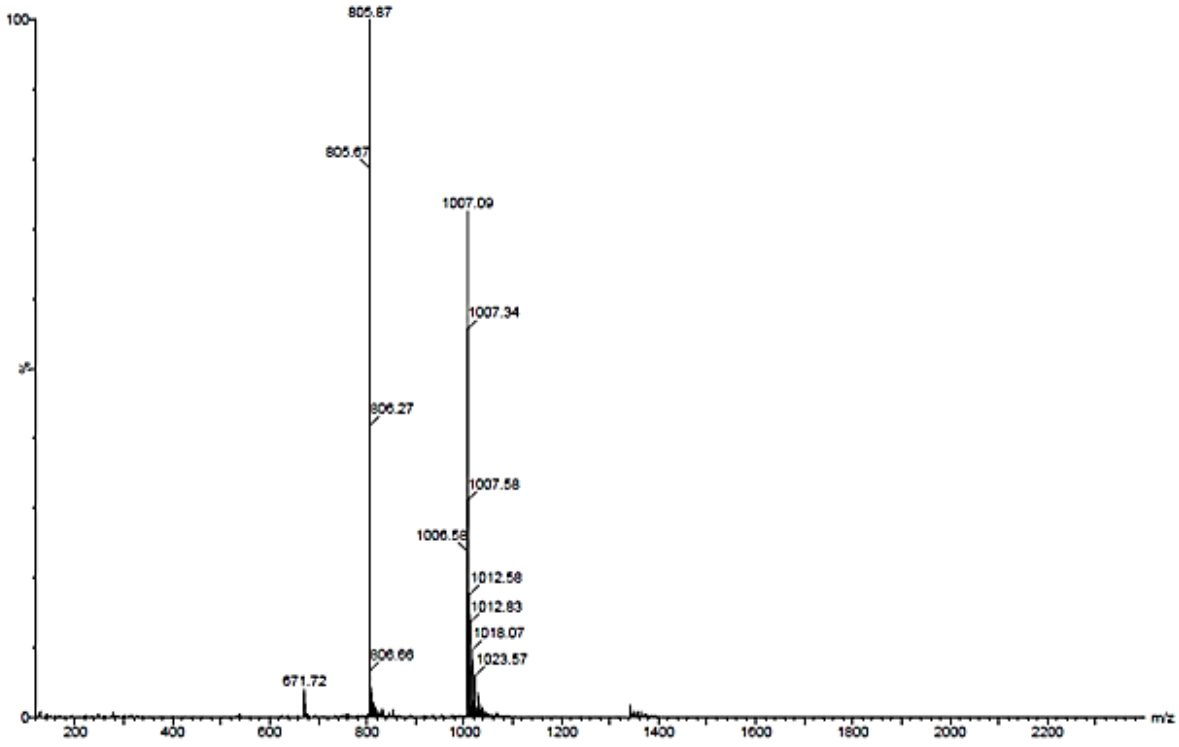
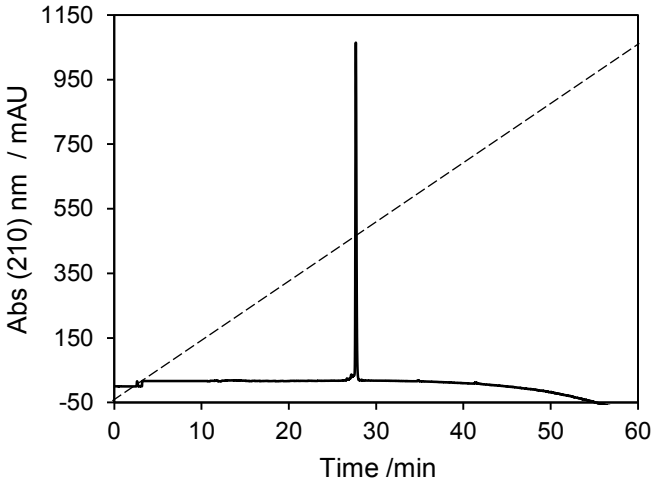


Figure A.3: a) Analytical HPLC trace of pure GM3 (retention time 25.8 min.) using a linear 0 to 100% MeCN + 0.05% TFA gradient in H_2O + 0.05% TFA over 60 minutes. b) Electrospray mass spectrum of pure GM3 (MW 4024.7 g/mol).

a)



b)

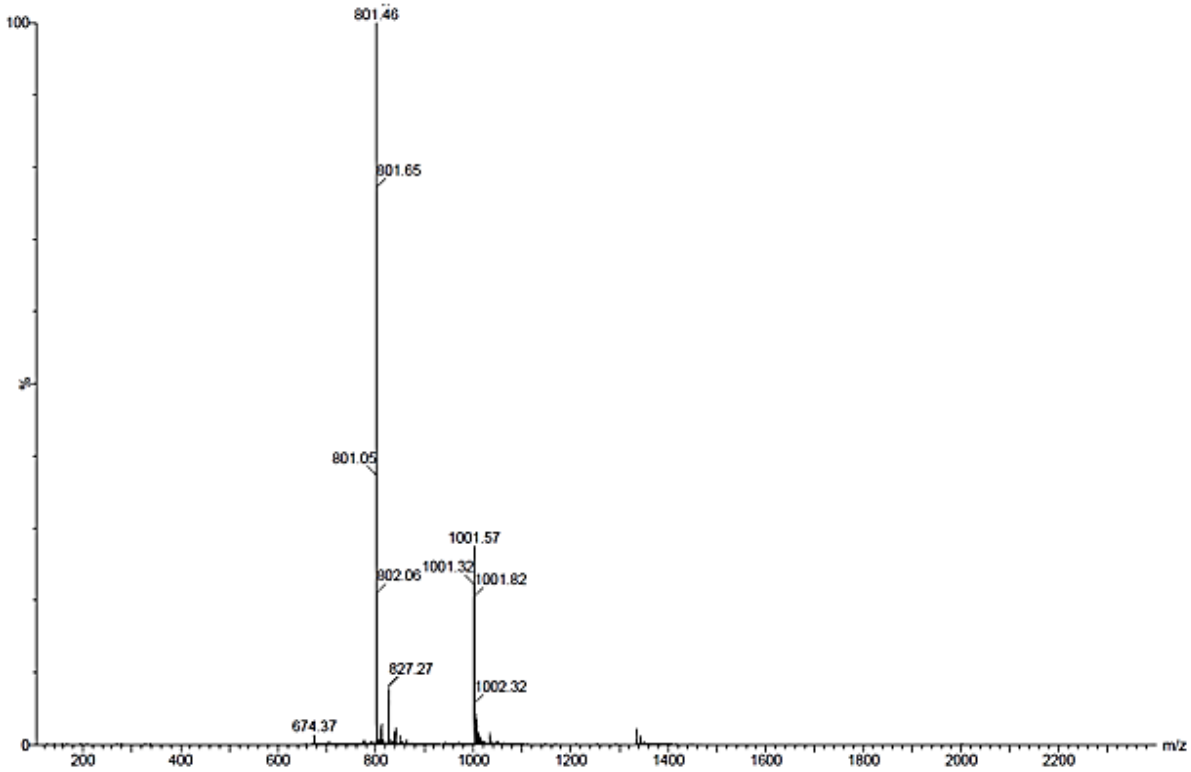
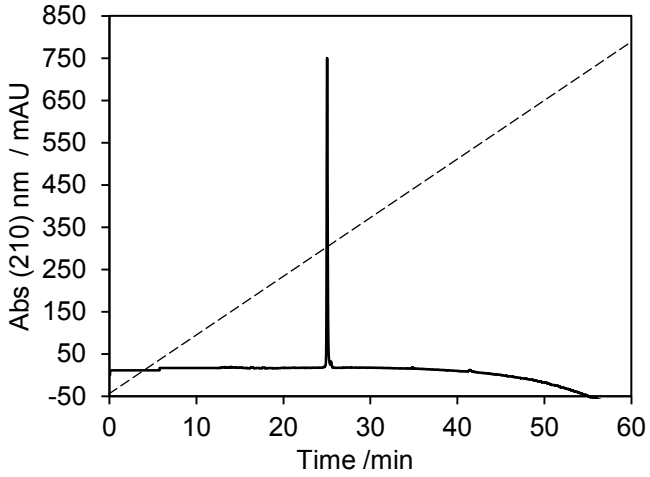


Figure A.4: a) Analytical HPLC trace of pure CS1-2 (retention time 27.7 min.) using a linear 0 to 100% MeCN + 0.05% TFA gradient in H_2O + 0.05% TFA over 60 minutes. b) Electrospray mass spectrum of pure CS1-2 (MW 4002.6 g/mol).

a)



b)

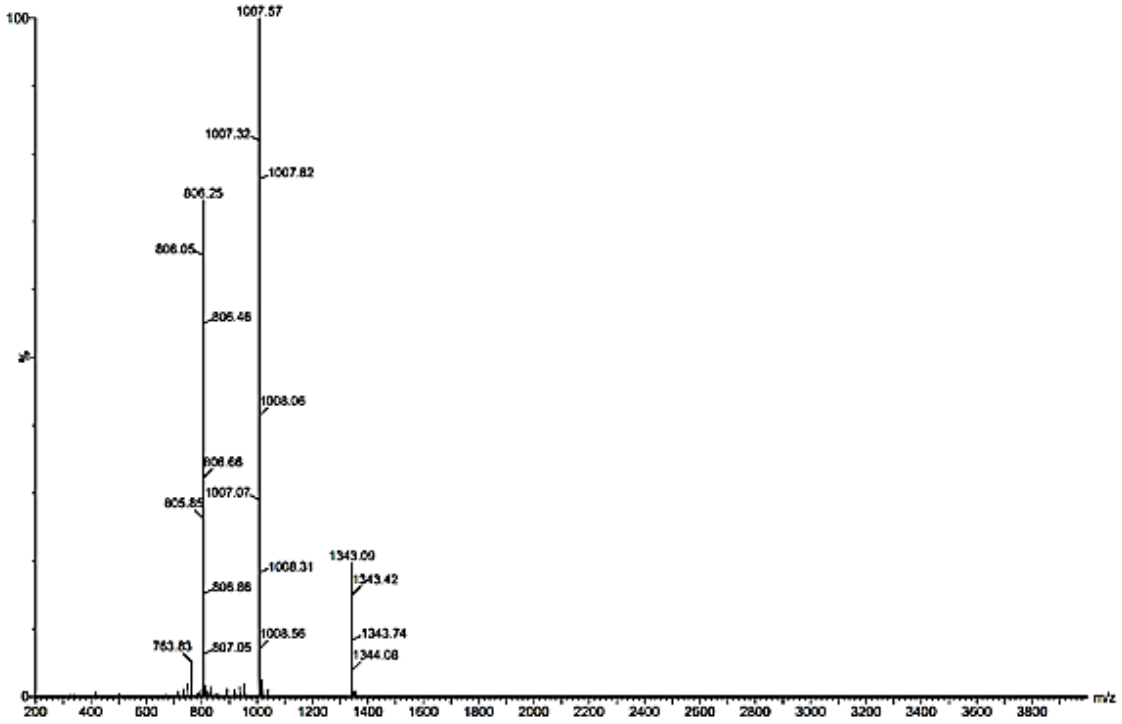
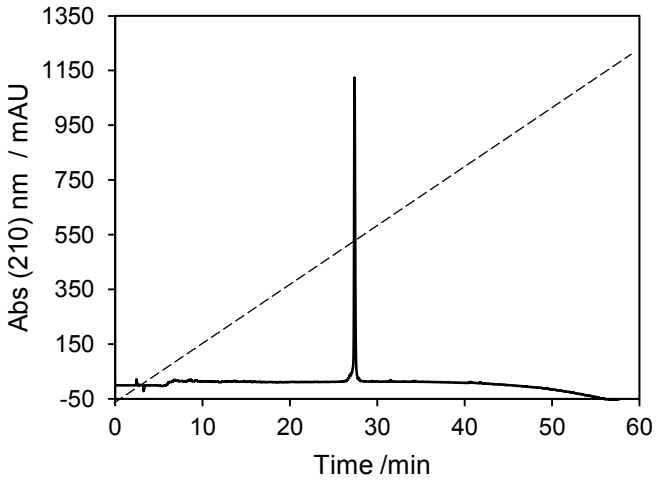


Figure A.5: a) Analytical HPLC trace of pure GM4 (retention time 25.0 min.) using a linear 0 to 100% MeCN + 0.05% TFA gradient in H_2O + 0.05% TFA over 60 minutes. b) Electrospray mass spectrum of pure GM4 (MW 4026.6 g/mol).

a)



b)

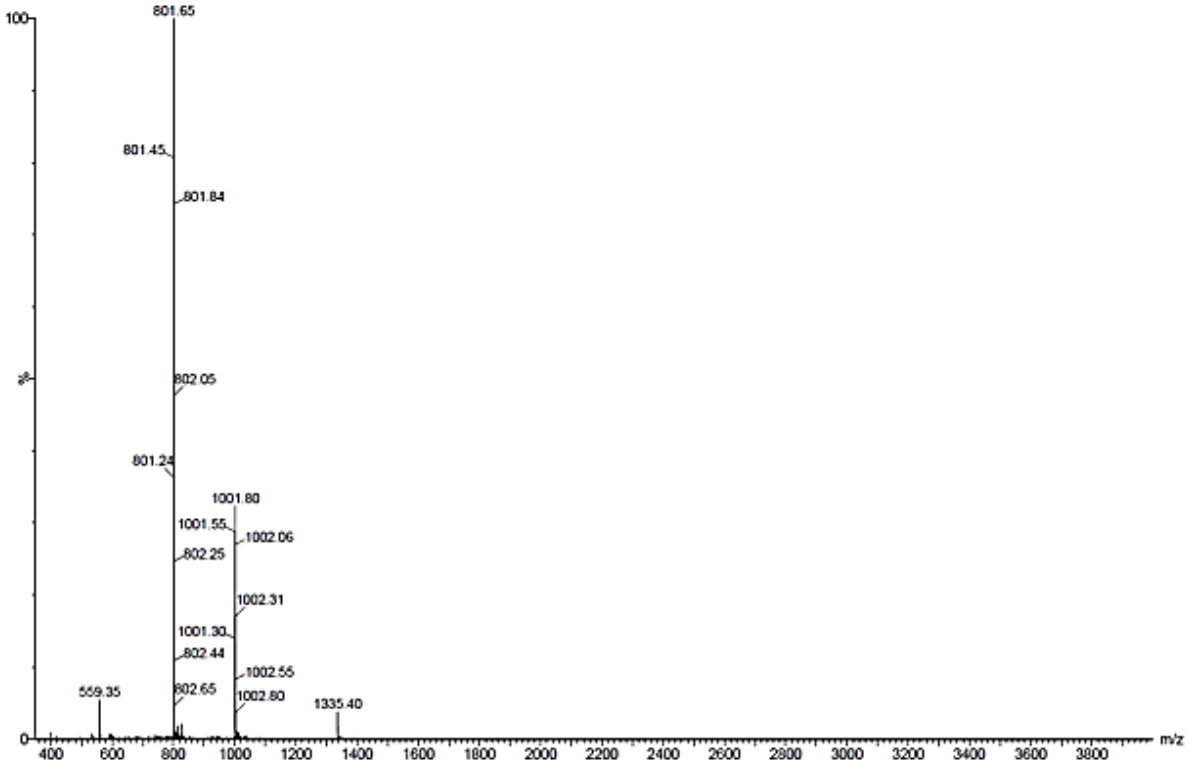
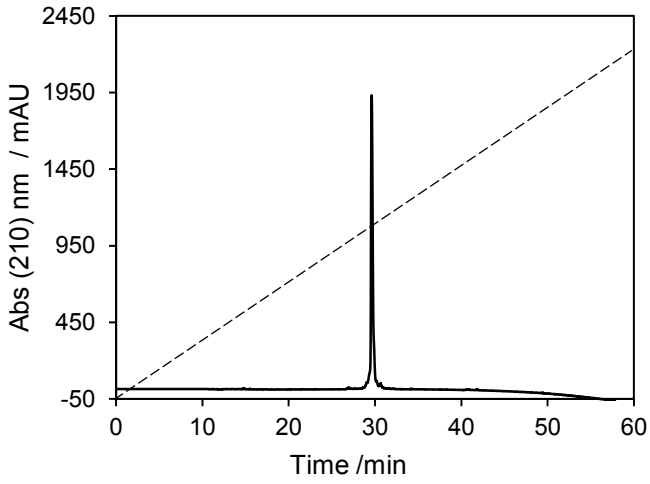


Figure A.6: a) Analytical HPLC trace of pure MB1-1 (retention time 27.4 min.) using a linear 0 to 100% MeCN + 0.05% TFA gradient in H_2O + 0.05% TFA over 60 minutes. b) Electrospray mass spectrum of pure MB1-1 (MW 4003.6 g/mol).

a)



b)

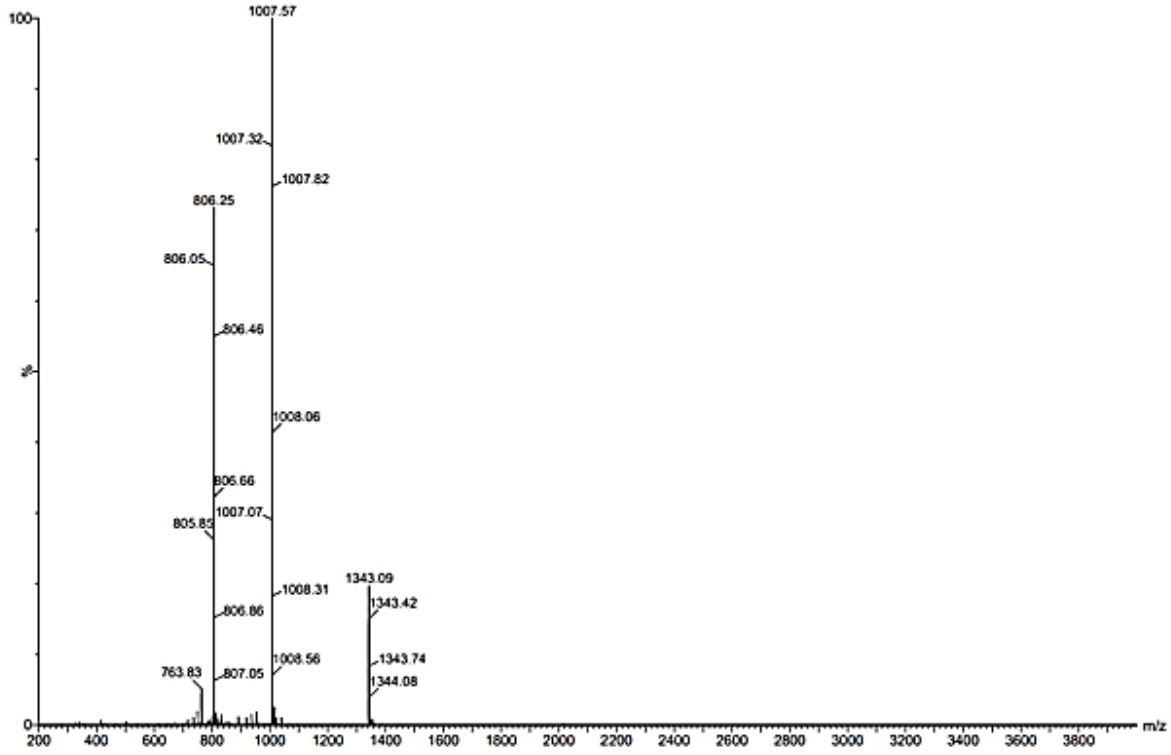
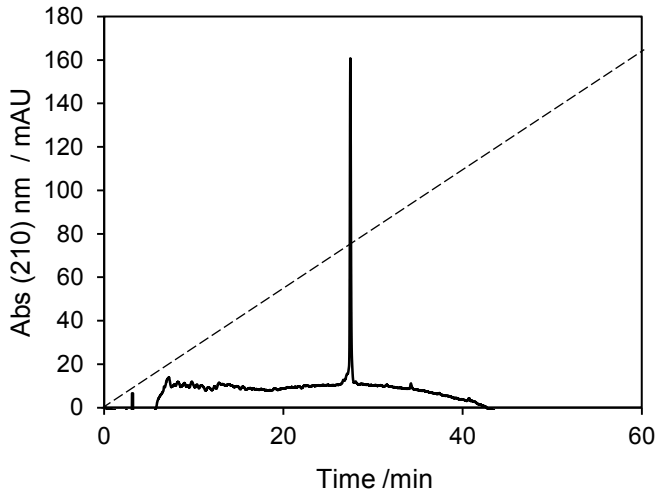


Figure A.7: a) Analytical HPLC trace of pure MB1-4 (retention time 29.6 min.) using a linear 0 to 100% MeCN + 0.05% TFA gradient in H_2O + 0.05% TFA over 60 minutes. b) Electrospray mass spectrum of pure MB1-4 (MW 4003.6 g/mol).

a)



b)

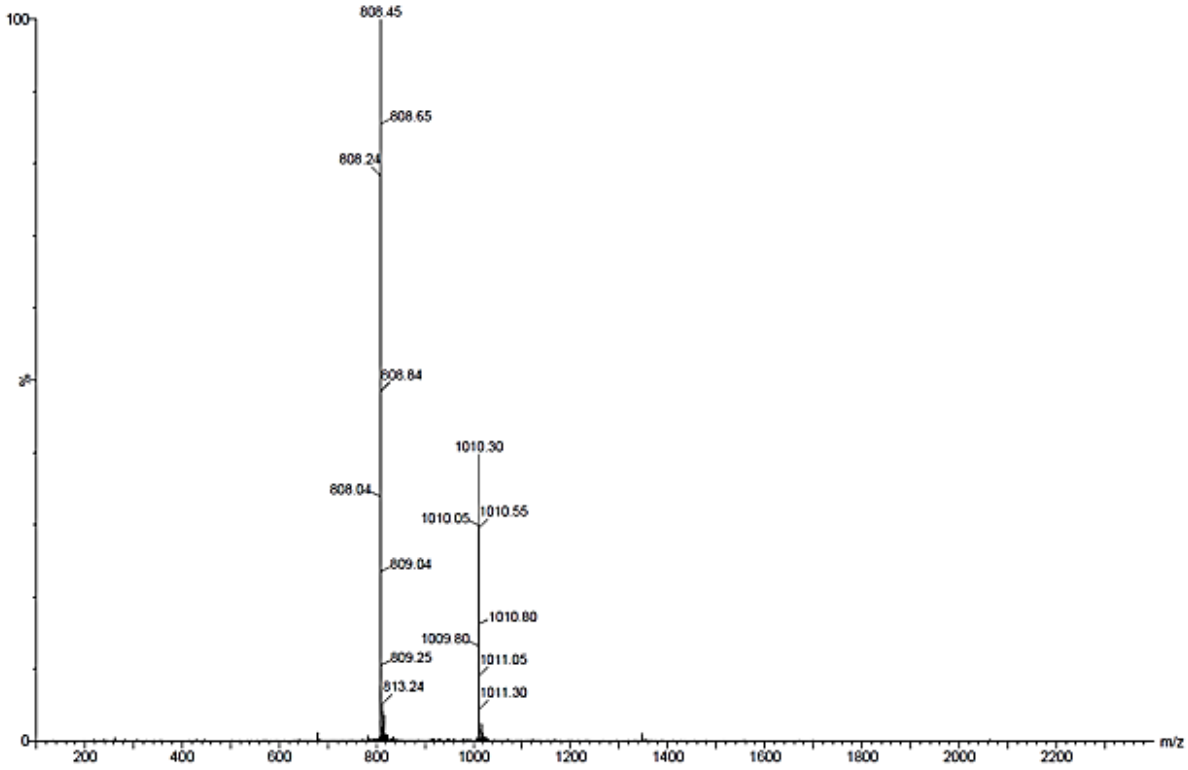
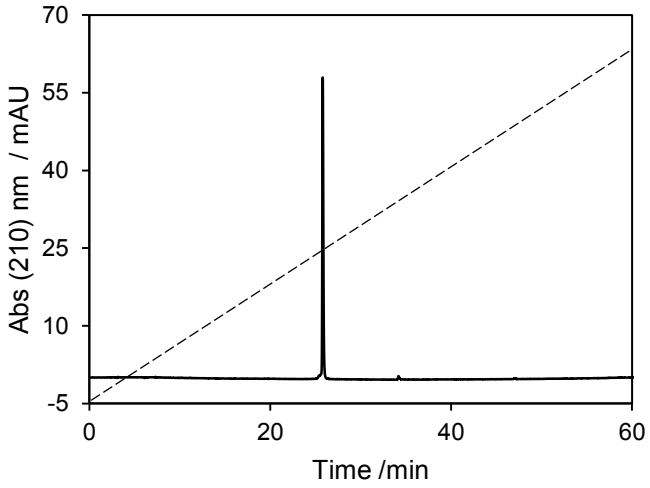


Figure A.8: a) Analytical HPLC trace of pure MB1-1 2F (retention time 27.8 min.) using a linear 0 to 100% MeCN + 0.05% TFA gradient in H_2O + 0.05% TFA over 60 minutes. b) Electrospray mass spectrum of pure MB1-1 2F (MW 4037.6 g/mol).

a)



b)

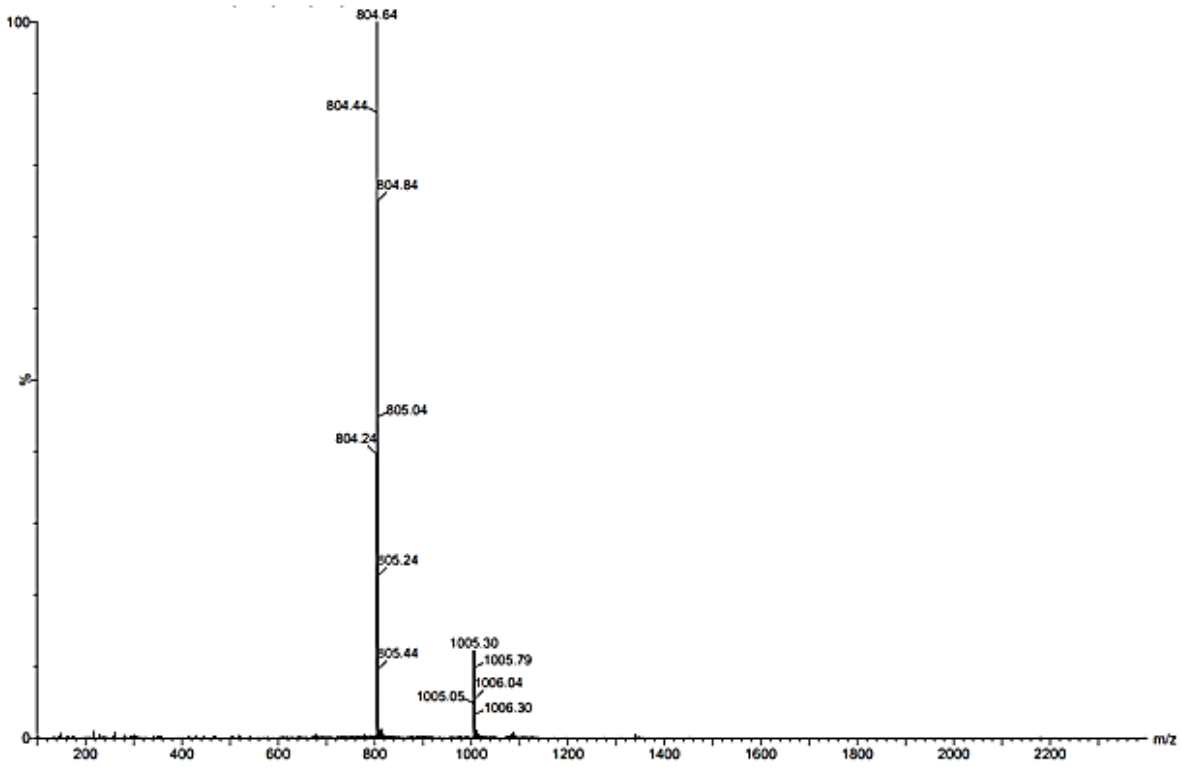
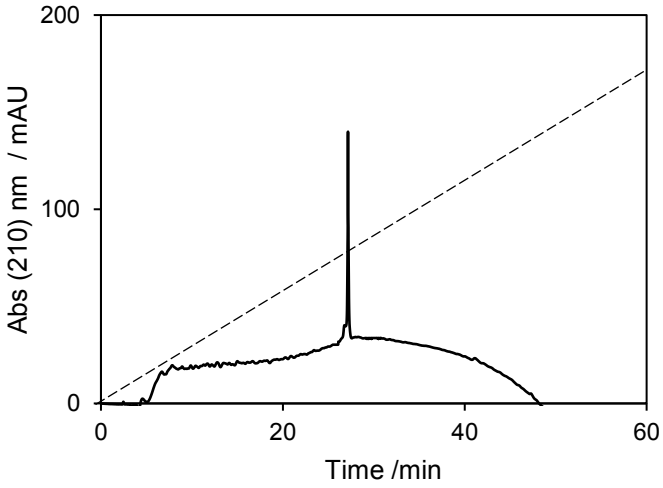


Figure A.9: a) Analytical HPLC trace of pure MB1-1 2W (retention time 25.8 min.) using a linear 0 to 100% MeCN + 0.05% TFA gradient in H_2O + 0.05% TFA over 60 minutes. b) Electrospray mass spectrum of pure MB1-1 2W (MW 4076.6 g/mol).

a)



b)

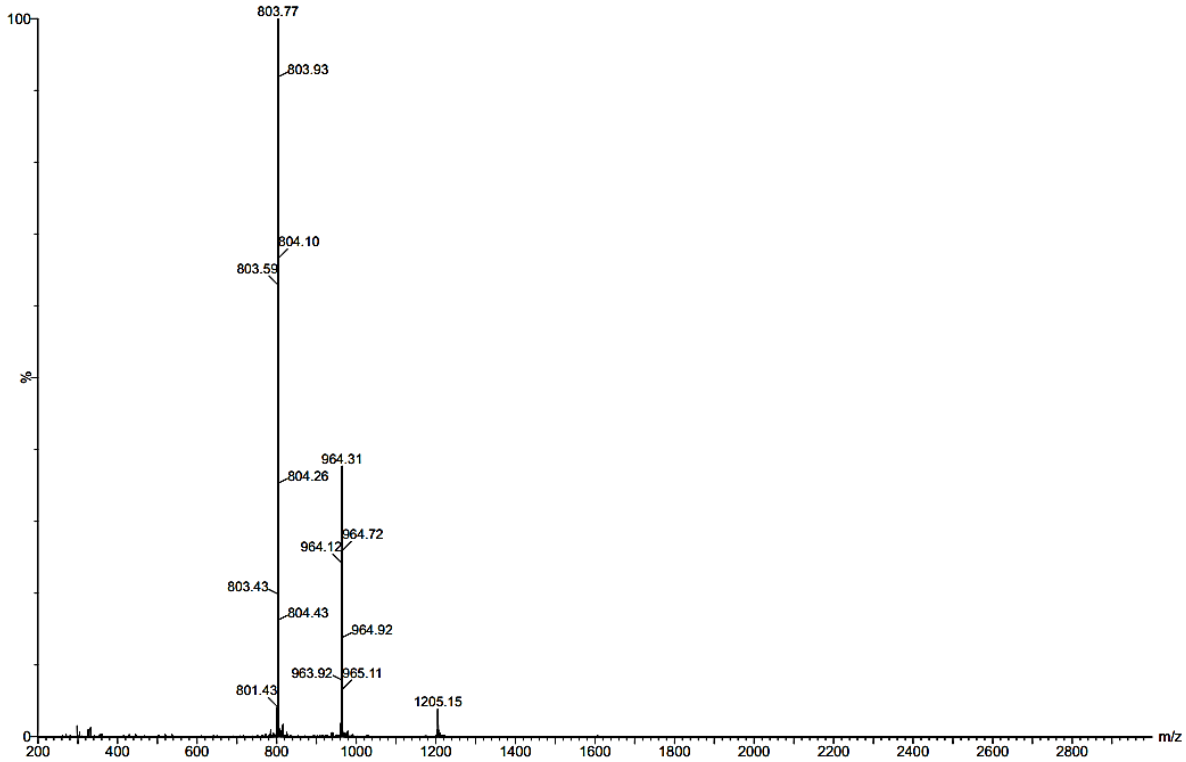
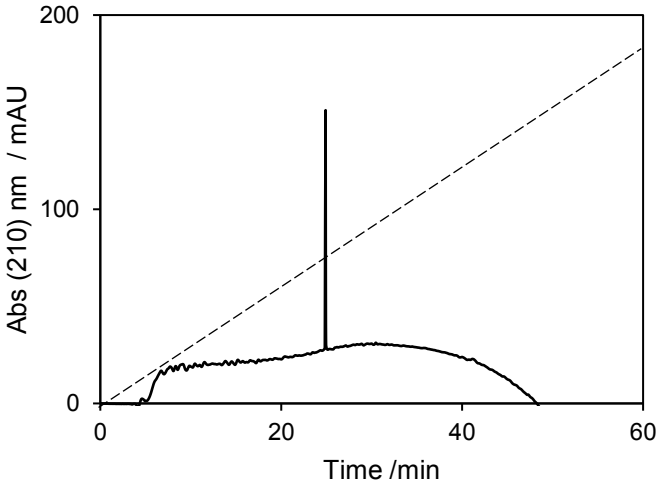


Figure A.10: a) Analytical HPLC trace of pure LS2-1,2 (retention time 27.2 min.) using a linear 0 to 100% MeCN + 0.05% TFA gradient in H_2O + 0.05% TFA over 60 minutes. b) Electrospray mass spectrum of pure LS2-1,2 (MW 4817.5 g/mol).

a)



b)

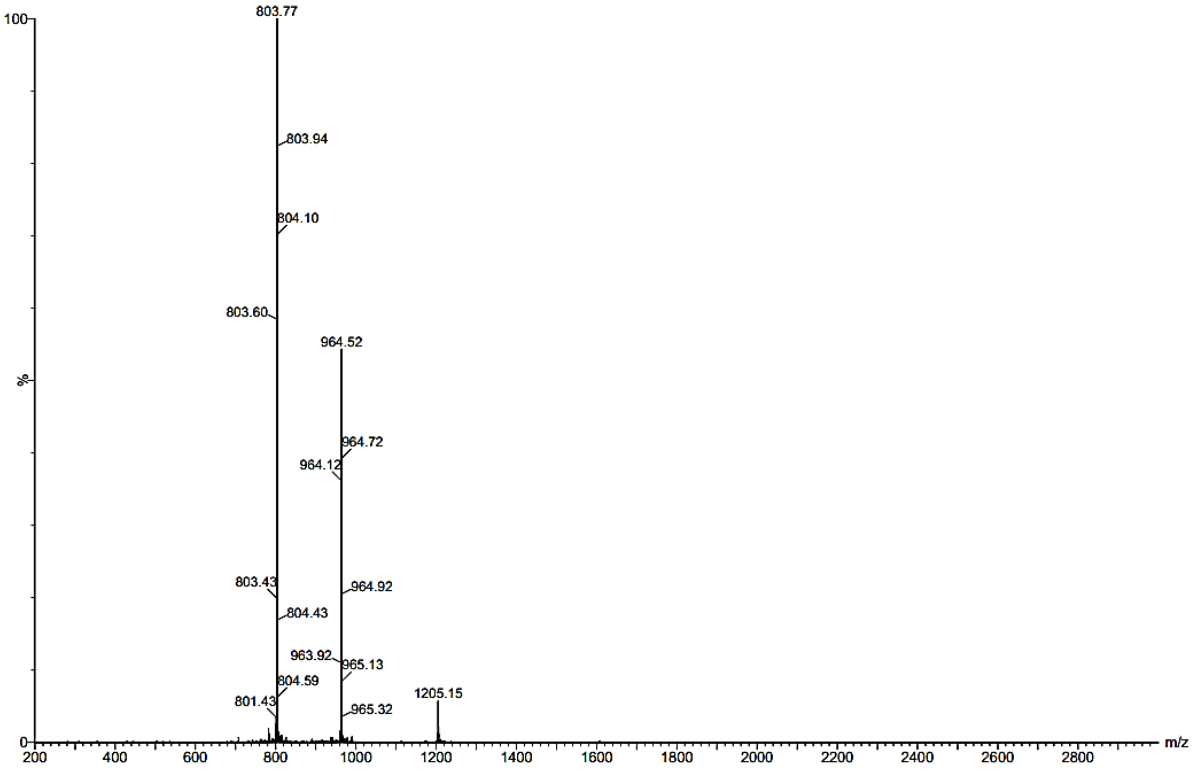
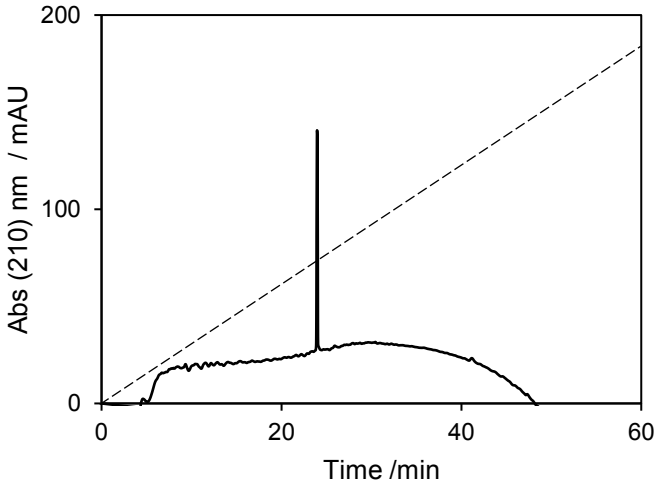


Figure A.11: a) Analytical HPLC trace of pure LS2-1,3 21W (retention time 24.9 min.) using a linear 0 to 100% MeCN + 0.05% TFA gradient in H_2O + 0.05% TFA over 60 minutes. b) Electrospray mass spectrum of pure LS2-1,3 21W (MW 4818.4 g/mol)

a)



b)

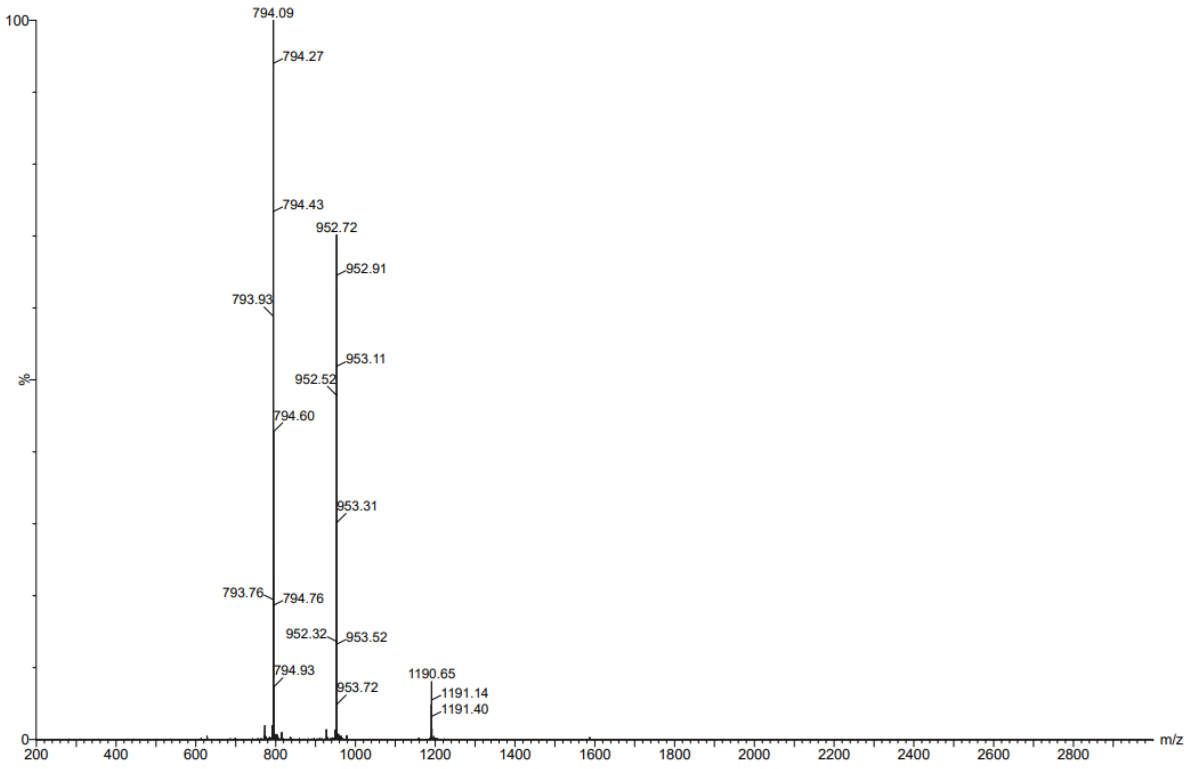
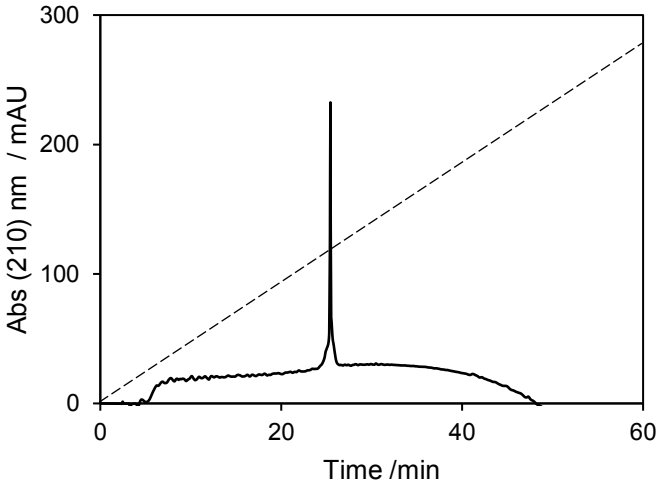


Figure A.12: a) Analytical HPLC trace of pure LS2-1,3 21Q (retention time 23.0 min.) using a linear 0 to 100% MeCN + 0.05% TFA gradient in H_2O + 0.05% TFA over 60 minutes. b) Electrospray mass spectrum of pure LS2-1,3 21Q (MW 4759.4 g/mol).

a)



b)

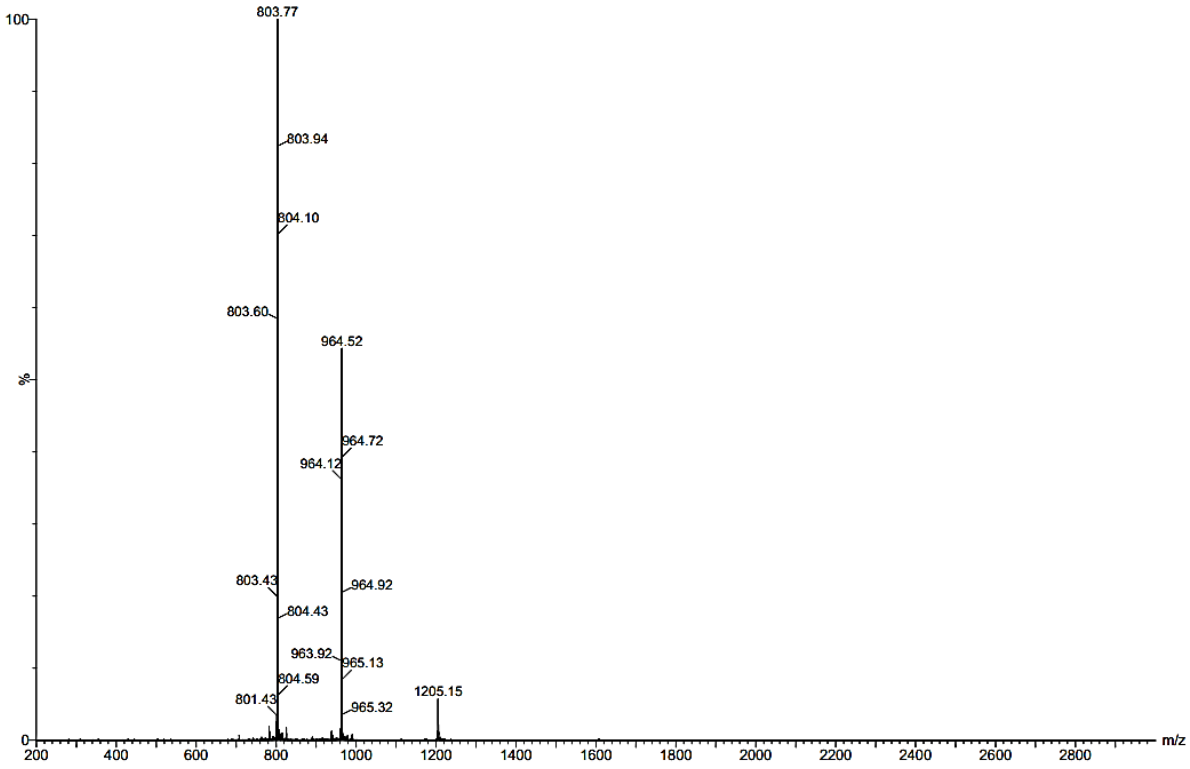
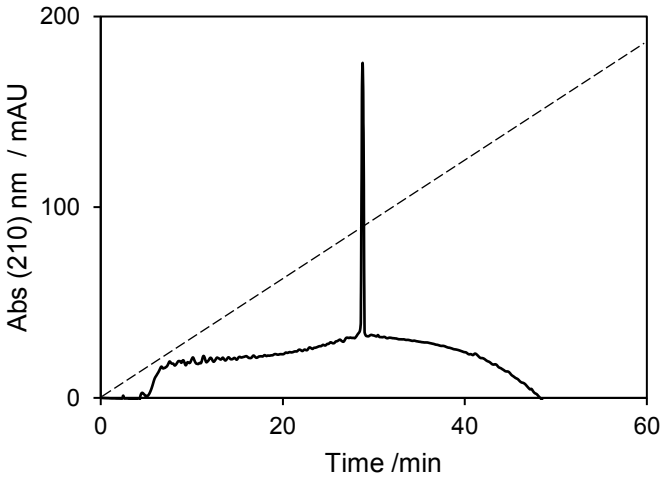


Figure A.13: a) Analytical HPLC trace of pure LS2-2,3 (retention time 25.4 min.) using a linear 0 to 100% MeCN + 0.05% TFA gradient in H_2O + 0.05% TFA over 60 minutes. b) Electrospray mass spectrum of pure LS2-2,3 (MW 4818.4 g/mol).

a)



b)

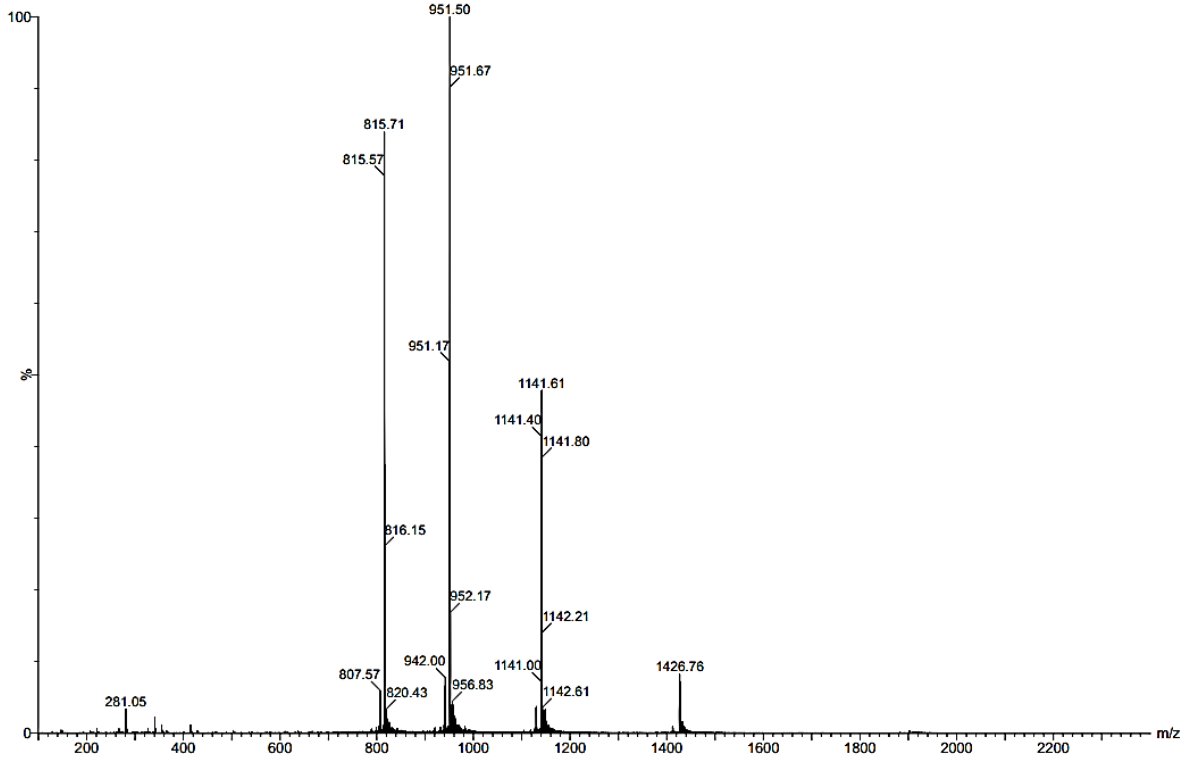
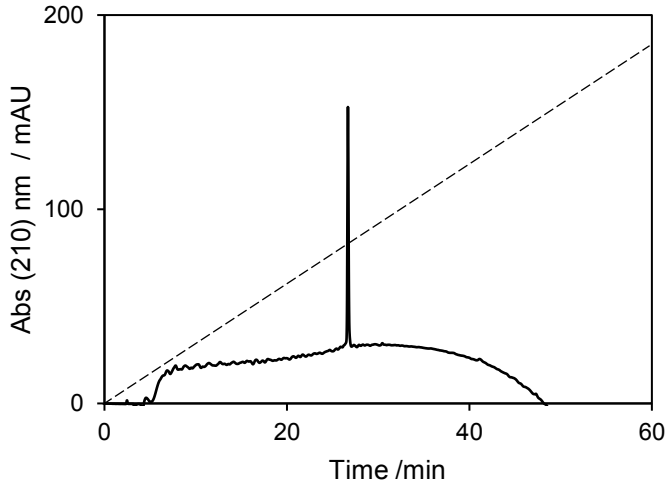


Figure A.14: a) Analytical HPLC trace of pure GM2 (retention time 28.8 min.) using a linear 0 to 100% MeCN + 0.05% TFA gradient in H_2O + 0.05% TFA over 60 minutes. b) Electrospray mass spectrum of pure GM2 (MW 5631.3 g/mol).

a)



b)

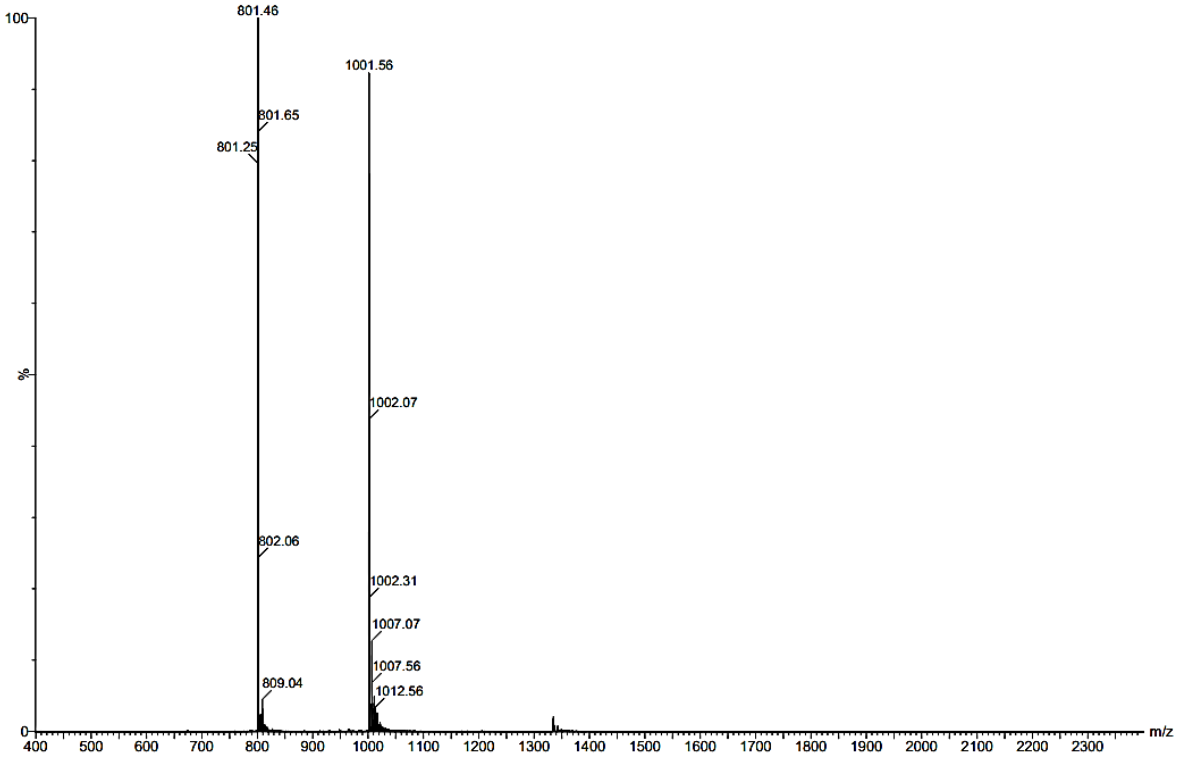


Figure A.15: a) Analytical HPLC trace of pure CS1-1 (retention time 26.7 min.) using a linear 0 to 100% MeCN + 0.05% TFA gradient in H_2O + 0.05% TFA over 60 minutes. b) Electrospray mass spectrum of pure CS1-1 (MW 4002.6 g/mol).

APPENDIX B

MATLAB SCRIPTS

B.1 Script 1: r_1 as a function of r_{MH} and τ_m (Chapters 3 & 4)

```
% Giulia Molinaro
% School of Chemistry, University of Birmingham

% MATLAB script
% to determine r1 using a range of constants and variables

% Computes and plots r1 as a function of tm and r
% Mesh plot and surface plot available

%--------------------------------------------------------------------------

format long

%% Constants

% H2O = molar concentration of water (mM)
H2O = 55600;

% YH = proton gyromagnetic ratio (rad/(s*T))
YH = 2.675e8;

% uB = Bohr magneton (J/T)
uB = 9.274e-24;

% g = g-factor
g = 2;

% s = spin quantum number
% Cu
s = 1/2;
% Gd
%s = 7/2;

%--------------------------------------------------------------------------

%% Variables
% q = number of coordinated waters
q = 1;

% r = ion-proton distance (m)

nr = 100;
r = linspace(2.5e-10,3.5e-10,nr)

% tm = water residence time (s)
tm = logspace(-10,-5,200)
```

```
%B = magnetic field (T)
B = 1.4;
%B = 7;

%WH = Larmor frequency of proton (rad/s)
WH = YH * B;

%tR = rotational correlation time (s)
tR = 6.9e-9;

%ts= electron relaxation time (s)
ts = 5e-9

%--------------------------------------------------------------------------

%% Calculations
[X,Y] = meshgrid(tm,r);

% tC = total rotational correlation time (s)
tC = 1./(1/tR + 1/ts + 1./X);

% T1m = relaxation time (s)
k1 = (2/15)*(1e-14)* YH^2 * g^2 * uB^2 * s *(s+1) ./ (Y.^6);
v1 = 3.*tC./(1+ WH^2 .* tC.^2);
T1m = 1./(k1.*v1)

% r1 = relaxivity (mM-1*s-1)
k2 = (q/H2O);
% Extension of tm to match the size of T1m:
% nr is the number of q-values defined above
tmext = repmat(tm,nr,1);

r1 = k2 ./ (T1m + tmext)

%--------------------------------------------------------------------------

%% 3D Plots
h = figure;
A = axes;

% Option 1: mesh plot
%mesh(X,Y,r1)
% Option 2: surface plot
surf(X,Y,r1)
set(A,'XScale','log')

% Labels and title
xlabel('{\it{\tau}}_m / s');
ylabel('{\it{r}} / m\times10^{-10}');
zlabel('r1 / mM-1*s-1', 'Rotation',0);
title({'1.4 T, q=1, ts=5ns'});

% Colorbar
colorbar('peer',A,'westoutside');

% Colormap
```

```
colormap(rgb);

saveas(gcf,'GM_fig_7_0903.pdf')

%-------------------------------------------------------------------------

%% Save input data to ASCII file
filename = 'GM_set_7_0903.txt';
fid = fopen(filename, 'w');
fprintf(fid, date);
%timestamp = datestr(now, 'dd/mm/yy HH:MM')
varset = [q; B; tR];
fprintf(fid, ': q=%4.1f; B=%6.2f T; tR=%12.4e s',varset);
fclose(fid);

%-------------------------------------------------------------------------
```

B.2 Script 2: r_1 as a function of τ_R and τ_m (Chapter 7)

```
% Giulia Molinaro
% School of Chemistry, University of Birmingham

% MATLAB script
% to determine r1 using a range of constants and variables

% Computes and plots r1 as a function of tm and tr
% Mesh plot and surface plot available

%--------------------------------------------------------------------------

format long

%% Constants

% H2O = molar concentration of water (mM)
H2O = 55600;

% YH = proton gyromagnetic ratio (rad/(s*T))
YH = 2.675e8;

% uB = Bohr magneton (J/T)
uB = 9.274e-24;

% g = g-factor
g = 2;

% s = spin quantum number
% Cu
s = 1/2;
% Gd
%s = 7/2;

%--------------------------------------------------------------------------

%% Variables
% q = number of coordinated waters
q = 1;

%tr = rotational correlation time (s)
nr = 100;
tr = logspace(-10,-7,100)

%ts= electron relaxation time (s)

ts=5e-9

% tm = water residence time (s)
tm = logspace(-10,-7,200)

%B = magnetic field (T)
B = 1.4;

%WH = Larmor frequency of proton (rad/s)
```

```
WH = YH * B;

%distance M-H (r)
r=2.7e-10
%r=3.1e-10

%--------------------------------------------------------------------------

%% Calculations
[X,Y] = meshgrid(tm,tr);

% tC = total rotational correlation time (s)
tC = 1./(1./X + 1./Y + 1/ts);

% T1m = relaxation time (s)
k1 = (2/15)*(1e-14)* YH^2 * g^2 * uB^2 * s *(s+1) ./ (r^6);
v1 = 3.*tC./(1+ WH^2 .* tC.^2);
T1m = 1./(k1.*v1)

% r1 = relaxivity (mM-1*s-1)
k2 = (q/H2O);
% Extension of tm to match the size of T1m:
%  nr is the number of q-values defined above
tmext = repmat(tm,nr,1);

r1 = k2 ./ (T1m + tmext)

%--------------------------------------------------------------------------

%% 3D Plots
h = figure;
A = axes;

% Option 1: mesh plot
%mesh(X,Y,r1)
% Option 2: surface plot
surf(X,Y,r1)
set(A,'XScale','log')
set(A,'YScale','log')

% Labels and title
xlabel('{\it{\tau}}_m / s');
ylabel('{\it{\tau}}_R / s');
zlabel('r1 / mM-1*s-1', 'Rotation',0);
title({'1.4 T, q=1, 2.7 A'});

% Colorbar
colorbar('peer',A,'westoutside');

% Colormap
colormap(rgb);

saveas(gcf,'GM_fig_60.pdf')

%--------------------------------------------------------------------------

%% Save input data to ASCII file
```

```
filename = 'GM_set_60.txt';
fid = fopen(filename, 'w');
fprintf(fid, date);
%timestamp = datestr(now, 'dd/mm/yy HH:MM')
varset = [q; B; r];
fprintf(fid, ': q=%4.1f; B=%6.2f T; tR=%12.4e s',varset);
fclose(fid);

%--------------------------------------------------------------------------
```